MISC-88-01

Transverse Load Distribution at Ultimate Limit States in Single Span Slab-on-Girder Bridges with Compact Steel Girders

Ontario
Ministry
of
Transportation
Research and
Development
Branch

Technical Report Documentation Page

Transverse Load Distribution at Ultimate Limit States in Single Span Slab-on-Girder Bridges with Compact Steel Girders

Author(s):	A. G. Razaqpur, Principal Investigator M. Nofal, Research Assistant
Number:	MISC-88-01
Date of Publication:	September 1988
Ministry Contact:	Baidar Bakht
Abstract:	An extensive analytical and experimental investigation was undertaken to study the load distribution characteristics of simply supported composite concrete slab on compact steel girder bridges at all stages of loading. Detailed parametric analyses were conducted to find the influence of many geometric and loading factors upon load distribution. The results were compared with available methods of load distribution analysis and with the provisions of the Ontario Highway Bridge Design Code. The analytical tool employed was the nonlinear finite element method. Because compact sections were used, only material nonlinearities were dealt with. Special finite elements were developed to better simulate the behaviour of the bridge and its components. This included a special element for the simulation of the shear studs that connect the concrete slab to the steel girders. All aspects of the analytical model were verified by comparing the results with available experimental data and/or closed form solutions. In addition, a large scale three girder bridge was designed and tested to further verify the analytical procedure and to study the load distribution characteristics of such bridges. The comparison between the finite element results and the experimental data in all cases was favourable. The analysis of the parametric study results revealed that none of the available methods can predict the load distribution characteristics of composite slab-on-girder bridges under all loading conditions. However, it was determined that the OHBD code yields results that are on the conservative side.
Comments:	
Key words:	
Distribution:	Limited.
Copyright Status:	Crown copyright © 1988 Ministry of Transportation

MISC-88-01

Transverse Load Distribution at Ultimate Limit States in Single Span Slab-on-Girder Bridges with Compact Steel Girders

A. G. Razaqpur
Principal Investigator
Carleton University

M. Nofal
Research Assistant
Carleton University

Published by
The Research and Development Branch
Ministry of Transportation, Ontario
Hon. Ed Fulton, Minister
D.G. Hobbs, Deputy Minister

Published without prejudice as to the application of the findings.
Crown copyright reserved; however, this document may be reproduced for non-commercial purposes with attribution to the Ministry.

For additional copies, contact:
The Editor, Technical Publications
Room 320, Central Building
1201 Wilson Avenue
Downsview, Ontario
Canada M3M 1J8

Telephone: (416) 235-3480
CNCP Dialcom Electronic Mail: 23:MIN006

September 1988

ABSTRACT

An extensive analytical and experimental investigation was undertaken to study the load distribution characteristics of simply supported composite concrete slab on compact steel girder bridges at all stages of loading. Detailed parametric analyses were conducted to find the influence of many geometric and loading factors upon load distribution. The results were compared with available methods of load distribution analysis and with the provisions of the Ontario Highway Bridge Design code.

The analytical tool employed was the nonlinear finite element method. Because compact sections were used, only material nonlinearities were dealt with. Special finite elements were developed to better simulate the behavior of the bridge and its components. This included a special element for the simulation of the shear studs that connect the concrete slab to the steel girders.

All aspects of the analytical model were verified by comparing the results with avaliable experimental data and/or closed form solutions. In addition, a large scale three girder bridge was designed and tested to further verify the analytical procedure and to study the load distribution characteristics of such bridges. The comparison between the finite element results and the experimental data in all cases was favourable.

The analysis of the parametric study results revealed that none of the available methods can predict the load distribution characteristics of composite slab-on-girder bridges under all loading conditions. However, it was determined that the OHBD code yields results that are on the conservative side.

ACKNOWLEDGMENTS

The authors would like to thank Mr. Baidar Bakht, the Principal Research Engineer of the Ministry of Transportation of Ontario, for his constant support and valuable suggestions regarding both the analytical and experimental aspects of the current study.

We would also like to thank Mr. Ken McMartin, the manager of the Civil Engineering laboratories, and the structural laboratory staff, for their help and enthusiasm during the preparation and testing of the bridge model. Thanks are also due to Mr. Stanley Conley for writing the software used in collecting the experimental data.

TABLE OF CONTENTS

ABSTRACT ii

ACKNOWLEDGMENTS iii

TABLE OF CONTENTS iv

LIST OF TABLES viii

LIST OF FIGURES xiii

LIST OF IMPORTANT NOTATIONS xx

1 INTRODUCTION 1

- 1.1 The Problem 1
- 1.2 Objective and Scope 2

2 LITERATURE REVIEW 5

- 2.1 General 5
- 2.2 Previous Work 5
- 2.3 Existing Methods of Analysis 10
  - 2.3.1 *Elastic Methods* 10
  - 2.3.2 *Plastic Methods* 10
- 2.4 Codes Approach 13
- 2.5 Load Distribution Factor Based on Nonlinear Analysis 16

3 THE FINITE ELEMENT PROGRAM 19

- 3.1 General 19
- 3.2 General Description of *NONLACS* 19
- 3.3 Basic Equations of Finite Element 20
- 3.4 The Finite Elements Employed 21
  - 3.4.1 *The Bar Element* 22
  - 3.4.2 *Shear Connector Element* 22
  - 3.4.3 *Refined Plane Quadrilateral Element (RQUAD4)* 24
    - 3.4.3.1 *Element Formulation* 25
    - 3.4.3.2 *Short Cantilever Beam under Tip Load* 28
    - 3.4.3.3 *Pure inplane Bending of a Square Plate* 29

3.4.3.4 *Tapered Skew Cantilever with Uniform Shear at the Free End* 29
3.4.4 *Four Node Quadrilateral Bending Element (QBE)* 30
3.4.5 *Quadrilateral Facet Shell Element (QFSE)* 31

3.5 Material Modelling 33
3.5.1 *Concrete Modelling* 34
3.5.2 *Modelling Reinforcing and Prestressing Steel* 37
3.5.3 *Modelling Steel as a Continuum* 37

3.6 Nonlinear Analysis Method 40

4 VERIFICATION OF FINITE ELEMENT PROGRAM BY EXPERIMENTAL DATA 43
4.1 General 43

4.2 Verification of Steel Plasticity Model 43
4.2.1 *Cantilever Beam Subjected to Tip Load* 44
4.2.2 *Simply Supported Beam under Uniform Line Load* 45
4.2.3 *Plate under Uniform Load* 45

4.3 Verification of the Shear Connector Element and the Composite Structures Analysis Capability 46
4.3.1 *Imperial College Beams* 47
4.3.2 *University of Alberta Continuous Beam* 48
4.3.3 *University of Tennessee Multi-Girder Bridge* 49

5 EXPERIMENTAL INVESTIGATION 52

5.1 General 52

5.2 Bridge Model 53

5.3 Material Properties 54

5.4 Experimental Set-up 55

5.5 Instrumentation and Data Aquisition 56

5.6 Finite Element Analysis of the Bridge Model 57

5.7 Experimental Results 58
5.7.1 *Load-Deflection of Girders* 59
5.7.2 *Strain Variation in Girders Flanges* 60
5.7.3 *Strain Variation in the Concrete* 60
5.7.4 *Strain Variation in Transverse Reinforcement* 61
5.7.5 *Slip of Concrete-Steel Interface* 62
5.7.6 *Moment Variation in the Girders* 62
5.7.7 *Distribution Parameter, D_d, of the Girders* 63

6 PARAMETRIC STUDY 65

6.1 Selection of Parameters 65

6.2 Selection and Design of Bridges 66

6.3 Presentation of Results 67

6.4 Parametric Study 68

6.4.1 *Truck Position* 68

6.4.1.1 *Longitudinal Truck Position* 68

6.4.1.2 *Transverse Truck Position (Edge Distance)* 71

6.4.2 *Bridge Width* 74

6.4.3 *Span / Width Ratio* 76

6.4.4 *Girder Spacing* 78

6.4.5 *Number of Girders* 81

6.4.6 *Slab/Girder Stiffness Ratio* 84

6.4.7 *Degree of Interaction* 87

7 ANALYSIS OF PARAMETRIC STUDY 92

7.1 General 92

7.2 Selection of Available Methods for Comparison 92

7.3 Effect of Different Parameters upon D_d 93

7.3.1 *Longitudinal Truck Position* 93

7.3.2 *Transverse Truck Position (Edge Distance)* 93

7.3.3 *Bridge Width* 94

7.3.4 *Bridge Width/Span Ratio* 95

7.3.5 *Girder Spacing* 95

7.3.6 *Number of Girder* 96

7.3.7 *Slab/Girder Stiffness Ratio* 96

7.3.8 *Degree of Interaction* 97

8 SUMMARY AND CONCLUSIONS 99

8.1 Summary 99

8.2 Conclusions 100

8.3 Recommendations for Future Work 101

REFERENCES 103

TABLES 109

FIGURES 141

APPENDIX A 276

APPENDIX B 279

List of Tables

1 Distribution Parameter (Elastic Load) 109

2 Distribution Parameter (Ultimate Load) 110

3 Comparisons of Displacements and Stresses 111

4 Vertical deflection at C for different mesh sizes 111

5 Normal stress, σ_z, at A for different mesh sizes 112

6 Normal stress, σ_z, at B for different mesh sizes 112

7 Material Properties for Beam E11 112

8 Material Properties for Beam CB2 113

9 Analytical and Experimental Results comparison 113

10 University of Tennesse Bridge Material Properties 114

11 University of Tennesse Bridge Results comparison 114

12 Compressive Strength after 28 Days 114

13 Compressive Strength after Five Monthes 115

14 Tensile Strength after Five Monthes 115

15 Material Properties Used in the Analysis 115

16 D_d for Longitudinal Truck Position Parameter and Loading Case 1 for Three Girder Bridge (Maximum Moment) . . . 116

17 D_d for Longitudinal Truck Position Parameter and Loading Case 1 for Three Girder Bridge (Maximum Shear) 116

18 D_d for Longitudinal Truck Position Parameter and Loading Case 2 for Three Girder Bridge (Maximum Bending) . . . 116

19 D_d for Longitudinal Truck Position Parameter and Loading Case 2 for Three Girder Bridge (Maximum Shear) 117

20 D_d for Longitudinal Truck Position Parameter and Loading Case 1 for Four Girder Bridge (Maximum Moment) 117

21 D_d for Longitudinal Truck Position Parameter and Loading Case 1 for Four Girder Bridge (Maximum Shear) 117

22 D_d for Longitudinal Truck Position Parameter and Loading Case 2 for Four Girder Bridge (Maximum Bending) 118

23 D_d for Longitudinal Truck Position Parameter and Loading Case 2 for Four Girder Bridge (Maximum Shear) 118

24 D_d for Edge Distance Parameter Case 1 (Three Girder Bridge) 118

25 D_d for Edge Distance Parameter Case 2 (Three Girder Bridge) 119

26 D_d for Edge Distance Parameter Case 3 (Three Girder Bridge) 119

27 D_d for Edge Distance Parameter Case 1 (Four Girder Bridge) 119

28 D_d for Edge Distance Parameter Case 2 (Four Girder Bridge) 120

29 D_d for Edge Distance Parameter Case 3 (Four Girder Bridge) 120

30 D_d for Edge Distance Parameter Case 4 (Four Girder Bridge) 120

31 D_d for Bridge Width Parameter $B = 8m$ (Three Girder Bridge) 121

32 D_d for Bridge Width Parameter $B = 12m$ (Five Girder Bridge) 121

33 D_d for Bridge Width Parameter $b = 16m$ (Six Girder Bridge) 121

34 D_d for Span-Width Ratio Parameter $\frac{2b}{L} = 0.33$ (Case 1) 122

35 D_d for Span-Width Ratio Parameter $\frac{2b}{L} = 0.25$ (Case 1) 122

36 D_d for Span-Width Ratio Parameter $\frac{2b}{L} = 0.20$ (Case 1) 122

37 D_d for Span-Width Ratio Parameter $\frac{2b}{L} = 0.33$ (Case 2) 123

38 D_d for Span-Width Ratio Parameter $\frac{2b}{L} = 0.25$ (Case 2) 123

39 D_d for Span-Width Ratio Parameter $\frac{2b}{L} = 0.20$ (Case 2) 123

40 D_d for Span-Width Ratio Parameter $\frac{2b}{L} = 0.33$ (Case 3) 124

41 D_d for Span-Width Ratio Parameter $\frac{2b}{L} = 0.25$ (Case 3) 124

42 D_d for Span-Width Ratio Parameter $\frac{2b}{L} = 0.20$ (Case 3) 124

43 D_d for Girder Spacing Parameter $GS = 3.000$ in Three Girder System (Case 1) 125

44 D_d for Girder Spacing Parameter
$GS = 3.375$ in Three Girder System (Case 1) 125

45 D_d for Girder Spacing Parameter
$GS = 3.750$ in Three Girder System (Case 1) 125

46 D_d for Girder Spacing Parameter
$GS = 3.000$ in Three Girder System (Case 2) 126

47 D_d for Girder Spacing Parameter
$GS = 3.375$ in Three Girder System (Case 2) 126

48 D_d for Girder Spacing Parameter
$GS = 3.750$ in Three Girder System (Case 2) 126

49 D_d for Girder Spacing Parameter
$GS = 3.000$ in Three Girder System (Case 3) 127

50 D_d for Girder Spacing Parameter
$GS = 3.375$ in Three Girder System (Case 3) 127

51 D_d for Girder Spacing Parameter
$GS = 3.750$ in Three Girder System (Case 3) 127

52 D_d for Girder Spacing Parameter
$GS = 2.000$ in Four Girder System (Case 1) 128

53 D_d for Girder Spacing Parameter
$GS = 2.250$ in Four Girder System (Case 1) 128

54 D_d for Girder Spacing Parameter
$GS = 2.500$ in Four Girder System (Case 1) 128

55 D_d for Girder Spacing Parameter
$GS = 2.000$ in Four Girder System (Case 2) 129

56 D_d for Girder Spacing Parameter
$GS = 2.250$ in Four Girder System (Case 2) 129

57 D_d for Girder Spacing Parameter
$GS = 2.500$ in Four Girder System (Case 2) 129

58 D_d for Girder Spacing Parameter
$GS = 2.000$ in Four Girder System (Case 3) 130

59 D_d for Girder Spacing Parameter
$GS = 2.250$ in Four Girder System (Case 3) 130

60 D_d for Girder Spacing Parameter
$GS = 2.500$ in Four Girder System (Case 3) 130

61 D_d for Slab-Girder Stiffness Ratio Parameter
$\frac{I_{zs}}{I_{zG}} = 0.293$ (Case 1) 131

62 D_d for Slab-Girder Stiffness Ratio Parameter
$\frac{I_{zs}}{I_{zG}} = 0.382$ (Case 1) 131

63 D_d for Slab-Girder Stiffness Ratio Parameter
$\frac{I_{zs}}{I_{zG}} = 0.531$ (Case 1) 131

64 D_d for Slab-Girder Stiffness Ratio Parameter $\frac{I_{ss}}{I_{sG}} = 0.293$ (Case 2) 132

65 D_d for Slab-Girder Stiffness Ratio Parameter $\frac{I_{ss}}{I_{sG}} = 0.382$ (Case 2) 132

66 D_d for Slab-Girder Stiffness Ratio Parameter $\frac{I_{ss}}{I_{sG}} = 0.531$ (Case 2) 132

67 D_d for Slab-Girder Stiffness Ratio Parameter $\frac{I_{ss}}{I_{sG}} = 0.293$ (Case 3) 133

68 D_d for Slab-Girder Stiffness Ratio Parameter $\frac{I_{ss}}{I_{sG}} = 0.382$ (Case 3) 133

69 D_d for Slab-Girder Stiffness Ratio Parameter $\frac{I_{ss}}{I_{sG}} = 0.531$ (Case 3) 133

70 D_d for Total Number of Girders Parameter for Three Girder System (Case 1) 134

71 D_d for Total Number of Girders Parameter for Four Girder System (Case 1) 134

72 D_d for Total Number of Girders Parameter for Three Girder System (Case 2) 134

73 D_d for Total Number of Girders Parameter for Four Girder System (Case 2) 135

74 D_d for Total Number of Girders Parameter for Three Girder System (Case 3) 135

75 D_d for Total Number of Girders Parameter for Four Girder System (Case 3) 135

76 D_d for Total Number of Girders Parameter for Five Girder System (Case 3) 136

77 D_d for Total Number of Girders Parameter for Six Girder System (Case 3) 136

78 D_d for Degree of Interaction Parameter Degree of Composition = 0.3% (Case 1) 137

79 D_d for Degree of Interaction Parameter Degree of Composition = 50.0% (Case 1) 137

80 D_d for Degree of Interaction Parameter Degree of Composition = 100.0% (Case 1) 137

81 D_d for Degree of Interaction Parameter Degree of Composition = 600.0% (Case 1) 138

82 D_d for Degree of Interaction Parameter Degree of Composition = 0.3% (Case 2) 138

83 D_d for Degree of Interaction Parameter
Degree of Composition = 50.0% (Case 2) 138

84 D_d for Degree of Interaction Parameter
Degree of Composition = 100.0% (Case 2) 139

85 D_d for Degree of Interaction Parameter
Degree of Composition = 600.0% (Case 2) 139

86 D_d for Degree of Interaction Parameter
Degree of Composition = 0.3% (Case 3) 139

87 D_d for Degree of Interaction Parameter
Degree of Composition = 50.0% (Case 3) 140

88 D_d for Degree of Interaction Parameter
Degree of Composition = 100.0% (Case 3) 140

89 D_d for Degree of Interaction Parameter
Degree of Composition = 600.0% (Case 3) 140

List of Figures

1 Idealized Girder and its Loading According to D-Type Distribution Method . . . 141

2 OHBD Commercial Truck . . . 142

3 Truck Loading Configurations According to Codes . . . 143

4 Typical 3-D Bar Element . . . 144

5 Shear Stud Connector . . . 145

6 Typical Load-Slip Curve for Flexiable Shear Connector . . . 146

7 Finite Elements . . . 147

8 Displacement u_n due to$w_1 = 1$ . . . 147

9 Short Cantilever under Concentrated Tip Load . . . 148

10 Convergence Study of RQUAD4 and Comparison with Other Elements . 149

11 Square Plate under Inplane Bending . . . 150

12 Skew Tapered Cantilever under Uniform Shear at the Tip C . . . 151

13 Variation of Normal Stresses along Section A-B . . . 152

14 Bending Element QBE . . . 153

15 The Facet Shell Element QFSE . . . 153

16 Layered Finite Element . . . 154

17 Properties of Concrete
(a) Uniaxial Stress-Strain Relationship
(b) Schematic of Biaxial Failure Envelope . . . 155

18 Tensile Stress-Strain Relation for Concrete . . . 156

19 Stress-Strain Relation for Steel . . . 156

20 Cantilever Beam Used in Elasto-Plastic Study . . . 157

21 Cantliver Beam under Tip Load
(a) Load Tip Deflection curve
(b)progression of Plasticity . . . 158

22 Simply Supported Beam under Uniform Load . . . 159

23 Simply Supported Beam (a) Load Midspan Deflection
(b)progression of Plasticity . . . 160

24 Simply Supported Square Plate under Uniform Load . . . 161

25 Simply Supported Square Plate under Uniform Load
(a) Load-Central Point Deflection Curve
(b) Elastic and Plastic Zones at Collapse Load 162

26 Yam and Chapman's Simply Supported Beam 163

27 Typical Finite Element Mesh Use
(a)Mesh Details for Different Parts
(b)Elements Used and Their Details
(c)Numbering Scheme 164

28 Yam and Chapman's Simply Supported Beam
(a) Load Midspan Deflection Curve
(b) Slip Distribution along the Beam axis
at Load P=45 tons 165

29 Yam and Chapman's Continuous Beam 166

30 Finite Element Mesh Utilized 167

31 Yam and Chapman's Continous Beam
(a) Deflection Curve
(b) Slip Distribution along the Span
(c) Strain Profile along the span in the Bottom Flange
of the Steel Beam at P = 12.2 tons 168

32 Univeristy of Alberta Continuous Beam CB2 169

33 Beam CB2
(a) Finite Element and Boundary Conditions
(b) Details of Shell Elements in the Positive Moment Regions
(c) Details of Shell Elements in the Negaitive Moment Regions 170

34 Load Maximum Deflection of University of Alberta Continuous Beam . . 171

35 Progression of Yielded and Cracked Regions Through
the Depth for Univeristy of Alberta Continuous Beam CB2 172

36 Actual and Idealized Cross Section of Tennessee Multigirder Bridge . . . 173

37 University of Tennessee Multigirder Bridge 174

38 Finite Element Mesh Used for Tennessee Bridge 175

39 Load Maximum Deflection Curve of
University of Tennessee Multigirder Bridge 176

40 General Layout of Bridge Model 177

41 Shear Studs Details 178

42 Desposition of Bottom Reinforcement Layer 179

43 Bridge Support Details 180

44 Construction Stages of Bridge Model 181

45 Stress-Strain Relationship of Reinforcing Bars 182

46 Stress-Strain Relationship of Used for Steel Beams 182

47 Experimental Loading System 183

48 Experimental Set-up 184

49 Longitudinal Strain Gauges Locations in the Steel Beams 185

50 Longitudinal Strain Gauges Locations on the Concrete Surface 186

51 Locations of Strain Gauges Attached to Transverse Slab Reinforcement 187

52 LVDT's Locations 188

53 Details of LVDT's Attachment 189

54 Schematic Detail of a Typical LVDT Used for Slip Measurement 190

55 Finite Element Idealization of Half Bridge 191

56 some Problems with Transfer Elements 192

57 Punching of Concrete under the Heaviest Concentrated Load 193

58 Load-Maximum Deflection Curves of Bridge Girders 194

59 Deflection Curves of Bridge Girders at Various Stages of Loading 195

60 Variation of Strain along the Bottom Flange of Bridge Girders 196

61 Variation of Strain along the Top Flange of Bridge Girders 197

62 Variation of Strain along the Top Surface of the Concrete Slab 198

63 Variation of Strain on the Bottom Transverse Steel Reinforcement Layer 199

64 Variation of Strain on the Top Transverse Steel Reinforcement Layer 200

65 Slip at Slab-Girder Interface at 500 mm from Right Support 201

66 Longitudinal Moment Variation of the Bridge Girders 202

67 Variation of the Girders Distribution Parameter with Increased Loading 203

68 Variation of Distribution along the Bridge Girders 204

69 The $\alpha - \theta$ Plane Showing the Bridges Analyzed in this Study 205

70 Longitudinal Truck Positions Considered 206

71 Transverse Truck Positions Considered 207

72 Effect of Longitudinal Truck Position on Load-Maximum Deflection of Bridge LP1 208

73 Effect of Longitudinal Truck Position on Load-Maximum Deflection of Bridge LP2 209

74 Effect of Longitudinal Truck Position on
Load-Maximum Deflection of Bridges LP1 and LP2 210

75 Effect of Longitudinal Truck Position on
Moment Distribution in Bridges LP1 211

76 Effect of Longitudinal Truck Position on
Moment Distribution in Bridges LP2 212

77 Effect of Longitudinal Truck Position on
Moment Distribution in Bridges LP1 and LP2 213

78 Effect of Longitudinal Truck Position on
Distribution Parameter, D_d, ... 214

79 Vehicle-Edge Distance
(a) Definition
(b) Distances Considered for Bridge LP1
(c) Distance Considered for LP2 215

80 Effect of Transverse Truck Position on
Load-Maximum Deflection of Bridge LP1 216

81 Effect of Transverse Truck Position on
Load-Maximum Deflection of Bridge LP2 217

82 Effect of Transverse Truck Position on
Deflection Distribution among the Girders of Bridges LP1 218

83 Effect of Transverse Truck Position on
Deflection Distribution among the Girders of Bridges LP2 219

84 Effect of Transverse Truck Position on
Moment Distribution in Bridges LP1 220

85 Effect of Transverse Truck Position on
Moment Distribution in Bridges LP2 221

86 Effect of Transverse Truck Position on
Total Moment Distribution of Bridges LP1 222

87 Effect of Transverse Truck Position on
Total Moment Distribution of Bridges LP2 222

88 Effect of Transverse Truck Position on
Distribution Parameter, D_d, ... 223

89 Bridge Geometry and Loading Used for
Bridge Width Effect Study 224

90 Effect of Bridge Width on Load-Maximum Deflection
of Bridges BW1, BW2 and BW3 225

91 Effect of Bridge Width on Moment Distribution
in Bridges BW1, BW2 and BW3 226

92 Effect of Bridge Width on
Distribution Parameter, D_d, ... 227

93 Transverse Loading Cases Used in Parameteric Study . . . 228

94 Effect of Span-Length to Width Ratio on Load-Maximum Deflection of Bridges LW1, LW2 and LW3 (Case 1) . . . 229

95 Effect of Span-Length to Width Ratio on Load-Maximum Deflection of Bridges LW1, LW2 and LW3 (Case 2 and 3) . . . 230

96 Effect of Span-Length to Width Ratio on Moment Distribution of Bridges LW1, LW2 and LW3 (Case 1) . . . 231

97 Effect of Span-Length to Width Ratio on Moment Distribution of Bridges LW1, LW2 and LW3 (Case 2 and 3) . . . 232

98 Effect of Span-Length to Width on Distribution Parameter, D_d, . . . 233

99 Effect of Girder Spacing on Load-Maximum Deflection of Bridges GS1, GS2 and GS3 (Case 1) . . . 234

100 Effect of Girder Spacing on Load-Maximum Deflection of Bridges GS1, GS2 and GS3 (Case 2 and 3) . . . 235

101 Effect of Girder Spacing on Load-Maximum Deflection of Bridges GS4, GS5 and GS6 (Case 1) . . . 236

102 Effect of Girder Spacing on Load-Maximum Deflection of Bridges GS4, GS5 and GS6 (Case 2) . . . 237

103 Effect of Girder Spacing on Load-Maximum Deflection of Bridges GS4, GS5 and GS6 (Case 3) . . . 238

104 Effect of Girder Spacing on Moment Distribution of Bridges GS1, GS2 and GS3 (Case 1) . . . 239

105 Effect of Girder Spacing on Moment Distribution of Bridges GS1, GS2 and GS3 (Case 2 and 3) . . . 240

106 Effect of Girder Spacing on Moment Distribution of Bridges GS4, GS5 and GS6 (Case 1) . . . 241

107 Effect of Girder Spacing on Moment Distribution of Bridges GS4, GS5 and GS6 (Case 2) . . . 242

108 Effect of Girder Spacing on Moment Distribution of Bridges GS4, GS5 and GS6 (Case 3) . . . 243

109 Effect of Girder Spacing on Distribution Parameter, D_d, (Bridges GS1, GS2 and GS3) . . . 244

110 Effect of Girder Spacing on Distribution Parameter, D_d, (Bridges GS4, GS5 and GS6) . . . 245

111 Effect of Number of Girder on Load-Maximum Deflection of Bridges NG3 and NG4 (Case 1) . . . 246

112 Effect of Number of Girder on Load-Maximum Deflection of Bridges NG3 and NG4 (Case 2) 247

113 Effect of Number of Girder on Load-Maximum Deflection of Bridges NG3 and NG4 (Case 3) 248

114 Effect of Number of Girder on Total Moments in Bridges NG3 and NG4 249

115 Effect of Number of Girder on Moment Distribution in Bridges NG3 and NG4 (Case 1) 250

116 Effect of Number of Girder on Moment Distribution in Bridges NG3 and NG4 (Case 2) 251

117 Effect of Number of Girder on Moment Distribution in Bridges NG3 and NG4 (Case 3) 252

118 Effect of Number of Girder on Distribution Parameter, D_d, ... 253

119 Effect of Slab-Girder Stiffness Ratio on Load-Maximum Deflection of Bridges ST1, ST2 and ST3 (Case 1) . . . 254

120 Effect of Slab-Girder Stiffness Ratio on Load-Maximum Deflection of Bridges ST1, ST2 and ST3 (Case 2 and 3) 255

121 Effect of Slab-Girder Stiffness Ratio on Moment Distribution in Bridges ST1, ST2 and ST3 (Case 1) 256

122 Effect of Slab-Girder Stiffness Ratio on Moment Distribution in Bridges ST1, ST2 and ST3 (Case 2 and 3) 257

123 Effect of Slab-Girder Stiffness Ratio on Distribution Parameter, D_d, ... 258

124 Shear Connector Load-Slip Relationships Employed in the Analysis . . . 259

125 Effect of Degree of Interaction on Load-Maximum Deflection of Bridges DI1, DI2, DI3 and DI4 (Case 1) 260

126 Effect of Degree of Interaction on Load-Maximum Deflection of Bridges DI1, DI2, DI3 and DI4 (Case 2) 261

127 Effect of Degree of Interaction on Load-Maximum Deflection of Bridges DI1, DI2, DI3 and DI4 (Case 3) 262

128 Effect of Degree of Interaction on Moment Distribution in Bridges DI1, DI2, DI3 and DI4 (Case 1) 263

129 Effect of Degree of Interaction on Moment Distribution in Bridges DI1, DI2, DI3 and DI4 (Case 2) 264

130 Effect of Degree of Interaction on Moment Distribution in Bridges DI1, DI2, DI3 and DI4 (Case 3) 265

131 Effect of Degree of Interaction on Distribution Parameter, D_d, ... 266

132 Variation of Distribution Parameter, D_d, with Longitudinal Postion of the Truck 267

133 Variation of Distribution Parameter, D_d, with Transverse Postion of the Truck 268

134 Variation of Distribution Parameter, D_d, with Bridge Width 269

135 Variation of Distribution Parameter, D_d, with Bridge Width/Span Ratio 270

136 Variation of Distribution Parameter, D_d, with Girder Spacing (Three Girder System) 271

137 Variation of Distribution Parameter, D_d, with Girder Spacing (Four Girder System) 272

138 Variation of Distribution Parameter, D_d, with Number of Girders 273

139 Variation of Distribution Parameter, D_d, with Slab/Girder Stiffness Ratio 274

140 Variation of Distribution Parameter, D_d, with Degree of Interaction 275

LIST OF IMPORTANT NOTATIONS

A_s	longitudinal or transverse reinforcement area
A	area of steel section
$[A]$	vector of polynomial coefficients
$\{a\}$	flow vector
$[B]$	strain-displacement matrix
b	half-width of the bridge
b	equivalent slippage
$[D]$	elasticity matrix
D_d	distribution parameter
$[D]_{ep}$	elasto-plastic constitutive matrix
D_f	distribution factor
D_x	longitudinal flexural rigidity per unit width
D_y	transverse flexural rigidity per unit width
D_{xy}, D_{yx}	longitudinal torsional rigidity per unit width
D_1, D_2	transverse torsional rigidity per unit width
$\{d\}$	vector of nodal displacements
$(d\epsilon_{ij})_e$	elastic strain increment tensor
$(d\epsilon_{ij})_p$	plastic strain increment tensor
E_c	secant modulus of elasticity of concrete at peak stress
E_o	intial tangent modulus of concrete
E_1, E_2	tangent moduli in the principal material directions.
E_G	Young's modulus of steel girders
E_c	Young's modulus of the concrete slab
$E^*{}_s$	strain hardening modulus of steel
$\{F\}_b$	vector of nodal forces due to body forces
$\{F\}_s$	vector of nodal forces due to surface tractions
$\{F\}_{\epsilon}^{-}$	vector of nodal forces due to intial strains
$\{F\}_{\sigma}^{-}$	vector of nodal forces due to intial stresses.
f	yield function
f_c'	compressive cylinder strength of concrete
$f'{}_t$	uniaxial tensile strength of concrete
f_y	yield strength of steel
G	shear modulus
G_{cr}	shear modulus of cracked concrete
H	hardening function
h	height of steel section
$J_2{}'$, $J_3{}'$	invariants of the deviatoric stress tensor
I_G	flexural moments of inertia of the girder cross-section.
J_G	torsional moments of inertia of the girder cross-section.
$[k]$	global structure stiffness matrix
$[k]_e$	element stiffness matrix
$[k]_{pp}$	plane stiffness matrix
$[k]_{bb}$	bending stiffness matrix
$[k]_{pb}$, $[k]_{bp}$	coupling stiffness matrices
l	span of the bridge.

M	total moment on a given section of the bridge
M_{AASHTO}	maximum moment in a single girder due to truck loading as given in the *AASHTO* code
M_G	girder moment
M_T	total longitudinal moment on a given section of the bridge
M_y	yielding moment of girder
N	No. of trucks/No. of traffic lanes
$[N]$	the shape functions matrix
$NL,$	number of traffic lanes
N_B	number of girders
P	concentrated load
P_u	ultimate load
Q	plastic potential
q	intensity of uniformly distributed surface load
q_s	intensity of uniformly distributed surface load
q_G	intensity of uniform line load resisted by the girder
$[T]$	transformation matrix
S	girder spacing
$\{R\}$	vector of applied nodal forces
V	element volume
u_i, v_i, w_i	displacements of node i in x, y and z directions
W_e	width of a design lane in meters
α	torsional characterizing parameter of an orthotropic plate
β	cracked shear constant used in nonlinear finite element
ϵ_x, ϵ_y, γ_{xy}	normal and shear strains in plane x-y
ϵ_{cu}	concrete strain at peak stress
γ	No. of girders/No. of lanes
θ	torsional characterizing parameter of an orthotropic plate
λ	shear slip
ν_c	Poisson's ratio of concrete
ν_s	Poisson's ratio of concrete
ρ	ratio of applied load
σ_x, σ_y, τ_{xy}	normal and shear stresses in plane x-y
$\{\chi\}$	vector of curvatures due to bending

1 INTRODUCTION

1.1 The Problem

Most of the present highway systems require improvement and expansion which involve the rehabilitation of existing bridges and the construction of new ones. This is in part due to the deterioration of old bridges, the introduction of new safety standards, the use of heavier trucks, and the increase in traffic volume.

Highway bridges are made of steel, reinforced concrete and prestressed concrete, or mixed concrete and steel. The latter type is referred to as composite bridges. The choice of different materials and structural systems in a bridge superstructure is governed by many criteria, including economic and structural requirements. Among the many types of structural systems, the slab-on-girder bridges are most suitable for short spans. Composite bridges of this type are the easiest and fastest to construct and to maintain. This is one reason for their popularity. For example, composite bridges represent 25% of all the bridges in Ontario. Most of these have been built over the past forty years. Their design has been based on lighter truck loads and elastic analysis. Today, however, because of the existence of heavier trucks, they cannot be fully utilised by all types of vehicles. Regulatory authorities, such as the Ministry of Transportation of Ontario *(MTO)*, are keen to develop analytical procedures that would enable them to evaluate the actual strength of such bridges. In other words, they would like to know their exact load distribution characteristics over the entire loading range up to failure.

Existing highway bridge codes, such as the Ontario Highway Bridge Design code *(OHBD)*, the American Association of Highway and Transportation Officials bridge code *(AASHTO)*, or the Canadian Standard Association *(CSA)* bridge code provide different methods for the prediction of the ultimate load capacity. This is achieved by multiplying the longitudinal and transverse moments and shears from elastic analysis by certain correction factors, called load fraction. Such simplifications are generally adequate for design purposes; however, they cannot be used to determine the actual distribution of loads in the post-elastic and near ultimate limit states. Therefore, in order to realistically assess the load carrying capacity of existing bridges, studies are needed to determine the distribution of loads beyond the elastic range. In conducting such studies, it is important that the effect of different parameters at advanced stages of loading be considered. This includes the material and geometric properties of the different parts of the bridge superstructure and the type of loading.

In a composite slab-on-girder bridge the main components are the reinforced concrete slab, the steel girders and the shear connectors that join the slab to the girders. In addition, any realistic analysis must also consider the interaction between these components. Although in some cases stiffeners and diaphragms may also be present, for the purpose of this study these will not be considered.

1.2 Objective and Scope

The objective of the work described herein is to determine how at inelastic and ultimate limit states vehicle loads are distributed by the slab to the girders in composite slab-on-girder bridges. Specifically, the answer to the following questions is sought:

[i] What is the effect of some key parameters on the inelastic and near ultimate load response of slab-on-girder bridges?

[ii] What are the magnitude and distribution of moments in each member and how do these vary with increased loading?

[iii] Knowing the distribution characteristics of these bridges, how should the existing relevant provisions of the codes, specifically the *OHBD* code, be modified to reflect the actual load distribution properties of composite bridges in the aforementioned limit states?

In seeking the answer to these questions, the following mode of operation is adhered to :

[i] The establishment of some key parameters that affect the load distribution characteristics of composite bridges.

[ii] A detailed elastic and nonlinear finite element analysis of the effect of these parameters.

[iii] Based on the result of the parametric study in step [ii], the establishment of some procedure for countenancing the influence of inelasticity on load distribution.

In order to investigate the influence of a large number of parameters, the analyses will deal primarily with the behavior of three and four girder bridges, albeit in some cases five and six girder systems have also been studied for comparative purposes. The range of girder numbers dealt with is deemed sufficient for arriving at meaningful conclusions.

The scope of this work is restricted to straight, simply supported prismatic members. Since the analytical procedure utilized herein is the nonlinear finite element method, the results of the analysis are subject to the same limitations as the finite element procedures used.

The analyses are limited to material nonlinearities, therefore large deformation and buckling are not considered. However, in selecting the girder sizes, only compact sections have been used which means that failure due to yielding will precede buckling of the steel girders. Furthermore, the reinforced concrete slab increases the buckling load of the girders which again implies that yielding will be the dominant mode of failure.

Finally, the choice of the finite element method as the analytical tool was motivated by economic considerations. If experimental studies are to be conducted, the large number of parameters involved require a great number of models. Since each model will cost at least five to seven thousand dollars, the total cost could very well run into tens or even hundreds of thousands of dollars. On the other hand, the finite element analysis, which can provide almost the same information, will cost only a fraction of the above amount. It is the authors' belief that the analytical model adopted here provides very accurate results. This will be demonstrated in later chapters of this report.

2 LITERATURE REVIEW

2.1 General

Since the beginning of this century, analytical and experimental studies have been conducted to investigate the behavior of composite structures in buildings and bridges. These studies have primarily focused on the general behavior and strength of such structures under different loading conditions and have been generally limited to single beams, either simply or continuously supported.

As stated earlier the main concern of the current study is to determine load distribution in slab-on-girder bridges at inelastic and ultimate states. Therefore, the following section will briefly review some of the previous work related to this topic. Some work related to load distribution in concrete and steel bridges will also be cited. The reason is that the load distribution characteristics of composite bridges are known to be similar to those of concrete and steel bridges at elastic stages.

2.2 Previous Work

Newmark (1920) developed the analytical procedure for determining longitudinal and transverse shears and moments for both composite and non-composite bridges. This procedure is similar to the moment distribution method developed by Hardy Cross (1932). Newmark, however, carried out extensive parametric study for different types of bridges. The result of his work was summarized in a series of tables that contained the fixed-end moments, distribution factors, and the carry-over factors for both non-composite and composite slab-on-girder bridges. His major finding was that the load distribution factor in such bridges is only a function of the girder spacing. In this fashion, he recommended that the distribution factor D_f be related to the girder spacing S as follows;

$$D_f = \frac{S}{K} \tag{2.1}$$

where K is a constant. Conservatively, he suggested a constant value of 1.676m (5.5$ft.$) for K. According to this procedure, the design live load moment for any girder (which includes the steel beam and a portion of the concrete slab) can be obtained by multiplying its D_f by the maximum moment that can be produced in the same girder by a single line of wheels of the design truck. It is worthwhile to mention that the current *AASHTO* code uses this formula for girder spacing up to 1.829m (6.0$ft.$) in order to determine the design moment for each girder in composite bridges. Some experimental studies were conducted at the University of Illinios (1948) to verify the above equation.

In addition to *AASHTO*, the *OHBD* and *CSA* codes also adopt the basic approach of Newmark for calculating the live load design moment for the girders. The procedure, often referred to as the D-type distribution method, essentially involves the isolation of a steel beam and its associated slab part subjected to a single line off wheels, Fig. 1. The design live load moment is obtained by multiplying the distribution factor D_f by the maximum moment caused by this load.

Obviously, Newmark's equation was based on elastic analysis and simplified assumptions. Later, especially in the early fifties, many investigators used more rigorous analyses based on the orthotropic plate theory. In this approach, the actual bridge was replaced by an equivalent orthotropic plate. This transformation, however, in many cases cannot fully simulate the real bridge behavior. Trenck (1954) introduced an exact theory of the so-called orthogonally stiffened plate which resulted in an eighth order differential equation. The constants of this equation are function of the bridge geometric and material properties. Unfortunately, obtaining a rigorous solution of such a high order equation is nearly impossible. Therefore, many investigators have used different assumptions to simplify the above mentioned equation with the resulting solution being applicable to bridges with some specific loading and boundary conditions.

In the early sixties, the advent of computers helped bridge analysts to use refined numerical techniques to study load distribution problems. They analyzed and evaluated different bridge responses due to various loading conditions. For example, Heins (1966) and Heins and Loony (1968) wrote a computer program which incorporated the so-called slope-deflection method of analysis. The method was used to determine the actual bridge strains and deflection. They modeled the bridge as a continuous orthotropic plate resting on flexible supports (bridge girders) which is an improvement over the procedure introduced by Newmark. They recommended that this method be used for analyzing bridges whose girders have torsional stiffness of some significance.

Later, Barés and Massonet (1968) and Cusén̈s and Pama (1975) developed a general solution to the orthotropic plate theory, which Rowe (1978) discussed in some detail. Because the orthotropic plate theory has received considerable attention in the past, we shall summarize the fundamentals of the method in the next sections.

The introduction of the limit state design philosophy motivated some investigators to use limit state analysis for evaluating the response of slab-on-girder bridges to overload. Heins and Kuo (1973) used the finite difference method in conjunction with bilinear relationships for stress-strain curves of the bridge material (both concrete and steel) to analyze composite bridges in the inelastic and ultimate limit states. They assumed full composite action *a priori*. Consequently, they proposed a load distribution factor for ultimate limit state. However, the study had a narrow scope and the effect of very few parameters were investigated. Their proposed equation will be presented in subsequent sections and we shall verify its applicability to the bridges analyzed in this report.

Fan (1974), based on experimental work, proposed the following distribution factor at ultimate,

$$D_f = \frac{2 \times \text{Number of Traffic Lanes}}{\text{Number of Girders}} \tag{2.2}$$

Fu et al (1976) carried out inelastic analyses similar to that used by Heins and Kuo

(1968) to verify the validity of the above equation. Again, only a few bridges were studied and the range of the parameters was not wide enough to arrive at definitive conclusions.

Bakht et al (1978) introduced a simplified method of analysis for load distribution in all types of slab-on-girder bridges and this method forms the basis of the Ontario Highway Bridge Design code recommendations. The method was derived using concepts from the orthotropic plate theory and the grillage analogy. They conducted an extensive parametric study and concluded that load distribution in bridges of this type is characterized by two intrinsic parameters, a flexural parameter θ and a torsional parameter α, which are function of the geometric and material properties of the bridge. Although this method is also based on linear elastic theory, it gives substantially better results than the *AASHTO* recommendations which assume that the girder spacing S is the only parameter that affects load distribution in slab-on-girder bridges. In the following chapters, the method will be explained and its validity will be examined. In particular we shall investigate whether it can be extended beyond the elastic limit.

Using linear elastic finite element techniques, Kōstem (1982) proposed the following equation for load distribution factor in concrete slab-on-concrete girder bridges:

$$D_f = (2\frac{N_L}{N_B}) + k_1(\frac{S}{L})^n + k_2 \tag{2.3}$$

where N_L, N_B, S, and L are the number of traffic lanes, number of girders, girder spacing and the span of the bridge respectively. k_1 and k_2 are geometric constants that depend on bridge width, number of girders, and number of traffic lanes, and n is a constant.

The above equation accounts for effects which may not exist in composite bridges. Nevertheless, it points the need for more accurate load distribution analysis methods and the inadequacy of current *AASHTO* provisions.

Additional studies were carried out by Heins and Jin (1984) and Roger (1986) to study the overload response of curved composite bridges. The former authors used the finite difference method while the latter used the finite element method.

They introduced different distribution factors for determining the moment fraction carried by each girder.

As mentioned earlier, many experimental studies have been conducted dealing with different aspects of composite structures. However, to the authors' knowledge, the only experimental work specifically related to load distribution in slab-on-girder bridges has been carried out by Chung et al (1986). In their experimental program, they tested a bridge model which consisted of six steel girders with steel end diaphragms and a cast-in-place concrete deck slab. The loading conditions were static and the bridge was simply supported. They subsequently used the experimental data to verify the results of their nonlinear finite element analyses using the commercially available program *ANSYS*. In the analytical model, full interaction was assumed between the slab and the girders. It is their observation that the assumption of full interaction between the slab and bridge girders is satisfactory and gives accurate results. This assumption will be examined in detail in this report. They also found that the diaphragms have no significant effect on load distribution. However, they stated that the slab to the girders rigidity of the model was much higher than in actual bridges, and due to this high stiffness, the effect of the diaphragm may not be very obvious. Fu et al (1976) had also found that diaphragms do not substantially affect load distribution in this kind of bridges.

According to Chung et al, the distribution factors they obtained were 15% to 17% higher than those obtained using *OHBD* code provisions. Therefore, they recommended that for ultimate load the distribution factors of *OHBD* code be modified by a factor equal to at least the shape factor of the girders cross-section. They also stated that the bridge response at ultimate is completely different than at elastic stages.

Finally, it must be emphasized that numerous other studies have been carried out by different investigators using either analytical or numerical techniques to study load distribution in bridges. Since these have been based on linear elastic analyses, and the main thrust of the current study is the problem of load distribution in the inelastic and ultimate states, their findings are not directly related to the current work, and consequently they have not been cited here.

2.3 Existing Methods of Analysis

In the following section the basic methods of analysis that have been used for the determination of the load distribution characteristics of composite bridges will be briefly presented. Since the current study focuses on load distribution in the inelastic states, the elastic methods will not be presented in full. However, the relevant recommendations of a few major codes of practice will be reviewed in more detail.

2.3.1 Elastic Methods

Elastic methods of analysis that have been used to obtain the load distribution characteristics of composite slab-on-girder bridges encompass the whole spectrum of classical and numerical methods. This includes the idealization of the bridge by one of the following substitute structures: a simple beam, a grillage or an orthotropic plate. In addition, the finite difference, finite strip, finite element, folded plate, and semi-continuum methods have been employed by different researchers. Numerous papers and books deal with each of these methods in detail, among them, Chu and Krishnamoorthy (1962), Vitols et al (1963), Cheung (1986), Heins and Loony (1969) and Cheung and Chan (1978). Since they assume the bridge to be composed of linear elastic materials that obey Hooke's law, they are not of direct relevance to the current work; therefore, we shall not discuss them further here.

2.3.2 Plastic Methods

Plastic methods of analysis that have been used for load distribution analysis include the plastic hinge concept, the yield line theory and elasto-plastic numerical methods.

In the first of these methods the bridge is idealized by an equivalent grillage and the substitute structure is analyzed using standard plastic hinge or limit analysis concepts. After the formation of sufficient number of hinges, the structure becomes a mechanism. The load corresponding to the formation of the mechanism is deemed to be the ultimate or the collapse load of the structure. Reddy (1960), Bhaumik and Zhenley (1967), and Sawks (1964) provide details of this method of analysis. Seible and Scordelis (1982) have extended this procedure to box girders.

Investigators have reported that the ultimate load of the bridge can be predicted with reasonable accuracy using this method. However, the method fails to give the actual distribution of the forces and moments in the slab. Also the determination of the equivalent stiffness properties of the various members of the grillage at all stages of loading is rather difficult. Therefore, its application in the study of detailed behavioral characteristics of composite bridges is inappropriate.

The yield line theory of Johansen, well-established for the evaluation of the ultimate strength of reinforced concrete slabs, has been extended to composite slab-on-girder bridges by Rowe (1966). Here the composite bridge is transformed to an equivalent orthotropic plate. Subsequently, the yield line theory is used to calculate the collapse load of the equivalent plate.

It is obvious that this method can only yield the ultimate load capacity of the bridge. However the procedures that allow the transformation of the composite bridge to an equivalent plate are based on elastic theories. Therefore, the application of this procedure to the inelastic range is questionable. Furthermore, even if the ultimate load is correctly calculated, this total moment must be apportioned to the various girders which is not an easy task. The application of this procedure to a problem with arbitrary loading and boundary conditions would be extremely difficult, if not impossible.

The finite difference method is a numerical procedure that has been applied to analyze composite bridge over their entire loading range. For example, Kuo and Heins (1980) modelled the slab and beams using this method. The basic procedure consists of writing the differential equations of the slab (plate) and the beams in difference form. It is then assumed that the total applied load q acting normal to the bridge surface is resisted by the slab and the girders, i.e.

$$q = q_s + \frac{q_G}{\lambda} \tag{2.4}$$

where q_s is the uniformly distributed surface load resisted by the slab, q_G is the uniform line load carried by the girders and λ is the girder spacing. On the other hand from basic theory

$$q_G = \frac{1}{EI}\frac{d^4w}{dx^4} \tag{2.5}$$

and

$$\frac{q_s}{D} = \frac{\partial^4 w}{\partial x^4} + \frac{2\partial^4 w}{\partial x^2 \partial y^2} + \frac{\partial^4 w}{\partial y^4} \tag{2.6}$$

In which EI is the flexural rigidity of the girders, $D = \frac{Eh^3}{12(1-\nu^2)}$ is the rigidity of the slab, h is the slab thickness, E is the elastic modulus, and ν is the Poisson's ratio. Now Eqs. (2.5) and (2.6) can be written in difference form and then substituted in Eq. (2.4) to obtain the differential equation of the slab-beam system in difference form. The equation is then applied to each node of the grid and the resulting system of equations are solved for the unknown nodal displacement, subject to the appropriate boundary conditions. The nodal moments and shears are calculated using the relevant difference equations. Complete details of the finite difference method with application to plates is given by Szilard (1974).

Obviously, in elasto-plastic analyses the load is incrementally applied and the state of stresses is checked at each increment. In this regard there is no difference between the finite difference and finite element methods. A more detailed description of the incremental solution technique will be given in subsequent chapters.

The finite difference method as described above will yield reasonable results for the nonlinear analysis of a bridge provided a refined mesh is used. However, it is a well-known fact that this method is difficult to apply to plates with arbitrary boundaries and its convergence for problems governed by the biharmonic equation is rather slow. Since in terms of computer time it requires at least as much time as the more versatile finite element method, there is no particular advantage in using this method nowadays.

The final method that has been applied for the elasto-plastic analysis of composite bridges in the past is the finite element method. Various degrees of approximation and idealization have been used. Since the current study also employs this method, it is fully explained in the following chapter.

From the overview of the available methods, it can be concluded that each is fraught with some difficulties. If the purpose of an analysis is to gain some insight into the basic nonlinear behavior of slab-on-girder bridges, then the grillage analogy can provide this insight provided the member stiffness properties are determined with sufficient accuracy. On the other hand, the yield line method can give an indication of the ultimate strength of the bridge. But for obtaining a complete picture of the behavior of the bridge over the entire range of loading, the most appropriate, albeit expensive, procedure to apply is the finite element method.

2.4 Codes Approach

The most important codes of practice for the analysis and design of composite bridges in North America are:

(a) Standard Specifications for Highway Bridges, American Association of Highway and Transportation Officials, *(AASHTO-77), 1977.*

(b) Ontario Highway Bridge Design Code *(OHBD), 1983.*

(c) Canadian Standards Association for Design of Highway Bridges *(CAN3-S6-M78), 1978.*

The codes specify two types of loading to be considered in design, the truck load and the lane load. The latter is not critical in load distribution analysis; hence only truck load will be discussed. The codes have devised an artificial truck that is suppose to simulate the actual loading condition. The configuration of this truck varies between the three codes. Fig. 2 shows the *OHBD* code truck. The loading configuration corresponding to this truck and the trucks of the other two codes is shown in Fig. 3. The recommended methods for the distribution of loads in the

AASHTO-77 and *CAN3-S6-M78* are identical, whereas the *OHBD* code method is different.

The first two codes specify that for a span with concrete floor supported by four or more steel stringers, the fraction of the wheel load carried by each girder shall not be less than the distribution factor, D_f, which is a dimensionless number and is specified in terms of the girder spacing S

$$D_f = \frac{S}{D_d} \tag{2.7}$$

where

$$D_d = 5.5'(1.676m) \text{ for } S \le 6'(1.829m)$$

or

$$D_d = 4.0'(1.219m) + 0.25S \text{ for } 6'(1.829m) < S < 14'(4.267m)$$

It can be observed that according to Eq. (2.7) the only parameter that influences the load distribution in slab-on-girder bridges is the girder spacing. This is of course an extreme simplification, for other factors also affect the distribution factor.

Realizing the inadequacy of Eq. (2.7) the *OHBD* code provides a more refined method of analysis which accounts for the material and geometric characteristics of the bridge. Although it still uses the same basic equation for D_f, the value of D_d is determined more accurately. It assumes that D_d depends upon two characteristics parameters, α and θ, where α is called the torsional parameter and θ the flexural parameter. These are given by

$$\alpha = \frac{D_{xy} + D_{yx} + D_1 + D_2}{2(D_x D_y)^{0.5}} \tag{2.8}$$

and

$$\theta = \frac{b}{L}\left(\frac{D_x}{D_y}\right)^{0.25} \tag{2.9}$$

where

b= half-width of the bridge

L=span of the bridge.

and the various $D's$ are given as follows:

$$D_x = \frac{E_G I_G}{S} + \frac{E_c t^3}{12} \tag{2.10}$$

$$D_y = \frac{E_c t^3}{12(1-\nu_c{}^2)} \tag{2.11}$$

$$D_{xy} = \frac{G_G J_G}{S} + \frac{G_c t^3}{6} \tag{2.12}$$

$$D_{yx} = \frac{G_c t^3}{6} \tag{2.13}$$

$$D_1 = D_2 = \nu_c D_y \tag{2.14}$$

where E, G and ν are, respectively, the Young's modulus, shear modulus and the Poisson's ratio, t is the concrete slab thickness, S is the girder spacing, and J_G and I_G are, respectively, the torsional and flexural moments of inertia of the girder cross-section. The subscript G refers to the girder and c refers to concrete.

The $D's$ shown in Eqs. (2.8) to (2.14) are indicative of the rigidities of the bridge in the longitudinal and transverse directions. For example D_x is the longitudinal flexural rigidity and D_{xy} the transverse torsional rigidity. The origin of these expressions can be traced to the orthotropic plate theory where similar expressions are used. Hence, it can be stated that the Ontario Highway Bridge Design code expressions for load distribution have been derived from orthotropic plate considerations.

Returning to the determination of D_d, the code gives the following expression:

$$D_d = D[1 + \frac{\mu C_f}{100}] \tag{2.15}$$

where

$$\mu = \frac{W_e - 3.3}{0.6} \leq 1.0 \tag{2.16}$$

and W_e = width of a design lane in meters.

D and C_f in Eq. (2.15) are assumed to be function of α and θ. The code provides special charts from which these two parameters can be determined for specific values of α and θ.

It can be seen that the *OHBD* code procedure is far more elaborate although relatively simple to apply. As described by Bakht and Jaeger (1985) the attractive feature of this procedure is that it unifies the load distribution analysis of almost all types of bridges. What distinguishes the different bridge cross-section is the manner in which the various rigidities, or D, values are calculated, the remaining steps are identical.

In this report, the validity of this equation in the elastic range will be verified, and then an attempt will be made to recommend the necessary modifications, if needed, in order to extend its applicability to the inelastic and ultimate limit states.

2.5 Load Distribution Factor Based on Nonlinear Analysis

Studies in this regard are scant and of limited scope. Kuo and Heins(1978) conducted some studies using an elasto-perfectly plastic finite difference model as described earlier. Accordingly, they used two methods to evaluate the load distribution characteristics of slab-on-girder bridges.

Method 1: In this method the distribution factor is given by

$$D_f = \frac{2(Max.\ \frac{M}{M_y})M_y}{N \times M_{AASHTO}} \tag{2.17}$$

where

M = Total longitudinal moment on a given section of the bridge

M_y = Yielding moment of girder

N = No. of trucks/No. of traffic lanes

M_{AASHTO} = Maximum moment in a single girder due to truck loading as given in the *AASHTO* code specifications.

Note that the first term in the numerator of Eq. (2.17) is the absolute maximum of all the girders in the bridge..

As can be seen D_f is based on the fraction of the total moment carried by each girder.

Method 2: In this method the distribution factor is based on the fraction of a line of truck wheels , i.e.

$$D_f = \frac{(\text{Max. } \frac{M}{M_y}) \times (\text{No. of line of wheels})}{(\Sigma \frac{M}{M_y})} \tag{2.18a}$$

or

$$D_f = \frac{(\text{Max. } \frac{M}{M_y}) \times (2 \times NL)}{(\Sigma \frac{M}{M_y})} \tag{2.18b}$$

where

NL = Number of traffic lanes

$\Sigma \frac{M}{M_y}$ = sum of moment ratios for all the girders across the bridge.

Using the above two methods, they obtained the D_d values listed in Tables 1 and 2 for the elastic analysis and ultimate limit states, respectively.

In Table 1, it can be seen that the two methods give results that are fairly close. Secondly, we observe that the $D_d = 5.5$, as suggested by *AASHTO*, is generally conservative.

At the ultimate limit state, the results in Table 2 show that again in general the two methods compare favorably. However, in this case the *AASHTO* values for D_d is conservative for all the bridges considered. This suggests that the bridges can carry more load than anticipated by current *AASHTO* requirements, a conclusion that is not unexpected.

These investigators further simplified the results of their finding by proposing the following equation for load distribution at ultimate limit state:

$$D_f = 3.45 - 1.809\gamma + 0.315\gamma^2 \tag{2.19}$$

where γ= No. of girders/No. of lanes

Equation (2.19) is applicable subjected to the following limitations:

$6' \leq$ girder spacing $\leq 9'$

$4 \leq$ No. of girder ≤ 9

$2 \leq$ No. of lanes ≤ 4

The latter equation was obtained from a least square fitting of the results in Table 2, with a standard deviation of two. To the writers' knowledge this is the only study that deals with load distribution at ultimate in sufficient detail. We shall examine the applicability of Eq. (2.19) later.

3 THE FINITE ELEMENT PROGRAM

3.1 General

It was mentioned in the beginning of this report that the nonlinear finite element technique will be used in the present study. In this chapter the finite element program and its development will be described. A composite bridge consists of three main components, each with its distinct behavior: the reinforced concrete slab, the steel girders, and the shear studs that connect the slab to the girders. In the subsequent sections the modelling of each of these components will be described.

The finite element program developed for the purpose of the current study is called *NONLACS* (NONLinear Analysis of Concrete and Steel). The origin of this program goes back to the program *FELARC* (Finite Element Layered Analysis of Reinforced Concrete). The latter was originally developed by Ghoneim (1978) and later enhanced and improved by Razaqpur (1982).

3.2 General Description of *NONLACS*

NONLACS utilizes the basic structure of *FELARC* and it adopts the same material model for concrete and the reinforcing steel bars. It can be used to trace the full nonlinear behavior of any reinforced concrete, steel or composite concrete-steel structure which can be modelled as an assemblage of thin shell elements. This includes beams, plates, shells, folded plates, box-girders, shear walls, etc. The analysis can also include time dependent phenomena such as creep and shrinkage and cyclic loads. The latter are not, however, germane to the subject of this report and therefore will not be discussed. The program has certain limitations. It does not consider the following effects: (*i*) large displacements or geometric nonlinearities,

(*ii*) fatigue effects, (*iii*) shear deformations normal to the plate and shell surfaces, (*iv*) bond slip at the interface of the concrete and reinforcing steel.

In composite slab-on-girder bridges these effects are not important. In this study the steel girders are assumed to be compact sections, thus yielding precedes buckling and large deformations. Also because the constituent parts of the bridge are relatively thin, shear deformations normal to the element surfaces can be assumed to be negligible.

3.3 Basic Equations of Finite Element

In order to establish a basis for the material models used, some basic equations of the finite element method, as used in this program, will be presented. Using the principle of minimization of the total potential energy, the following equation of equilibrium can be written:

$$[k]\{d\} = \{R\} + \{F\}_b + \{F\}_s + \{F\}_\epsilon^- + \{F\}_\sigma^- \tag{3.1}$$

where

$[k]$ = **structure stiffness matrix**

$\{d\}$ = **vector of nodal displacements**

$\{R\}$= **vector of applied nodal forces**

$\{F\}_b$ = **vector of nodal forces due to body forces**

$\{F\}_s$ = **vector of nodal forces due to surface tractions**

$\{F\}_\epsilon^-$ = **vector of nodal forces due to initial strains**

$\{F\}_\sigma^-$ = **vector of nodal forces due to initial stresses.**

The displacement field $\{\delta\}$ inside an element can be related to the nodal displacement $\{d\}^e$ as

$$\{\delta\} = [N]\{d\}^e \tag{3.2}$$

where $[N]$ is the shape functions matrix. Note that the superscript e is used to denote quantities at the element level. The strain $\{\epsilon\}$ and nodal displacements

$\{d\}^e$ are related by the strain-displacement matrix $[B]$ as:

$$\{\epsilon\} = [B]\{d\}^e \tag{3.3}$$

Using the constitutive matrix $[D]$, the element stresses are computed from the element strain as follows:

$$\{\sigma\} = [D](\{\epsilon\} - \{\bar{\epsilon}\}) + \{\bar{\sigma}\} \tag{3.4}$$

where $\{\bar{\epsilon}\}$ = vector of initial strains

and $\{\bar{\sigma}\}$ = vector of initial stresses.

By applying Eqs. (3.2) to (3.4), elements of Eq. (3.1) can now be written in more detail as:

$$[k] = \sum_e [k]^e$$

where

$$[k]^e = \int [B]^T [D][B] dV^e \tag{3.5}$$

$$\{F\}_b = \sum_e \int [N]^T \{g\} dV^e \tag{3.6}$$

$$\{F\}_s = \sum_e \int [N]^T \{p\} dS^e \tag{3.7}$$

$$\{F\}_{\bar{\epsilon}} = \sum_e \int [B]^T [D] \{\bar{\epsilon}\} dV^e \tag{3.8}$$

$$\{F\}_{\bar{\sigma}} = \sum_e \int [B]^T \{\bar{\sigma}\} dV^e \tag{3.9}$$

In the above $\{g\}$ and $\{p\}$ are vectors of body forces and surface tractions, respectively. These equations will be used in subsequent sections to elaborate on the various aspects of the finite element model developed.

3.4 The Finite Elements Employed

NONLACS contains five basic elements, namely, a two node bar element, a two node shear connector element, a high order four node plane quadrilateral element,

a four node plate bending quadrilateral element, and a four node shell element. The plane quadrilateral element and the shear connector element were developed for the purpose of this study. The bar element and the plate bending element are the same as those in *FELARC*.

3.4.1 The Bar Element

This is a standard truss element as shown in Fig. 4. It has two end nodes with a linear displacement field. Each node has three degrees of freedom u, v, and w in x, y, and z directions. Since the element is well established, it will not be discussed any further. It must, however, be mentioned that this element can be used to model any uniaxial member such as truss members or unbonded prestressed tendons.

3.4.2 Shear Connector Element

In composite slab-on-girders construction, the concrete slab is connected to the steel girders by means of shear connectors. One of the most common types of connectors in North America is the so-called stud connector. Figures 5 (a) and (b) show a typical stud connector. Because the connectors are deformable, under load there will be relative deformation or slip at the interface of the concrete slab and the steel girders. The load-slip characteristic of the connector is a function of many parameters whose detailed numerical modelling is complicated and not warranted. In the following the procedure for deriving the nonlinear stiffness matrix of the shear connector element will be shown where an empirical load-slip relationship has been utilized.

For the purpose of this study, the following empirical load-slip relationship, proposed by Yam and Chapman (1967), will be used.

$$F = a(1 - e^{-b\lambda}) \tag{3.10}$$

where F is the shear force acting on the connector and λ is the slip or relative deformation between its ends, a and b are constants and e is the base of natural logarithm. For the type of connectors used in the current study, Yam and Chapman have given $a = 30kN$ and $b = 3050\frac{1}{mm}$.

To write the stiffness matrix of this element, consider the two node bar element with a total of six displacement degrees of freedom, Fig. 5 (b). Because shear connectors are relatively short and because they transfer the load primarily by shear, it is assumed that their flexural and torsional stiffness are equal to zero. From basic finite element procedures, the nodal forces $\{F\}$ of this element can be related to the nodal displacements $\{u\}$ as

$$\begin{pmatrix} F_1 \\ F_2 \\ F_3 \\ F_4 \\ F_5 \\ F_6 \end{pmatrix} = \begin{pmatrix} k_1 & 0 & 0 & -k_1 & 0 & 0 \\ 0 & k_2 & 0 & 0 & -k_2 & 0 \\ 0 & 0 & k_3 & 0 & 0 & -k_3 \\ -k_1 & 0 & 0 & k_1 & 0 & 0 \\ 0 & -k_2 & 0 & 0 & k_2 & 0 \\ 0 & 0 & -k_3 & 0 & 0 & k_3 \end{pmatrix} \begin{pmatrix} u_1 \\ u_2 \\ u_3 \\ u_4 \\ u_5 \\ u_6 \end{pmatrix} \tag{3.11}$$

where $k_1 = \frac{EA}{L}$, E is the Young's modulus, A and L are the cross-sectional area and length of the element, respectively. Note that the bar is assumed to be elasto-plastic and therefore for an element yielding, $E = 0.0$. k_2 and k_3 are the shear stiffness coefficients of the bar. They can be determined from the experimental load-slip curve in Fig. 6.

Consider the increment of shear force ΔF in Fig. 6, which can be related to the increment of slip $\Delta\lambda$ as

$$\Delta F = k\Delta\lambda \tag{3.12}$$

where k is the slope of the curve and is given by

$$k = \frac{dF}{d\lambda}$$

Therefore,

$$k = abe^{-b\lambda} \tag{3.13}$$

This yields

$$\Delta F = abe^{-b\lambda}\Delta\lambda \tag{3.14}$$

For the element in Fig. 5, the slip in the y and z directions can be written as

$$\lambda_y = u_2 - u_5 \tag{3.15a}$$

$$\lambda_z = u_3 - u_6 \tag{3.15b}$$

or in incremental form:

$$\Delta\lambda_y = \Delta u_2 - \Delta u_5 \tag{3.16a}$$

$$\Delta\lambda_z = \Delta u_3 - \Delta u_6 \tag{3.16b}$$

where Δu_i is the increment of displacement due to an increment of shear force ΔF_i. Note that in some cases the location of shear connectors may not coincide with the nodal points in the finite element mesh. In these cases, the actual connector is substituted by two equivalent connectors which are positioned at the nearest nodal points. The cross-sectional area of the substitute connectors is found by linearly interpolating the area of the actual connector. This procedure is akin to the determination of equivalent nodal forces in the customary finite element procedures.

In the nonlinear incremental/iterative analysis procedure used in this report, increments of slip are summed up to obtain the total slip at any load level. Then the shear force corresponding to the total slip is determined from Eq. (3.10) and the shear stiffness of the bar for the next iteration is calculated using Eq. (3.13). The axial stiffness of the bar is found the same way as for an ordinary elasto-plastic truss element. In the next chapter, the validity of this procedure is ascertained by comparing the finite element results with experimental data.

3.4.3 Refined Plane Quadrilateral Element *(RQUAD4)*

The four node quadrilateral described here was developed specifically for the purpose of this study. Razaqpur initially developed the element for *NONLACS*; the writers carried out extensive tests to verify its implementation and performance. It will be referred to henceforth as refined quadrilateral or *RQUAD4*. Program *FELARC* contained a four node plane quadrilateral, called *QLC3*, which has a cubic displacement field in one direction and a linear field in the orthogonal direction. Therefore, in a geometrically isotropic displacement field it would yield poor results. On the other hand, in beam type structures its performance was good.

In fact, Sisodyia and Ghali (1973), who developed this element, recommended it mainly for the analysis of elongated structures such as beams, folded plates and box-girders.

RQUAD4 gives accurate results irrespective of the stress field. The element is geometrically isotropic and its stiffness can be derived from the stiffness matrix of *QUAD8*, the eight node isoparametric element. It should be mentioned that recently Allman (1984) introduced a triangular element similar to *RQUAD4*. However, the performance of the element was barely satisfactory. He derived the element using some elaborate manipulations. Cook (1986) pointed out that Allman's triangle can be derived using the stiffness matrix of the linear strain triangle in conjunction with kinematic transformation. Here Cook's suggested procedure is utilized to derive the stiffness of *RQUAD4*.

3.4.3.1 Element Formulation.

The element has three degrees of freedom per node as illustrated in Fig. 7 (a), and its displacement functions can be derived from the displacement functions of *QUAD8*, Fig. 7 (b). Typical nodal displacements u_i and v_i in the x and y directions, respectively, are the same as in *QUAD8* while w_i is a typical nodal-rotation normal to the plane of the element. Using the kinematic relationship described below, the degrees of freedom in *QUAD8* are related to the degrees of freedom in the new element.

Consider side $1-2$ of *RQUAD4* and introduce a unit rotation $w_1 = 1$ at node 1 as in Fig. 8. The displacement normal to side $1-2$, u_n, due to this rotation can be expressed as a cubic polynomial similar to the lateral displacement function for an ordinary beam, i.e.

$$u_n = -\frac{s(l-s)^2}{l^2} \tag{3.17}$$

where s is a local coordinate running from node 1 to 2, and l is the length of side $1-2$. For $s = \frac{l}{2}$,

$$(u_n)_{s=\frac{l}{2}} = \frac{-l}{8} \tag{3.18}$$

Similarly, for $w_2 = 1$

$$(u_n)_{s=\frac{l}{2}} = \frac{l}{8} \tag{3.19}$$

Therefore, for end rotations w_1 and w_2

$$(u_n) = l\frac{(w_2 - w_1)}{8} \tag{3.20}$$

Let us resolve u_n in Eq. (3.20) into its components in the x and y directions,

$$(u_{nx}) = l\frac{(w_2 - w_1)}{8} sin\theta \tag{3.21}$$

$$(u_{ny}) = l\frac{(w_2 - w_1)}{8} cos\theta \tag{3.22}$$

But from Fig. 7 (a), $sin\theta = \frac{(y_2 - y_1)}{l}$ and $cos\theta = \frac{(x_2 - x_1)}{l}$, where x_i, y_i are the coordinates of node i ($i = 1, 2$). Substituting for these quantities in Eqs. (3.21) and (3.22), we can write the total displacement components at the middle of side $1 - 2$ as:

$$u_5 = \frac{(u_1 + u_2)}{2} - (y_1 - y_2)\frac{(w_2 - w_1)}{8} \tag{3.23}$$

$$v_5 = \frac{(v_1 + v_2)}{2} + (x_2 - x_1)\frac{(w_2 - w_1)}{8} \tag{3.24}$$

Eqs. (3.23) and (3.24) can be written in matrix form as

$$\begin{pmatrix} u_5 \\ v_5 \end{pmatrix} = \begin{bmatrix} \frac{1}{2} & 0 & a & \frac{1}{2} & 0 & -a \\ 0 & \frac{1}{2} & -b & 0 & \frac{1}{2} & b \end{bmatrix} \begin{pmatrix} u_1 \\ v_1 \\ w_1 \\ u_2 \\ v_2 \\ w_2 \end{pmatrix} \tag{3.25}$$

where $a = \frac{y_1 - y_2}{8}$ and $b = \frac{x_1 - x_2}{8}$

By writing similar equations for the other mid-side nodes, the nodal displacements in *QUAD8*, $\{d\}$ are related to the corresponding displacements in *RQUAD4* $\{d^*\}$, as

$$\{d\} = [T]\{d^*\} \tag{3.26}$$

where [T] is the a 16 × 12 transformation matrix. In expanded form Eq. (3.26) is given by

$$\begin{pmatrix} u_1 \\ v_1 \\ u_2 \\ v_2 \\ u_3 \\ v_3 \\ u_4 \\ v_4 \\ u_5 \\ v_5 \\ u_6 \\ v_6 \\ u_7 \\ v_7 \\ u_8 \\ v_8 \end{pmatrix} = \begin{pmatrix} 1 & 0 & 0 & 0 & 0 & 0 & 0 & 0 & 0 & 0 & 0 & 0 \\ 0 & 1 & 0 & 0 & 0 & 0 & 0 & 0 & 0 & 0 & 0 & 0 \\ 0 & 0 & 0 & 1 & 0 & 0 & 0 & 0 & 0 & 0 & 0 & 0 \\ 0 & 0 & 0 & 0 & 1 & 0 & 0 & 0 & 0 & 0 & 0 & 0 \\ 0 & 0 & 0 & 0 & 0 & 0 & 1 & 0 & 0 & 0 & 0 & 0 \\ 0 & 0 & 0 & 0 & 0 & 0 & 0 & 1 & 0 & 0 & 0 & 0 \\ 0 & 0 & 0 & 0 & 0 & 0 & 0 & 0 & 0 & 1 & 0 & 0 \\ 0 & 0 & 0 & 0 & 0 & 0 & 0 & 0 & 0 & 0 & 1 & 0 \\ \frac{1}{2} & 0 & b_1 & \frac{1}{2} & 0 & -b_1 & 0 & 0 & 0 & 0 & 0 & 0 \\ 0 & \frac{1}{2} & a_1 & 0 & \frac{1}{2} & -a_1 & 0 & 0 & 0 & 0 & 0 & 0 \\ 0 & 0 & 0 & \frac{1}{2} & 0 & b_2 & \frac{1}{2} & 0 & -b_2 & 0 & 0 & 0 \\ 0 & 0 & 0 & 0 & \frac{1}{2} & a_2 & 0 & \frac{1}{2} & -a_2 & 0 & 0 & 0 \\ 0 & 0 & 0 & 0 & 0 & 0 & \frac{1}{2} & 0 & b_3 & \frac{1}{2} & 0 & -b_3 \\ 0 & 0 & 0 & 0 & 0 & 0 & 0 & \frac{1}{2} & a_3 & 0 & \frac{1}{2} & -a_3 \\ \frac{1}{2} & 0 & -b_4 & 0 & 0 & 0 & 0 & 0 & 0 & \frac{1}{2} & 0 & b_4 \\ 0 & \frac{1}{2} & -a_4 & 0 & 0 & 0 & 0 & 0 & 0 & 0 & \frac{1}{2} & a_4 \end{pmatrix} \begin{pmatrix} u_1 \\ v_1 \\ w_1 \\ u_2 \\ v_2 \\ w_2 \\ u_3 \\ v_3 \\ w_3 \\ u_4 \\ v_4 \\ w_4 \end{pmatrix} \tag{3.27}$$

where $a_i = \frac{(x_i - x_{i+1})}{8}$ and $b_i = \frac{(y_i - y_{i+1})}{8}$ for $i = 1, 2, 3$; and $a_4 = \frac{(x_1 - x_4)}{8}$ and $b_4 = \frac{(y_4 - y_1)}{8}$.

Using the principle of virtual work the stiffness $[k^*]$ and nodal load vector $\{F^*\}$ of *RQUAD4* can be related to the corresponding matrices $[k]$ and $\{F\}$ of *QUAD8* as:

$$[k^*] = [T]^T [k][T] \tag{3.28a}$$

and

$$\{F^*\} = [T]^T \{F\} \tag{3.28b}$$

The last two equations show that once the transformation matrix $[T]$ has been established, the remaining steps of the analysis are relatively straight forward.

The procedure described thus far is similar to the method suggested by Cook (1986) for Allman's triangle. Although Eqs. (3.28a) and (3.28b) will yield the desired stiffness and load matrices, it is possible to introduce further simplifications and to reduce the amount of calculations. The stiffness matrix, $[k]$, is given by

$$[k] = \int [B]^T [D][B] dV \tag{3.29}$$

where as usual $[B]$ is the strain-displacement matrix, $[D]$ is the elasticity matrix and V is the element volume. Hence according to Eq. (3.28a), $[k^*]$ can be written as:

$$[k^*] = [T]^T\left(\int [B]^T[D][B]dV\right)[T] \tag{3.30}$$

Rewriting the above equation

$$[k^*] = \int [T]^T[B]^T[D][B][T]dV \tag{3.31}$$

Let

$$[B^*] = [B][T] \tag{3.32}$$

then

$$[k^*] = \int [B^*]^T[D][B^*]dV \tag{3.33}$$

Therefore, if we transform the $[B]$ matrix of *QUAD8* according to Eq. (3.32), then the stiffness matrix of *RQUAD4* can be derived from Eq. (3.33). Consequently, computation time is reduced because Eq. (3.32) involves less multiplications. In this report the latter procedure was used. Element *QUAD8* is well established in the literature and the work by Hinton and Owen (1977) provides its full formulation, therefore we should not discuss it further.

To test the performance of *RQUAD4* extensive tests were carried out; all of these tests have shown that it is highly reliable. Here, for the sake of illustration, results of a few of the tests will be reported. For more test cases, reference can be made to Razaqpur and Nofal (1987). Further development of this element is currently underway by Aziz (1987).

3.4.3.2 Short Cantilever Beam under Tip Load

Fig. 9 shows a cantilever beam subjected to a concentrated load at its free end. The beam was analyzed using different mesh sizes and the convergence rate of the tip displacement δ_y, the longitudinal normal stress σ_x at point B and the shear τ_{xy} at point C was studied. Results of the analysis for *RQUAD4* and some other well-known elements are shown in Fig. 10 (a), (b), (c), and (d).

Figs. 10 (a) to (d) show that the current element converges more rapidly to the exact solution than the other elements. It is also obvious that the mesh size needed to calculate the exact displacements can be fairly coarse, but for obtaining the exact stresses a more refined mesh is required.

3.4.3.3 Pure Inplane Bending of a Square Plate

Fig. 11 shows an isotropic square plate subjected to pure bending. This plate was analyzed using the new element and the results for stresses and displacements at selected points are compared in Table 3 with the exact solution and with solutions obtained from other elements as reported by Allman (1984).

As can be observed the results for this element are comparable to the ones obtained by Allman. However, the current element has consistently performed well while Allman's element, as shown by Razaqpur and Nofal (1987), has shown poor performance in some cases.

3.4.3.4 Tapered Skew Cantilever with Uniform Shear at the Free End

As a final test case Fig. 12 shows a tapered-skew cantilever subjected to a uniform shear τ at the free end. This structure was first used by Cook (1974) to test the performance of several four node quadrilaterals, including some hybrid elements. Pian (1984) later used the same structure to check the performance of an improved hybrid element based on natural coordinates. Both Pian and Cook reported that none of the displacement based quadrilateral elements performed well in this problem. Here it is analyzed using element *RQUAD4*. It is important to note that the elements in this problem are arbitrary quadrilaterals and not square or rectangular.

First in conformity with Pain and Cook, the variation of the stress ratio $\frac{\sigma_a}{\tau}$ along section AB in Fig. 12 is determined. The previous investigators used a 4 × 4 mesh as shown in the figure. In this study, however, 3 × 3 and 5 × 5 meshes were used. The reason for this was to avoid too much interpolation for obtaining the stresses along AB. It must be mentioned that the stress sampling points in *RQUAD4* are the Gauss points. The variation of $\frac{\sigma_a}{\tau}$ is plotted in Fig. 13 for 3 × 3 and 5 × 5 meshes. The figure also depicts the results obtained using a 4×4 mesh of other types of elements. The reference solution, deemed to be the correct distribution, is the one obtained by Cook using a 16x16 mesh of the hybrid element HL.

In addition to the normal stress distribution at midspan, Tables 4 to 6 show the variation of other quantities at specific points. The comparison is made between the results of the current element along with those obtained by other investigators. The different types of elements listed in these tables are described in the work of Cook, and Bergan and Fellipa (1985). The quantities of interest are the tip deflection at point C, the minimum stress at B and the maximum stress at A. Considering the tip deflection obtained from the 4×4 mesh of the various elements, it is clear that the proposed element gives the closest value to that obtained from the 16×16 of the HL element.

From Fig. 13 and Tables 4 to 6 it can be observed that the *RQUAD4* element performs extremely well and that with the exception of Pian's hybrid element, it performs better than all the other elements, including the hybrid element HL, which is based on local $x' - y'$ axes. In summary, it is the authors' belief that the current element is very reliable and competitive.

3.4.4 Four Node Quadrilateral Bending Element *(QBE)*

This element is the quadrilateral version of the famous rectangular bending element developed by Zienkiewicz and Chung (1964). It was formulated by Ghoneim (1978) and its performance has been reported to be satisfactory for moderate deviations from the rectangular shape. Below the general features of the element will be briefly discussed; for complete details reference can be made to the work of Ghoneim (1978).

Figure 14 shows element *QBE*. The element has three degrees of freedom per node, the lateral displacement w and the normal rotations $\frac{\partial w}{\partial x}$ and $\frac{\partial w}{\partial y}$. The displacement function in terms of the natural ξ and η coordinates is given by

$$w = [p]\{\bar{A}\} \tag{3.34}$$

where

$$[P] = (1 \quad \xi \quad \eta \quad \xi^2 \quad \xi\eta \quad \eta^2 \quad \xi^3 \quad \xi^2\eta \quad \xi\eta^2 \quad \eta^3 \quad \xi^3\eta \quad \xi\eta^3) \tag{3.35}$$

and $\{\bar{A}\}$ is a vector that contains the polynomial coefficients. In this element, as in element *RQUAD4*, the geometry of the element is interpolated using the following relationships.

$$x = \sum_{i=1}^{4} \frac{1}{4}(1 + \xi\xi_i)(1 + \eta\eta_i)x_i \tag{3.36}$$

$$y = \sum_{i=1}^{4} \frac{1}{4}(1 + \xi\xi_i)(1 + \eta\eta_i)y_i \tag{3.37}$$

where x, y are the Cartesian coordinates of a general point, and ξ , η are the natural coordinates of the same point. x_i, y_i, ξ_i and η_i are, respectively, the Cartesian and natural coordinates of node i. Note that the summation is carried out over the four nodes.

3.4.5 Quadrilateral Facet Shell Element *(QFSE)*

Element *QFSE* is obtained by combining elements *RQUAD4* and *QBE*. The element has four nodes with six degrees of freedom at each node. Observe that because of material nonlinearity, the shell element is an anistropic shell in which the inplane and bending actions are assumed to be coupled. Figure 15 shows element *QFSE* and the associated coordinate system. The strain $\{\epsilon\}$ at a general point within the element can be written as

$$\{\epsilon\} = \{\epsilon_o\} - z\{\chi\} \tag{3.38}$$

where $\{\epsilon_o\}$ are the inplane strains of the projection of the same point on the reference plane, $\{\chi\}$ is the vector of curvatures due to bending and z is the local z coordinate of the point under consideration. From basic theory,

$$\{\epsilon\} = [B]_p\{d\}_p$$

and

$$\{\chi\} = [B]_b\{d\}_b$$

where the subscript p and b stand for inplane and bending components. Eq. (3.38) can be rewritten as

$$\{\epsilon\} = \left([B]_p \quad -z[B]_b \right) \begin{pmatrix} d_p \\ d_b \end{pmatrix} = [B]\{d\} \tag{3.39}$$

The stiffness of the element is given by

$$[k] = \int [B]^T [D][B] dV \tag{3.40}$$

Substituting for $[B]$ from Eq. (3.39) into Eq.(3.40), we get

$$\begin{aligned} [k] &= \int \begin{pmatrix} [B]_p{}^T[D][B]_p & -z[B]_p{}^T[D][B]_b \\ -z[B]_b{}^T[D][B]_p & z^2[B]_b{}^T[D][B]_b \end{pmatrix} dV \\ &= \begin{pmatrix} [k]_{pp} & [k]_{pb} \\ [k]_{bp} & [k]_{bb} \end{pmatrix} \end{aligned} \tag{3.41}$$

The diagonal terms are the stiffness of elements *RQUAD4* and *QBE* respectively. The off-diagonal terms are the coupling matrices that will be non zero if the material properties are not symmetric with respect to the middle surface of the shell. This happens when yielding and cracking takes place in some fibers above or below the middle surface and not in others. In the program, plate and shell elements are divided into layers as illustrated in Fig. 16. Each layer is assumed to be in a state of plane stress. Within the thickness of each layer, the stresses and material properties are assumed to be constant.

In evaluating the submatrices that comprise the elements of the stiffness matrix, the volume integral is splitted into a summation through the thickness and an area integral over the surface of the element. For example,

$$\begin{aligned} [k]_{pp} &= \int [B]_p{}^T [D][B]_p dV \\ &= \int\int [B]_p{}^T (\int_z [D] dz) [B]_p dx dy \end{aligned} \tag{3.42}$$

The line integral is denoted by $[D]_{pp}$ and is calculated in the following fashion:

$$[D]_{pp} = \int_z [D] dz = \sum_{i=1}^{n} (z_{i+1} - z_i)[D]_i \tag{3.43a}$$

where z_{i+1} and z_i are the z coordinates of the top and bottom surfaces of layer i and n is the total number of layers in a given element. Of course, the constitutive matrix $[D]_i$ for each layer will depend upon whether the layer is concrete, smeared reinforcement or steel. This will be further explained in the sections dealing with material modelling. The remaining submatrices in Eq. (3.40) are evaluated in a similar fashion, and the line integral evaluation for the remaining terms is given by

$$[D]_{pb} = -\int_z z[D]dz = -\frac{1}{2}\sum_{i=1}^{n}({z^2}_{i+1} - {z^2}_i)[D]_i \qquad (3.43b)$$

$$[D]_{bb} = \int_z z^2[D]dz = \frac{1}{3}\sum_{i=1}^{n}({z^3}_{i+1} - {z^3}_i)[D]_i \qquad (3.43c)$$

It must be mentioned that the equivalent nodal forces $\{F\}_{\bar{\sigma}}$ and $\{F\}_{\bar{\epsilon}}$ due to intial stress and strain are similarly calculated. Specifically,

$$\{F\}_{\bar{\epsilon}} = \int\int \begin{pmatrix} {[B]^T}_p\{\sigma_{\bar{\epsilon}}\}_p \\ {[B]^T}_b\{\sigma_{\bar{\epsilon}}\}_b \end{pmatrix} dxdy$$

and

$$\{F\}_{\bar{\sigma}} = \int\int \begin{pmatrix} {[B]^T}_p\{\sigma_{\bar{\sigma}}\}_p \\ {[B]^T}_b\{\sigma_{\bar{\sigma}}\}_b \end{pmatrix} dxdy \qquad (3.44)$$

where

$$\{\sigma_{\bar{\epsilon}}\}_p = \int [D]\{\bar{\epsilon}\}dz = \sum_{i=1}^{n}(z_{i+1} - z_i)[D]_i\{\bar{\epsilon}_i\} \qquad (3.45)$$

$$\{\sigma_{\bar{\epsilon}}\}_b = -\int z[D]\{\bar{\epsilon}\}dz = -\frac{1}{2}\sum_{i=1}^{n}({z^2}_{i+1} - {z^2}_i)[D]_i\{\bar{\epsilon}_i\} \qquad (3.46)$$

$$\{\sigma_{\bar{\sigma}}\}_p = \int \{\bar{\sigma}\}dz = \sum_{i=1}^{n}(z_{i+1} - z_i)\{\bar{\sigma}_i\} \qquad (3.47)$$

$$\{\sigma_{\bar{\sigma}}\}_b = -\int z\{\bar{\epsilon}\}dz = -\frac{1}{2}\sum_{i=1}^{n}({z^2}_{i+1} - {z^2}_i)\{\bar{\sigma}_i\} \qquad (3.48)$$

once again the $[D]_i$ matrix is dependent upon the layer material and the level of stress as discussed next.

3.5 Material Modelling

The materials involved in the present study are concrete, reinforcing and prestressing steel and steel plates. In the following the constitutive models used for each material will be described. Although the uniaxial reinforcing bars are a special case of the continuum case dealt with by theory of plasticity, the historical development of the program *NONLACS* has separated these into two distinct materials.

3.5.1 Concrete Modelling

The concrete model described here is the same as in program *FELARC*. The intrinsic shape of the stress-strain curves for both uniaxial and biaxial cases are shown in Figs. 17 (a) and (b). This relation is comprised of two parts: Part *I* is represented by the equation proposed by Saenz (1964):

$$\sigma = \frac{E_o \epsilon}{1 + (\frac{E_o}{E_s} - 2)\frac{\epsilon}{\epsilon_{cu}} + (\frac{\epsilon}{\epsilon_{cu}})^2} \tag{3.49}$$

where, as shown in Fig. 17(a),

E_s = secant modulus of elasticity at peak stress

E_o = intial tangent modulus

σ = stress

ϵ = strain

ϵ_{cu} = strain at peak stress.

Part *II* traces the Smith-Young (1955) model according to the following expression:

$$\sigma = \sigma_c(\frac{\epsilon}{\epsilon_{cu}})e^{(1-\frac{\epsilon}{\epsilon_{cu}})} \tag{3.50}$$

where σ_c is the compressive strength and e is the base of natural logarithm. Under biaxial or combined stress fields, concrete is assumed to behave as a stress-induced orthotropic material. This implies that the intial tangent moduli in the two principal directions are different except for the case $\frac{\sigma_1}{\sigma_2} = 1$, where σ_1 and σ_2 are the major and minor principal stresses.

This so-called orthotropy is caused by the confinement of microcracking and the Poisson's effect. This model was proposed by Darwin and Pecknold (1977), which permits the utilization of experimental data from uniaxial tests to develop the constitutive matrix for the biaxial or combined stress cases. The basis for its development is given by the original authors and will not be reproduced here. The model works as described below.

For any point the principal stresses σ_1 and σ_2 are calculated; the ratio $\frac{\sigma_1}{\sigma_2}$ is then used, in conjunction with the failure envelope of biaxially loaded concrete, Fig. 17, to establish its strength and stress-strain relationship in each of the principal stress directions. The pertinent stress-strain relationship is used to calculate the elastic modulus. For example, for principal direction i, E_i is given by

$$E_i = \frac{d\sigma_i}{d\epsilon_{iu}} = \frac{E_o(1 - r_i{}^2)}{[1 + (\frac{E_o}{E_s} - 2)r_i + r_i{}^2]^2} \tag{3.51}$$

where $r_i = \frac{\epsilon_{iu}}{\epsilon_{ic}}$ and

$$\epsilon_{iu} = \sum \Delta\epsilon_{iu} = \sum \frac{\Delta\epsilon_i}{1 - \nu\alpha n} \tag{3.52}$$

in Eq. (3.52) $\Delta\epsilon_i$ is the actual increment of strain in direction i, ν is the Poisson's ratio, $\alpha = \frac{\sigma_j}{\sigma_i}$, and $n = \frac{E_i}{E_j}$, where j is the conjugate direction to i. The E_i and E_j for the current iteration are obtained from the preceding iteration. The failure envelope used in the current work is the one proposed by Kupfer and Gerstle (1973) and is schematically illustrated in Fig. 17 (b). The equations pertinent to the different parts of the envelope are given by Darwin and Pecknold (1977). Note that in establishing the stress-strain curve for each direction, the same basic expressions given by Eqs. (3.49) and (3.50) are used. However, the strain, ϵ, in these expressions is replaced by the equivalent strain ϵ_{iu}.

Once the stress-strain relationship in each direction has been established, increments of stress $\{\Delta\sigma\}$ are related to the increments of strain $\{\Delta\epsilon\}$ as

$$\{\Delta\sigma\} = [D]\{\Delta\epsilon\} \tag{3.53}$$

where $[D]$ is the constitutive matrix proposed by Darwin and Pecknold and is given by

$$[D] = \frac{1}{1 - \nu^2} \begin{pmatrix} E_1 & \nu\sqrt{E_1 E_2} & 0 \\ \nu\sqrt{E_1 E_2} & E_2 & 0 \\ 0 & 0 & \frac{1}{4}(E_1 - E_2 - 2\nu\sqrt{E_1 E_2}) \end{pmatrix} \tag{3.54}$$

in which E_1 and E_2 are the tangent moduli in the principal material directions. The principal material directions coincide with the principal stress directions for uncracked concrete. For cracked concrete, these directions are parallel and normal to the cracks. The values of E_1 and E_2 are function of the stress level. Therefore, if σ_1 or σ_2 exceeds the concrete strength, yielding is assumed in the particular direction. On the other hand, if the compressive strain in one of these directions exceeds the ultimate concrete strain, the concrete is regarded as crushed. When the latter happens, the $[D]$ matrix becomes null.

Cracking is monitored by checking the magnitude of σ_1 and σ_2. When the principal tensile stress at a point equals or exceeds the tensile strength of concrete, cracking is assumed perpendicular to the particular direction. If, for example, $\sigma_1 \geq f'_t$, where f'_t is the tensile strength of concrete, then the $[D]$ matrix reduces to

$$[D] = \begin{pmatrix} 0 & 0 & 0 \\ 0 & E_2 & 0 \\ 0 & 0 & \beta G \end{pmatrix} \tag{3.55}$$

where G is the elastic shear modulus and β is the shear retention factor with a value less than unity.

The factor β is used to account in an approximate fashion for the shear stiffness due to aggregate interlock and dowel action. This approach is now well established in the literature. As stated by Razaqpur (1982) the device of shear retention gives acceptable results provided the concrete is not severly under reinforced for either normal or shear stresses. Accounting for the effect of cracks according to the foregoing procedure is often referred to as the smeared crack approach in contrast to the discrete crack approach. Various models have been proposed for the discrete crack approach by other investigators, but for practical reasons they are not very appealing.

In addition to shear transfer capability after the formation of cracks, concrete is also able to transfer tension between the cracks. This phenomenon is called tension-stiffening which has a significant effect on the magnitude of deflections after cracking. *NONLACS* treats this phenomenon the same as *FELARC* by assuming a descending branch for concrete in tension, Fig. 18. After the formation of cracks at a given point, concrete can still carry some tension but it is assumed to have zero stiffness normal to the direction of the crack (see the step line in Fig. 18). Again this effect is smeared over a finite area which in the current program is the tributary area of a Gauss integration point.

3.5.2 Modelling Reinforcing and Prestressing Steel

Ordinary reinforcing bars and prestressing tendons and bars are modelled as an elasto-plastic strain-hardening material. The bilinear stress strain relationship in Fig. 19 is used. As can be noticed in this figure, in case of unloading, and reloading the so-called Bauschinger effect, or the reduction in the yield stress of steel due to cyclic loading, is considered. The material parameters, f_y, E_s, E_s^*, and ϵ_{su}, which are respectively, the yield stress, the Young's modulus, the strain-hardening modulus and the ultimate strain, must be input to define this relationship

3.5.3 Modelling Steel as a Continuum

For modelling the steel as a continuum, such as the steel girders in a composite bridge or steel plates and shells, theory of plasticity is used. The motivation for this is that classical theory of plasticity has been found to accurately model metal structures. Because theory of plasticity is well established and explained in the literature (Hill 1950, Owen and Hinton 1980), the discussion here will be succinct.

First it must be mentioned that as in concrete structures, for steel structures also a layered model is used. The model adopted here is based on the so-called incremental theory of plasticity in which the total plastic strain is obtained by summing the plastic strain increments. It is assumed that the total strain increment $d\epsilon_{ij}$ is given by

$$d\epsilon_{ij} = (d\epsilon_{ij})_e + (d\epsilon_{ij})_p \tag{3.56}$$

in which $(d\epsilon_{ij})_e$ and $(d\epsilon_{ij})_p$ are the elastic and plastic strain increment tensors, respectively.

The elastic strain increment can be obtained from the following well-known tensor equation

$$(d\epsilon_{ij})_e = \frac{d\sigma_{ij}'}{2G} + \frac{(1-2\nu)}{E}\delta_{ij}d\sigma_{\alpha\alpha} \tag{3.57}$$

where G is the shear modulus, also referred to as the *Lame'* constant, $d\sigma_{ij}'$ is the deviatoric stress increment and δ_{ij} is the Kronecker delta. The plastic strain increment is obtained from the flow rule.

$$(d\epsilon_{ij})_p = d\lambda\frac{\partial Q}{\partial\sigma_{ij}} \tag{3.58}$$

where Q is the plastic potential and $d\lambda$ is a constant. Q is a function of the second and third invariants of the deviatoric stress tensor, J_2' and J_3'. The reason for the latter assumption is explained by Hill (1970). The foregoing stress invariants are given by

$$J_2' = \frac{1}{2}\sigma_{ij}'\sigma_{ij}' \tag{3.59}$$

$$J_3' = \frac{1}{3}\sigma_{ij}'\sigma_{jk}'\sigma_{ki}' \tag{3.60}$$

where the deviatoric stress is given by

$$\sigma_{ij}' = \sigma_{ij} - \frac{1}{3}\sigma_{\alpha\alpha}\delta_{ij} \tag{3.61}$$

Since the yield function, f, is also a function of J_2' and J_3', Q is assumed to be equal to f and therefore,

$$(d\epsilon_{ij})_p = d\lambda\frac{\partial f}{\partial\sigma_{ij}} \tag{3.62}$$

The latter assumption leads to the so-called associated theory of plasticity. Also Eq. (3.62) implies that the plastic strain increment is normal to the yield surface; this is referred to as the normality condition.

By combining Eqs. (3.61) and (3.62), Eq. (3.56) can be rewritten as

$$(d\epsilon_{ij}) = \frac{d\sigma_{ij}'}{2G} + \frac{(1-2v)}{E}\delta_{ij}d\sigma_{\alpha\alpha} + d\lambda\frac{\partial f}{\partial\sigma_{ij}} \tag{3.63}$$

which relates increments of total strain to increments of stress.

The constant $d\lambda$ can be obtained in explicit form after some manipulations and is given by [Owen and Hinton 1980]:

$$d\lambda = \frac{\{a\}^T\{d\sigma\}}{H + \{d_D\}^T\{a\}} \tag{3.64}$$

where

$$\{a\} = \frac{\partial f}{\partial \sigma_{ij}}$$

$$\{d_D\} = [D]\{a\}$$

and

$$H = \frac{E_s{}^*}{1 - \frac{E_s{}^*}{E}}$$

In the above equations $E_s{}^*$ is the strain hardening modulus obtained from the uniaxial stress-strain curve, and H is referred to as the hardening function. Substituting Eq. (3.64) into Eq. (3.63) and rearranging yields the following relationship between the increments of stress and strain in the elasto-elastic state

$$\{d\sigma\} = [D]_{ep}\{d\epsilon\}$$

where $[D]_{ep}$ is the elasto-plastic constitutive matrix and is given by

$$[D]_{ep} = [D] - \frac{\{d_D\}\{d_D\}^T}{H + \{d_D\}^T\{a\}} \tag{3.65}$$

Eq. (3.65) is the equivalent of Eq. (3.54) used for concrete.

Note that the vectors $\{a\}$ and $\{d_D\}$ are dependent upon the yield function. For the purpose of the analyses performed in this work, the well-known Huber-von Mises yield criterion was employed. This criterion is based on the assumption that if

$$\sqrt{3}(J_2{}')^{\frac{1}{2}} \geq \sigma_y \tag{3.66}$$

then plastic flow occurs. In Eq. (3.66), $J_2{}'$ is explicitly given by

$$J_2{}' = \frac{1}{2}[\sigma_x{}'^2 + \sigma_y{}'^2 + \sigma_z{}'^2] + \tau_{xy}^2 + \tau_{yz}^2 + \tau_{zx}^2 \tag{3.67}$$

The quantity on the left-hand side of Eq. (3.66) is referred to as the effective or equivalent stress. Therefore, it can be stated that according to Huber-von Mises criterion, if the effective stress equals or exceeds the uniaxial yield stress, then plastic flow is assumed to occur.

The matrices $\{a\}$ and $\{d_D\}$ for this yield criterion and under plane stress condition are given by

$$\{a\}^T = \frac{\sqrt{3}}{2(J_2')^{\frac{1}{2}}}\{\sigma_x',\ \sigma_y',\ 2\tau_{xy},\ \sigma_z'\} \tag{3.68}$$

and

$$\{d_D\} = \frac{E}{1-\nu^2}\begin{pmatrix} a_1 + \nu a_2 \\ a_2 + \nu a_1 \\ \frac{1-\nu}{2}a_3 \\ a_4 + \nu(a_1 + a_2 - a_4) \end{pmatrix} \tag{3.69}$$

For Huber-von Mises criterion the $[D]_{ep}$ can be explicitly derived and is given by Yamada et al. (1969):

$$\begin{pmatrix} d\sigma_x \\ d\sigma_y \\ d\tau_{xy} \end{pmatrix} = \frac{E}{S}\begin{pmatrix} \sigma'^2_y + 2R & & Sym. \\ -\sigma'_x\sigma'_y + 2\nu R & \sigma'^2_x + 2R & \\ -\frac{\sigma'_x+\nu\sigma'_y}{1+\nu}\tau_{xy} & -\frac{\sigma'_y+\nu\sigma'_x}{1+\nu}\tau_{xy} & \frac{T}{2(1+\nu)} + \frac{2H}{9E}(1-\nu)\bar{\sigma}^2 \end{pmatrix}\begin{pmatrix} d\epsilon_x \\ d\epsilon_y \\ d\gamma_{xy} \end{pmatrix} \tag{3.70}$$

where

$$\begin{pmatrix} R \\ S \\ T \end{pmatrix} = \begin{pmatrix} \frac{2H}{9E}\bar{\sigma}^2 + \frac{\tau^2_{xy}}{1+\nu} \\ T + 2(1-\nu^2)R \\ \sigma'^2_x + 2\nu\sigma'_x\sigma'_y + \sigma'^2_y \end{pmatrix} \tag{3.71}$$

in which, $\bar{\sigma} = \frac{1}{3}\sigma_{\alpha\alpha}\delta_{ij}$. An analogous expression can be derived for the plane strain case.

Finally, it must be mentioned that *NONLACS* admits other well known criteria, such as Tresca, Mohr-Coulomb and Drucker-Prager. These will not be discussed here because, as mentioned earlier, only the Huber-von Mises criterion has been used throughout this report.

3.6 Nonlinear Analysis Method

It was mentioned earlier that an incremental-iterative procedure is applied to solve the system of nonlinear equations. The nonlinearity dealt with in here is due to the nonlinear stress-strain relationship of the materials involved. Specifically, the constitutive matrix $[D]$ is a function of the stress level, i.e.

$$[D] = f(\{\sigma\}) \tag{3.72}$$

Since stresses are dependent on the nodal displacements, it is obvious that the stiffness matrix, which contains $[D]$, is also a function of the nodal displacements. This makes Eq. (3.1) nonlinear.

If we denote the total nodal force vector on the right-hand side of Eq. (3.1) by $\{F\}$, then it can be rewritten as:

$$[k]\{d\} = \{F\} \tag{3.73}$$

It should be observed that $[k]$ is a function of $\{d\}$. Since $[k]$ is not known *a priori*, the solution of Eq. (3.73) requires an iterative procedure. In implementing this procedure, the load is divided into a number of increments. After the application of a load increment i, for the first iteration the tangent stiffness evaluated at the end of the preceding load increment, $[k]_{i-1}$, is used to evaluate the incremental displacements $\{\Delta d\}_i$ as

$$[k]_{i-1}\{\Delta d\}_i = \{\Delta F\}_i \tag{3.74}$$

where $\{\Delta F\}_i$ is the vector of incremental load corresponding to increment i. Using $\{\Delta d\}_i$, the incremental strains $\{\Delta\epsilon\}_i$ are calculated according to Eq. (3.3). The incremental strains are added to th previous total strains to obtain the new total strains. These total strains are then used in conjunction with the available stress-strain relations to obtain the new total stresses.

The internal nodal forces corresponding to the total stresses are next evaluated, and then equilibrium is checked between the internal and external forces. If there are any residual forces, these are reversed in direction and applied as new nodal forces. This procedure is repeated until equilibrium is satisfied within prescribed limits. More details of nonlinear analysis are given among others by Zienkiewicz(1976) and Bathe(1978).

In the next chapter, it will be demonstrated that very good agreement can be achieved between experimental data and the finite element results obtained from *NONLACS*.

4 VERIFICATION OF FINITE ELEMENT PROGRAM BY EXPERIMENTAL DATA

4.1 General

In this chapter the accuracy of the various material models described in Chapter 3 is verified by comparing either theoretically exact solutions or experimentally acquired data for some steel, composite beams, and a multi-girder bridge with the corresponding finite element results.

As previously stated, the concrete model in *NONLACS* is identical to the model in *FELARC*. The accuracy of this model has been established by Ghoneim (1978), Barakat (1980), and Razaqpur (1982), who have made numerous comparisons with avaliable experimental data on beams, plates, plane panels, push-off specimens and box-girders, with favorable agreement between the experimental and finite element results. Therefore, no additional comparisons will be presented pertaining to this aspect of the program.

In the current study, the validity of the steel plasticity model, the shear connector model and the applicability of the program to composite structures will be presented.

4.2 Verification of Steel Plasticity Model

To ascertain the correct implementation of the plasticity model for steel structures, two simple structures, (a cantilever and simply supported beam), and a steel plate are analyzed over the entire loading range up to full plastification. The results of these analyses are then compared with well-established analytical solutions. It is worthwhile to mention that the exact solutions are based on elastic-ideally plastic behavior.

4.2.1 Cantilever Beam Subjected to Tip Load

Fig. 20 (a) shows a cantilever beam subjected to a concentrated load P at the free end. The dimensions and material properties for the beam are shown in the same figure. The beam was divided into twelve elements along the span, Fig. 20 (b). The load was gradually increased from zero to 2.25 kN, which corresponds to the ultimate load.

Timoshenko (1955) has shown the closed form solution to the problem for the entire range of loading up to failure. The solution was presented by normalizing the loads and deformations with respect to the yield load and deflection. In this solution the shear deformations are neglected, therefore the dimensions of the beam were selected such that the effect of shear energy upon the behavior of the beam will be minimal.

Figure 21 (a) shows the normalized load versus tip deflection curve of the beam. It can be noticed that the comparison of *NONLACS* prediction and the exact solution is almost identical for the case of elastic-perfectly plastic material with Poisson's ratio equal zero. For Poisson's ratio, $\nu = 0.3$, the displacement in elastic stages is reduced by about 3%. The ultimate capacity, on the other hand, was increased by the same ratio. Using strain hardening for the structural steel yields the same behavior in the elastic stages as that of elastic-idealy plastic case. But it increases the ultimate load by about 3.5%. Of course, these differences are very small and they are expected. Furthermore, it can be concluded that neglecting the Poisson's ratio and strain hardening effects will not introduce any serious error in the analysis for this type of structures.

The progression of the plastic hinge is shown in Fig. 21(b). As indicated in the figure, the development of the plastic hinge is localized at the fixed end. The finite element analysis indicates that the failure of this structure is due to the development of one fully plastic cross section at the clamped end. This is consistent with the usual upper bound solutions.

4.2.2 Simply Supported Beam under Uniform Line Load

The second test case involves the simply supported steel beam under a constant line load q shown in Fig. 22 (a). The beam was analyzed using the finite element mesh in Fig. 22 (b) in which symmetry was explored. The material of the beam was assumed to be elasto-perfectly-plastic. This would allow for comparing the result with available classical solution of the problem.

The load was incremented according to the value of ρ which is given by

$$\rho = 25 \times \frac{q}{\sigma_y} \tag{4.1}$$

The above equation can be easily derived by equating the plastic moment at midspan to the applied load q and using the given dimensions. Thus $\rho = 0.667$ corresponds to the first yield and $\rho = 1.000$ to the ultimate load.

Results of the analysis are shown in Fig. 23. Fig. 23 (a) shows the load-midspan deflection in nondimensionalized form. The results also show the classical solution of this problem and it can be seen that the two solutions match very closely.

The progression of plasticity and the location of the plastic hinge are shown in Fig. 23 (b). We notice that as soon as the midspan section becomes fully plastic, the beam reaches its ultimate load.

4.2.3 Plate under Uniform Load

The two cases presented in the preceding sections both involve plane stress behavior. In this section a simply supported square plate is analyzed to study the accuracy of the plasticity model in plate bending situations.

Figure 24 shows the plate dimensions, material properties and loading. The plate is assumed to be elastic-perfectly-plastic. Since it possesses two lines of symmetry, only one quarter is modeled. The 6 × 6 mesh used to model the quarter plate is also shown in Fig. 24. Five layers were used through the thickness to capture the progression of plasticity.

Figure 25 (a) shows the load versus central deflections of the plate. The loads and deflections are once again normalized with respect to the load causing first yield and the corresponding central deflection. The same figure also illustrates the theoretical solution of this problem as given by Hodge (1959). The agreement between the results of *NONLACS* and the theoretical solution is evident.

An alternative solution of the problem in which strain hardening was considered is also presented. The strain hardening modulus E^*_s was assumed to be $0.1E_s$. It appears from Fig. 25 (a) that strain hardening does not significantly alter the ultimate load capacity of this plate.

In addition to the load-deflection response, Fig. 25 (b) shows the progression of plasticity and the formation of the plastic yield line. The yield line pattern and the plastification zones are expected from theoretical considerations. Therefore, it can be concluded that *NONLACS* plasticity model is capable of capturing the full response of steel structures up to failure.

4.3 Verification of the Shear Connector Element and the Composite Structures Analysis Capability

Since the principal objective of this study is the behavior of composite slab-on-girder bridges, it is essential that the nonlinear analysis capabilities of *NONLACS* pertinent to this problem be verified. In this section we shall use experimental data from available literature to achieve the above objective. Of course, the shear connector model described earlier will also be verified by means of these analyses. In the following chapter the results of a large scale in-house experiment will be presented and compared with those predicted by program *NONLACS*.

4.3.1 Imperial College Beams

Yam and Chapman (1967) and (1972) tested a number of simply supported and continuous composite beams at Imperial College. Here we will analyze one of each of the two types of beams. The simply supported beam selected is beam $E11$ of the series. Fig. 26 illustrates the beam and its dimensions. The beam consists of a concrete slab and a steel girder, connected together by means of shear studs. The material properties of the beam are listed in Table 7. It should be stated that in the analysis the constant a and b in Eq. (3.10) were assumed to be $a = 30kN$ and $b = 3050\frac{1}{mm}$, respectively. These are the values suggested by Yam and Chapman.

The beam was analyzed using *NONLACS* and the finite element idealization is shown in Fig. 27. Since the original authors reported only the load-midspan deflection and the slip at the concrete-steel interface at load $448kN$ (45tons), here the available experimental curves for both quantities are compared with the analytical results.

Fig. 28(a) shows the load maximum deflection curve for the beam while Fig. 28(b) illustrates the slip variation along it. It can be noticed that the comparison is favorable for both quantities although some difference exists between the curves. This can be partly due to the uncertainty in the tensile strength of concrete. For practical purposes, the differences can be considered negligible. It is interesting to note that *NONLACS* ultimate load is almost equal to the experimental value.

The slip variation in Fig. 28(b) shows good agreement with the experimental values measured on the left side of the beam centerline. The results on the right side do not compare as well. This is, however, due to the normal variations encountered in experimental work. Since the beam is symmetric, the finite element results reflect symmetry and therefore cannot obviously capture such variations.

Next the continuous beam (Yam and Chapman 1972) shown in Fig. 29 was analyzed. This is beam *CBI* of these investigators. The beam has two equal spans and although the experimental loads over the two spans were slightly different

$128.54kN$ and $130.53kN$ (12.9tons and13.1tons), for the purpose of the analysis here they were assumed to be equal. The motivation for this was to save computational resources.

In beam CB1 two rows of studs were used to connect the slab to the beam. the studs were uniformly spaced at $146mm$ (4.74 inches), throughout the span. Each stud had a $50mm$ (2 inch) long shank with a $9mm$ ($\frac{3}{8}$ inch) diameter. The yield stress of the steel beam was $f_y = 270MPa$ $(39,000psi)$, its Young's modulus was $E_s = 200 \times 10^3 MPa$ $(26.8 \times 10^6 psi)$ and the strain hardening was assumed to be $E^*{}_s = 0.1E_s$. The concrete strength was $f'_c = 47.6MPa$ $(6900psi)$ with $E_c = 26.7 \times 10^3 MPa$. For the longitudinal reinforcement, the yield stress $f_y = 270MPa$ $(40,000psi)$ and its Young's modulus $E_s = 200 \times 10^3 MPa$ $(26.8 \times 10^6 psi)$.

The finite element idealization of the beam is shown in Fig. 30. Due to symmetry about two axes, only one quarter of the beam was modelled. Figures 31 (a), (b), and (c) show the deflected shape,the slip, or relative deformation, along the concrete-steel interface and the longitudinal strain profile along the lower most fiber of the beam flange. In compliance with the experimental data, these quantities were plotted at $P = 108.5kN$ (12.2 tons), which corresponds to 86.5% of the ultimate load $P_u = 125.5$ kN (14.1 tons).

The favorable comparison between the analytical results and experimental data in all three figures verifies the accuracy of the analytical model. In particular, the comparison of the load-slip graphs demonstrate the validity of the shear connector model developed here. Of course, there is some difference between the experimental and analytical results, nevertheless the differences are within acceptable limits.

4.3.2 University of Alberta Continuous Beam

Since the shear connector model developed here is based on the experimental data of Yam and Chapman (1967), it is important to determine if the model can predict the behavior of composite beams with shear connectors different than those used by them.

Here a continuous beam, called $CB2$, tested by Hamada and Longworth (1976) at the University of Alberta will be analyzed. The shear connectors used in this beam were not identical to those used by Yam and Chapman. It should be stated that the value of a and b used in the shear connector model was the same as that in Yam and Chapman beams.

The dimensions and loading of the beam are shown in Fig. 32, and the pertinent material properties are listed in Table 8. Again, due to symmetry one quarter of the beam was modelled. The finite element mesh employed is given in Fig. 33 which also shows the layer system utilized in the slab.

Fig. 34 shows the analytical and experimental load-midspan curve of the beam. It can be observed that the two curves match rather closely. Additionally, Table 9 compares the experimentally observed and analytically computed load values at which cracking and/or yielding occurred at various locations in the beam. We observe that the differences are quite small.

The progression of the plastic strain in the steel beam and the cracked zones in the concrete slab, as predicted by finite element, are shown in Figs. 35 (a) to (d). It can be seen from the latter figures that the beam failed by crushing of the concrete in the compression zones after the yielding of the beam web in the same cross-section. This is inferred because the depth of plastic zones did not reach the full depth of the beam before failure, 35(d).

4.3.3 University of Tennessee Multi-Girder Bridge

The final example analyzed using *NONLACS* is a multi-girder bridge tested to failure by investigators from the University of Tennessee. This was one of four bridges that were slated for demolition in order to make room for a reservoir. The bridge was dubbed as Bridge # 1.

The bridge is symmetric with four continuous spans, with the end spans equal to $21.34m$ ($70'$) and the center spans equal to $27.43m$ ($90'$). It had been originally designed according to *AASHTO* code requirements for a *HS-20* truck loading in

1963. The deck slab was 178mm (7 in.) thick with a total width of 10.52m ($34'-6''$). This width includes the curbs as illustrated in Fig. 36 (a). It can be noticed that the curbs are not at the same level as the deck slab. However, in the finite element analysis, they were assumed to be at the same level. This simplifies the analysis and will not have any appreciable influence over the behavior of the bridge. Hence the idealized cross-section of the bridge is shown in Fig. 36 (b). The latter figure shows that the deck slab is supported by four $W36 \times 170$ steel beams with a uniform spacing of 2.54m ($8'-4''$). The steel beams were reinforced with $267mm \times 24.4mm$ cover plates in the support regions. This is illustrated in Figs. 37 (a) and (b), which show the full elevation and plan of the bridge. In the same figures the loading points are also shown.

In the experiment the loads were applied by means of 890 kN (200 kips) center hole resting on bearing grills The grills were made of $W14 \times 30$ steel joist beams spaced at 1.17m and 0.76m ($64''$) and ($30''$), respectively. They rested on concrete pads that were poured directly on the bridge deck. The solid squares in Fig. 37 show the location of these pads.

Observe that the loads are applied symmetrically. Hence in the analysis only half of the bridge was modelled. The finite element discritization is illustrated in Fig. 38. The mesh consists of 126 shell elements and 30 shear connector elements. In the analysis, the loads were considered as point loads because the dimension of the pads were relatively small compared to the slab dimensions.

The material properties for the concrete slab, the steel beams, and the reinforcements are given in Table 10. However, full details of the reinforcement were not available, therefore its distribution was approximated using current practice. Also, the actual length of the cover plates was not avaliable; therefore, this was ignored in the analysis. This may have some effect over the predicted behavior of the bridge.

Results of the analysis are shown in Fig. 39. The figure depicts the load versus the deflection of the midpoint of the loaded span. The same figure also shows the corresponding experimental curve. It can be observed that in general the comparison is favorable. The maximum difference between the analytical and experimental values is about 4%. In addition to the load deflection curve, Table 11 gives a qualitative comparison of the observed and analytical damage induced by increased loading. Here again there are differences between the two sets of data, but considering the many approximations introduced in the analysis, such as disregard of the cover plates, the comparison is resonable.

In view of the favorable comparisons between the finite element and experimental results for a wide range of composite and steel structures in this chapter, it can be stated that the finite element program *NONLACS* is capable of tracing the overall behavior of composite beams and bridges over the whole loading range upto failure. Although the program can also simulate some detailed aspects of the behavior of such structures, this would in general require a finer mesh and more accurate modelling of the regions affected by such details. For the purpose of the current study, such details are not considered significant. It should be stated that the available test data studied in this chapter most often did not contain all the material parameters needed for the purpose of the nonlinear analysis. Hence some assumptions had to be made. In the next chapter we shall present the results of in-house experiment conducted for the purpose of this study. The distribution of strains and deformations over the entire bridge will be compared with the predicted values obtained from *NONLACS*.

5 EXPERIMENTAL INVESTIGATION

5.1 General

Nonlinear analytical models must be verified by comparing their predictions with experimentally obtained results. For the analytical model to be acceptable, there must be a reasonable agreement, from an engineering point of view, between the two sets of results. Furthermore, all North American codes specify that for any abnormal situation of bridge design or evaluation, the test of a bridge model must be carried out. Since in this study the nonlinear finite element analysis is the main tool employed for investigating the effect of different parameters upon the behavior of slab-on-girder bridges, such verification becomes essential to fulfill both of the above objectives.

In Chapter 4 of this report the comparison between the analytical results of *NONLACS* and experimental data obtained by others was shown to be excellent. However, these tests did not include sufficiently detailed information to allow comparison of the load distribution characteristics

In Chapter 2, however, it was stated that in contrast to the massive amount of analytical studies reported, relatively little experimental research has been directed towards the problem of load distribution at ultimate load levels.

Based on this overview, it can be stated that there is a lack of available experimental data concerning composite slab-on-girder bridges load distribution behavior. Consequently, in this chapter the experimental programme conducted will be described and the results of the experiment will be presented. Detailed comparison of deformations, both deflections and strains, with corresponding finite element results will be shown. Comparison will also be made for load distribution parameter D_d

and the bending moments in the girders. Successful verification of *NONLACS* will enable us to conduct the parametric study in the next chapter confidently.

5.2 Bridge Model

To achieve the objectives of the experimental programme, the bridge prototype and model were designed according to *OHBD* code recommendations. This includes all bridge components, i.e. steel beams, concrete slab, and shear studs. The bridge prototype is a two lane bridge, $6.24m$ wide and $18.00m$ long. It has three $W840 \times 170$ compact steel beams spaced at $1.86m$. The concrete slab has a total thickness of $182mm$.

A $\frac{1}{3}$ model was designed to simulate the latter prototype. In the model the steel beams are three $W250 \times 39$ sections spaced at $620mm$. The general layout is given in Fig. 40, which shows that the slab has dimensions of $2060 \times 6205mm$. Each beam has two rows of equally spaced studs for a total of 80 shear studs. The studs were welded to the top flange of beams, as shown in Fig. 41. The deck was composed of a $70mm$ concrete slab with two layers of reinforcing steel, each layer having longitudinal and transverse bars. Fig. 42 shows the disposition of the bottom layer. The reinforcement used was the minimum according to *OHBD* code specifications. It must be noted that for practical reasons the slab in the model was thicker than that of the prototype which may have some effect upon the final results. The design failure load for the model is $500kN$.

The three girders were roller supported at one end and hinged at the other. The actual details of the supports are shown in Fig. 43. In addition, due to the high concentration of forces at the supported ends, end stiffeners were used as illustrated in the latter figure. It can be observed that to prevent the slip between the half cylindrical portions of the hinge support and the bottom flange of the beam, the two were welded together. Both supports were machined to a fine finish in order to reduce as much as possible, the frictional forces developing at the supports.

The erection of the bridge consisted of three stages. The first stage was concerned with the installation of the strain gauges in the top and the bottom flanges of the steel beams, and the construction of the formwork (see Fig. 44); the second stage consisted of placing the reinforcing and casting the concrete slab in place; the third phase involved the curing of concrete, positioning of the bridge in the testing frame and the installation of concrete strain gauges and the LVDT's.

5.3 Material Properties

A total of 11 test cylinders were cast concurrently with the bridge deck. The cylinders were filled from random batches during the casting operation. This number was deemed to yield a representative sample of the concrete used in constructing the bridge model. It must be mentioned that the specimens were taken at the beginning, middle and end of the casting of the slab. The cylinders were then cured in a similar fashion as the bridge concrete slab. The bridge deck was moist cured for 28 days by spraying it with water and keep it covered by a plastic sheet. Three 28 day old specimens were tested under uniaxial compression using Tinius Olsen $60000lb$ universal testing machine. Table 12 summarizes the results of the test. As can be seen, the average compressive strength was $f_c' = 42.1MPa$.

To find the effect of concrete age upon its strength, another four cylinders were tested using the same machine five months after placing the concrete. Table 13 illustrates the results of the tested cylinders.

Comparing the results of the above two tests, it can be noted that the average compressive strength increased by almost 3.6%.

In parallel another four specimens were tested using the split cylinder test method to determine the tensile strength of concrete. Table 14 shows the variation of f'_t. As can be seen, this variation is about 190% which is expected for concrete under tension.

The stress-strain characteristics of the reinforcing bars were determined from test coupons cut from bars used in the bridge. The coupons dimensions were the same as those recommended by *ASTM* standards. The tensile strains were measured using a clip-on-gauge with a 25*mm* base length. Fig. 45 shows the plot of the stress-strain relationship of the reinforcement. The plot was done automatically using the *Olsen* plotter, but was copied for better reproduction.

For the steel beams tensile tests will be performed on coupons taken from the three beams. These coupons will be selected from both flanges and webs at midspan and near the supports. The test procedure will be similar to that used for the reinforcing bars. However, since further testing of the bridge is planned, this could not be performed presently. Therefore, for now, an elasto-plastic stress-strain relationship, with a yield stress of $300MPa$ was assumed, Fig. 46. This was the yield stress suggested by the supplier.

5.4 Experimental Set-up

The bridge was originally cast next to the testing frame and rolled into position six months after casting. The testing rig consisted of self-reacting frame, an *MTS* controller system, two actuators and an *HP* micro computer in conjunction with *MTS* data acquistion system. Figure 47 illustrates the actual position of the hydraulic jacks and details of the loading system. The photograph in Fig. 48 shows the overall set-up of the experiment.

As can be seen in Fig. 47, the load was applied in a symmetrical fashion over the centerline of the bridge. The three point loads had design ultimate values of $54kN$, $252kN$ and $180kN$. The first two loads were applied through a $667kN$ ($150kips$) jack by means of a spreader beam. The third load was applied by means of the $490kN$ jack ($110kips$). The two jacks were, respectively dubbed as west and east actuators.

The loading scheme described is intended to simulate the *OHBD* code truck (see Fig. 2.2) in a modified form. The modified truck combines the two lines of wheels into a single line. Furthermore, the two $70kN$ axle loads in Fig. 5 are combined into a single axle. The reason for these modifications is to reduce the number of loading points which in the current model would be otherwise rather close to each other.

The actuator loads were applied through $83mm \times 200mm$ steel plattens. The plattens were placed above the central girder flange. Unfortunately, after the application of approximately $500kN$ total load, some modifications had to be made to the load transfer arrangement. This will be described in more detail later.

5.5 Instrumentation and Data Aquisition

Measurements of strains in the steel beams, reinforcement and concrete deck were made using electrical strain gauges. The gauges were sensitive to 0.01 micro strain with a standard deviation of 5%. For each steel beam the gauges were installed in the top (designated as *GTnn* where *nn* is the number of the strain gauge) and the bottom flanges (designated as *GBnn*) as illustrated in Fig. 49. As can be seen from the latter figure the bottom flange of each beam had a total of eight gauges while the top flange had only six. All 14 gauges of each beam were placed to measure the longitudinal strains. A total of 24 gauges were placed on the top surface of the slab to measure longitudinal strain. The gauges were placed in three equal rows directly above the longitudinal centerline of the steel beams. These are designated as *GCnn*, Fig. 50. Strain gauges were also attached to the transverse reinforcing bars for measuring transverse strains. These strain gauges are referred to as *GTBnn* or *GBBnn*, for the top and the bottom steel layers respectively. The motivation for this was to ensure the workability of the gauges even after the initiation of expected longitudinal cracks in the concrete. They were placed both on top and bottom steel layers. Fig. 51 shows the distribution of both longitudinal and transverse strain gauges.

The displacements of the bridge were measured using a total of 27 *LVDTs* (Linear Variable Differential Transformers). Five *LVDTs* were placed longitudinally under each beam to monitor the vertical deflection. Another eight were used to measure the transverse displacements at two sections at midspan of the bridge. Fig. 52 illustrates the distribution of the *LVDTs* in plan. To hold the *LVDTs* in position, five angles were attached to the machine frame. Fig. 53 shows the manner in which the *LVDTs* were supported.

To measure shear slip near the supports, i.e. at sections of maximum shear, four *LVDTs* were used. Fig. 54 shows schematically details of a typical *LVDT* used for such measurement. They were positioned at two locations on only two beams (the central and one of the outer beams). The first *LVDT* was located 300*mm* from the support and the second one placed 200*mm* from the first. It is worthwhile to mention that the *LVDTs* had different strokes varying from 32*mm* (1.25″) to 152*mm* (6″). However, the longer ones were placed in the areas where large deformation was expected. For the shorter ones, whenever the displacement exceeded their stroke, they were removed.

Finally both the strain gauges and the *LVDTs* were controlled automatically. The different readings were recorded using the *HP* microcomputer which displayed the strains and the displacement during the test. This ensured the workability of the individual gauges or *LVDTs*. It is interesting to mention that for each load increment two sets of data were collected, the first one just after steady reading on each actuator, and the second one just before applying the following load increment. In this fashion the second reading would indicate any creep or damage undergone by a certain gauge. Each reading took about 1.5 minutes and the gauge channels were arranged in such a way that the strains at the midspan of the bridge in both direction were recorded first. The precise order in which the strain gauges readings were recorded was in accordance to the strain gauge numbers shown in Figs. 50 to 52. Hence, the reading of strain gauge 1 was recorded first and that of gauge 100 was recorded last.

5.6 Finite Element Analysis of the Bridge Model

Before the experimental results are presented, it would be useful to mention that the bridge was analyzed by the finite element method. The results of this analysis will be compared with the corresponding experimental data in subsequent sections.

Below the finite element idealization of the bridge will be briefly described.

In the analysis half of the bridge was modelled due to the symmetry of the problem. The finite element mesh employed is illustrated in Fig. 55. The steel and concrete material properties used in the analysis are tabulated in Table 15.

The load was then applied by small increments until failure occurred at $804kN$. Failure was found to be intiated by the steel beams rather than concrete slab. The loading scheme was identical to that described for the experiment. The load was applied monotonically and no unloading was accounted for as in the experimental programme. Other aspects of the finite element idealization were similar to those of the various beams and bridges analyzed in the previous chapter.

5.7 Experimental Results

The load was applied in increments of $20kN$ up to first yield then it was reduced to $10kN$ and finally to $5kN$. As a nonlinear finite element analysis had been conducted prior to actual testing, the finite element results were used to establish the load incrementation. The two actuators were supplied pressure by the same hydraulic system, and the loads in the two were manually regulated.

As the load was incremented to approximately $533kN$ ($120kips$), the roller under the west actuator slipped to one side which caused the flange of the I-section that was transferring the load to the roller to buckle. Fig. 56 shows a photograph of the loading point after the buckling of the beam. Hence the bridge had to be unloaded and the problem was corrected. The bridge was subsequently reloaded up to $533kN$. The close comparison of the deflection readings showed that no damage had incurred as a result of this problem.

The load was then incremented to approximately $711kN$ ($160kips$) at which time the east actuator tilted to one side and again the specimen had to be unloaded. After correcting this problem too, the bridge was reloaded up to $766kN$ ($172.2kips$). At this juncture the actuators stroke was exhausted and the test had to be stopped.

Large deformations were recorded at the end of the experiment and a visible plastic hinge had formed in the central beam. The soffit of the concrete slab was severly damaged with longitudinal and diagonal cracks forming near the central portion of the bridge. The cracks were, however, limited to one side of the beam. No large cracks formed on the top surface of the deck slab but the loading platten under the larger point load punched through the concrete slab and was eventually resting on the top flange of the steel beam. Fig. 57 shows a photograph for the damaged concrete under this point load. It is believed that the bridge may be able to carry another $40kN$ ($9.5kips$). This is based on the predicted ultimate strength of the bridge by finite element. As will be shown later in this chapter, the excellent agreement between the finite element predictions and the experimental results at all stages of loading convinces the authors that the difference between the experimental and analytical values of the ultimate load would be in the range of 2.3%. In any event, it is not essential to know the actual ultimate load for the purpose of this study. It is, however, planned to modify the loading frame and reload the bridge to failure. This modification will need some time.

In the following the different experimentally measured strains and deflections will be presented. Concurrently, the prediction of the finite element program *NONLACS* will be plotted for the same quantities, the good correlation for all quantities will be self-evident.

5.7.1 Load-Deflection of Girders

The load-maximum deflection of the three steel girders are plotted in Fig. 58. The measured deflections are those recorded by *LVDTs* #7, #8 and #9 in the three girders, respectively. The corresponding finite element predictions are also plotted. It is interesting to mention that the finite element analysis was conducted prior to the actual execution of the test. Of course, the unloadings that became necessary during the course of the experiment were not accounted for in the finite element analysis.

Fig. 59 shows the deflected shape of the three beams at different stages of loading.

The loading values shown in these graphs is the gross load of the two actuators. Here again the comparison between the experimental and analytical values is rather good. The small differences that exist are negligible and in some cases due to unavailability of measured values at some locations.

As expected the loaded girder undergoes slightly higher deflection but the difference between the deflection values of the three girders is relatively small.

5.7.2 Strain Variation in Girders Flanges

The variation of the longitudinal strain along the top and the bottom flanges of the steel girders are plotted in Figs. 60 and 61, respectively. The strains are plotted for the different levels of loading as shown in the figures. Notice that in some cases it appears that the measured and predicted values of strains do not compare as closely as the deflections. In fact this may not be so because where there appears to be relatively larger disagreement, experimental values are lacking. Wherever, there is a measured value, the difference between the two sets of results are quite small.

By comparing the strains in the top and the bottom flanges, we notice that the top flange does not undergo large strains. Since the yield strain is 2000 microstrains, we notice that the top flange strains do not exceed 350 microstrains. This is expected because the concrete slab provides a large part of the compressive resistance. It is also obvious from Fig. 60 that the tensile strains in bottom flange have exceeded five times the yield strain at the section of maximum moment. Hence, the bridge is definitely within a small percentage of its ultimate load.

Since the strain comparisons are quite favorable, it can be asserted that the predicted moment field by finite element analysis is a true representation of the actual moments in the bridge.

5.7.3 Strain Variation in the Concrete

The variation of the longitudinal strain on the top surface of the concrete as measured by the *GCnn* series of strain gauges are plotted in Fig. 62. Since the location of these gauges coincided with the axes of the three girders, the strains are referred to the girders. The strains are again plotted for different levels of loading together with their analytically predicted values. In this case also the comparison between the two sets of strains is rather favorable.

It can be noticed that the maximum strain in the concrete has reached 0.002 which is equal to the strain corresponding to maximum concrete stress. Thus the concrete at the section of maximum moment and on the axis of the central girder has reached its ultimate capacity. This is in accordance with visual observations which showed the concrete in this region to be severly distressed.

Along the axes of the outer girders, however, the maximum measured strain is less than 0.002. Hence these girders may still be capable of carrying a small amount of load.

5.7.4 Strain Variation in Transverse Reinforcement

To assess the transverse moments distribution in the slab, the strains in the transverse top and bottom steel reinforcement layers were measured at several locations as illustrated in Fig. 51. Although these moments are not studied in any detail in this report, nevertheless for the verification of the finite element program it is useful to study their variation.

The comparison between the measured and calculated strains, as given by the finite element analysis, is shown in Figs. 63 and 64. It can be noticed that good agreement exists between the two sets of results. Observe that at some locations the steel strain exceeds 0.0005, which is greater than the cracking strain of concrete. This means that at these locations, the concrete must have cracked. These locations appear to be near the soffit of the slab. Interestingly, visual observations confirmed the formation of these cracks. No crack was visible on the top surface at the time of the formation of the bottom surface cracks. In this regard also the finite element results agree with the experimental findings.

5.7.5 Slip of Concrete-Steel Interface

It may be recalled that a special finite element was developed to model this phenomenon. An attempt was made to devise a method for measuring the slip (see Fig. 54). The slip at the same locations were calculated by finite element.

Figure 65 shows the variation of slip with increased loading. It can be seen that the comparison between the analytical and experimental results is poor. The experimental results show almost zero slip up to $380kN$, which is almost 48% of the ultimate load. The finite element results, on the other hand, show that slip starts almost immediately after loading.

The reason for this discrepancy may be disregard of the adhesive and frictional forces by the analytical model. Also it is doubtful that the measuring device gave accurate readings for such small displacements. Despite this discrepancy, fortunately, it appears that this does not have any appreciable effect upon either the load-deflection relationship or strains.

5.7.6 Moment Variation in the Girders

Obviously moments cannot be directly measured, hence the comparison of moments is based on calculated values. The calculated moments were obtained using the experimentally measured strain profiles in conjunction with the stress-strain relationships of concrete and steel. The steel was assumed to be elasto-perfectly-plastic while for concrete a parabolic stress-strain curve was utilized. The moments were calculated by dividing the beam into a number of layers. The force in each layer was calculated and the moment resultant of these forces was obtained at the location of the geometric centroid of the girder. This same procedure was used in the finite element calculations because the finite element program also does not output moments directly. In the case of finite element results, the layer stresses obtained from the output were used to obtain the longitudinal moment at any section.

Figure 66 shows the variation of longitudinal bending moments in the three girders at various stages of loading. We observe that the measured and calculated moments for all girders and at all stages of loading are in good accord. The small discrepancies are again due to lack of sufficient experimental data points. Most importantly, the finite element program captures the overall behavior of the bridge with a high degree of accuracy. This should enable us to conduct the parametric study in the next chapter with the knowledge that the finite element results yield the actual effect of a given parameter upon the load distribution characteristics of composite slab-on-girder bridges.

5.7.7 Distribution Parameter, D_d, of the Girders

As stated in Chapter 2, the distribution parameter, D_d, can be used to determine the design moment, M_G, for any girder. This is given by

$$M_G = \frac{S}{D_d} \times [\frac{M_T}{\text{No. of Wheels}}] \tag{5.1}$$

where M_T is the total moment at a given section of the bridge and S is the girder spacing. Eq. (5.1) can be rewritten as

$$D_d = S[\frac{M_T}{M_G \times \text{No. of Wheels}}] \tag{5.2}$$

Hence the distribution parameter for any girder can be calculated using Eq. (5.2). The total moment at any section is given by statics while M_G can be calculated using the girder moment obtained from the finite element or experimental data (see Fig. 66).

Using Eq. (5.2) the D_d variation of the three girders was calculated and is plotted in Fig. 67. The corresponding finite element values are also plotted in the same figure. Notice that in plotting this figure the maximum girder moments were used. It can be seen that the experimental and analytical values are in good agreement. Observe that as the D_d graph of girder $G2$ rises, those of girders $G1$ and $G3$ drop in value. This means that girder $G2$ attracts less load while the other two girders resist a higher portion. Of course, this happens after yielding of girder $G2$.

Finally, for the sake of illustration the D_d variation along the girders are plotted in Fig. 68 for two stages of loading. The first of these corresponds to a total load of $268kN$ ($60kips$) at which stage the bridge is still behaving elastically. The second level of loading corresponds to $762kN$ ($172.2kips$) which is near the ultimate load. We observe that near ultimate level the experimental and analytical values agree very well. However, for girder $G2$ at the elastic level at least at one point the difference seems somewhat large. But again this is due to the way the graphs are drawn than to the actual variance between the two sets of results.

In conclusion, the experimental programme in this chapter verifies the finite element results. The good agreement between the experimental and analytical values at all stages of loading together with the results shown in the preceding chapter demonstrate that the nonlinear finite element method, and in particular the material and finite element models adopted in program *NONLACS*, are capable of predicting the full response of composite slab-on-girder bridges at all stages of loading. In the next chapter this program will be utilized to conduct a detailed parametric study of load distribution in this kind of bridges.

6 PARAMETRIC STUDY

6.1 Selection of Parameters

It has been generally recognized by many investigator, Bakht and Jaeger (1980) and Heins and Kuo(1977), that some of the main parameters that influence load distribution in slab-on-girder bridges are:

i, bridge width

ii, span/width ratio

iii, girder spacing

iv, number of girders

v, number of lanes loaded

vi, truck position

vii, edge distance (distance of the outmost axle to the free edge of the bridge cross-section)

viii, relative rigidity of slab to girder

In this study the effect of the above parameters on the distribution of loads over the complete loading range up to failure will be considered. We would also consider the effect of slip at the slab-girder interface. In addition to the above parameters, the wheel contact area may also have some influence on load distribution in this kind of bridges, Bakht et al. (1979). Here we will not consider the latter effect because the simulation of wheel loads by point loads is an artifice that yields reasonable results for practical applications. If need be, this effect can be reflected by the magnitude of the axle loads of the artificial trucks devised by the codes.

In selecting the range of the parameters, the *OHBD* code was used as a guide. For example, the code recommends that simple span slab-on-girder bridges are feasible for spans of up to $24m$. Hence, none of the bridges studied here has a span exceeding $24m$. However, in some cases extreme values of certain parameter have been used mainly to establish the bounds of the effect of a particular parameter.

To show the extent to which the bridges studied here are representative of actual bridges, let us consider the $\alpha - \theta$ plane in Fig. 69. Bakht et al. (1979) studied many existing bridges and established that the $\alpha - \theta$ values within the shaded region characterize the overwhelming majority of them. The square symbols in this figure show the $\alpha - \theta$ coordinates of the bridges studied here. It can be seen that they all fall within the shaded zone and are well distributed.

6.2 Selection and Design of Bridges

The bridges analyzed were designed according to the recommendation of the *OHBD* code. Specifically, the procedure of Section 3.7.1 of the code was used and incorporated in a computer program to find the design moments. However, no load or material factors were applied. Standard design procedures, based on plastic distribution of stresses, were used to determine section dimensions and reinforcement.

A total of 80 cases were analyzed. The analyses were carried on the *FPS* attached processor with the Honeywell *CP6* as the host computer. It is worthwhile to mention that each case took an average of six *CPU* hours. Obviously, this is a tremendous amount of computing resources, but the relative cost compared to experimental work is quit small.

For the sake of easy reference, a mnemonic system will be used to identify the various bridges. Each bridge will be referred to by two letters and one number. The two letters denote the abbreviation of the relevant parameter while the number is the order of a particular bridge in the given series. For example, *GS*3 signifies the parameter *G*irder *S*pacing and 3 stands for the third bridge in this series. Table 1 in Appendix A shows the pertinent dimensions of all the bridges analyzed. Note that the steel girders are all compact sections according to *CISC* designation.

The material properties for all the bridges were assumed as follows: concrete strength 30 MPa, concrete Young's modulus $E_c = 28 \times 10^3 MPa$, $\nu_c = 0.15$, girder steel $f_y = 300MPa$, $E_s = 200 \times 10^3 MPa$, $E^*{}_s = 0.0E_s$, $\nu_s = 0.30$, reinforcing steel $f_y = 400MPa$, $E_s = 200 \times 10^3 MPa$. The properties of the the shear connectors were assumed to be: $E_s = 200 \times 10^3 MPa$ $f_y = 300MPa$, The constants a and b in Eq. (3.10) were assumed to be 30 kN and 3050 $\frac{1}{mm}$, respectively, unless otherwise specified.

6.3 Presentation of Results

The finite element program outputs for each loading step stresses, strains, curvature, moments, membrane forces, and deflections at selected points (the element nodes and Gauss points). The plethora of information it provides is indeed overwhelming. We will, however, limit ourselves to basically two quantities: the load-deflection curves and the longitudinal moment of the girders.

To demonstrate the effect of each parameter, the variation of the above two quantities under increasing load will be plotted for each girder. The load-deflection curves are rather useful because they show the elastic limit, the onset of inelasticity and yield, and the occurrence of failure. They also give the ultimate capacity of the bridge and their shape is indicative of the stability of the numerical analysis.

The moment diagrams in their raw form give some indication of the load distribution at various levels of loading at different sections along the bridge. They also identify the critical section and the critical girder in a given bridge. However, from load distribution point of view these raw diagrams are not as useful as the D_d diagrams to be discussed below. For this reason, in this chapter only the moment diagrams for the elastic (under one truck) and at ultimate limit states will be plotted.

To get a proper feeling about the load distribution and to relate the findings of this study to the provisions of the code, we shall plot the distribution parameter D_d for the girders. It may be recalled from Chapter 2 that the D-type distribution forms the basis of both the *OHBD* and *AASHTO* codes. If at any level of loading the D_d values obtained from finite element analysis become less than the code value for a given girder, then it signifies that the provisions of the codes are not safe. On the other hand, the larger the finite element values compared to the code, the more conservative is the code. It must be mentioned that the D_d values in the code are based upon the most critical loading case for any girder. In this study we obtain the D_d values for individual loading cases. Therefore, the comparison with the code should be for the most critical of the loading cases studied. We shall elaborate on these statements later in this chapter.

Finally, to relate the applied loads to the design load, all loads are expressed in terms of the number of *OHBD* trucks. In other words, the actual wheel loads are normalized with respect to the wheel loads suggested by the *OHBD* code. Hence, when the load is shown to be one truck, it does not imply that only one truck is placed on the bridge. There could be any number of trucks but the wheel load in each will correspond to the wheel loads of the code truck. Since the bridges were all designed for one truck level, it means that the larger the number of trucks at failure, the more conservative the design.

6.4 Parametric Study

In this section the effect of various parameters mentioned earlier will be presented. For each parameter the distribution characteristics will be studied through the D_d diagrams. It must be emphasized that the main objective of the current study is to establish trends rather than to obtain exact numerical values. Hence, the range of the parameters studied is deemed to be adequate for this purpose.

6.4.1 Truck Position

The study of truck position involves the longitudinal and transverse locations of the truck and the number of lanes that need to be loaded in order to induce the maximum possible moment in the bridge. In the following these will be studied.

6.4.1.1 Longitudinal Truck Position

According to the *OHBD* code, to produce maximum longitudinal moment in a bridge, first the bridge must be idealized as a single beam and then the truck must be placed in such a manner that it will produce maximum longitudinal moment in this idealized beam. Obviously, the supposition here is that the number of girders and transverse position of the truck do not influence this moment. For narrow to medium width bridges this seems reasonable; for wider bridges this will overestimate the moments. This premise is based mainly upon elastic analysis. However, due to the incidence of inelasticity, a redistribution of forces and moments may occur. The objective of the analyses in this section is to investigate whether the longitudinal truck position that induces the maximum moment in the girders at elastic level will also produce a similar moment field in the inelastic stages. Once the critical load position has been established, for all subsequent analyses the truck will be longitudinally placed in this position.

To study this parameter, two bridges were analyzed, each for two different positions of the *OHBD* truck. The bridges have been denoted as $LP1$ and $LP2$, where $LP1$ is a three girder bridge and $LP2$ is a four girder one. Except for this difference, the two bridges are identical as illustrated in Fig. 70. The figure also illustrates the two truck positions used. The first load configuration is in accordance with the code for producing maximum longitudinal moment, while the second one is an alternative position used mainly to induce maximum shear in the girders.

It must be mentioned that for simply supported bridges of this type, the span length does not generally exceed 24 m. Therefore, the two truck positions used in this analysis cover basically all practical longitudinal positions of the truck. Transversely, the truck position could also vary. Hence, for each of the two longitudinal positions of the truck, two transverse positions are assumed as shown in Fig. 71. Note that either one or two lanes are loaded. The transverse positions in Fig. 71 are assumed to be representative of the many possible locations that the truck can occupy across the bridge. For easy reference, the girders in the bridges are numbered. The numbering scheme that is used throughout this report is shown in Fig. 71. Henceforth, the girders will be referred to as $G1$, $G2$, etc. according to this scheme.

Results of the analysis are shown in Figs. 72 to 78. Figures 72, 73, and 74 show the load maximum deflection curves of the different girders, corresponding to the two truck positions. It is obvious from these figures that position 1 induces larger displacements at every level of loading in each girder of both bridges, irrespective of transverse load position. The ultimate load obtained from position 1 is also smaller, thus it is a more critical case of loading.

The above conclusions are also borne out by the moment diagrams of the girders for different levels of loading. Figs. 75 to 77 show the longitudinal moment distribution in the girders of bridges $LP1$ and $LP2$. The diagrams are plotted for one truck load which represents the load producing elastic behavior, and for failure load, representing the ultimate state. It is clear that at the elastic load level in both bridges the moment resulting from the first position is almost always larger than that caused by position two. This is not always the case at ultimate. It can be seen that at some locations in the different girders, for example $G1$ and $G3$ in bridge $LP1$, the moments due to position 2 exceed those due to position 1. This is not totally unexpected, for the location of the plastic hinge affects both the redistribution of loads in the girders and the magnitude of the failure load. The implication of this statement is that the plastic hinges in the two cases form at different locations. The important observation, however, is that at all levels of loading the maximum moment in each girder is greater due to position 1. This can be observed in Figs. 75 to 77.

As far as the distribution parameter is concerned, Fig. 78 shows the variation of D_d with load. At elastic level, this parameter has negligible effect upon load distribution. After yielding and before failure, as can be seen the slope of the descending and ascending branches of D_d for the two load positions is almost the same with the actual values becoming identical at failure. Of course, the onset of yield takes place at different load levels, so the curves do not coincide with each other. Hence, this parameter is insignificant insofar as load distribution is concerned.

In summary, the longitudinal position of the truck used in elastic analysis, in accordance with the recommendation of the code, is also suitable for inelastic behavior studies. Therefore, in all the subsequent analyses in this report, longitudinally this truck position will be utilized.

6.4.1.2 Transverse Truck Position (Edge Distance)

Elastic analysis shows that the maximum intensity of longitudinal moments in an orthotropic plate, representing a slab-on-girder bridge, increases with increased eccentricity of the load with respect to the longitudinal center line of the bridge. For example, Bakht and Jaeger (1980) have shown that moving a uniform load patch, with a very small contact area, from the middle to the free edge of the bridge can increase the moments intensity by a factor of 1.25. For multiple loads with larger contact areas, on the other hand, they have reported that this increase would be smaller. Nevertheless, the intensity of the longitudinal moments increase with the proximity of the wheels to the free edges of the slab. Both *OHBD* and *AASHTO* codes specify a minimum distance of $0.6m$ (2.0 ft) between the face of the curb and the center line of the outer line of wheels. This distance is called the vehicle-edge distance, b_s, which is shown in figure 79 (a). The extreme case of the wheel placed at the free edge is not practical. For ultimate load conditions, they recommend a total distance of $1.0m$ (3.28 ft) from the free edge. According to the *OHBD* code, this distance yields very small contribution from the external portions of the bridge to the total flexural rigidity.

To investigate how load distribution characteristics are affected by this parameter, the three and four girder bridges described in the previous article were re-analyzed for different transverse positions of the truck. The transverse positions were selected to cover nearly all possible positions of the truck across the bridge. Longitudinally the truck was located in position 1 as described in the preceeding section. The three transverse locations of the truck used are shown in Figs. 79 (b) and (c). Note that the bridges have symmetric cross-section, therefore, the illustrated cases cover essentially all the important transverse vehicle positions.

The effect of this parameter upon the behavior of the two bridge systems is demonstrated in Figs. 80 to 88. Figs. 80(a) to (c) show the load-maximum deflection curves for the three girder bridge for position 1, 2, and 3, respectively, while Figs. 81(a) to (d) display the same for the four girder one. Notice that with the vehicle in transverse position 1 (near the free edge), girder *G*1 in both systems carries more load than the other girders. As the vehicle moves closer to the center of the bridge, more load sharing takes place among the girders. Also it can be seen that the ultimate load capacity of the three girder bridge is 30% higher for position 3 than position 1. For the four girder bridge, the increase is 25%.

To see how the participation of the individual girders in resisting the applied loads varies with this parameter, Figs. 82 and 83 illustrate the load-maximum deflection curve of the individual girders. It is clear that the transverse position, or the so-called vehicle edge distance, has a more significant effect upon the behavior of the exterior girders for both elastic and ultimate load levels. This is shown in Figs. 82(a) and (c) for *G*1 and *G*3 for the three girder system, and in Figs. 83 (a) and (d) for *G*1 and *G*4 for the four girder one. For the interior girders, however, it seems that the transverse position has little influence upon the girders behavior in the elastic stages. This is in good agreement with the code. At ultimate the behavior of the interior girder is slightly affected by this parameter. This is expected since the failure loads are not the same for the three position. It is more appropriate to state that the proximity of load to a girder appreciably affects the moment in that girder.

The moment diagrams for the individual girders, as well as the total moment in each bridge, are given in Figs. 84 to 87 for the elastic and ultimate loads. Once again, Figs. 84(a) to (c) and 85(a) to (d) demonstrate that the transverse position has some effect upon the behavior of the exterior girders even at elastic stages. On the other hand, the moments for the interior girders are not very much influenced by this parameter. At ultimate both the interior and exterior girders are affected by this parameter. For example, girders $G1$ and $G2$ in the three girder bridge carry the highest moment due to the first position. This means less load sharing in the system. The same is true about $G1$ and $G2$ in the four girder bridge. So, the transverse location of the truck is important and that the critical position varies from one girder to another. Obviously, the girder nearest the load carries the highest proportion of the total load. In other words, no single location of the truck will produce critical moment in all the girders. For this reason, the code recommends that each girder be designed for a critical moment obtained from the product of the distribution factor and the longitudinal maximum moment produced by one line of wheels.

Fig. 88 shows the distribution parameter D_d from zero loading up to failure for the different truck positions. As can be seen in these figures, reducing the vehicle edge distance substantially increases the elastic moment resisted by the external girder closest to the load. At ultimate the same basic trend exists, i.e. the D_d value for the load position 1 is the smallest for both the external and internal girders. By placing the load closer to the bridge center line, the load distribution characteristics are dramatically improved. However, in practice this cannot be assumed because the truck can occupy any location across the bridge.

The latter figures also show that the wider the bridge, the worst are its load distribution characteristics. In other words, if the truck is placed closer to the free edge of the section in a wider bridge, then the girders at some distance from the load will hardly participate in resisting the loads. This is of course at elastic level. At ultimate, the remote girders tend to participate but they do not reach their ultimate capacity before failure. The reason for this may be that the slab fails before the latter girders can reach their ultimate capacity. Failure of the slab will prevent any load transfer between the girders. Hence, the ultimate capacity of the bridge cannot be assumed to be the sum of the ultimate moments of the girders in this case.

6.4.2 Bridge Width

Elastic studies reported in the literature have shown that bridge width has an important influence upon load distribution characteristics of composite slab-on-girder bridges. Thus, three bridges were analyzed to investigate the effect of this parameter upon load distribution throughout the entire loading range. The bridges have width of 8m, 12m, and 16m, with a constant span length of 16m, and are designated as $BW1$, $BW2$, and $BW3$, respectively. It should be mentioned that the girder spacing, steel beam cross-section and the concrete slab thickness were held constant for the three bridges. Varying bridge width and maintaining other parameters constant yields constant values for the different rigidities (i.e. D_x, D_y, D_{xy}, D_{yx}, D_1, and D_2). This means that these bridges have the same torsional parameter α but different flexural parameter θ. This is due to the fact that θ is linearly related to the bridge width, which can be written as

$$\theta = c \times b \tag{6.1}$$

where $c = \frac{1}{L}(\frac{D_x}{D_y})^{0.25}$, and b is the half width of the bridge. For the three bridges under consideration c is a constant. Since these bridges have the same torsional properties and different flexural parameters, the loading configurations which induce maximum moment in the girders provide sufficient data for arriving at some meaningful conclusion with regard to their load distribution characteristics.

Figures 89 (a), (b), and (c) show the cross-sections and the loading configurations. Note that in these cases instead of the *OHBD* truck, an artificial truck similar to the *AASHTO* truck was used. The reason for this substitution was to take advantage of symmetry in the analysis, without which the computer memory requirements would have been prohibitive. The actual manner in which the bridges are loaded is shown in Fig. 89 (d). We observe that $BW1$ is subjected to four lines of wheel (two trucks), $BW2$ is subjected to six lines of wheel and $BW3$ to eight lines of wheel; in this fashion the number of wheels to number of girders in bridges $BW1$ and $BW3$ were made the same.

Figures 90 to 92 summarize the behavior of the three bridges. The load-maximum deflection curves, as given in Figs 90 (a), (b), and (c), show that, this parameter affects the ultimate load of bridge $BW1$ significantly. Although there is some difference between the ultimate load of $BW2$ and $BW3$, for practical purposes, it is negligible. Furthermore, the girders in $BW1$ yield at a much lower load level than those of the other two bridges.

It is to be remarked that these bridges have the same span length and flexural rigidity per unit width. Therefore, the total flexural rigidity for each bridge varies linearly with its width. Also, if we calculate the D_d values for exterior and interior girders, they will be different by a maximum of 9% for the exterior girders and by 12.5% for the interior girders. If we divide the number of wheels by the number of girders in each bridge, [illegible] the load per girder expressed in terms of wheels/girder would be 0.67, 0.60, and 0.67 for the three bridges, respectively. Hence, according to these calculations, bridges $BW1$ and $BW3$ should yield at approximately the same number of trucks while $BW2$ is expected to yield at a higher load.

Obviously the graphs in Fig. 90 (a) and (b) do not indicate this. It can be observed that the bridge width does affect the ultimate load. However, an increase in bridge width does not lead to a linear increase in either the yield load or the ultimate capacity of the bridge. For these bridges the slab widths were in the ratio 1 : 1.5 : 2.00, while the ultimate loads were in the ratio 1 : 1.333 : 1.455, respectively.

It must be realized that even at the elastic level the bridge width has influence upon load distribution. Figures 91 (a), (b), and (c) show the moment diagram of the girders in the three bridge at one truck level and at ultimate. We can see that girder $G2$ in $BW1$ carries a higher moment than girder $G3$ and $G4$ in $BW3$. The reason that girder $G3$ in $BW2$ carries the same moment as $G3$ and $G4$ in $BW3$ is that the load per girder in $BW3$ is higher than $BW2$.

The difference in moments becomes more obvious at ultimate. Here it can be seen that the girders in $BW1$ carry smaller moments than those in $BW2$ and $BW3$. Theoretically, the ultimate moment capacity of the girders in the three bridges is the same. Since the moment in the girders of $BW1$ are approximately 2400 kN.m and those in $BW2$ and $BW3$ are about 2800 kN.m, it is argued that for $BW1$ the excessive load after yielding of girder $G2$ leads to high compressive stresses in the slab which causes crushing of concrete. Thus the composite section does not reach its ultimate capacity. In addition, the effective width of the slab in bridge $BW1$ is less than those of $BW2$ and $BW3$. It appears that the girders in the other two bridges realize their ultimate capacity.

To show the nature of load distribution at both elastic and ultimate load stages, Figs. 92(a), (b), and (c) illustrate the D_d graphs for the three bridges. In these figures we can see that the distance between the D_d graphs of the different girders is approximately 0.008, which is for practical purposes negligible. This means that the load is shared nearly equally by the three girders even before any yielding has occurred in any of the girders. For Bridge $BW2$ this distance is 0.28 and therefore the load is not equally distributed to its component girders.

If, on the other hand, we compare the D_d values for the different girders in the three bridges, with their corresponding code values, we observe that for $BW3$ the code slightly underestimates the girder moments while for the narrower bridges it overestimates the actual moments. This is, of course, at the elastic level. Overall, however, in the elastic stage the code values are conservative. Considering the inelastic stage, including the failure load level, the D_d values for all the bridges follow approximately the same trend. In conclusion, it can be stated that as far as elastic load levels is concerned, this parameter has some influence over the load distribution behavior of the 12 m wide bridge, but it has little effect over those of the 8 and 16 m wide bridges. Between the onset of inelasticity and failure, again the effect of this parameter is most visible for bridge $BW2$. At ultimate, as usual, all the girders have the same distribution parameter.

6.4.3 Span / Width Ratio

According to the *OHBD* code the flexural parameter θ is a linear function of $\frac{b}{L}$, where b is the half width of the bridge and L is the span length. The torsional parameter α is, on the other hand, independent of this quantity. The ratio $\frac{b}{L}$ can, however, vary by either changing b, L, or both in different proportions. It has been reported that in the elastic state, the variation of L within reasonable limits does not significantly influence the load distribution characteristics of slab-on-girder bridges (Bakht et al (1978)).

Here we will examine the influence of $\frac{b}{L}$ by analyzing bridges with a constant width of 8 m and span lengths of 12 m, 16 m, and 20 m. This yields $\frac{b}{L}$ values of 0.333, 0.25, and 0.20.

The detailed dimensions of these bridges, denoted as $LW1$, $LW2$, and $LW3$, are given in Appendix A. Each bridge has three girders with the loading consisting of one or two trucks positioned at different locations across the bridge, Fig. 93.

Results of the analysis are shown in Figs. 94 to 98. Figures 94 and 95 show the load-maximum deflection curves for the girders. As expected, the deflection increases with an increase in span length. Also since the moment at each section along the bridge is proportional to the span length (not necessarily linearly), bridge $LW2$, which has the longest span, fails at approximately 3.3 truck levels in the eccentric loading case and at 4 truck levels in the non-eccentric cases.

It is rather curious to observe that in loading cases one and three the load causing yielding in the loaded girders is practically the same in all three bridges. But for the same level of loading statics shows that the total maximum moment in a short span bridge is smaller than a long span bridge. Since all the girders in these bridges have the same yielding moment capacity, it means that the loaded girder in the short span bridge attracts a higher proportion of the total load compared to that in a long span bridge. Hence, the D_d value is smaller for short span bridges. It should be remarked that for the three bridges under discussion, the D_d value according to the code is almost identical for both the exterior and interior girders.

Figures 96 and 97 show the normalized moment diagrams for one truck (elastic loads) and near failure. To remove the obvious effect of the span length, the moments are normalized with respect to the span length L. The moments are actually proportional to L^n, where it is difficult to ascertain the value of n. Hence the moments are normalized both with respect to L and L^2. The moment diagrams normalized with respect to L^2 show a more consistent distribution of moments along the girders. The latter figures show that although at the elastic stage the moment in different girders of $LW1$ and $LW2$ are almost the same, at ultimate these moments are substantially different. Of course the failure load for the two bridges is different. Nevertheless, the ultimate moment differences are much larger than the difference between the ultimate loads. This again is an indication of the different load distribution characteristics.

The distribution parameter D_d for these bridges is plotted in Fig. 98. considering the vertical distance between the D_d graphs of the exterior and interior girders in the three bridges, it is obvious that in relative terms the short span bridge has the worst load distribution characteristics in all three loading cases. As expected, loading case one is the worst loading case from the point of view of load distribution. Note that in all cases the distribution characteristics improve beyond yield. The most significant improvement is observed in load case one. It may be noticed that in this loading case the D_d values of the three bridges at ultimate load are not the same. The shorter span bridge has a somewhat lower D_d value, which means higher moment in the loaded external and central girders. In all other cases, the D_d values for both the exterior and interior girders are practically the same at ultimate state.

It is important to mention that in the stages between the elastic and the ultimate levels, the D_d values of the three bridges differ noticeably. Therefore, $\frac{b}{L}$ does have some influence upon the load distribution characteristics of slab-on-girder bridges.

6.4.4 Girder Spacing

This parameter is generally assumed to have significant influence upon load distribution in slab-on-girder bridges. Both the *OHBD* and *AASHTO* codes adopt a linear relation between the distribution factor, D_f, and the girder spacings ,S, provided the distribution parameter D_d is kept constant. In fact, according to *AASHTO* S is the only parameter that affects the distribution characteristics of this type of bridges. In the *OHBD* code, the distribution factor D_f is a function of S and D_d, but in practice D_d is nearly constant for a wide range of bridges, which results in a linear relationship between D_f and S. It should be realized that the code equations are based on linear elasticity. It remains to be investigated whether they are also applicable at the inelastic and near ultimate states.

In the current study the influence of girder spacing, S, was studied by analyzing three and four girder bridges, each with three different girder spacing. These bridges are denoted as bridges $GS1$ to $GS6$ whose dimensions and structural details are given in Appendix A. $GS1$ to $GS3$ have three girders with girder spacing of 3.750, 3.375, and 3.000 respectively, while $GS4$ to $GS6$ have four girders with girder spacing of 2.50, 2.25, and 2.00 m. respectively. The calculated D_d value according to *OHBD* for all the internal girders is 2.0 and for the external girders is 2.0125. Hence, the only variable in each of the two bridge systems is the girder spacing. Each bridge was analyzed for three different transverse loading positions as noted earlier. This required a total of 18 cases to be analyzed.

Figures 99 to 110 show the effect of this parameter upon the deflection and moments of the various girders and upon the distribution characteristics of the two bridges. Figs. 99 to 100 illustrate the load-maximum deflection curves for the different girders in the three girder bridges; Figs. 101 to 103 depict the same in the four girder bridges. It can be seen in these figures that irrespective of the truck position, this parameter has an effect upon both the deflections after yielding and on the magnitude of the ultimate load. The ultimate load tends to increase with an increase in girder spacing. This, however, may be more due to a reduction in the length of the overhang slab. Notice, however, that this parameter affects the inelastic deflections and ultimate load of the girders in the three girder bridges much more than those of the four girder bridges. In the elastic range, we observe that the girder spacing has negligible effect upon the deformations of slab-on-girder bridges.

It also appears that the onset of yield is not governed by the change in girder spacing. It is important to remark that within the range studied here, the girder spacing does not have a significant effect upon the distribution of loads. Changing the girder spacing within a very wide range is expected to affect both deflections and the yielding load. Such wide variations do not, however, occur in practice.

For the three girder bridges, we see in Figs. 104 and 105 that at elastic load level in the first loading case, increasing the girder spacing reduces the longitudinal moment in the girders while for symmetric loading, in cases 2 and 3, the opposite takes place. It is difficult to discern any trend at ultimate because the ultimate moments in these figures correspond to different ultimate loads.

If we consider the four girder bridges, we notice rather interesting results. For loading case 1, Fig. 106, it can be seen that at elastic load level girder moments are hardly affected by girder spacing. At ultimate, on the other hand, there is a significant difference in the moment values of the various girders. It appears that a reduction in girder spacing substantially reduces the moment in girders located far from the applied loads. This trend agrees with the code equation but the relation is not necessarily linear. Although there is difference among the ultimate load values of the three bridges, the substantial reduction noted cannot be attributed to the difference in load values. In loading case 2, a similar trend is noticed. For example, Fig. 107 shows that the moment in girder $G4$ diminishes substantially with reduced spacing. In loading case 3, however, the difference in the moment values is small and the trend at ultimate is similar to that at elastic level, Fig. 108. Based on these observations it can be tentatively concluded that girder spacing has a significant impact upon the moment in eccentrically loaded bridges. The impact is greatest on girders situated far from the load.

Although the moment diagrams have provided some information concerning the elastic and ultimate load behavior of these bridges, the load distribution characteristics can be best established by studying the distribution parameter D_d. Figure 109 and 110 show the variation of D_d with the level of loading.

Figure 109 shows that at elastic level a reduction in girder spacing improves the load distribution characteristics. This is particularly true for the symmetric loading configurations. As far as the ultimate load is concerned, it can be seen that regardless of girder spacing, the girders eventually carry the same moment in any given bridge. It is, however, clear that a reduced girder spacing also reduces the D_d values at ultimate.

The above observations apply to both the three and the four girder bridges. Figure 110 shows the D_d variation for the four girder bridge in different load cases. Here we notice the same trend as in the three girder system, but the actual magnitude of the D_d values are not the same. It can therefore be stated that the girder spacing has a noticeable effect upon the ultimate load and inelastic deformations of the slab-on-girder bridges. It also has an appreciable influence upon the distribution characteristics at ultimate. A decrease in girder spacing tends to decrease the girder moments for a bridge of constant width.

The observed reduction of the D_d is not accounted for by the code because according to the code all the bridges considered in this section have the same D_d value. The effect of girder spacing is included in the calculation of D_f, which is not discussed here. Since girder spacing is a physical dimension, its value does not change with the level of load. Therefore, any change in D_f value in the inelastic stages must be reflected by the D_d values. In some cases it can be observed that at ultimate the difference in the D_d values for different girder spacing is about 35%. For the same bridges at elastic level this difference is much smaller. Hence, the code recommendations are applicable for elastic condition but not for ultimate loads.

6.4.5 Number of Girders

The *OHBD* code does not explicitly recognized the number of girders in a bridge as a significant parameter influencing the load distribution characteristics of slab-on-girder bridges. While this appears reasonable at the elastic level, the same cannot be concluded a *priori* at the inelastic levels. Hence two bridges, denoted as $NG3$ and $NG4$, are analyzed to study the effect of number of girders upon load distribution in the inelastic stages. Details of these bridges are given in Appendix A.

Bridges $NG3$ and $NG4$ have three and four girders respectively. Both bridges have the same span length and breadth, but not the same girder spacing. It is of course impossible to keep both the bridge width and girder spacing constant while simultaneously increasing the number of girders. However, the two bridges have identical D_d values for both the exterior and interior girders. This was achieved by using different size girders in the two bridges.

Results of the analyses for the three loading cases are given in Figs. 111 to 118. Figures 111 to 113 show the load-maximum deflection curves of the various girders due to loading cases 1 to 3, respectively. It can be seen that the girder beneath the applied load undergoes almost the same deflections in both bridges and for all cases of loading. Furthermore, the onset of inelasticity occurs at almost the same load level. Although for the other girders in the two bridges there is some difference in the magnitude of deformations even at the elastic level, this difference may be more due to the distance of load from the free ends of the overhang slabs (so-called edge distance) than due to the number of girders.

At the inelastic level, however, there is a noticeable difference between the two bridges. For instance, in loading case 1, the ultimate load of bridge $NG4$ is much higher than that of $NG3$. But for the other two loading cases there appears to be little difference between their ultimate loads. Between the onset of inelasticity and ultimate stage, however, the deformations of $NG3$ are larger then those of $NG4$. This demonstrates that in bridges with a small number of girders, the yielding of one girder increases the deformations of the remaining girders much faster than in bridges with many girders.

The moment diagrams of the girders at the elastic (one truck load) and failure load levels are shown in Figs. 114 to 117. Of course, it is expected that the individual girders in $NG3$ carry a higher load than those of $NG4$. These figures show that at the elastic level, the girder directly beneath the load in $NG3$ has a higher moment than the corresponding girder in $NG4$. But it appears that the other girders sometimes have identical moment diagrams. This is in agreement with the observation that the proximity of the load has the most significant effect upon the moments and deformations of a girder.

At ultimate some results are almost the same as in the elastic stage, particularly for loading case 2 and 3. First, it may be recalled that the ultimate load for the latter loading cases is practically the same for both bridges. Thus, the total moment at any section in the two bridges is the same. Obviously, in $NG3$ the moment in each girder would be larger than in $NG4$. If we use the present *OHBD* code equation, then since D_d is the same for the girders in the two bridges, the distribution factor D_f would be proportional to the girder spacing S. The ratio of the girder spacing in $NG3$ to that in $NG4$ is 1.2. Hence, the girders in $NG3$ are expected to carry 20% more moment than the corresponding girders in $NG4$. Figures 115 to 117 show that in many cases the girders in $NG3$ carry at least 40% more moment. It can, therefore, be stated that the number of girders influences the manner in which loads are distributed at ultimate level.

This statement is further verified by the D_d diagrams of the two bridges in Fig. 118. At the elastic level, we see that in $NG3$ the load is carried mainly by girders $G1$ and $G2$, with $G1$ carrying almost twice the load carried by $G2$. $G3$ carries practically no load because its D_d value is so large that it was out of the range of Fig. 118(a). Note that according to the *OHBD* code, the D_d for $G1$ and $G2$ are 2.013 and 1.95. Hence the girders would be expected to carry practically the same load. In $NG4$ also most of the load is carried by girders $G1$ and $G2$. In this case the difference between the moments of the two girders is somewhat smaller although still $G1$ carries a higher moment than $G2$. Note, however, that the actual moment carried by each girder is smaller than the design moment, hence the code is on the safe side.

For load cases 2 and 3, $NG3$ has better load sharing properties than $NG4$. The difference among the moments of $G1$, $G2$, and $G3$ for $NG3$ is a maximum of 8%. On the other hand, for $NG4$, the difference is higher in load case 2 (about 35%)

but much smaller in load case 3. It must be emphasized that in all cases the *OHBD* code values are on the conservative side.

At ultimate, the D_d values are very close for all the girders in both bridges. Load case 1 is an exception as has been stated before. Comparing the two bridges, we observe that in loading case 2, the D_d values of the two bridges are almost identical. In load case 3, there is 25% difference between the D_d values of $NG3$ and $NG4$. Figure 118(c) shows that the girders in $NG4$ have a higher D_d value than those of $NG3$. Since from the design point of view loading case 3 is more pertinent, it can be claimed that the number of girders influences the load distribution characteristics of slab-on-girder bridges in at least some loading cases. The higher the number of girders, the smaller the distribution factor D_f compared to the corresponding elastic values.

Finally, for case 2 and 3, it can be seen that the distribution factor at ultimate $(D_f)_u$ may be written as

$$(D_f)_u = \frac{\text{Number of Wheels}}{\text{Number of Girders}} \tag{6.2}$$

This confirms the experimental finding of Fan (1974). For case 1, on the other hand, this cannot be applied. Since cases 2 and 3 are symmetric cases of loading, as was the case in Fan's experiments, it is concluded that the above equation could be used for determining the load distribution characteristics for slab-on-girder bridges at ultimate load, provided the loading is symmetric and more particularly all lanes are loaded.

6.4.6 Slab/Girder Stiffness Ratio

It may be recalled from Section 2.3 that the distribution parameter D_d in accordance with the *OHBD* code provisions is a function of the torsional parameter α and the flexural parameter θ, which in turn are functions of the torsional and the flexural rigidities of the transformed cross-section of the bridge. The flexural rigidity for example, is obtained by:

$$D_x = (D_x)_S + (D_x)_G \tag{6.3}$$

where $(D_x)_S$ is the flexural rigidity of a unit width of the slab, and $(D_x)_G$ is an equivalent rigidity obtained by dividing the transformed girder flexural rigidity by the girder spacing. Equations similar to Eq. (6.3) are given for the other flexural and torsional quantities.

We observe in Eq. (6.3) that the relative magnitude of $(D_x)_S$and $(D_x)_G$ are not significant; the important quantity is their sum D_x. It can, therefore, be argued that, insofar as elastic behavior is concerned, the relative stiffness of the slab with respect to the girder has no influence upon the load-distribution characteristics of slab-on-girder bridges. It cannot, however, be *a priori* assumed that the same assumption applies to the inelastic and ultimate limit states. Therefore, in this section the effect of the slab-girder stiffness ratio on the load-distribution properties of composite slab-on-girder bridges throughout the loading range will be studied.

For this purpose three bridges are analyzed, namely $ST1$, $ST2$, and $ST3$. All the bridges have the same dimensions with the exception of the slab thickness. As shown in Appendix A, the slab thickness for these are $175mm$, $225mm$ (the value recommended by the code) and $275mm$. Following the same scheme of loading as in the previous cases, three transverse position of the truck were studied.

Figures 119 to 123 show the results of the analyses for the different cases of loading. The load-maximum deflection curves for each girder is displayed in Figs. 119 and 120. As can be seen in Fig. 119, for slab thickness equal to $175mm$ or $225mm$, there is hardly any difference between the two load deflection curves for the first case of loading. Fig. 120, however, shows that there is some difference for the other two loading cases. In the same figures, we notice that the failure load for $ST3$ is higher than those of $ST1$ and $ST2$, and most importantly that the slab-girder stiffness ratio does not influence the occurrence of first yield.

Considering any of the three loading cases, we notice that first yielding in all three bridges occur in the same girder and at the same load level. Since the moment corresponding to first yield is approximately the same for the three bridges, we can conclude that up to first yield a typical girder in the three bridges carries the same amount of moment. Hence the load distribution in the elastic range is not noticeably affected by this parameter, which is in agreement with the provisions of the *OHBD* code. The same cannot be said about the distribution of loads near failure as will be shown a little later.

Figs. 121 and 122 show the girder moment diagrams corresponding to first truck and failure loads. It is clear that irrespective of the slab-girder stiffness ratio the moment diagram for the different girders is almost the same for the first truck level. This confirms the earlier statement made concerning the negligible effect of this parameter at elastic level. On the contrary, at failure there is a substantial difference among these diagrams.

Consider next the D_d diagrams for these bridges. Figures 123 (a), (b), and (c) illustrate these for the three loading cases, respectively. It can be observed that at the elastic level, the bridge with slab thickness equal to $225mm$ has the least load sharing capability. The vertical distance between the D_d value of the loaded and the unloaded girders is the largest for this bridge. Of the three loading cases, once again the eccentric load case, truck position 1, leads to least load sharing in the bridge (Note that the vertical scale for the three figures is not the same).

At the inelastic stages, for load cases 2 and 3 essentially the trend of elastic behavior continues while for case 1 there is a change in the load distribution characteristics of bridges $ST2$ and $ST3$. After approximately two trucks (the load corresponding to the onset of inelastic behavior), the load distribution characteristics of bridge $ST2$ improves relative to those of $ST3$. For example, at four truck level the D_d value of the loaded girder ($G1$) and the unloaded girder ($G2$) are 2.685 and 2.997 for $ST2$ and 2.664 and 3.531 for $ST3$.

It is useful at this juncture to compare the D_d values for these bridges calculated in accordance with the provisions of the code. Strictly speaking the D_x, D_y, D_{xy}, and D_{yx} values of these bridges are not constant. This can be found in Appendix B, which shows the values of $(D_x)_s$, $(D_x)_G$, and D_x for the three bridges. The numbers in the appendix indicate that the relative stiffness of the slab/girder increases by almost 80% from $ST1$ to $ST3$. The corresponding D_z values, on the other hand, increases only 26%. It may also be useful to compare the maximum difference for α and θ values for these bridges. It appears that α increases by 34% while θ decreases by 13%. According to the *OHBD* code, the D_d values corresponding to these α and θ differ by a maximum of 0.6%, which is of course negligible. Consequently, the three bridges are expected to have identical distribution characteristics at the elastic level.

It is, therefore, concluded that the slab-girder stiffness ratio has some influence upon load distribution in load case 1, and that this influence varies from elastic to inelastic stages. Quantitatively this may not be important, for this loading case does not necessarily produce the greatest amount of moment in the girders and therefore, the girders design will be governed by other loading cases. For one lane bridges, loading case 1 governs the design.

6.4.7 Degree of Interaction

The behavior of composite members under load is dependent upon the degree of interaction between the constitutive parts of the structure. For a concrete slab resting on steel beams, interaction occurs either via friction at the interface of the slab and beam flange or by means of mechanical shear connectors. Although different types of devices are available as shear connectors, the most prevalent type is the so-called shear studs. Shear transfer by friction is not reliable and it deteriorate at small load levels; hence, shear studs will be the main vehicle for the transfer of the horizontal forces from the slab to the steel girders.

Full interaction between the slab and the beam is rare and probably impossible so long as flexible shear connectors are used. Furthermore, the strength and deformations of composite bridges are not a linear function of the stiffness of the shear connectors. Elastic analysis shows that a composite section capable of developing 50% interaction has a moment capacity equal to 94% of that of a fully composite section. Of course, the associated deflections of the partially composite section are much larger. On the other hand, a section with zero composite action has typically a moment capacity of 35 – 50% of that of fully composite section with identical dimensions *CISC*, (1985).

In practice, both *OHBD* and *AASHTO* codes assume full interaction if there is a sufficient number of connectors between the concrete slab and the girders. The minimum number and spacing of the connectors needed to ensure this condition are specified. Bridges with no-interaction are not, however, permitted by *AASHTO*. The *OHBD* code, on the other hand, allows no-interaction and provides a procedure similar to that of complete interaction for load distribution analysis.

According to the code, the load distribution analysis of full and zero interaction follow a similar procedure. In fact, for two otherwise identical bridges, one with full interaction and the other with zero interaction, the only difference in the analysis would be the flexural rigidity D_x. We can write the equation of the characterizing parameters α and θ for the two as

$$\alpha = \frac{c_1}{(D_x)^{0.5}} \tag{6.4}$$

$$\theta = c_2(D_x)^{0.25} \tag{6.5}$$

where c_1 and c_2 are constants. From Eqs. (6.4) and (6.5) it is clear that an increase in D_x, i.e. increase in degree of interaction, increases θ and reduces α. From Fig. 3.7.1 of the code this yields a smaller D_d value. The reduction will be in the order of 5 – 7% which is not significant. Since the above procedure is based on elastic analysis, it is difficult to ascertain its validity in the inelastic ranges. In this section we will analyze a four girder bridge with various degrees of interaction. The degree of interaction is simulated by changing the flexibility of the shear connectors. This can be achieved by reference to Eq. (3.10) which relates the shear force in the connector to its slip or shear deformation. By adjusting the constants a and b in this equation, one can generate the desired degree of interaction. The shear force-slip curves used in the current analyses are given in Fig. 124.

For the purpose of this study the stiffest case is referred to as full interaction while the remaining cases signify partial interaction. The initial stiffness of the studs, k_o, for the different cases are in the ratio of 0.003,0.500, 1.000 and 6.000. We shall refer to these cases as $DI1$, $DI2$, $DI3$, and $DI4$, where $DI3$ represents the studs used by Yam and Chapman and $DI4$ represents no interaction.

Results of the analysis are shown in Figs. 125 to 131. The load-maximum deflection curves of the girders are illustrated in Figs. 125 to 127. It can be observed that the load carrying capacity of the bridge is not seriously affected by the flexibility of the shear connectors; however, the increase in flexibility leads to larger deformations even at elastic load levels. As expected, the ultimate load capacity of the bridge is substantially smaller for zero interaction (non-composite action) compared to full interaction. With no interaction the bridge fails at approximately three truck load levels; with full interaction it fails at almost six trucks. In the intermediate ranges, with the exception of the first case of loading, the difference among ultimate loads is somewhat small. This is in accordance with the experimental finding of Devies (1974).

It is interesting to note that the difference between the girders with full interaction and those whose shear studs follow Yam and Chapman's equation is relatively small. The maximum difference between the deformation is about 5%. As for ultimate load capacity, the two bridges have practically identical values. Therefore, the assumption of full interaction in a bridge whose superstructure has sufficient studs is quite acceptable.

The moment variation in the girders is shown in Figs. 128 to 130 for the three loading cases. Fig. 128 shows that under unsymmetric loading conditions girder $G1$ in all four bridges practically reaches its ultimate value. But the ultimate moment for zero interaction is smaller than the other three cases. Also, as expected in the former case even at the elastic level most of the load is resisted by the loaded girder. Hence it has poor load sharing characteristics. Curiously, at the elastic level $G1$ in the bridge with 50% interaction carries the least moment, a phenomenon that is unexpected. However, if we look at girder $G3$ in this bridge, we notice that it carries a higher moment than the corresponding girder in the other three bridges.

It can also be seen that girders $G2$ to $G4$ in the bridge with no interaction do not reach their ultimate capacity. This is obviously expected because the shear transfer necessary to achieve this cannot occur. Finally, Fig. 128 shows that only girders $G1$ and $G2$ reach their ultimate capacity even with full interaction.

Fig. 129 shows the moment diagrams of loading case 2. In this case it appears that even the loaded girder, $G2$, in no interaction case did not achieve its ultimate capacity. However, the total moment carried by all the girders in this bridge is larger than in loading case 2. From this figure it is also clear that the higher the degree of interaction the better the load sharing under both elastic and inelastic conditions.

Next let us consider the third loading case, Fig. 130. Here due to symmetry girders $G1$ and $G4$, and girders $G2$ and $G3$ carry the same moments. We observe that from load sharing view point this loading case is very favorable. In this case the effect of degree of interaction on the moments in the girders is relatively small. Since in the zero interaction case the ultimate moment capacity of the girder is smaller, it can be stated that under this loading condition, all bridges reach their ultimate capacity, and the effect of degree of interaction is negligible.

As far as the influence of degree of interaction upon load distribution is concerned, let us consider Fig. 131, which shows the D_d diagrams of the three loading cases. We have omitted the D_d diagrams of some girders in certain cases because of their large values. For the remaining girders, we can see that the D_d diagrams of the girder for zero interaction never intersect. This means that full load sharing never takes place. Also the D_d value of the girders in this bridge remains basically constant with a slight variation due to the onset of inelasticity. The best load sharing under elastic conditions occurs when flexible connectors are used. At ultimate, the load sharing characteristics of partial and full interaction bridges are practically the same.

In conclusion, from a practical point of view the case of zero interaction is not recommended and in the other cases, it appears that the influence of degree of interaction upon load sharing is relatively small. More specifically, if the shear connectors are designed according to the recommendations of the code, then for practical purposes full interaction can be assumed.

7 ANALYSIS OF PARAMETRIC STUDY

7.1 General

In the preceeding chapter results of detailed parametric study were presented. The study showed how certain parameters affect load distribution in composite slab-on-girder bridges. The graphs of the distribution parameter, D_d, versus the applied load also indicated that with increased inelasticity more load sharing takes places among the girders. In general, the lower and upper bounds of D_d, were found to correspond to the elastic (service) and ultimate load conditions.

In this chapter the variation of D_d as a function of the various parameters will be shown for both the elastic and ultimate limit states. In addition, the predicted values obtained from *OHBD* code and from some available methods, as described in Chapter 2 , will be presented. In this fashion, it will become easier to ascertain the influence of a given parameter upon D_d and the extent to which available methods are able to predict it.

7.2 Selection of Available Methods for Comparison

It may be recalled that the *OHBD* code contains a rather refined procedure for load distributions analysis. Other bridge design codes cannot predict this aspect of bridge behavior with the same degree of precision. Hence, for the purpose of the current study the predicted values of D_d per *OHBD* code will be used for comparison. Of the available analytical methods, we shall use the suggested methods of Fan (1974) and Heins (1980). These were described in Chapter 2. The other methods either do not directly apply or are essentially a variation upon the latter two.

7.3 Effect of Different Parameters upon D_d

7.3.1 Longitudinal Truck Position

Although this parameter was not studied in detail because it was found that the critical longitudinal position can be easily identified, nevertheless, for the two truck positions studied (note that for each longitudinal position two transverse types of loading were considered), the variation of D_d at the elastic and ultimate load stages is plotted in Figs. 132(a) to (c). In these figures, the broken lines represent the D_d variation at the elastic level while the solid lines show the same at ultimate. The graphs identified by the girder number are those obtained from the finite element analysis. It can be seen in these figures that as far as load distribution is concerned this parameter has little influence upon D_d. We also notice that the code procedure yields conservative values for both bridges and under all load conditions. Similarly, Heins's method is even more conservative, but it appears that Fans method predicts the D_d values at ultimate rather well, particularly in the symmetric loading cases.

7.3.2 Transverse Truck Position (Edge Distance)

It was stated before that a quantitative assessment of the impact of transverse truck position can be obtained by considering the so-called edge distance. Neither the code nor any other method explicitly considers this parameter in the calculation of D_d.

Figures 133(a) and (b) illustrate the variation of D_d as a function of the edge distance for three and four girder bridges, respectively. The figures also show the predictions of existing methods. It should be pointed out that the graphs identified by the symbols $G1$, $G2$, etc. are those obtained from the finite element analysis. The solid lines indicate the ultimate load and the broken lines the service load (one truck). The available methods do not make a distinction between the D_d values of the girders or the level of loading. The exception is the *OHBD* code which gives different values for the interior and exterior girders. We observe that the effect of this parameter is rather pronounced for small edge distances. However, as the distance increases, its effect diminishes rapidly. As expected, wee see that none of the existing methods can predict the variation of D_d in this case. However, here again the predicted values are on the conservative side. It is important to point out that in the four girder bridge (Fig. 133 b) the moment reversal in girder four, which occurs under ultimate load, has to be accounted for. Obviously, if the girder is subjected to a moment causing tension in the slab, its capacity will be substantially less than under a positive moment of the same magnitude. This reversal happens under ultimate condition and not under service load. This will clearly affect the ultimate capacity of the bridge.

7.3.5 Bridge Width

It may be recalled that three, five and six girder bridges with a constant span length and variable width were symmetrically loaded to study this parameter. The variation of D_d versus the bridge width, obtained from these analyses, is plotted in Fig. 134 together with the predictions of available methods.

It is interesting to observe that D_d varies in a bilinear fashion (actually it may be parabolically). The finite element analyses and Heins and Fan's methods all show this basic behavior. In fact Fan's method coincides with the finite element results at ultimate. This confirms the earlier statement made that Fan's method correctly predicts the variation of D_d at ultimate provided the load is symmetric. Heins's method gives rather conservative values. The code, on the other hand, yields conservative values for narrow to medium width bridge but gives unconservative values for bridge width wider than 13m.

It is not possible at this juncture to suggest modifications to the code provisions because the unsymmetric loading case may not be the critical transverse load position. Further analysis is needed to fully study this aspect. In conclusion it can be stated that bridge width is an important parameter and that very narrow and very wide bridge have practically the same type of load distribution characteristics.

7.3.4 Bridge Width/Span Ratio

In the previous section we varied the bridge width by keeping the span constant. In this section the variation of D_D was studied for bridges in which their width, b, was held constant while varying their span length, l.

Graphs of D_d versus b/l are plotted in Fig. 135 (a), (b) and (c) for three transverse load positions. We notice that the effect of this parameter is relatively small. We also notice that in load case 1 and 2, none of the existing method can properly predict the actual values of D_d for a given b/l and they are all conservative in their estimates. In case 3, however, Fan's method again yields results that are identical to those of the finite element analysis.

In conclusion the effect of b/l on the variation of D_d is relatively small and for practical purposes negligible.

7.3.5 Girder Spacing

The variation of D_d versus girder spacing in three and four girder bridges is plotted in Figs. 136 and 137, respectively. We notice that D_d varies linearly with girder spacing in both bridges. A similar trend is shown by Heins and Fan but according to the code, this parameter has no influence on D_d. The actual values obtained from the finite element analysis are, however, in some cases substantially different from those predicted by existing methods. It appears that Fan's method gives very good correlation with the finite element results. From the design point of view, load case 3 is the governing load case for both the three and four girder bridges. In this case, Fan's predictions are almost the same as the finite element results.

It is, therefore, concluded that girder spacing is an important parameter as far as load distribution is concerned. Its effect is not entirely accounted for by the current provision of the code and that Fan's method gives a much better assessment of the D_d value.

7.3.6 Number of Girder

Three, four, five and six girder bridges were subjected to symmetric loading as shown in Fig. 138 (a), to study the variation of D_d versus number of girders. The results are plotted in the latter figure. We notice again that both Heins and Fan correctly predict the basic trend, namely that D_d increases from three to four girder bridges but diminishes in value beyond four girders. Unfortunately, the code predicted trend does not coincide with this observation. Of course, Heins's estimates are rather conservative, particularly for large number of girders. Fan's method as usual, gives very good correlation with the finite element results.

The loading case discussed above is generally the critical loading case in design, but in order to study the effect of other loading cases, the three and four girder bridges were reanalyzed for the truck positions shown in Figs. 138 (b) and (c). Analysis of the five and six girder bridges for these loadings would have required an exorbitant amount of computer storage and time.

The variation of D_d in the latter two cases are shown in Figs. 138 (b) and (c). In these the basic trend of loading case (1) is evident but the actual values are substantially different. Furthermore, none of the available methods give the actual values of D_d.

It is, therefore, concluded that the girder spacing is an important parameter which affects the load distribution properties of slab-girder composite bridges. Its influence in the elastic and ultimate states is nearly the same.

7.3.7 Slab/Girder Stiffness Ratio

The variation of D_d versus the slab/girder stiffness ratio of a three girder bridge is plotted in Fig. 139 (a), (b) and (c). It can be seen that the effect of this parameter is relatively small and for all practical purposes negligible. This trend is also shown by the available methods. The predicted trend of the code is in close agreement with the finite element results. But the actual values are quite different. The values according to the available methods are rather conservative, particularly in loading cases 1 and 2. However, since these cases will not be the governing cases in design, they are not as important as loading case 3, Fig. 139 (c). In this case Fan's prediction agrees closely with the finite element results.

In conclusion, an increase in slab thickness from that recommended by the code does not lead to better load distribution either at the elastic or ultimate states.

7.3.8 Degree of Interaction

The effect of degree of interaction upon D_d is plotted in Figs. 140 (a) to (c). The abscissa of these graphs show the ratio of the intial stiffness of the shear connectors used to the intial stiffness of those used by Yam and Chapman (1974) (see Section 6.4.8).

We notice that except for the uncommon case of zero interaction, the effect of this parameter on D_d is negligible. This is in accordance with previous statements made in Chapter 6. In load case 1 and 3 (symmetric loading), Fan's results are in good agreement with finite element finite element findings. But no method has beem able to predict the moment reversal in girder $G4$ that occurs at ultimate under unsymmetrical loading. As mentioned before, this needs to be considered to ensure that the steel girder alone, without contribution from the concrete slab, would be able to carry the induced moment. It must pointed out that the discrepancy among the actual values predicted by available methods and the finite element results is rather large in load case 1. It is due to the scale of the ordinates that the graphs seem so close.

In conclusion, we can state that for the common cases of even nominal shear transfer between the concrete slab and steel girders, the effect of the flexibility of shear connectors upon the load distribution characteristics of composite bridges is small and definitely negligible.

In this chapter we have observed that certain parameters have a strong effect upon the load distribution characteristics of composite slab-on-girder bridges at both the elastic and ultimate load levels. In general, the *OHBD* code does not predict these effects. However, for almost all practical situations the D_d values obtained from the code are on the safe side. Of the methods available for load distribution evaluation, Fan's method gives excellent correlation with the finite element results when the bridge is symmetrically and fully loaded. For practical designs, this loading case generally governs and therefore Fan's method can be used to evaluate the load distribution characteristics of this type of bridges at ultimate. In other loading cases, comparatively, Fan's method is still better than the code and Heins's methods.

It is important to mention that the load distribution characteristics of slab-on-girder bridges at ultimate are not the same as at elastic state. The variation of D_d with load can be approximated to be bilinear, with the two lines intersecting at the onset of yield in one of the girders.

Whereas at the elastic level the girders directly below the load resist a higher portion of the applied load, at ultimate, in case of symmetric loading, all the girders carry practically the same load. This load corresponds to the ultimate capacity of the girders. When the bridge is subjected to unsymmetrical loading, the girders farthest from the load carry much less load and at ultimate moment reversal takes place in these girders. Hence, the ultimate load of the bridge in this case is not the sum of the ultimate loads of the girders.

Finally, the finite element analyses in Chapter 7 have yielded much more information than presented in the last two chapters. Also, the manner in which the results in these chapters were presented is one of many possible ways. However, regardless of the manner of presentation, it is believed that the trends that have been established will be useful in improving the *OHBD* code provisions. Further elaboration on or discussion of the results would require more time and space and are beyond the scope of this report.

8 SUMMARY AND CONCLUSIONS

8.1 Summary

An extensive analytical and experimental program was undertaken to study the load distribution characteristics of simply supported slab-on-girder composite bridges over the entire loading range up to failure.

A detailed literature review was conducted to establish the current state of the art. It was found out that with respect to load distribution at ultimate state there is a paucity of relevant material, both analytically and experimentally. This lead to the work described in this report.

Because of its versatility, the nonlinear finite element method was adopted as the method of analysis. New procedures and finite elements were added to the basic framework of an existing program to determine the nonlinear response of slab-on-girder bridges to overload. The added features were verified by analyzing some composite beams and bridges tested by other investigators. The comparison between the analytical and experimental results was found to be very good. To further verify more detailed aspects of the program, a $\frac{1}{3}$-scale direct model of a $18m$ prototype bridge was designed and tested in the laboratory. The detailed comparison of the analytical and experimental results for this bridge corroborated the earlier findings.

Subsequently, a detailed parametric study was undertaken to determine the influence of a number of geometric and loading parameters upon the load distribution properties of this type of bridges. These analyses showed that the level of loading, position of the load and some geometric characteristics of the bridge influence load distribution. Furthermore, comparison of the finite element results with available methods, including that of *OHBD* code, revealed that most of the existing methods cannot accurately predict the load distribution properties of composite slab-on-girder bridges under all types of loading. However, for nearly all loading conditions, the *OHBD* code method was found to yield safe , albeit conservative, results.

The tables from table 16 to table 89 summarize the distribution parameter values obtained from the parametric study. The listed values correspond to the elastic behavior, i.e. under one truck level, and to the failure or ultimate condition. The symbols used are the same as in the main chapters. For reference, the computed values from finite element analysis are compared with those obtained from the *OHBD* code recommendations. This is expressed as a percentage as follows:

$$\frac{D_d(\text{FEM}) - D_d(\text{code})}{D_d(\text{code})} \times 100$$

As the tables show, this percentage varies from as low as 3.5% to as high as 400% or even more. It is, therefore, difficult to recommend any specific value because it depends on the geometric characteristics and loading condition of the bridge.

8.2 Conclusions

1. The nonlinear finite element method is an accurate and powerful tool for the analysis of slab-on-girder composite bridges, including the study of their load distribution characteristics.
2. Experimental work in this regard should be limited to the verification of some new modelling procedures used in the finite element analysis.
3. The load distribution characteristics of this type of bridge are affected by many parameters, including the position of the truck across the bridge, the number of lanes loaded, the level of loading and some geometric properties and dimensions of the bridge.
4. Of the many parameters considered, it was determined that edge distance, bridge width, number of girders, girder spacing and the number of loaded girders have a marked effect upon load distribution.

5. The load distribution characteristics improve with increased level of loading. The best load sharing generally occurs just prior to failure. At this stage all the girders attain their ultimate capacity. This, however, is not the case under unsymmetrically applied loads.
6. The governing case for design purposes is generally a symmetrical one in which all lanes are loaded. In this case at least one available simple method of load distribution analysis yields results that compare closely with the nonlinear finite element analysis.
7. The *OHBD* code cannot in general predict the influence of many parameters upon load distribution, either at the elastic or ultimate states. However, in nearly all cases, its predicted values are on the safe side, and in some instances rather conservative.
8. Bridges with no composite action between the concrete slab and the steel girders have very poor distribution properties and are not recommended. However, a reasonable number of shear connectors will improve load distribution substantially.
9. Increase in slab thickness, particularly beyond that recommended by the code, has negligible beneficial effect upon load distribution.

8.3 Recommendations for Future Work

The current study was restricted to simply supported concrete slab on compact steel beam bridges. Although such bridges constitute a large number of actual bridges, it is recommended to study the load distribution properties of

- Continuous bridges
- Skew bridges
- Curved bridges
- Bridges with stiffeners, bracings, and/or diaphragms.
- Bridges with noncompact sections.

- Composite concrete slab-on-concrete girder bridges.

We restricted our attention in this report to the longitudinal moments. It may also be interesting to investigate the longitudinal shear and transverse bending moment in the slab. These are not, however, generally as important as longitudinal moment. The following changes and improvements can be implemented in the finite element program *NONLACS*

- Addition of a beam element to represent the steel girders. This will save greatly in terms of computational resources.
- The addition of geometrically nonlinear capability to analyze noncompact sections and instability effects.
- Addition of a better plate bending element, especially if skew bridges are to be analyzed.

Finally, an experimental program will be needed to verify the applicability of the finite element program to the many types of bridges listed above. A better device for measuring the slip at the slab-beam interface is also needed. The modification of the shear force-slip relationship used in this study can be then more carefully achieved, if necessary. To account for the effect of the adhesive and frictional forces that exist at lower levels of loading, more accurate experimental data is needed.

REFERENCES

[1] American Association of Highway and Transportation Officials (*AASHTO*), "Standard Specifications for Highway Bridges," Eleventh Ed. Washington D. C., 1973.

[2] Allman, D.J., " A Compatible Triangular Element Including Vertex Rotations for Plane Elasticity Analysis," Computers & Structures, V.19, pp. 1-8, 1984.

[3] Aziz, O., "Private Communication," Carleton University, Ottawa, 1987.

[4] Bakht, B., Cheung, M. S., and Aziz, T. S. "The Application of Simplified Method of Calculating Longitudinal moments to the Proposed Ontario Highway Bridge Design Code," Canadian Journal of Civil Engineering, Vol. 6, No. 1, pp. 36-50, 1979.

[5] Bakht, B. and Jaeger, L. G., "Bridge Analysis Simplified," McGraw-Hill Book Co., Bewrkshire, 1985.

[6] Bathé, R. J., "Finite Element Procedures in Engineering Analysis," Prentice-Hall, New Jersey, 1982.

[7] Barakat, M. A. "New Approaches to Shear Problems," Ph.D. Thesis, Department of Civil Engineering, The University of Calgary, Calgary, Canada, 1980.

[8] Barés, R. and Massonnet, C., "Analysis of Beams and Grids and Orthotropic Plates by the Guyon-Massonnet-Bares Method," Crossby Lockwood, London, 1968.

[9] Bergan, P. G., and Fellipa, C. A., "A Triangular Membrane Element with Rotational Degrees of Freedom," Computer Methods in Applied Mechanics and Engineering, No. 50, pp. 25-69, 1985.

[10] Brockenbrough, R. L., "Distribution Factors for Curved I-Girder Bridges," Proc. ASCE, Vol. 112, No. 10, Oct., pp. 2200-2215, 1986.

[11] Canadian Standards Association, "Code for Design of Highway Bridges *(CANS-S6-M78)*," Rexdale, Canada, 1978.

[12] Cheung, M. S., Gardner, N. J., and Ng, S. F., "Load Distribution Characteristics of Slab-on-Girder Bridges at Ultimate," Proceedings of the Second International Conference on Short and Medium Span Bridges, Ottawa, Canada, Vol. 2, pp. 461-485, 1986.

[13] Cheung, M. S., and Chan, M. Y. "Finite Strip Evaluation of Effective Flange Width of Bridge Girders," Canadian Journal of Civil Engineer, Vol. 5, pp. 174-185, 1978.

[14] Cheung, Y. K., "The Finite Strip Method in The Analysis of Elastic Plates with Two Opposite Simply Supported Ends," Proc. Inst. Civil Engng. 40, 1-7 1968.

[15] Chu, K. H., and Krishnamoorthy, G., "Moments in Composite Beam Bridges by Orthotropic Plate Theory," ACI Journal, Vol. 59, No. 5 May, 1962.

[16] Chu, K. H., and Krishnamoorthy, G., "Use of Orthotropic Plate Theory in Bridge Design," Proc. ASCE, Vol. 88, No. ST 3, pp. 35-77, 1962.

[17] Cook, R. D. "Concepts and Applications of Finite Element Analysis," 2ed Ed., John Wiley and sons, New York, 1981.

[18] Cook, R.D., " Improved Two-Dimensional Finite Element ", ASCE Journal of the Struct. Div., ST9, pp.1851-1863, 1974.

[19] Cook, R.D., " On the Allman Triangle and Related Quadrilateral Element," Computers & Structures, V.22, No.6, pp. 1065-67, 1986.

[20] Cuséns, A. R., and Pama, R. P. "Bridge Deck Analysis," John Wiley and sons, London, 1975.

[21] Darwin, D., and Pecknold, D. A., "Nonlinear Biaxial Stress-Strain Law for Concrete," Journal of the Engineering Mechanics Division, ASCE, Vol. 103, No. EM4, April 1977.

[22] Devies, C., "Tests on Half-Scale Steel-Concrete Composite Beams with Welded

Stud Connectors," The Structural Engineer, Vol. 47, No.1, pp. 29-40, 1969.

[23] Fan, H. M., "Effective Width of Composite Bridges at Ultimate Load," Ph.D. Dissertation, University of Maryland, 1974.

[24] Fu, C. C., Heins, C. P., "Inelastic Analysis of Continuous, Composite Highway Bridges," Report No. 62, Federal Highway Administration, Baltimore, Md Maryland Div. U.S.A., June 1976.

[25] Ghoneim, G. A. M., "Nonlinear Analysis of Concrete Structures," Ph.D. Thesis, Department of Civil Engineering, The University of Calgary, Calgary, Canada, August 1978.

[26] Ghoneim, G. A. M., and Ghali, A., "User Manual for Computer Program *FELARC* (Finite Element Layered Analysis of Concrete)," Report No. CE78-15, Department of Civil Engineering, The University of Calgary, Calgary, Canada, May 1979.

[27] Ghoneim, G. A. M., and Ghali, A., "Nonlinear Analysis of Concrete Structures," Canadian Journal of Civil Engineering, Vol. 9, No. 3, pp. 489-501, 1982.

[29] Hamada, S., and Longworth, J., "Buckling of Composite Steel Beams in Negative Bending," Proc. ASCE Vol. 100, No. ST11, pp. 2205-2223, 1973.

[30] Hamada, S., and Longworth, J., "Ultimate Strength of Composite Beams," Proc. ASCE Vol. 102, No. ST7, pp. 1463-1478, 1976.

[31] Heins Jr.,C. P., and Looney, C. T. G., "Bridge Analysis Using Orthotropic Plate Theory," Proc. ASCE Vol. 94, No. ST2, pp. 565-592, 1968.

[32] Heins Jr.,C. P., and Looney, C. T. G., "Bridge Tests Predicted by Finite Difference Plate Theory," Proc. ASCE Vol. 95, No. ST2, pp. 249-265, 1969.

[33] Heins, C. P., Kuo, J. T. C., "Ultimate Live Load Distribution Factor for Bridges," Proc. ASCE Vol. 101, No. ST7, pp. 1481-1496, 1975.

[34] Heins, C. P., and Fan, H. M., "Effective Composite beam Width at Ultimate Load," Proc. ASCE Vol. 102, No. ST11, pp. 2163-2179, 1976.

[35] Heins, C. P., and Jin, o. J., "Live Load Distribution on Braced Curved I-

girders," Proc. ASCE Vol. 110, No. 3, pp. 523-530, 1984.

[36] Hill, R., "The Mathematical Theory of Plasticity," Oxford University Press, Oxcford, 1950.

[37] Hodge, P. G. Jr., "Plastic Analysis of Structures," Chapter 10, McGraw-Hill Book Co., Bewrkshire, 1959.

[38] Kōstem, C. N., "Over Loading Response of Multi-Girder Bridges," Analysis and Design of Bridges, NATO ASI Series: Applied Sciences No. 74, pp. 49-56,1984.

[39] Kōstem, C. N., "Distribution in Prestressed Concrete Highway Bridges," Analysis and Design of Bridges, NATO ASI Series: Applied Sciences No. 74, pp. 213-223, 1984.

[40] Kupfer, H., and Gerstle, K. H., "Behavior of Concrete under Biaxial Stresses," Journal of the Engineering Mechanics Division, ASCE, Vol. 99, No. EM4, August 1973.

[41] Kuo J. T. C., and Heins, C. P., "Live Load Distribution on Simple Span I-beam Composite Highway Bridges," No. 52, Progress report No. 52 to Federal Highway Administration, Baltimore, Md Maryland Div. U.S.A., June 1968.

[42] Newmark, N. M., "Design of I-beams Bridge," Highway Bridge Floor Symposium, Journal of of the structural division, ASCE, Vol. 93, STI, pp. 305-331, 1948.

[43] Newmark, N. M., Siess, C. P., and Viest, I. M., "Tests and Analysis of Composite Beams with Incomplete Interaction," Proceeding Society for Experimental Stress Analysis, Vol. 9, No. 1, pp. 75-92, 1951.

[44] *OHBD* code, "Ontario Highway Bridge Design Code," Ministry of Transportation of Ontario, Downsview, Ontario, Canada, 1983.

[45] Owen, D. R. J., and Hinton, E., "Finite Elements in Plasticity: Theory and Practice," Pineridge Press, Swansea, 1980.

[46] Pian, T.H., " Evaluation of Assumed Stress Hybrid Finite Element," ART in FEM Technology, J. Robenson (Edit), pp. 602-619, 1984.

[47] Razaqpur, A. G., "Web-Flange Connections: Analysis and Design," Ph.D. Thesis, Department of Civil Engineering, The University of Calgary, Calgary, Canada, December 1982.

[48] Razaqpur, A. G., and Nofal, M. E., "Performance of a New Quadrilateral Finite Element with Rotational Degrees of Freedom," Proceeding of 5th. World Congress, J. Robenson (Edit), pp. 121-130, 1987.

[49] Reddy, V. M., "Ultimate Load Behavior of Composite Steel Concrete Bridge Deck Structures," Indian Concrete Journal, May, 1969.

[50] Rowe, R. E., "Concrete Bridge Design," C. R. Books, London 1962.

[51] Saenz, L. D., "Discussion of Equation for the Stress-Strain Curve of Concrete by Desayi and Krishnan," American Concrete Institute Journal, Vol. 61, No. 9, September 1964.

[52] Sawko, F., "Effect of Strain Hardening on the Elasto-Plastic Behavior of Beams and Grillages," Proceedings of the Institute of Civil Engineers, pp. 489-503, 1964.

[53] Seible, F., and Scordelis, A. C., "Nonlinear Behavior and Failure Analysis of Multi-Cell RC Box-Girder Bridges," Proceedings of the Second International Conference on Short and Medium Span Bridges, Toronto, Canada, pp. 391-405, 1982.

[54] Sisodyia, R. G., and Ghali, A., "Analysis of Box-Girder Bridges of Arbitrary Shape," Publications, IABSE, Vol. 33-I, pp. 208-218, 1973.

[55] Smith, G. M., and Young, L. E., "Ultimate Theory in Flexure by Exponential Function," Journal of the American Concrete Institute, Vol. 52, No. 3, November 1955.

[56] Szilard, R., "Theory and Analysis of Plates," Prentice-Hall Inc., New Jersey, 1974.

[57] Timoshenko, S., "Strength of Materials," D. Van Nostrand Co., 1955.

[58] Viest, I. M., "Review of Research on Composite Steel-Concrete Beams," Proc.

ASCE, Vol. 86, No. ST 6, pp. 1-21, 1960.

[59] Vitols, V., Clifton, R. J., and Au, T., "Analysis of Composite Beam Bridges by Orthotropic Plate Theory," ASCE Vol. 89, No. ST 4, pp. 71-96, 1963.

[60] Wegmuller, A. W., and Amer, H. N., "Nonlinear Response of Composite Steel-Concrete Bridges," Computer & Structures Vol. 7, pp. 161-169, 1977.

[61] Wegmuller, A. W., "Overload Behavior of Composite Steel-Concrete Bridges," Proc. ASCE Vol. 103, No. ST9, pp. 1799-1819, 1977.

[62] Yamada, Y., Kawai, T., Yashimura, N., and Sakurai, T., "Analysis of the Elastic-Plastic Problems by the Matrix Methods in Structural Mechanics," Wright-Pattersin Air Force Base, Ohio, 1969.

[63] Yam, L. C. P., and Chapman, J. C., "The Inelastic Behavior of Simply Supported Composite Beams of Steel and Concrete," Proceeding of Civil Engineer pp. 651-683, 1968.

[64] Yam, L. C. P., and Chapman, J. C., "The Inelastic Behavior of Continuous Composite Beams of Steel and Concrete," Proceeding Institution of Civil Engineer pp. 487-501, 1972.

[65] Zienkiewicz, O. C., "The Finite Element Method", 3rd edition, McGraw-Hill Book Co., Bewrkshire, 1983.

[66] Zienkiewicz, O. C., and Chung, Y. K., "The Finite Element Method for Analysis of Elastic and Orthotropic Slabs," Proceedings of Institution of Civil Engineers, Vol. 28, pp. 471-488, 1964.

TABLES

Table 1: Distribution Parameter (Elastic Load)

Span	Spacing	2-Lanes		3-Lanes		4-Lanes	
(ft.)	(ft.)	Method 1	Method 2	Method 1	Method 2	Method 1	Method 2
40	6.0	5.68	5.94	5.45	5.50	5.23	5.23
	7.0	6.03	5.92	5.23	5.29	5.30	5.22
	8.0	6.27	6.14	5.45	5.27	5.26	5.16
	9.0	6.51	6.42	5.42	5.33	5.31	5.16
50	6.0	5.82	5.87	5.25	5.19	5.12	4.97
	7.0	6.34	5.87	5.25	5.31	5.12	5.00
	8.0	6.35	6.50	5.34	5.36	5.07	5.15
	9.0	6.65	6.28	5.32	5.15	5.18	5.00
60	6.0	5.91	5.80	5.33	5.24	5.07	4.80
	7.0	6.11	6.17	5.20	5.35	5.10	4.93
	8.0	6.41	6.62	5.39	5.46	5.05	4.96
	9.0	6.65	6.89	5.75	5.05	5.20	4.90
70	6.0	6.27	5.74	5.40	5.16	5.03	4.65
	7.0	6.16	6.30	5.25	5.48	5.10	5.22
	8.0	6.45	6.65	5.41	5.48	5.01	4.91
	9.0	6.72	6.93	5.38	5.50	5.15	4.87
80	6.0	6.00	6.55	5.37	5.64	5.03	5.26
	7.0	6.23	6.51	5.40	5.69	5.04	4.67
	8.0	6.62	6.95	5.45	5.62	4.98	4.84
	9.0	6.95	7.32	5.48	5.70	5.18	4.77
90	6.0	6.03	6.63	5.41	5.79	4.98	4.52
	7.0	6.26	6.55	5.43	5.80	5.11	4.73
	8.0	6.74	7.08	5.51	5.71	5.01	4.87
	9.0	7.11	7.46	5.57	5.80	5.37	5.34
100	6.0	6.07	5.48	5.46	5.89	5.10	6.59
	7.0	6.28	6.57	5.45	5.83	5.17	5.40
	8.0	6.86	7.18	5.55	5.75	5.10	5.32
	9.0	—	—	—	—	—	—

Table 2: Distribution Parameter (Ultimate Load)

Span	Spacing	2-Lanes		3-Lanes		4-Lanes	
(Ft.)	(Ft.)	Method 1	Method 2	Method 1	Method 2	Method 1	Method 2
40	6.0	6.68	7.44	6.22	6.76	6.17	6.67
	7.0	7.03	6.79	6.37	6.96	6.02	6.01
	8.0	7.69	7.94	6.18	6.28	6.12	6.70
	9.0	7.98	8.26	6.35	6.71	5.76	5.71
50	6.0	7.35	7.44	6.34	6.83	6.45	6.68
	7.0	7.35	7.00	6.39	6.93	5.82	6.41
	8.0	7.63	7.99	6.58	6.63	6.36	6.72
	9.0	7.88	7.57	7.03	7.28	6.00	6.66
60	6.0	7.50	7.33	5.68	5.75	6.64	6.64
	7.0	7.09	7.00	6.40	6.92	6.13	6.95
	8.0	7.62	7.96	6.42	6.66	6.40	6.65
	9.0	8.33	8.91	6.75	6.52	6.15	6.72
70	6.0	7.43	6.75	6.95	6.84	5.90	6.07
	7.0	7.06	7.00	6.38	6.94	6.17	6.74
	8.0	7.83	7.95	6.42	6.64	6.20	6.35
	9.0	9.45	8.91	6.97	7.35	6.30	6.36
80	6.0	6.88	7.51	6.52	6.95	6.23	6.58
	7.0	6.94	7.00	6.77	6.96	6.81	6.92
	8.0	7.70	8.00	6.67	8.00	6.37	6.51
	9.0	8.83	8.99	7.09	7.46	6.65	6.70
90	6.0	6.92	7.52	6.29	6.98	6.71	6.61
	7.0	6.84	6.00	6.67	6.99	7.20	6.72
	8.0	7.66	8.00	6.48	6.66	6.55	6.72
	9.0	8.39	8.96	6.97	7.43	6.65	6.62
100	6.0	6.98	7.52	6.56	6.98	6.10	6.59
	7.0	6.75	7.00	6.38	6.95	6.20	6.71
	8.0	7.92	7.97	6.42	6.64	6.48	6.77
	9.0	—	—	—	—	—	—

Table 3: Comparisons of Displacements and Stresses for Square Plate Under Inplane Bending

Element Type	Mesh size	$\frac{Eu_c}{\sigma_o a}$	$\frac{Ev_c}{\sigma_o a}$	$\frac{E\Omega_c}{\sigma_o}$	$\frac{E\sigma_x}{\sigma_o}$
	1×1	0.451	−0.287	−0.960	0.944
Allman	2×2	0.482	−0.309	−0.966	0.989
Triangle	4×4	0.494	−0.320	−0.982	0.996
	8×8	0.498	−0.324	−0.991	0.998
RQUAD4	3×3	0.505	−0.310	−1.008	1.060
	4×4	0.499	−0.310	−1.005	0.990
QLC3	3×3	0.445	−0.200	−0.960	1.003
	4×4	0.455	−0.270	−0.998	0.850
Exact		0.500	−0.325	−1.000	1.000

Table 4: Vertical deflection at C for different mesh sizes

Element	2×2	3×3	4×4	5×5	8× 8	16×16	32×32
HL	18.17		22.03			23.81	
HG	22.32		23.23			23.91	
Q4	11.85		18.30			23.43	
Q6	22.94		23.48				
QM6	21.05		23.02				
CST	11.92		18.28		22.02	23.41	
FF	20.36		22.42		23.41	23.79	23.91
RQUAD4	21.60	23.26	23.90	23.95			

Table 5: Normal stress, σ_x, at A for different mesh sizes

Element	2×2	3×3	4×4	5×5	8× 8	16×16	32×32
HL	0.1582		0.1980			0.2294	
HG	0.0933		0.1628			0.2225	
$Q4$	0.1281		0.1905			0.2358	
$Q6$	0.1866		0.2210				
$QM6$	0.1900		0.2239				
CST	0.0760		0.1498		0.1999	0.2217	
FF	0.1700		0.2129		0.2309	0.2333	0.2359
$RQUAD4$		0.2239		0.2308			

Table 6: Normal stress, σ_x, at B for different mesh sizes

Element	2×2	3×3	4×4	5×5	8× 8	16×16	32×32
HL	−0.1335		−0.1700			−0.2008	
HG	−0.1394		−0.1566			−0.1952	
$Q4$	−0.0916		−0.1510			−0.2002	
$Q6$	−0.1936		−0.1936				
$QM6$	−0.1565		−0.1853				
CST	−0.0360		−0.1002		−0.1567	−0.1844	
FF	−0.1804		−0.1706		−0.1902	−0.1961	−0.2012
$RQUAD4$		−0.1800		−0.1985			

Table 7: Material Properties for Beam *E11*

Loading	Point Load at Midspan
f_y (psi)	34400
E_s (psi)	26.6×10^6
f_c (psi)	7250
ϵ_{uc}	0.0045
Connector Details	$\frac{1}{2}''$ × 2" headed Studs
No. of Connector	100

Table 8: Material Properties for Beam CB2

Concrete	
f_c (psi)	5460.0
f_t (psi)	440.
E_c (psi)	4.258×10^6
ν_c	0.2
ϵ_u	0.005
Steel Reinforcement	
f_y (psi)	51600.0
E_s (psi)	29×10^6
ν_s	0.30
ϵ_y	0.002
Steel beam	
f_y(web) (psi)	49100.0
E_s(web) (psi)	30.2×10^6
E_s(flanges) (psi)	45200.0
f_y(flanges) (psi)	32.1×10^6
ν_s	0.3
ϵ_y	0.2

Table 9: University of Alberta Beam Results Comparison

Defintion	Analytical (kN)	Exprimental (kN)
Complete Cracking over the Intrior Support	265	260
Bottom Flange First Yielding	425	439
Web Yielding	500	507
Complete Cracking at Load	570	590
Failure Load	610	605

Table 10: University of Tennesse Bridge Material Properties

Loading	8 Points Patch Load
f_y	300 MPa
E_s	200×10^3 MPa
ϵ_y	0.2
ν_s	0.3
f_c	30 MPa
f_t	3 MPa
E_c	28×10^3 MPa
ϵ_{uc}	0.0045
ν_c	0.15
Connector Details	The Minimum as specified by Codes
(Reinforcement)	The Minimum as Specified by Codes

Table 11: University of Tennesse Bridge Results Comparison

Defintion	Analytical (kN)	Exprimental (kN)
Complete Cracking over the Intrior Supports	2500	2650
Bottom Flange First Yielding	3000	3125
Failure Load	5450	5559

Table 12: Compressive Strength at 28 Days

Cylinder	Diameter	Length	Area	Total Load	Ultimate Stress
#	D	L	$A = \frac{\pi \times D^2}{4}$	P_u	$f_c' = \frac{P_u}{A}$
	mm	mm	mm^2	N	MPa
1	149.0	305.0	17436	725100	41.590
2	145.0	305.0	16513	700600	42.427
3	150.0	305.0	17671	747300	42.290

Table 13: Compressive Strength after Five Months

Cylinder	Diameter	Length	Area	Total Load	Ultimate Stress
#	D	L	$A = \frac{\pi \times D^2}{4}$	P_u	$f_c' = \frac{P_u}{A}$
	mm	mm	mm^2	N	MPa
1	149.0	305.0	17436	760642	43.626
2	150.5	305.0	17789	772874	43.449
3	150.5	305.0	17789	772874	43.449
4	147.0	305.0	16971	747297	44.035

Table 14: Tensile Strength after Five Months

Cylinder	Diameter	Length	Area	Total Load	Ultimate Stress
#	D	L	$A = \pi \times D \times L$	P_u	$f_t' = 2\frac{P_u}{A}$
	mm	mm	mm^2	N	MPa
1	145.0	305.0	138937	255771	3.682
2	150.0	305.0	143728	210066	2.923
3	147.0	305.0	140853	307926	4.372
4	150.0	305.0	143728	270005	3.757

Table 15: Material Properties Used in the Analysis

Material Constant	Concrete	Reinforcing Steel	Structural Steel
f'_c	42.1	—	—
f'_t	3.5	—	—
σ_y	—	400	300
ϵ_y	0.0005	0.002	0.002
ϵ_u	0.0045	0.02	0.02

Note: For detials of the results listed in tables x to y, refere to Chapter 6 and Chapter 7.

Table 16: D_d for Longitudinal Truck Position Parameter and Loading Case 1 for Three Girder Bridge (Maximum Moment)

Girder	Finite Element Values		Code	$\frac{D_{d(FEM)}-D_{d(Code)}}{D_{d(Code)}} \times 100$	
#	Elastic	Ultimate		Elastic	Ultimate
G1	2.2460	2.2500	2.1600	3.9815	4.1667
G2	2.2570	2.2500	2.1762	3.7129	3.3912
G3	2.2460	2.2500	2.1600	3.9815	4.1667

Table 17: D_d for Longitudinal Truck Position Parameter and Loading Case 1 for Three Girder Bridge (Maximum Shear)

Girder	Finite Element Values		Code	$\frac{D_{d(FEM)}-D_{d(Code)}}{D_{d(Code)}} \times 100$	
#	Elastic	Ultimate		Elastic	Ultimate
G1	2.2460	2.2500	2.1600	3.9815	4.1667
G2	2.2570	2.2500	2.1762	3.7129	3.3912
G3	2.2460	2.2500	2.1600	3.9815	4.1667

Table 18: D_d for Longitudinal Truck Position Parameter and Loading Case 2 for Three Girder Bridge (Maximum Bending)

Girder	Finite Element Values		Code	$\frac{D_{d(FEM)}-D_{d(Code)}}{D_{d(Code)}} \times 100$	
#	Elastic	Ultimate		Elastic	Ultimate
G1	2.7250	3.0900	2.1600	26.1574	43.0556
G2	4.1290	3.0900	2.1762	89.7344	41.9906
G3	8.4670	12.5000	2.1600	291.9907	478.7037

Table 19: D_d for Longitudinal Truck Position Parameter and Loading Case 2 for Three Girder Bridge (Maximum Shear)

Girder	Finite Element Values		Code	$\frac{D_{d(FEM)} - D_{d(Code)}}{D_{d(Code)}} \times 100$	
#	Elastic	Ultimate		Elastic	Ultimate
G1	2.7210	3.1190	2.1600	25.9722	44.3981
G2	4.1180	3.1170	2.1762	89.2289	43.2313
G3	8.5560	11.6500	2.1600	296.1111	439.3519

Table 20: D_d for Longitudinal Truck Position Parameter and Loading Case 1 for Four Girder Bridge (Maximum Moment)

Girder	Finite Element Values		Code	$\frac{D_{d(FEM)} - D_{d(Code)}}{D_{d(Code)}} \times 100$	
#	Elastic	Ultimate		Elastic	Ultimate
G1	2.5440	2.5700	2.2943	10.7526	12.0607
G2	2.5950	2.5680	2.3370	11.0398	9.8845
G3	2.5950	2.5680	2.3370	11.0398	9.8845
G4	2.5440	2.5700	2.2943	10.7526	12.0607

Table 21: D_d for Longitudinal Truck Position Parameter and Loading Case 1 for Four Girder Bridge (Maximum Shear)

Girder	Finite Element Values		Code	$\frac{D_{d(FEM)} - D_{d(Code)}}{D_{d(Code)}} \times 100$	
#	Elastic	Ultimate		Elastic	Ultimate
G1	2.5440	2.5700	2.2943	10.7526	12.0607
G2	2.5950	2.5680	2.3370	11.0398	9.8845
G3	2.5950	2.5680	2.3370	11.0398	9.8845
G4	2.5440	2.5700	2.2943	10.7526	12.0607

Table 22: D_d for Longitudinal Truck Position Parameter and Loading Case 2 for Four Girder Bridge (Maximum Bending)

Girder	Finite Element Values		Code	$\frac{D_{d(FEM)}-D_{d(Code)}}{D_{d(Code)}} \times 100$	
#	Elastic	Ultimate		Elastic	Ultimate
G1	3.1880	3.6910	2.2943	38.9531	60.8770
G2	3.9980	3.6910	2.3370	71.0740	57.9375
G3	6.7290	5.1150	2.3370	187.9332	118.8703
G4	15.1400	24.2800	2.2943	559.8963	1001.9000

Table 23: D_d for Longitudinal Truck Position Parameter and Loading Case 2 for Four Girder Bridge (Maximum Shear)

Girder	Finite Element Values		Code	$\frac{D_{d(FEM)}-D_{d(Code)}}{D_{d(Code)}} \times 100$	
#	Elastic	Ultimate		Elastic	Ultimate
G1	3.1920	3.6130	2.2943	39.1274	57.4772
G2	4.1360	3.5140	2.3370	76.9790	50.3637
G3	6.5640	5.8760	2.3370	180.8729	151.4335
G4	14.0700	21.2800	2.2943	513.2589	827.5160

Table 24: D_d for Edge Distance Parameter Case 1 (Three Girder Bridge)

Girder	Finite Element Values		Code	$\frac{D_{d(FEM)}-D_{d(Code)}}{D_{d(Code)}} \times 100$	
#	Elastic	Ultimate		Elastic	Ultimate
G1	2.7250	3.0900	2.1600	26.1574	43.0556
G2	4.1290	3.0900	2.1762	89.7344	41.9906
G3	8.4670	12.5000	2.1600	291.9907	478.7037

Table 25: D_d for Edge Distance Parameter
Case 2 (Three Girder Bridge)

Girder	Finite Element Values		Code	$\frac{D_{d(FEM)}-D_{d(Code)}}{D_{d(Code)}} \times 100$	
#	Elastic	Ultimate		Elastic	Ultimate
G1	3.3450	3.6670	2.1600	54.8611	69.7685
G2	3.9870	3.6670	2.1762	83.2093	68.5047
G3	5.6330	5.5000	2.1600	160.7870	154.6296

Table 26: D_d for Edge Distance Parameter
Case 3 (Three Girder Bridge)

Girder	Finite Element Values		Code	$\frac{D_{d(FEM)}-D_{d(Code)}}{D_{d(Code)}} \times 100$	
#	Elastic	Ultimate		Elastic	Ultimate
G1	4.2220	4.1350	2.1600	95.4630	91.4352
G2	3.9430	4.1350	2.1762	81.1874	90.0101
G3	4.2220	4.1350	2.1600	95.4630	91.4352

Table 27: D_d for Edge Distance Parameter
Case 1 (Four Girder Bridge)

Girder	Finite Element Values		Code	$\frac{D_{d(FEM)}-D_{d(Code)}}{D_{d(Code)}} \times 100$	
#	Elastic	Ultimate		Elastic	Ultimate
G1	2.7000	3.2110	2.2943	17.6830	39.9555
G2	4.0690	3.2110	2.3370	74.1121	37.3984
G3	7.8230	5.4170	2.3370	234.7454	131.7929
G4	28.9900	20.8400	2.2943	1163.6000	1008.3000

Table 28: D_d for Edge Distance Parameter
Case 2 (Four Girder Bridge)

Girder	Finite Element Values		Code	$\frac{D_{d(FEM)}-D_{d(Code)}}{D_{d(Code)}} \times 100$	
#	Elastic	Ultimate		Elastic	Ultimate
G1	3.1920	3.5340	2.2943	39.1274	54.0339
G2	4.1360	3.5330	2.3370	76.9790	51.1767
G3	6.5640	6.0990	2.3370	180.8729	160.9756
G4	14.0700	20.6000	2.2943	513.2589	797.8773

Table 29: D_d for Edge Distance Parameter
Case 3 (Four Girder Bridge)

Girder	Finite Element Values		Code	$\frac{D_{d(FEM)}-D_{d(Code)}}{D_{d(Code)}} \times 100$	
#	Elastic	Ultimate		Elastic	Ultimate
G1	3.9290	4.4480	2.2943	71.2505	93.8718
G2	4.1980	4.4520	2.3370	79.6320	90.5006
G3	5.6690	4.8840	2.3370	142.5760	108.9859
G4	9.1490	8.0380	2.2943	298.7709	250.3465

Table 30: D_d for Edge Distance Parameter
Case 4 (Four Girder Bridge)

Girder	Finite Element Values		Code	$\frac{D_{d(FEM)}-D_{d(Code)}}{D_{d(Code)}} \times 100$	
#	Elastic	Ultimate		Elastic	Ultimate
G1	3.5460	3.8910	2.2943	54.5569	69.5942
G2	3.1350	3.8830	2.3370	34.1463	66.1532
G3	4.3920	3.9140	2.3370	87.9332	67.4797
G4	5.8380	4.3400	2.2943	154.4567	89.1645

Table 31: D_d for Bridge Width Parameter
$B = 8m$ (Three Girder Bridge)

Girder	Finite Element Values		Code	$\frac{D_{d(FEM)} - D_{d(Code)}}{D_{d(Code)}} \times 100$	
#	Elastic	Ultimate		Elastic	Ultimate
G1	2.0600	2.0630	2.0000	3.0000	3.1500
G2	2.0680	2.0620	2.0125	2.7578	2.4596
G3	2.0680	2.0620	2.0000	3.4000	3.1000

Table 32: D_d for Bridge Width Parameter
$B = 12m$ (Five Girder Bridge)

Girder	Finite Element Values		Code	$\frac{D_{d(FEM)} - D_{d(Code)}}{D_{d(Code)}} \times 100$	
#	Elastic	Ultimate		Elastic	Ultimate
G1	2.3200	2.2920	2.1000	10.4762	9.1429
G2	2.4160	2.2920	2.2000	9.8182	4.1818
G3	2.0330	2.2920	2.2000	-7.5909	4.1818
G4	2.4160	2.2920	2.2000	9.8182	4.1818
G5	2.3200	2.2920	2.1000	10.4762	9.1429

Table 33: D_d for Bridge Width Parameter
$b = 16m$ (Six Girder Bridge)

Girder	Finite Element Values		Code	$\frac{D_{d(FEM)} - D_{d(Code)}}{D_{d(Code)}} \times 100$	
#	Elastic	Ultimate		Elastic	Ultimate
G1	2.0670	2.0620	2.2000	-6.0455	-6.2727
G2	2.0520	2.0620	2.2500	-8.8000	-8.3556
G3	2.0680	2.0620	2.2500	-9.0889	-8.3556
G4	2.0680	2.0620	2.2500	-9.0889	-8.3556
G5	2.0520	2.0620	2.2500	-8.8000	-8.3556
G6	2.0670	2.0620	2.2000	-6.0455	-6.2727

Table 34: D_d for Span-Width Ratio Parameter

$\frac{2b}{L} = 0.33$ (Case 1)

Girder	Finite Element Values		Code	$\frac{D_{d(FEM)} - D_{d(Code)}}{D_{d(Code)}} \times 100$	
#	Elastic	Ultimate		Elastic	Ultimate
G1	2.3590	2.8000	1.9750	19.4430	41.7722
G2	4.8110	2.8000	2.0205	138.1094	38.5796
G3	28.6500	-23.8500	1.9750	1350.6000	-1307.6000

Table 35: D_d for Span-Width Ratio Parameter

$\frac{2b}{L} = 0.25$ (Case 1)

Girder	Finite Element Values		Code	$\frac{D_{d(FEM)} - D_{d(Code)}}{D_{d(Code)}} \times 100$	
#	Elastic	Ultimate		Elastic	Ultimate
G1	2.4780	3.1600	1.9750	25.4684	60.0000
G2	4.6960	3.1600	2.0205	132.4177	56.3969
G3	19.9300	-70.1000	1.9750	909.1139	-3649.4000

Table 36: D_d for Span-Width Ratio Parameter

$\frac{2b}{L} = 0.20$ (Case 1)

Girder	Finite Element Values		Code	$\frac{D_{d(FEM)} - D_{d(Code)}}{D_{d(Code)}} \times 100$	
#	Elastic	Ultimate		Elastic	Ultimate
G1	2.6100	3.2760	1.9750	32.1519	65.8734
G2	4.6450	3.2760	2.0205	129.8936	61.8411
G3	14.6500	-102.7000	1.9750	641.7722	-5300.0000

Table 37: D_d for Span-Width Ratio Parameter
$\frac{2b}{L} = 0.33$ (Case 2)

Girder	Finite Element Values		Code	$\frac{D_{d(FEM)} - D_{d(Code)}}{D_{d(Code)}} \times 100$	
#	Elastic	Ultimate		Elastic	Ultimate
G1	4.6540	4.4880	1.9750	135.6456	127.2045
G2	4.2210	4.5240	2.0205	108.9087	123.9050
G3	4.6540	4.4880	1.9750	135.6456	127.2045

Table 38: D_d for Span-Width Ratio Parameter
$\frac{2b}{L} = 0.25$ (Case 2)

Girder	Finite Element Values		Code	$\frac{D_{d(FEM)} - D_{d(Code)}}{D_{d(Code)}} \times 100$	
#	Elastic	Ultimate		Elastic	Ultimate
G1	4.5940	4.4400	1.9750	132.6076	124.8101
G2	4.3220	4.6250	2.0205	113.9074	128.9037
G3	4.5940	4.4400	1.9750	132.6076	124.8101

Table 39: D_d for Span-Width Ratio Parameter
$\frac{2b}{L} = 0.20$ (Case 2)

Girder	Finite Element Values		Code	$\frac{D_{d(FEM)} - D_{d(Code)}}{D_{d(Code)}} \times 100$	
#	Elastic	Ultimate		Elastic	Ultimate
G1	4.5730	4.5060	1.9750	131.5443	128.1519
G2	4.3620	4.4880	2.0205	115.8872	122.1232
G3	4.5730	4.5060	1.9750	131.5443	128.1519

Table 40: D_d for Span-Width Ratio Parameter
$\frac{2b}{L} = 0.33$ (Case 3)

Girder	Finite Element Values		Code	$\frac{D_{d(FEM)} - D_{d(Code)}}{D_{d(Code)}} \times 100$	
#	Elastic	Ultimate		Elastic	Ultimate
G1	2.2460	2.2500	1.9750	13.7215	13.9241
G2	2.2570	2.2500	2.0205	11.7050	11.3586
G3	2.2460	2.2500	1.9750	13.7215	13.9241

Table 41: D_d for Span-Width Ratio Parameter
$\frac{2b}{L} = 0.25$ (Case 3)

Girder	Finite Element Values		Code	$\frac{D_{d(FEM)} - D_{d(Code)}}{D_{d(Code)}} \times 100$	
#	Elastic	Ultimate		Elastic	Ultimate
G1	2.2460	2.2500	1.9750	13.7215	13.9241
G2	2.2570	2.2500	2.0205	11.7050	11.3586
G3	2.2460	2.2500	1.9750	13.7215	13.9241

Table 42: D_d for Span-Width Ratio Parameter
$\frac{2b}{L} = 0.20$ (Case 3)

Girder	Finite Element Values		Code	$\frac{D_{d(FEM)} - D_{d(Code)}}{D_{d(Code)}} \times 100$	
#	Elastic	Ultimate		Elastic	Ultimate
G1	2.2460	2.2500	1.9750	13.7215	13.9241
G2	2.2570	2.2500	2.0205	11.7050	11.3586
G3	2.2460	2.2500	1.9750	13.7215	13.9241

Table 43: D_d for Girder Spacing Parameter
$GS = 3.000$ in Three Girder System (Case 1)

Girder	Finite Element Values		Code	$\frac{D_{d(FEM)} - D_{d(Code)}}{D_{d(Code)}} \times 100$	
#	Elastic	Ultimate		Elastic	Ultimate
G1	2.3590	2.8000	2.1840	8.0128	28.2051
G2	4.8110	2.8000	2.2848	110.5655	22.5490
G3	28.6500	-23.8500	2.1840	1211.8000	-1192.0000

Table 44: D_d for Girder Spacing Parameter
$GS = 3.375$ in Three Girder System (Case 1)

Girder	Finite Element Values		Code	$\frac{D_{d(FEM)} - D_{d(Code)}}{D_{d(Code)}} \times 100$	
#	Elastic	Ultimate		Elastic	Ultimate
G1	2.6690	3.2000	2.1534	23.9435	48.6022
G2	5.3980	3.2000	2.2533	139.2047	42.0139
G3	30.6200	-26.2600	2.1534	1321.9000	-1319.5000

Table 45: D_d for Girder Spacing Parameter
$GS = 3.750$ in Three Girder System (Case 1)

Girder	Finite Element Values		Code	$\frac{D_{d(FEM)} - D_{d(Code)}}{D_{d(Code)}} \times 100$	
#	Elastic	Ultimate		Elastic	Ultimate
G1	3.0100	3.6090	2.1175	42.1488	70.4368
G2	5.8760	3.7350	2.2000	167.0909	69.7727
G3	32.3300	-87.3700	2.1175	1426.8000	-4226.1000

Table 46: D_d for Girder Spacing Parameter
$GS = 3.000$ in Three Girder System (Case 2)

Girder	Finite Element Values		Code	$\frac{D_{d(FEM)}-D_{d(Code)}}{D_{d(Code)}} \times 100$	
#	Elastic	Ultimate		Elastic	Ultimate
G1	4.6540	4.3890	2.1840	113.0952	100.9615
G2	4.2210	4.7410	2.2848	84.7426	107.5018
G3	4.6540	4.3890	2.1840	113.0952	100.9615

Table 47: D_d for Girder Spacing Parameter
$GS = 3.375$ in Three Girder System (Case 2)

Girder	Finite Element Values		Code	$\frac{D_{d(FEM)}-D_{d(Code)}}{D_{d(Code)}} \times 100$	
#	Elastic	Ultimate		Elastic	Ultimate
G1	5.3320	4.9140	2.1534	147.6084	128.1973
G2	4.5990	5.3810	2.2533	104.1007	138.8053
G3	5.3320	4.9140	2.1534	147.6084	128.1973

Table 48: D_d for Girder Spacing Parameter
$GS = 3.750$ in Three Girder System (Case 2)

Girder	Finite Element Values		Code	$\frac{D_{d(FEM)}-D_{d(Code)}}{D_{d(Code)}} \times 100$	
#	Elastic	Ultimate		Elastic	Ultimate
G1	6.0440	5.5420	2.1175	185.4309	161.7237
G2	4.9390	5.8000	2.2000	124.5000	163.6364
G3	6.0440	5.5420	2.1175	185.4309	161.7237

Table 49: D_d for Girder Spacing Parameter
$GS = 3.000$ in Three Girder System (Case 3)

Girder	Finite Element Values		Code	$\frac{D_{d(FEM)} - D_{d(Code)}}{D_{d(Code)}} \times 100$	
#	Elastic	Ultimate		Elastic	Ultimate
G1	2.2440	2.2500	2.1840	2.7473	3.0220
G2	2.2620	2.2500	2.2848	-0.9979	-1.5231
G3	2.2440	2.2500	2.1840	2.7473	3.0220

Table 50: D_d for Girder Spacing Parameter
$GS = 3.375$ in Three Girder System (Case 3)

Girder	Finite Element Values		Code	$\frac{D_{d(FEM)} - D_{d(Code)}}{D_{d(Code)}} \times 100$	
#	Elastic	Ultimate		Elastic	Ultimate
G1	2.5140	2.5320	2.1534	16.7456	17.5815
G2	2.5660	2.5290	2.2533	13.8774	12.2354
G3	2.5140	2.5320	2.1534	16.7456	17.5815

Table 51: D_d for Girder Spacing Parameter
$GS = 3.750$ in Three Girder System (Case 3)

Girder	Finite Element Values		Code	$\frac{D_{d(FEM)} - D_{d(Code)}}{D_{d(Code)}} \times 100$	
#	Elastic	Ultimate		Elastic	Ultimate
G1	2.7830	2.8140	2.1175	31.4286	32.8926
G2	2.8740	2.8100	2.2000	30.6364	27.7273
G3	2.7830	2.8140	2.1175	31.4286	32.8926

Table 52: D_d for Girder Spacing Parameter
$GS = 2.000$ in Four Girder System (Case 1)

Girder	Finite Element Values		Code	$\frac{D_{d(FEM)}-D_{d(Code)}}{D_{d(Code)}} \times 100$	
#	Elastic	Ultimate		Elastic	Ultimate
G1	2.0530	2.6240	2.1175	-3.0460	23.9197
G2	3.1560	2.6240	2.2275	41.6835	17.8002
G3	6.2580	3.7240	2.2275	180.9428	67.1829
G4	27.6900	-56.9200	2.1175	1207.7000	-2788.1000

Table 53: D_d for Girder Spacing Parameter
$GS = 2.250$ in Four Girder System (Case 1)

Girder	Finite Element Values		Code	$\frac{D_{d(FEM)}-D_{d(Code)}}{D_{d(Code)}} \times 100$	
#	Elastic	Ultimate		Elastic	Ultimate
G1	2.3090	2.7680	2.1250	8.6588	30.2588
G2	3.5640	2.7680	2.2360	59.3918	23.7925
G3	7.0010	3.9540	2.2360	213.1038	76.8336
G4	31.0100	-21.8600	2.1250	1359.3000	-1128.7000

Table 54: D_d for Girder Spacing Parameter
$GS = 2.500$ in Four Girder System (Case 1)

Girder	Finite Element Values		Code	$\frac{D_{d(FEM)}-D_{d(Code)}}{D_{d(Code)}} \times 100$	
#	Elastic	Ultimate		Elastic	Ultimate
G1	2.5740	3.1000	2.1450	20.0000	44.5221
G2	3.9330	3.1000	2.2440	75.2674	38.1462
G3	7.7110	4.2150	2.2440	243.6275	87.8342
G4	36.2100	-20.4700	2.1450	1588.1000	-1054.3000

Table 55: D_d for Girder Spacing Parameter
$GS = 2.000$ in Four Girder System (Case 2)

Girder	Finite Element Values		Code	$\frac{D_{d(FEM)}-D_{d(Code)}}{D_{d(Code)}} \times 100$	
#	Elastic	Ultimate		Elastic	Ultimate
G1	3.5460	3.8910	2.1175	67.4616	83.7544
G2	3.1350	3.8830	2.2275	40.7407	74.3210
G3	4.3920	3.9140	2.2275	97.1717	75.7127
G4	5.8380	4.3480	2.1175	175.7025	104.9587

Table 56: D_d for Girder Spacing Parameter
$GS = 2.250$ in Four Girder System (Case 2)

Girder	Finite Element Values		Code	$\frac{D_{d(FEM)}-D_{d(Code)}}{D_{d(Code)}} \times 100$	
#	Elastic	Ultimate		Elastic	Ultimate
G1	3.3090	4.0910	2.1250	55.7176	92.5176
G2	3.3060	4.0910	2.2360	47.8533	82.9606
G3	5.1090	4.1360	2.2360	128.4884	85.4204
G4	7.7590	6.3200	2.1250	265.1294	197.4118

Table 57: D_d for Girder Spacing Parameter
$GS = 2.500$ in Four Girder System (Case 2)

Girder	Finite Element Values		Code	$\frac{D_{d(FEM)}-D_{d(Code)}}{D_{d(Code)}} \times 100$	
#	Elastic	Ultimate		Elastic	Ultimate
G1	4.5740	4.5450	2.1450	113.2401	111.8881
G2	3.7810	4.5450	2.2440	68.4938	102.5401
G3	5.5160	4.5960	2.2440	145.8111	104.8128
G4	8.5910	7.0220	2.1450	300.5128	227.3660

Table 58: D_d for Girder Spacing Parameter

$GS = 2.000$ in Four Girder System (Case 3)

Girder	Finite Element Values		Code	$\frac{D_{d(FEM)}-D_{d(Code)}}{D_{d(Code)}} \times 100$	
#	Elastic	Ultimate		Elastic	Ultimate
G1	1.9800	2.0000	2.1175	-6.4935	-5.5490
G2	2.0200	2.0000	2.2275	-9.3154	-10.2132
G3	2.0200	2.0000	2.2275	-9.3154	-10.2132
G4	1.9800	2.0000	2.1175	-6.4935	-5.5490

Table 59: D_d for Girder Spacing Parameter

$GS = 2.250$ in Four Girder System (Case 3)

Girder	Finite Element Values		Code	$\frac{D_{d(FEM)}-D_{d(Code)}}{D_{d(Code)}} \times 100$	
#	Elastic	Ultimate		Elastic	Ultimate
G1	2.2140	2.2500	2.1250	4.1882	5.8824
G2	2.2880	2.2500	2.2360	29.1592	0.6261
G3	2.2880	2.2500	2.2360	29.1592	0.6261
G4	2.2140	2.2500	2.1250	4.1882	5.8824

Table 60: D_d for Girder Spacing Parameter

$GS = 2.500$ in Four Girder System (Case 3)

Girder	Finite Element Values		Code	$\frac{D_{d(FEM)}-D_{d(Code)}}{D_{d(Code)}} \times 100$	
#	Elastic	Ultimate		Elastic	Ultimate
G1	2.4110	2.5000	2.1450	12.4009	16.5501
G2	2.5960	2.5000	2.2440	7.4421	11.4082
G3	2.5960	2.5000	2.2440	7.4421	11.4082
G4	2.4110	2.5000	2.1450	12.4009	16.5501

Table 61: D_d for Slab-Girder Stiffness Ratio Parameter $\frac{I_{ss}}{I_{sG}} = 0.293$ (Case 1)

Girder	Finite Element Values		Code	$\frac{D_{d(FEM)}-D_{d(Code)}}{D_{d(Code)}} \times 100$	
#	Elastic	Ultimate		Elastic	Ultimate
G1	2.5160	2.8500	1.7500	43.7714	62.8571
G2	4.7140	2.8500	2.0000	135.7000	42.5000
G3	17.4900	-21.2900	1.7500	899.4000	-1316.6000

Table 62: D_d for Slab-Girder Stiffness Ratio Parameter $\frac{I_{ss}}{I_{sG}} = 0.382$ (Case 1)

Girder	Finite Element Values		Code	$\frac{D_{d(FEM)}-D_{d(Code)}}{D_{d(Code)}} \times 100$	
#	Elastic	Ultimate		Elastic	Ultimate
G1	2.3590	2.8000	1.8500	27.5135	51.3514
G2	4.8110	2.8000	2.0125	139.0559	39.1304
G3	28.6500	-23.8500	1.8500	1448.6000	-1389.2000

Table 63: D_d for Slab-Girder Stiffness Ratio Parameter $\frac{I_{ss}}{I_{sG}} = 0.531$ (Case 1)

Girder	Finite Element Values		Code	$\frac{D_{d(FEM)}-D_{d(Code)}}{D_{d(Code)}} \times 100$	
#	Elastic	Ultimate		Elastic	Ultimate
G1	2.5720	2.9780	1.8500	39.0270	60.9730
G2	4.6960	2.9780	2.0125	133.4410	47.9752
G3	15.4100	-156.8300	1.8500	733.0000	-8577.3000

Table 64: D_d **for Slab-Girder Stiffness Ratio Parameter** $\frac{I_{ss}}{I_{sG}} = 0.293$ **(Case 2)**

Girder	Finite Element Values		Code	$\frac{D_{d(FEM)}-D_{d(Code)}}{D_{d(Code)}} \times 100$	
#	Elastic	Ultimate		Elastic	Ultimate
G1	4.5840	4.4620	1.7500	177.3714	154.9714
G2	4.3390	4.5770	2.0000	116.9500	128.8500
G3	4.5840	4.4620	1.7500	177.3714	154.9714

Table 65: D_d **for Slab-Girder Stiffness Ratio Parameter** $\frac{I_{ss}}{I_{sG}} = 0.382$ **(Case 2)**

Girder	Finite Element Values		Code	$\frac{D_{d(FEM)}-D_{d(Code)}}{D_{d(Code)}} \times 100$	
#	Elastic	Ultimate		Elastic	Ultimate
G1	4.6540	4.4860	1.8500	151.5676	142.4865
G2	4.2210	4.5300	2.0125	109.7391	125.0932
G3	4.6540	4.4860	1.8500	151.5676	142.4865

Table 66: D_d **for Slab-Girder Stiffness Ratio Parameter** $\frac{I_{ss}}{I_{sG}} = 0.531$ **(Case 2)**

Girder	Finite Element Values		Code	$\frac{D_{d(FEM)}-D_{d(Code)}}{D_{d(Code)}} \times 100$	
#	Elastic	Ultimate		Elastic	Ultimate
G1	4.5760	4.4640	1.8500	147.3514	141.2973
G2	4.3540	4.5720	2.0125	116.3478	127.1801
G3	4.5760	4.4640	1.8500	147.3514	141.2973

Table 67: D_d for Slab-Girder Stiffness Ratio Parameter $\frac{I_{ss}}{I_{sG}} = 0.293$ (Case 3)

Girder	Finite Element Values		Code	$\frac{D_{d(FEM)}-D_{d(Code)}}{D_{d(Code)}} \times 100$	
#	Elastic	Ultimate		Elastic	Ultimate
G1	2.2460	2.2500	1.7500	28.3429	28.5714
G2	2.2590	2.2500	2.0000	12.9500	12.5000
G3	2.2460	2.2500	1.7500	28.3429	28.5714

Table 68: D_d for Slab-Girder Stiffness Ratio Parameter $\frac{I_{ss}}{I_{sG}} = 0.382$ (Case 3)

Girder	Finite Element Values		Code	$\frac{D_{d(FEM)}-D_{d(Code)}}{D_{d(Code)}} \times 100$	
#	Elastic	Ultimate		Elastic	Ultimate
G1	2.2260	2.2510	1.8500	20.3243	21.6757
G2	2.2990	2.2480	2.0125	14.2360	11.7019
G3	2.2260	2.2510	1.8500	20.3243	21.6757

Table 69: D_d for Slab-Girder Stiffness Ratio Parameter $\frac{I_{ss}}{I_{sG}} = 0.531$ (Case 3)

Girder	Finite Element Values		Code	$\frac{D_{d(FEM)}-D_{d(Code)}}{D_{d(Code)}} \times 100$	
#	Elastic	Ultimate		Elastic	Ultimate
G1	2.2460	2.2500	1.8500	21.4054	21.6216
G2	2.2580	2.2500	2.0125	12.1988	11.8012
G3	2.2460	2.2500	1.8500	21.4054	21.6216

Table 70: D_d for Total Number of Girders Parameter for Three Girder System (Case 1)

Girder	Finite Element Values		Code	$\frac{D_{d(FEM)}-D_{d(Code)}}{D_{d(Code)}} \times 100$	
#	Elastic	Ultimate		Elastic	Ultimate
G1	2.3590	2.8000	2.1175	11.4050	32.2314
G2	4.8110	2.8000	2.2000	118.6818	27.2727
G3	28.6500	-23.8500	2.1175	1253.0000	-1226.3000

Table 71: D_d for Total Number of Girders Parameter for Four Girder System (Case 1)

Girder	Finite Element Values		Code	$\frac{D_{d(FEM)}-D_{d(Code)}}{D_{d(Code)}} \times 100$	
#	Elastic	Ultimate		Elastic	Ultimate
G1	2.5740	3.1000	2.1450	20.0000	44.5221
G2	3.9330	3.1000	2.2440	75.2674	38.1462
G3	7.7110	4.1250	2.2440	243.6275	83.8235
G4	36.2100	-21.2900	2.1450	1588.4000	-1092.5000

Table 72: D_d for Total Number of Girders Parameter for Three Girder System (Case 2)

Girder	Finite Element Values		Code	$\frac{D_{d(FEM)}-D_{d(Code)}}{D_{d(Code)}} \times 100$	
#	Elastic	Ultimate		Elastic	Ultimate
G1	4.3890	4.6540	2.1175	107.2727	119.7875
G2	4.7410	4.2210	2.2000	115.5000	91.8636
G3	4.3890	4.6540	2.1175	107.2727	119.7875

Table 73: D_d for Total Number of Girders Parameter for Four Girder System (Case 2)

Girder	Finite Element Values		Code	$\frac{D_{d(FEM)} - D_{d(Code)}}{D_{d(Code)}} \times 100$	
#	Elastic	Ultimate		Elastic	Ultimate
G1	4.5450	4.2050	2.1450	111.8881	96.0373
G2	4.5450	3.7810	2.2440	102.5401	68.4938
G3	4.5960	5.5160	2.2440	104.8128	145.8111
G4	7.0220	8.5910	2.1450	227.3660	300.5128

Table 74: D_d for Total Number of Girders Parameter for Three Girder System (Case 3)

Girder	Finite Element Values		Code	$\frac{D_{d(FEM)} - D_{d(Code)}}{D_{d(Code)}} \times 100$	
#	Elastic	Ultimate		Elastic	Ultimate
G1	2.2440	2.2500	2.1175	5.0295	6.2574
G2	2.2620	2.2500	2.2000	2.8182	2.2727
G3	2.2440	2.2500	2.1175	5.0295	6.2574

Table 75: D_d for Total Number of Girders Parameter for Four Girder System (Case 3)

Girder	Finite Element Values		Code	$\frac{D_{d(FEM)} - D_{d(Code)}}{D_{d(Code)}} \times 100$	
#	Elastic	Ultimate		Elastic	Ultimate
G1	2.4110	2.5000	2.1450	12.4009	16.5501
G2	2.5960	2.5000	2.2440	15.6863	11.4082
G3	2.5960	2.5000	2.2440	15.6863	11.4082
G4	2.4110	2.5000	2.1450	12.4009	16.5501

Table 76: D_d for Total Number of Girders Parameter for Five Girder System (Case 3)

Girder	Finite Element Values		Code	$\frac{D_{d(FEM)}-D_{d(Code)}}{D_{d(Code)}} \times 100$	
#	Elastic	Ultimate		Elastic	Ultimate
G1	2.3200	2.2920	2.1000	10.4762	9.1429
G2	2.4160	2.2920	2.2000	9.8182	4.1818
G3	2.2230	2.2920	2.2000	1.0455	4.1818
G4	2.4160	2.2920	2.2000	9.8182	4.1818
G5	2.3200	2.2920	2.1000	10.4762	9.1429

Table 77: D_d for Total Number of Girders Parameter for Six Girder System (Case 3)

Girder	Finite Element Values		Code	$\frac{D_{d(FEM)}-D_{d(Code)}}{D_{d(Code)}} \times 100$	
#	Elastic	Ultimate		Elastic	Ultimate
G1	2.0670	2.0620	2.2000	-6.0455	-6.2727
G2	2.0520	2.0620	2.2500	-8.8000	-8.3556
G3	2.0680	2.0620	2.2500	-8.0889	-8.3556
G4	2.0680	2.0620	2.2500	-8.0889	-8.3556
G5	2.0520	2.0620	2.2500	-8.8000	-8.3556
G6	2.0670	2.0620	2.2000	-6.0455	-6.2727

Table 78: D_d for Degree of Interaction Parameter
Degree of Composition = 0.3% (Case 1)

Girder	Finite Element Values		Code	$\frac{D_{d(FEM)}-D_{d(Code)}}{D_{d(Code)}} \times 100$	
#	Elastic	Ultimate		Elastic	Ultimate
G1	1.8330	1.8320	2.0737	11.6073	11.6555
G2	2.9490	2.5130	2.1000	40.4286	19.6667
G3	9.1070	9.9600	2.1000	333.6667	375.2381
G4	18.1800	13.6200	2.0737	776.6938	756.7970

Table 79: D_d for Degree of Interaction Parameter
Degree of Composition = 50.0% (Case 1)

Girder	Finite Element Values		Code	$\frac{D_{d(FEM)}-D_{d(Code)}}{D_{d(Code)}} \times 100$	
#	Elastic	Ultimate		Elastic	Ultimate
G1	3.0840	2.0000	2.0000	54.2000	0.0000
G2	3.6140	2.0000	2.0125	79.5776	0.6211
G3	4.3940	4.1740	2.0125	118.3354	107.4037
G4	5.5070	15.5900	2.0000	175.3500	879.5000

Table 80: D_d for Degree of Interaction Parameter
Degree of Composition = 100.0% (Case 1)

Girder	Finite Element Values		Code	$\frac{D_{d(FEM)}-D_{d(Code)}}{D_{d(Code)}} \times 100$	
#	Elastic	Ultimate		Elastic	Ultimate
G1	3.0350	2.0000	2.0000	51.7500	0.0000
G2	3.5460	2.0000	2.0125	76.1968	0.6211
G3	4.3920	3.9960	2.0125	118.2360	98.6584
G4	5.8380	16.3100	2.0000	191.9000	915.5000

Table 81: D_d for Degree of Interaction Parameter
Degree of Composition = 600.0% (Case 1)

Girder	Finite Element Values		Code	$\frac{D_{d(FEM)}-D_{d(Code)}}{D_{d(Code)}} \times 100$	
#	Elastic	Ultimate		Elastic	Ultimate
G1	3.0380	2.0000	2.0000	51.9000	0.0000
G2	3.4790	2.0000	2.0125	72.8696	0.6211
G3	4.3900	4.0000	2.1250	118.1366	98.7578
G4	6.1310	20.0000	2.0000	206.6000	1100.1000

Table 82: D_d for Degree of Interaction Parameter
Degree of Composition = 0.3% (Case 2)

Girder	Finite Element Values		Code	$\frac{D_{d(FEM)}-D_{d(Code)}}{D_{d(Code)}} \times 100$	
#	Elastic	Ultimate		Elastic	Ultimate
G1	2.5600	2.5000	2.0737	23.4506	20.5575
G2	3.4790	3.3780	2.1000	65.6667	60.8571
G3	5.1150	5.2630	2.1000	143.5714	150.6190
G4	7.9050	8.7720	2.0737	281.2027	323.0120

Table 83: D_d for Degree of Interaction Parameter
Degree of Composition = 50.0% (Case 2)

Girder	Finite Element Values		Code	$\frac{D_{d(FEM)}-D_{d(Code)}}{D_{d(Code)}} \times 100$	
#	Elastic	Ultimate		Elastic	Ultimate
G1	3.1840	3.9970	2.0000	59.2000	99.8500
G2	3.6140	4.1740	2.0125	79.5776	107.4037
G3	4.3940	4.2210	2.0125	68.6460	109.7391
G4	5.5070	3.6590	2.0000	175.3500	82.9500

Table 84: D_d for Degree of Interaction Parameter
Degree of Composition = 100.0% (Case 2)

Girder	Finite Element Values		Code	$\frac{D_{d(FEM)}-D_{d(Code)}}{D_{d(Code)}} \times 100$	
#	Elastic	Ultimate		Elastic	Ultimate
G1	3.1350	3.6820	2.0000	56.7500	84.1000
G2	3.5460	3.9980	2.0125	76.1988	98.6584
G3	4.3920	4.1340	2.0125	118.2360	105.4161
G4	5.8380	4.5310	2.0000	191.9000	126.5500

Table 85: D_d for Degree of Interaction Parameter
Degree of Composition = 600.0% (Case 2)

Girder	Finite Element Values		Code	$\frac{D_{d(FEM)}-D_{d(Code)}}{D_{d(Code)}} \times 100$	
#	Elastic	Ultimate		Elastic	Ultimate
G1	3.1080	4.0000	2.0000	55.4000	100.0000
G2	3.4790	4.0000	2.0125	72.8696	98.7578
G3	4.3900	4.0000	2.1250	118.1366	98.7578
G4	6.1310	4.0000	2.0000	206.6000	100.0000

Table 86: D_d for Degree of Interaction Parameter
Degree of Composition = 0.3% (Case 3)

Girder	Finite Element Values		Code	$\frac{D_{d(FEM)}-D_{d(Code)}}{D_{d(Code)}} \times 100$	
#	Elastic	Ultimate		Elastic	Ultimate
G1	1.9780	1.9810	2.0737	4.6149	4.4703
G2	2.0230	2.0190	2.1000	3.6667	3.8571
G3	2.0230	2.0190	2.1000	3.6667	3.8571
G4	1.9780	1.9810	2.0737	4.6149	4.4703

Table 87: D_d for Degree of Interaction Parameter
Degree of Composition = 50.0% (Case 3)

Girder	Finite Element Values		Code	$\frac{D_{d(FEM)}-D_{d(Code)}}{D_{d(Code)}} \times 100$	
#	Elastic	Ultimate		Elastic	Ultimate
G1	1.9850	2.0000	2.0000	0.7500	0.0000
G2	2.0150	2.0000	2.0125	0.1242	0.6211
G3	2.0150	2.0000	2.0125	0.1242	0.6211
G4	1.9850	2.0000	2.0000	0.7500	0.0000

Table 88: D_d for Degree of Interaction Parameter
Degree of Composition = 100.0% (Case 3)

Girder	Finite Element Values		Code	$\frac{D_{d(FEM)}-D_{d(Code)}}{D_{d(Code)}} \times 100$	
#	Elastic	Ultimate		Elastic	Ultimate
G1	1.9860	2.0000	2.0000	0.7000	0.0000
G2	2.0150	2.0000	2.0125	0.1242	0.6211
G3	2.0150	2.0000	2.0125	0.1242	0.6211
G4	1.9860	2.0000	2.0000	0.7000	0.0000

Table 89: D_d for Degree of Interaction Parameter
Degree of Composition = 600.0% (Case 3)

Girder	Finite Element Values		Code	$\frac{D_{d(FEM)}-D_{d(Code)}}{D_{d(Code)}} \times 100$	
#	Elastic	Ultimate		Elastic	Ultimate
G1	1.9870	2.0000	2.0000	0.6500	0.0000
G2	2.0130	2.0000	2.0125	0.0248	0.6211
G3	2.0130	2.0000	2.0125	0.0248	0.6211
G4	1.9870	2.0000	2.0000	0.6500	0.0000

FIGURES

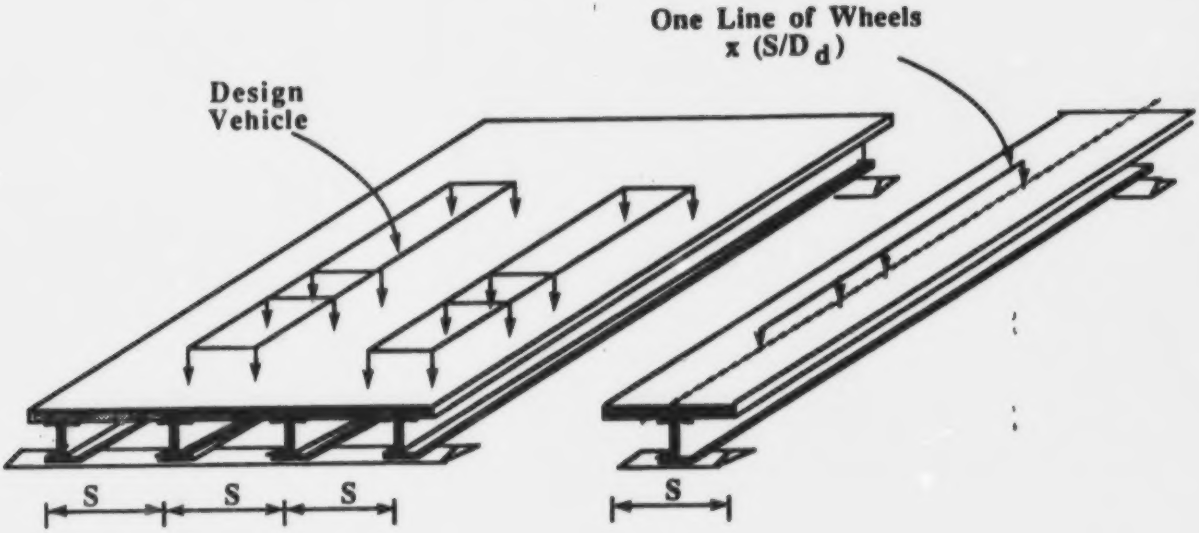
One Line of Wheels
x (S/D d)
Design
Vehicle
S
S
S
S

Fig. 1: Idealized Girder and its Loading According to D-Type Distribution Method

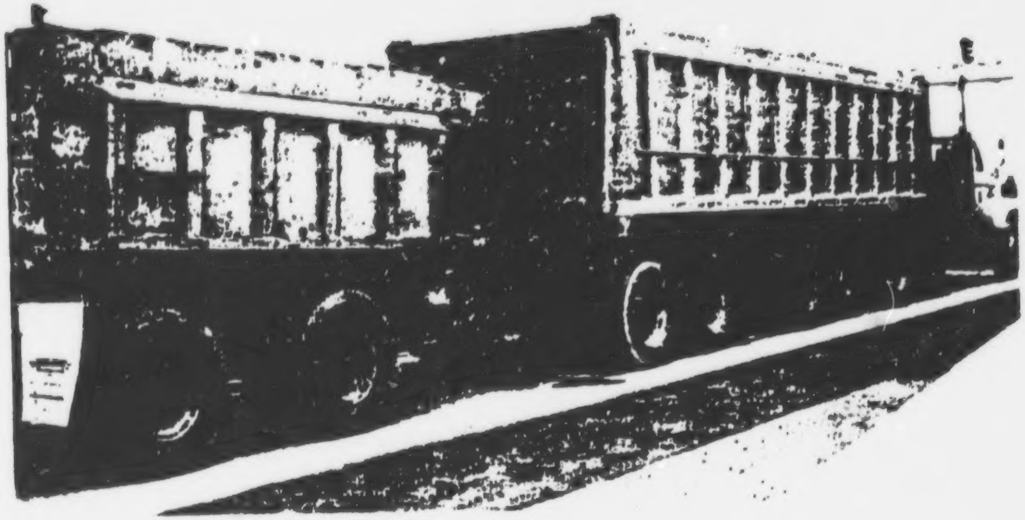

Fig. 2: OHBD Commercial Truck

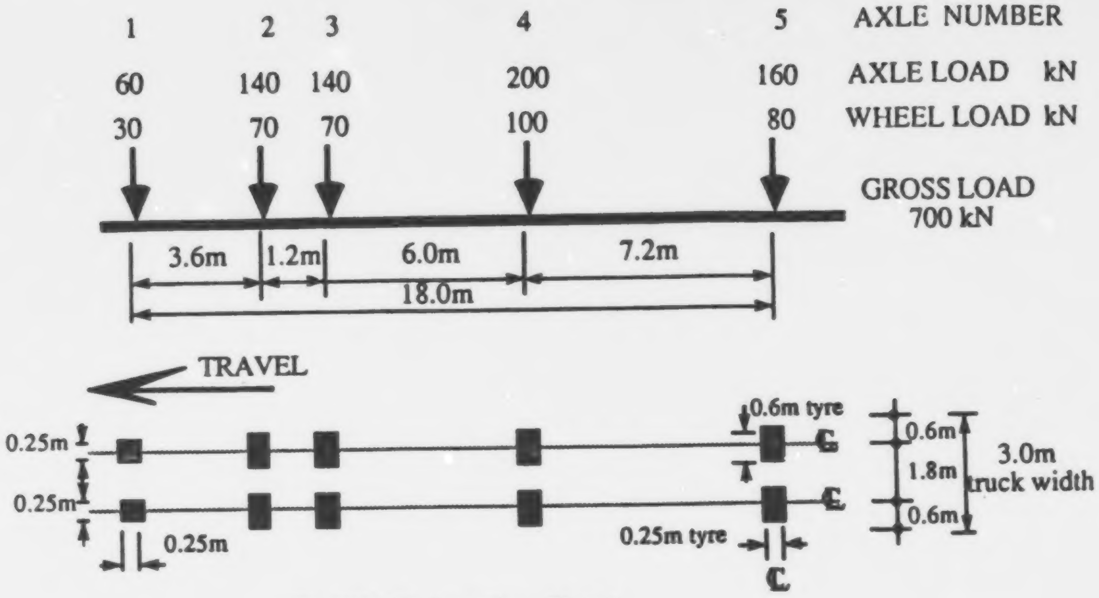
1 2 3 4 5 AXLE NUMBER
60 140 140 200 160 AXLE LOAD kN
30 70 70 100 80 WHEEL LOAD kN
GROSS LOAD
700 kN
3.6m
1.2m
6.0m
7.2m
18.0m
TRAVEL
0.6m tyre
0.25m
0.25m
0.25m
0.25m tyre
0.6m
1.8m
0.6m
3.0m
truck width

(I) OHBD Loading Truck

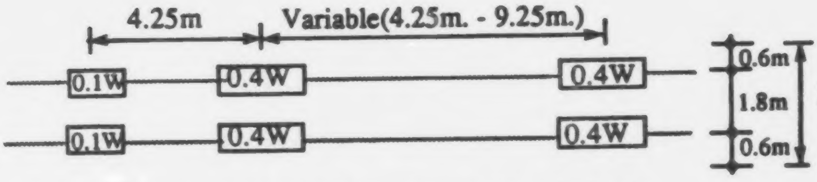
4.25m
Variable(4.25m. - 9.25m.)
0.1W
0.4W
0.4W
0.1W
0.4W
0.4W
0.6m
1.8m
0.6m
3.0m

W=COMBINED LOAD ON THE FIRST TWO AXIES (kN)

(II) MS-77 Loading Truck

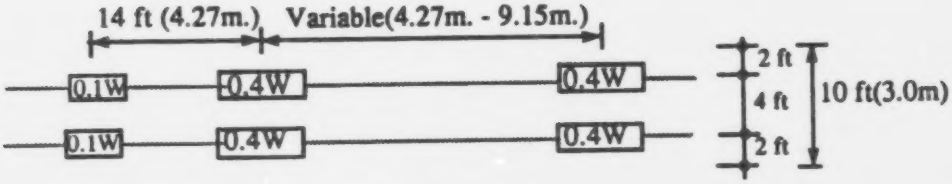
14 ft (4.27m.)
Variable(4.27m. - 9.15m.)
0.1W
0.4W
0.4W
0.1W
0.4W
0.4W
2 ft
4 ft
2 ft
10 ft(3.0m)

(III) HS AASHTO Loading Truck

Fig. 3: Truck Loading Configurations According to Codes

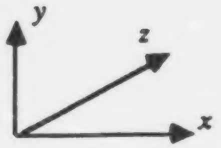

Cartesian Coordinates

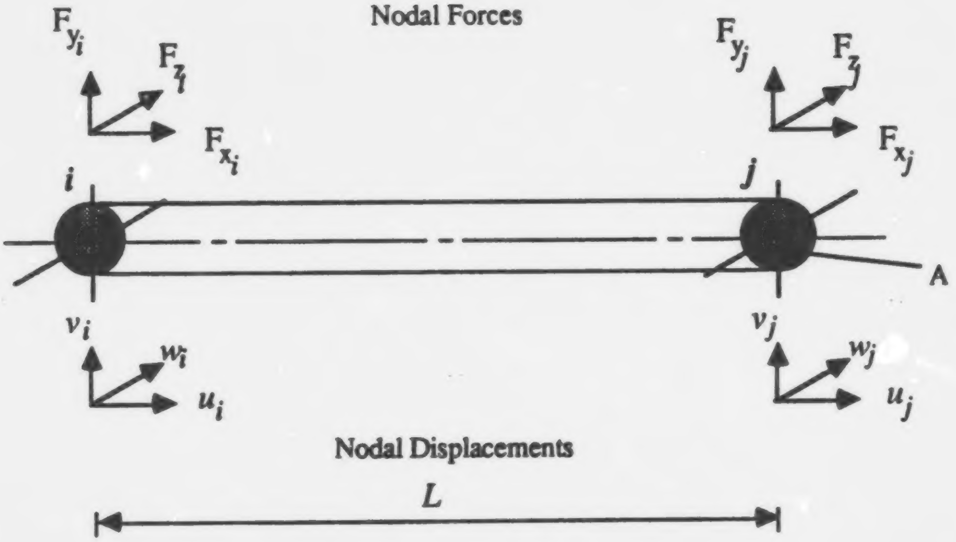
Nodal Forces
F_{y_i}
F_{z_i}
F_{x_i}
F_{y_j}
F_{z_j}
F_{x_j}
i
j
A
v_i
w_i
u_i
v_j
w_j
u_j
Nodal Displacements
L

Truss Element

Fig. 4: Typical 3-D Bar Element

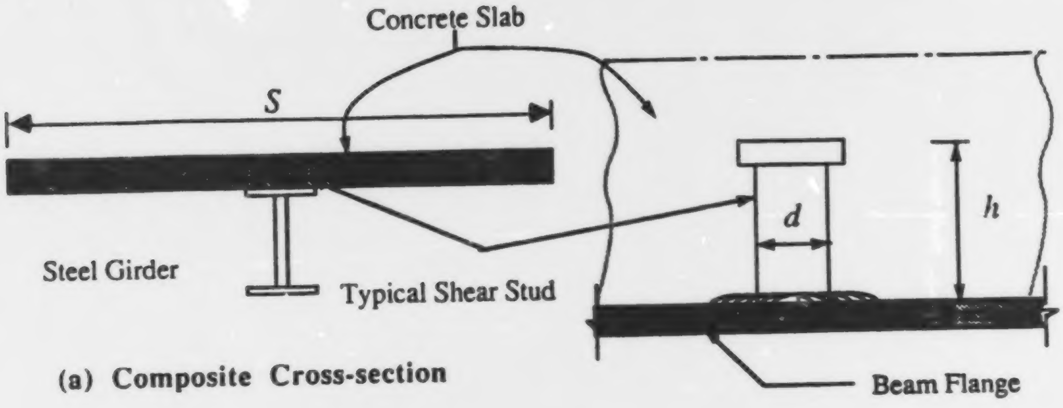
Concrete Slab
S
d
h
Steel Girder
Typical Shear Stud
Beam Flange

(a) Composite Cross-section

(b) Shear Stud Detail

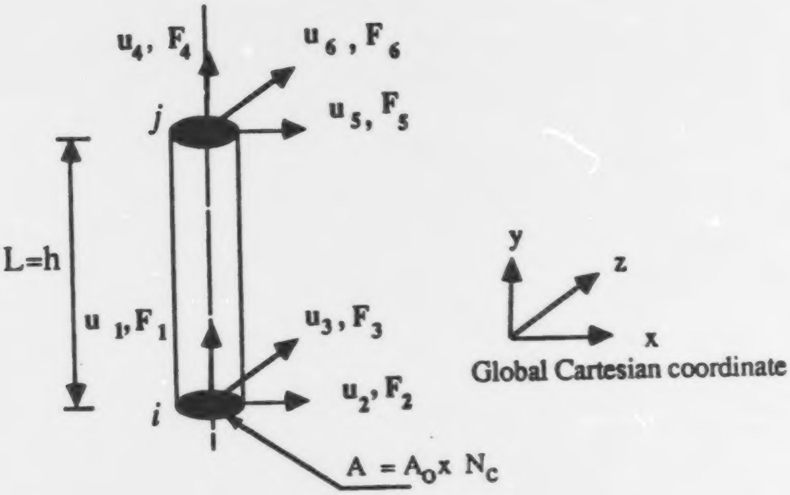
u_4, F_4
u_6, F_6
j
u_5, F_5
L=h
u_1, F_1
u_3, F_3
u_2, F_2
i
$A = A_0 \times N_c$
y
z
x
Global Cartesian coordinate

Note:

A_0= Area of One Connector

N_C= Total Number of Connectors within Element Length

(c) Finite Element Idealization of the Shear Stud

Fig. 5: Shear Stud Connector

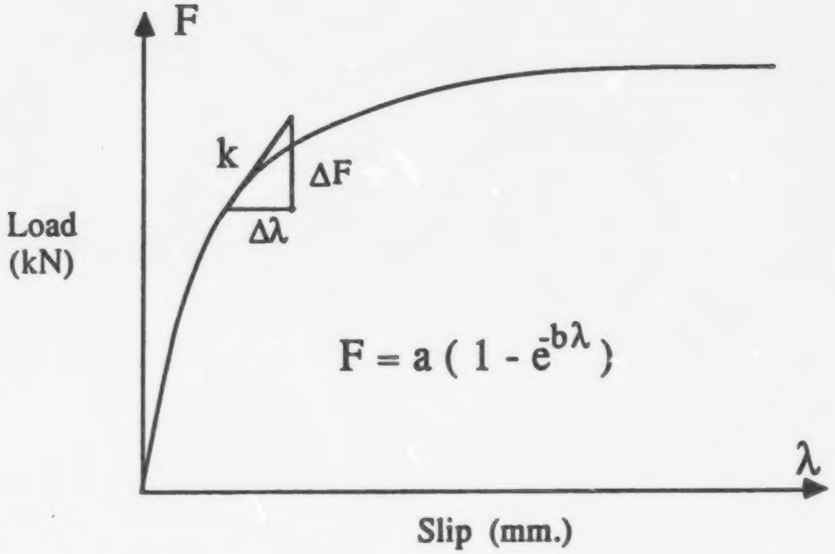

Fig. 6: Typical Load-Slip Curve for Flexiable Shear Connector

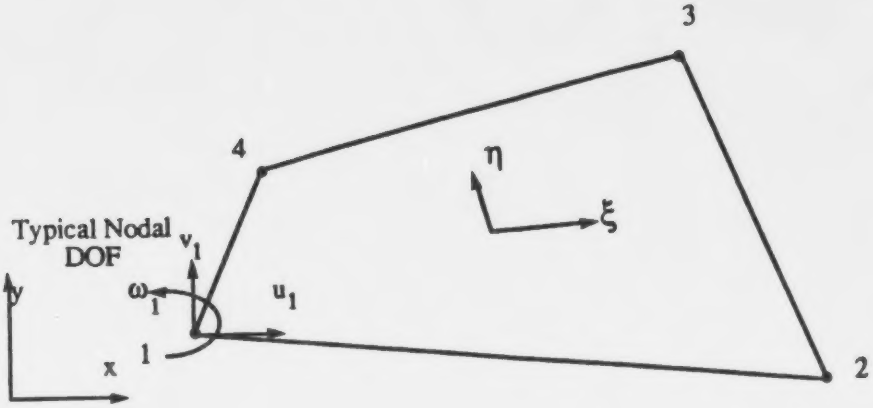
3
4
η
ξ
Typical Nodal DOF
v_1
ω_1
u_1
y
x
1
2

(a) New Element (RQUAD4)

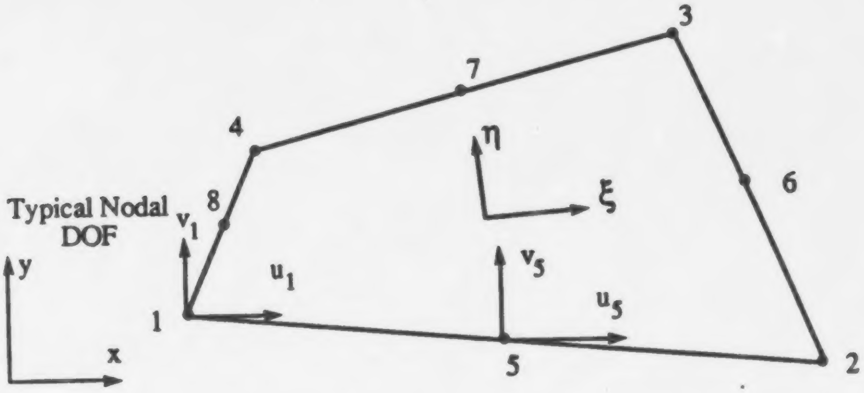
3
7
4
η
6
ξ
Typical Nodal DOF
8
v_1
y
u_1
v_5
u_5
1
x
5
2

(b) Eight-Node Quadrilateral Element (QUAD8)

Fig. 7: Finite Elements

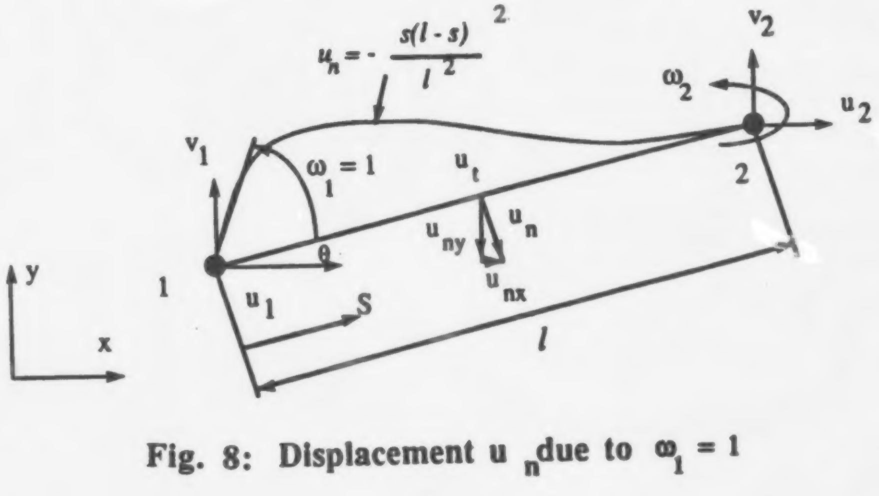
$u_n = -\frac{s(l-s)^2}{l^2}$
v_2
ω_2
u_2
v_1
$\omega_1 = 1$
u_t
2
u_{ny}
u_n
θ
u_{nx}
y
1
u_1
S
x
l

Fig. 8: Displacement u_n due to $\omega_1 = 1$

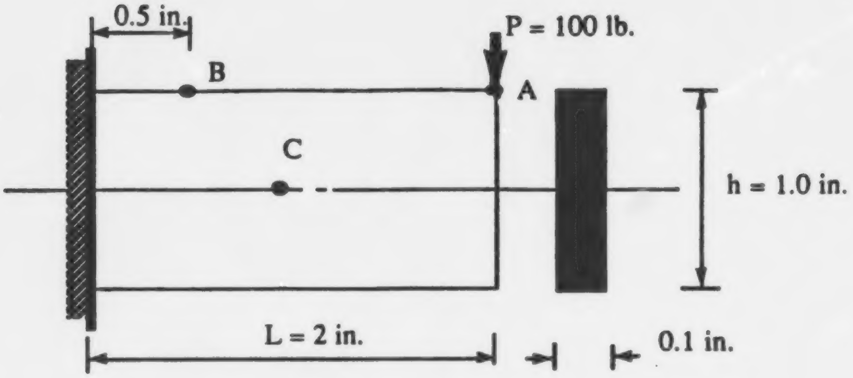
0.5 in.
P = 100 lb.
B
A
C
h = 1.0 in.
L = 2 in.
0.1 in.

(a) Beam and its Load **(b) Cross-section**

Material Constants

$E = 10^6$ psi

$\nu = 0.3$

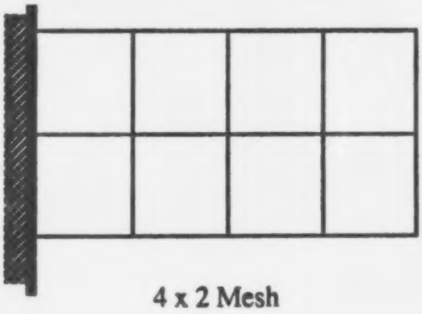

(c) Typical Mesh Size Used

Fig. 9: Short Cantilever under Concentrated Tip Load

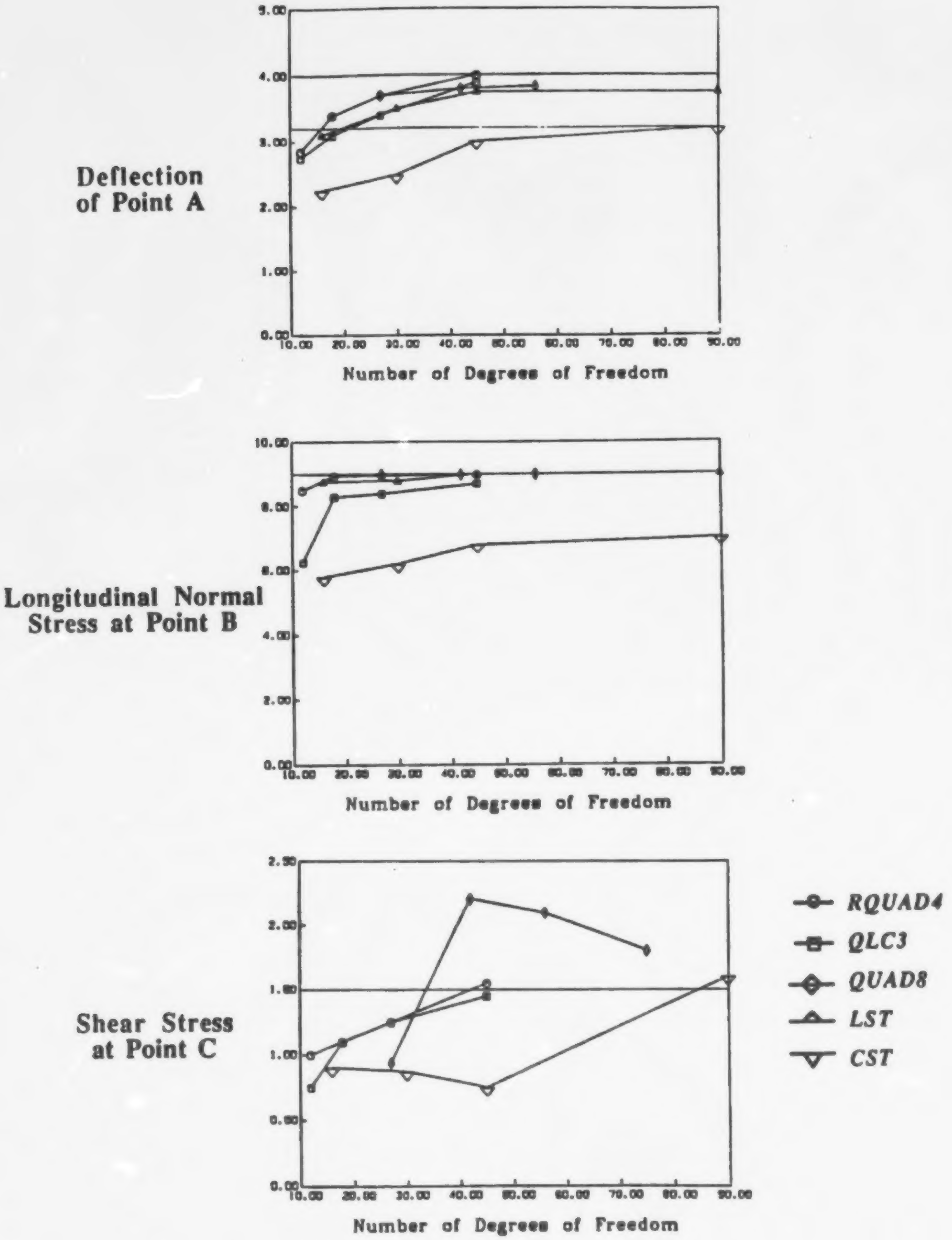

Fig. 10: Convergence Study of RQUAD4 and Comparison with Other Elements

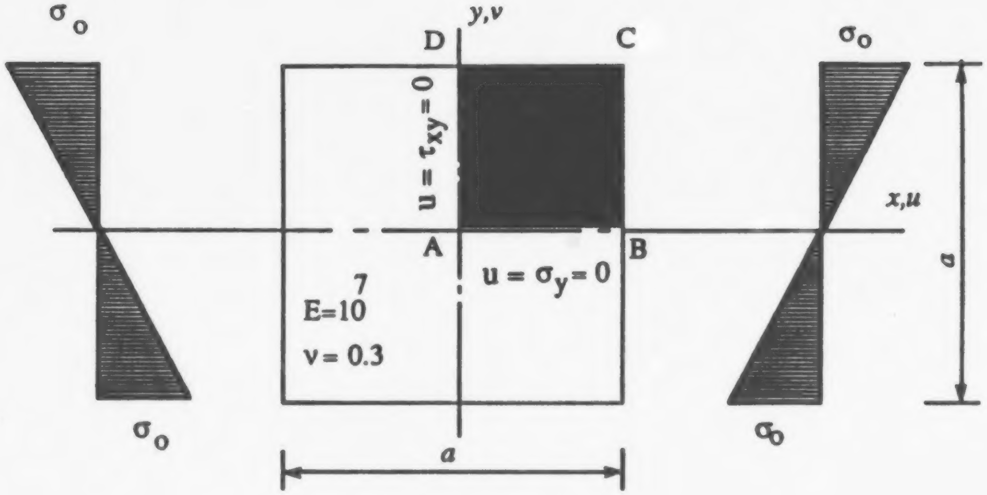
σ_o
y,ν
D
C
σ_o
u = τ_xy = 0
x,u
A
B
u = σ_y = 0
E=10^7
ν = 0.3
a
σ_o
a
σ_o

Fig. 11: Square Plate under Inplane Bending

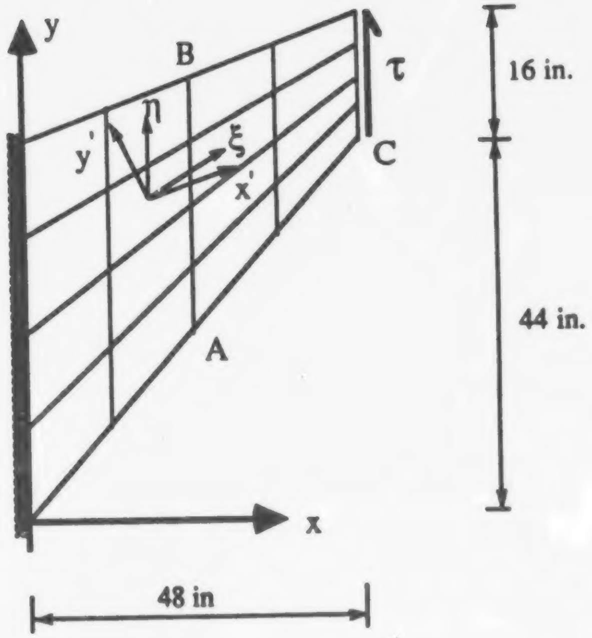
y
B
η
ξ
y'
x'
τ
C
16 in.
44 in.
A
x
48 in

Fig. 12: Skew Tapered Cantilever under Uniform Shear at the Tip

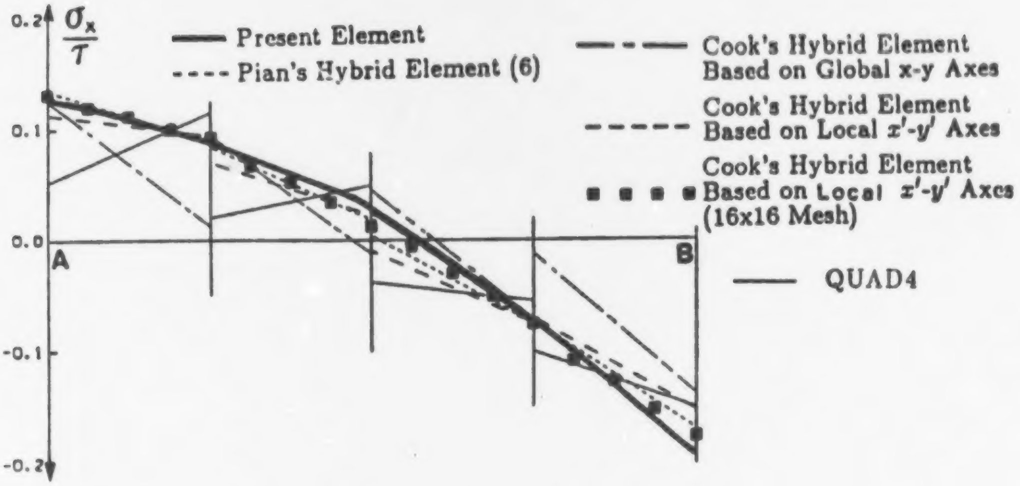

Fig. 13: **Variation of Normal Stresses σ_x along Section A-B**

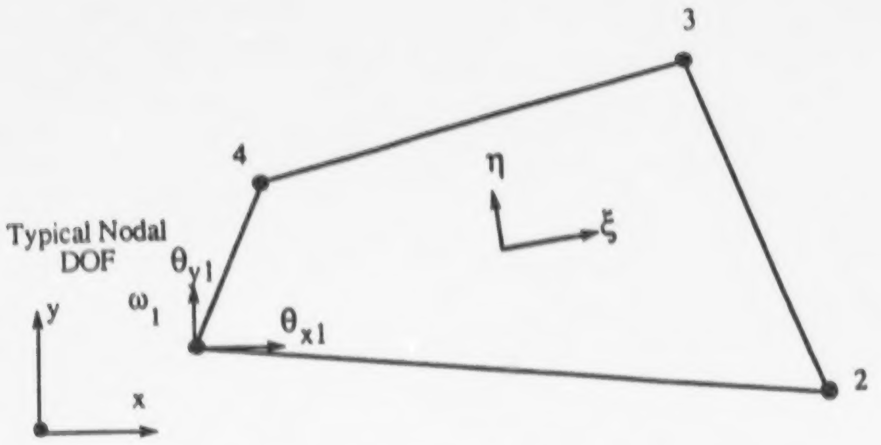
3
4
η
ξ
Typical Nodal DOF
θy1
ω1
θx1
y
x
2

Fig. 14: Bending Element QBE

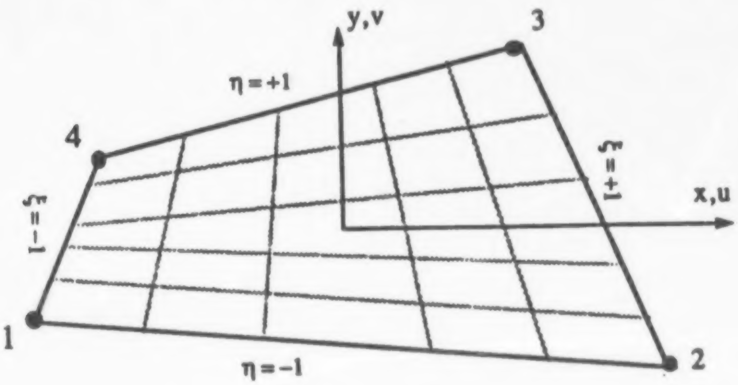
y,v
3
η=+1
4
ξ=+1
x,u
ξ=−1
1
η=−1
2

(a) Nodal Numbering, Local Axes, and Natural Coordinate System

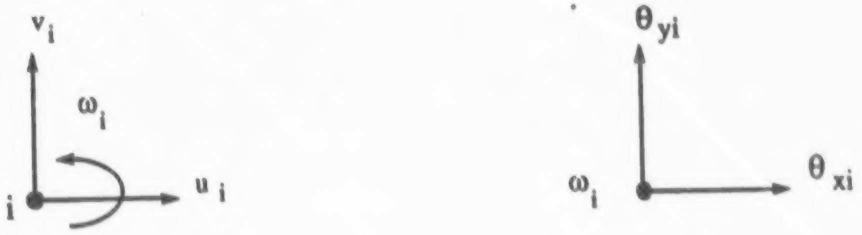
vi
ωi
i
ui
θyi
ωi
θxi

(b) Nodal Degrees of Freedom for RQUAD4 Element

(c) Nodal Degrees of Freedom for QBE Element

Fig. 15: The Facet Shell Element QFSE

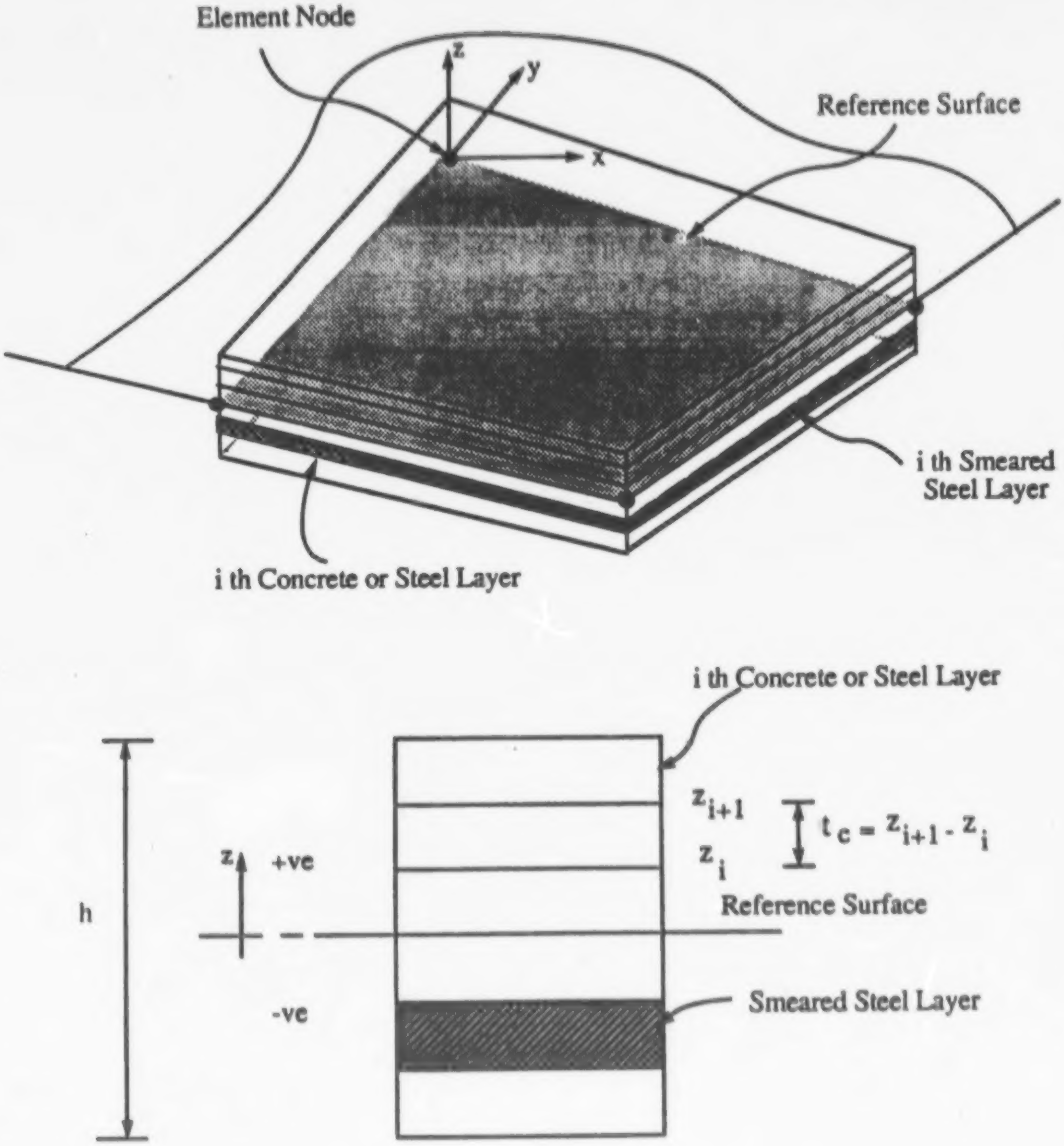
Element Node
z
y
x
Reference Surface
i th Smeared Steel Layer
i th Concrete or Steel Layer
i th Concrete or Steel Layer
z_{i+1}
z_i
$t_c = z_{i+1} - z_i$
z
+ve
-ve
h
Reference Surface
Smeared Steel Layer

Fig. 16: Layered Finite Element

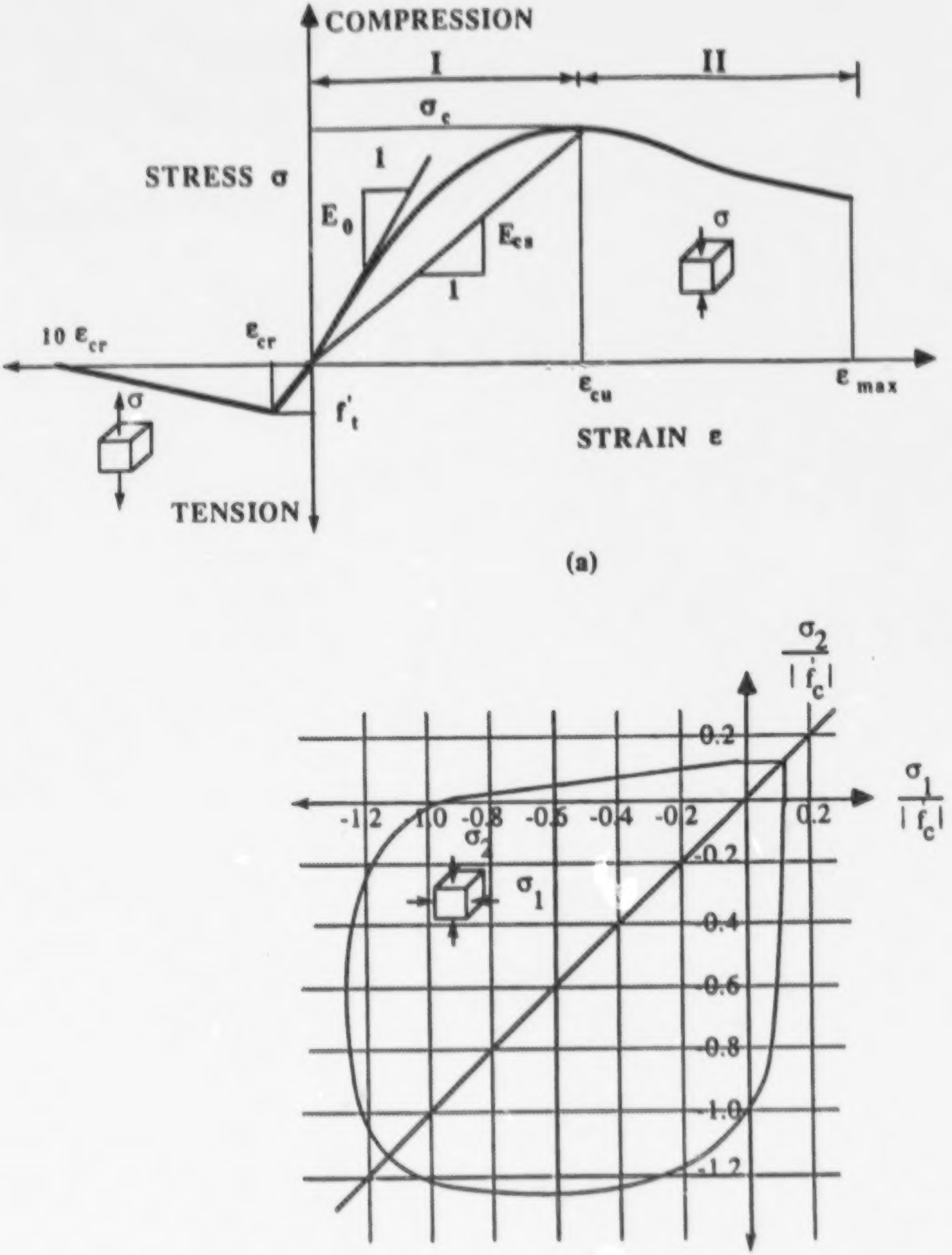
COMPRESSION
I
II
σ_c
STRESS σ
1
E_0
E_{cs}
1
σ
10 ε_{cr}
ε_{cr}
σ
f'_t
ε_{cu}
ε_{max}
STRAIN ε
TENSION
$\frac{\sigma_2}{|f'_c|}$
$\frac{\sigma_1}{|f'_c|}$
0.2
-1.2
-1.0
-0.8
-0.6
-0.4
-0.2
0.2
-0.2
-0.4
-0.6
-0.8
-1.0
-1.2
σ_2
σ_1

(a)

(b)

Fig. 17: Properties of Concrete
(a) Uniaxial Stress-Strain Relationship
(b) Schematic of Biaxial Failure Envelope

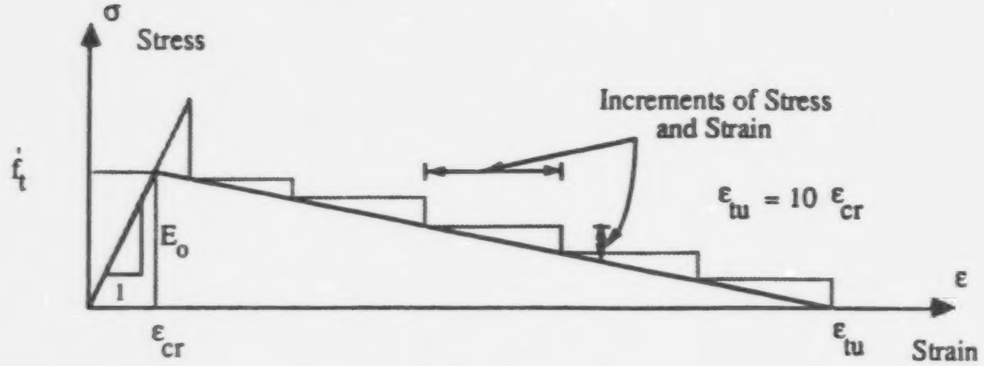
σ
Stress
f'_t
Increments of Stress and Strain
$\varepsilon_{tu} = 10\ \varepsilon_{cr}$
E_o
1
ε
ε_{cr}
ε_{tu}
Strain

Fig. 18: Tensile Stress-Strain Relation for Concrete

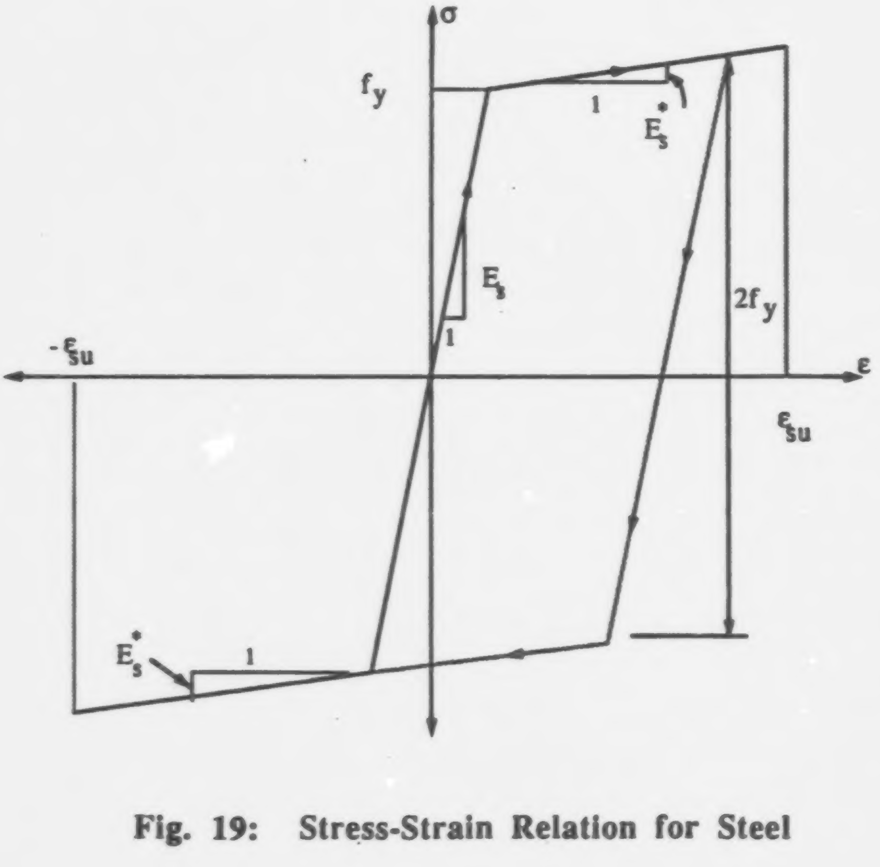
σ
f_y
1
E_s^*
E_s
1
$2f_y$
$-\varepsilon_{su}$
ε
ε_{su}
E_s^*
1

Fig. 19: Stress-Strain Relation for Steel

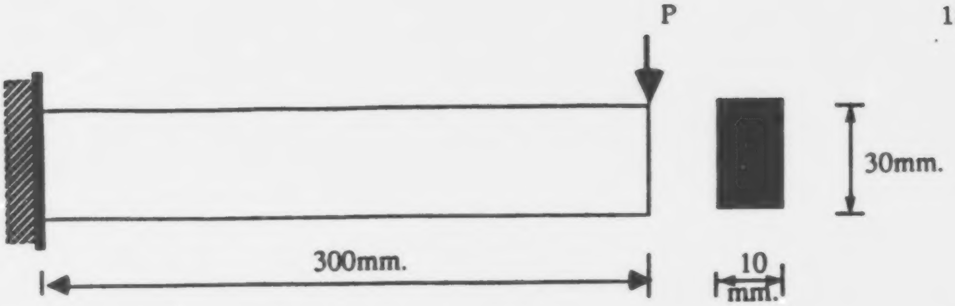

Material Properties

E_s = 200 x 10^3 MPa

σ_y = 300.0 MPa

ν = 0.0

(a) Beam Dimensions, Material Properties, and Loading

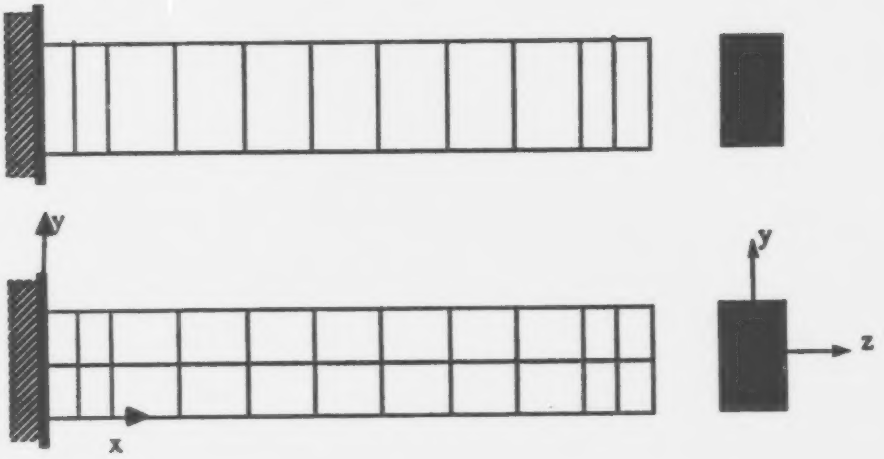

(b) Finite Element Meshes Employed in the Analysis

Fig. 20: Cantilever Beam Used in Elasto-Plastic Study

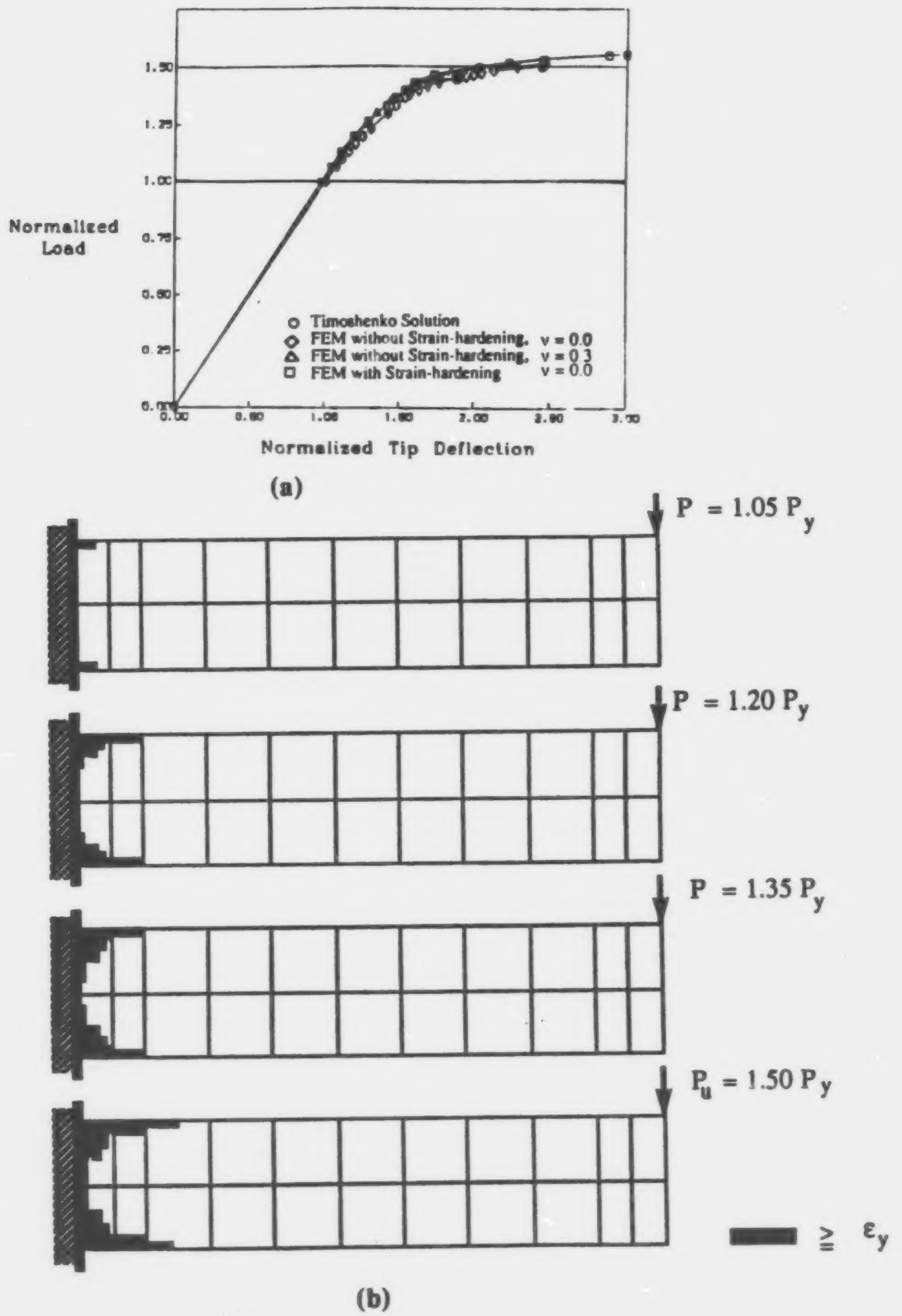

Fig. 21: Cantilever Beam under Tip Load
(a) Load Tip Deflection Curve
(b) Progression of Plasticity

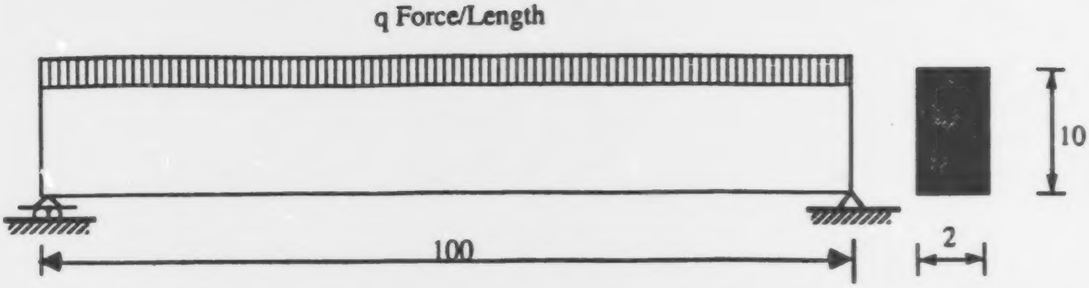
q Force/Length
100
2
10

$$\rho = 25\frac{q}{\sigma_y} \qquad 0 \leqq \rho \leqq 1.0$$

(a) Simply Supported Beam Dimensions and Load

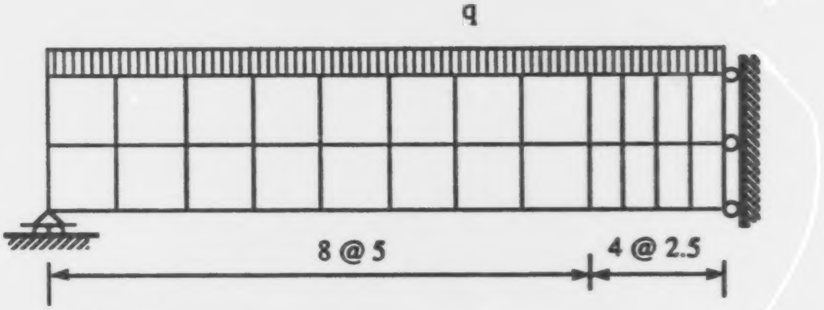

Material Properties

$E_s = 200 \times 10^3$ MPa

$\sigma_y = 300.0$ MPa

$\nu = 0.0$

(b) Finite Element Mesh Utilized

Fig. 22: Simply Supported Beam under Uniform Load

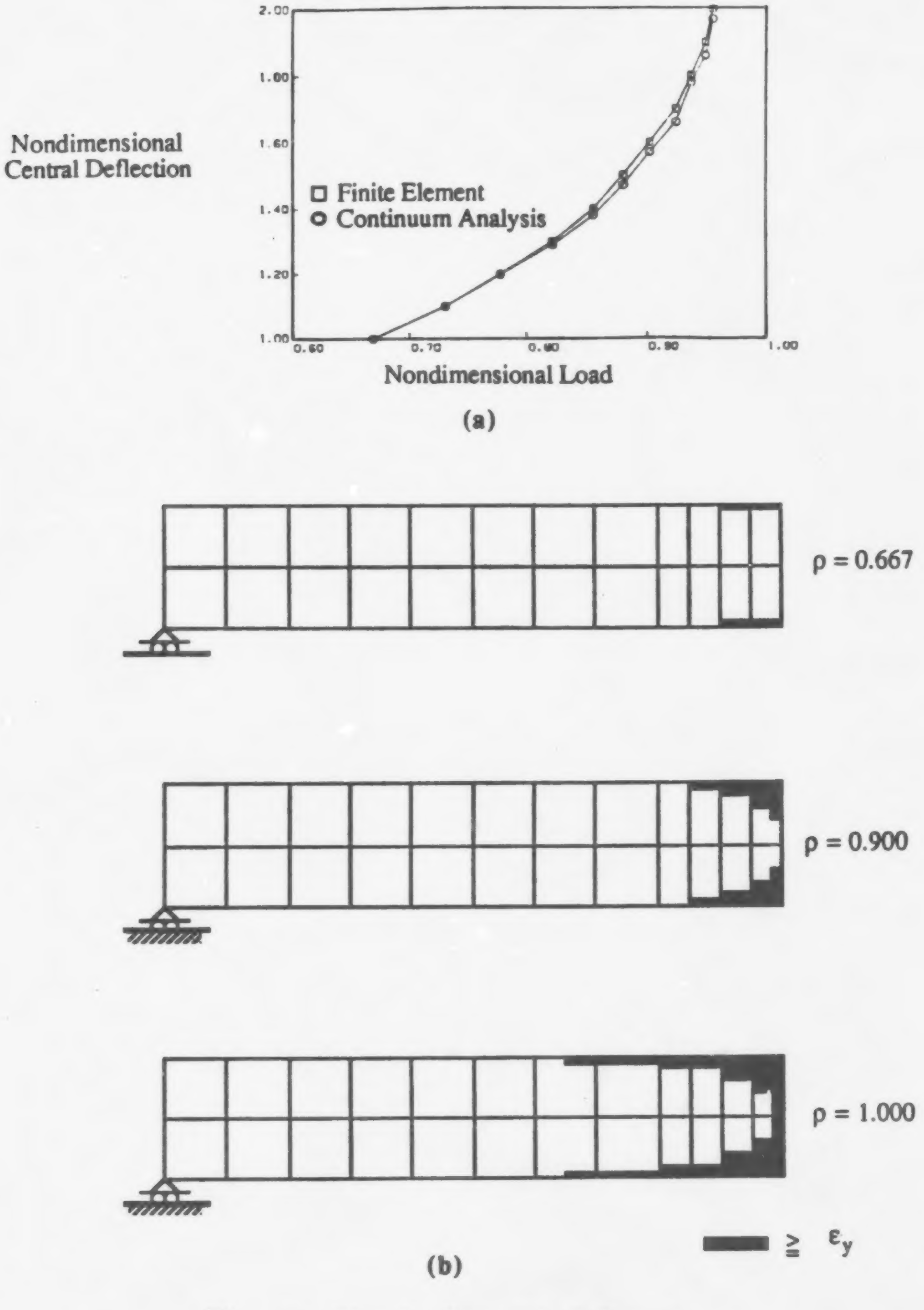

Fig. 23: Simply Supported Beam
(a) Load Midspan Deflection
(b) Progression of Plasticity

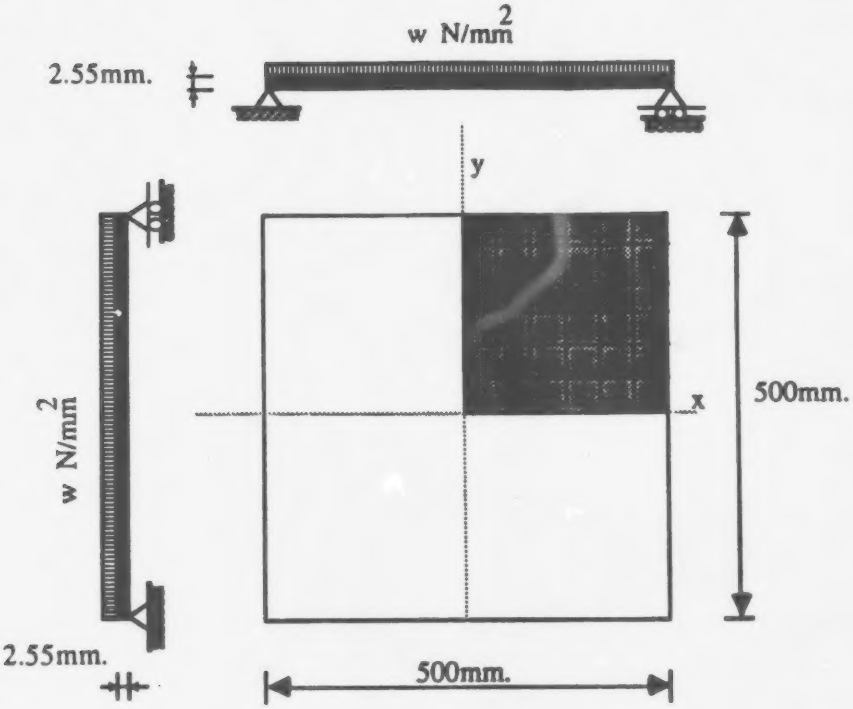
w N/mm^2
2.55mm.
y
x
500mm.
w N/mm^2
2.55mm.
500mm.

Thickness = 2.55 mm. (0.1 in.)

E = 200 x 10^3 MPa (10 x 10^6 psi)

ν = 0.3

Yield Moment = 400 N.mm/mm (90 lb.in/in)

Fig. 24: Simply Supported Square Plate under Uniform Load

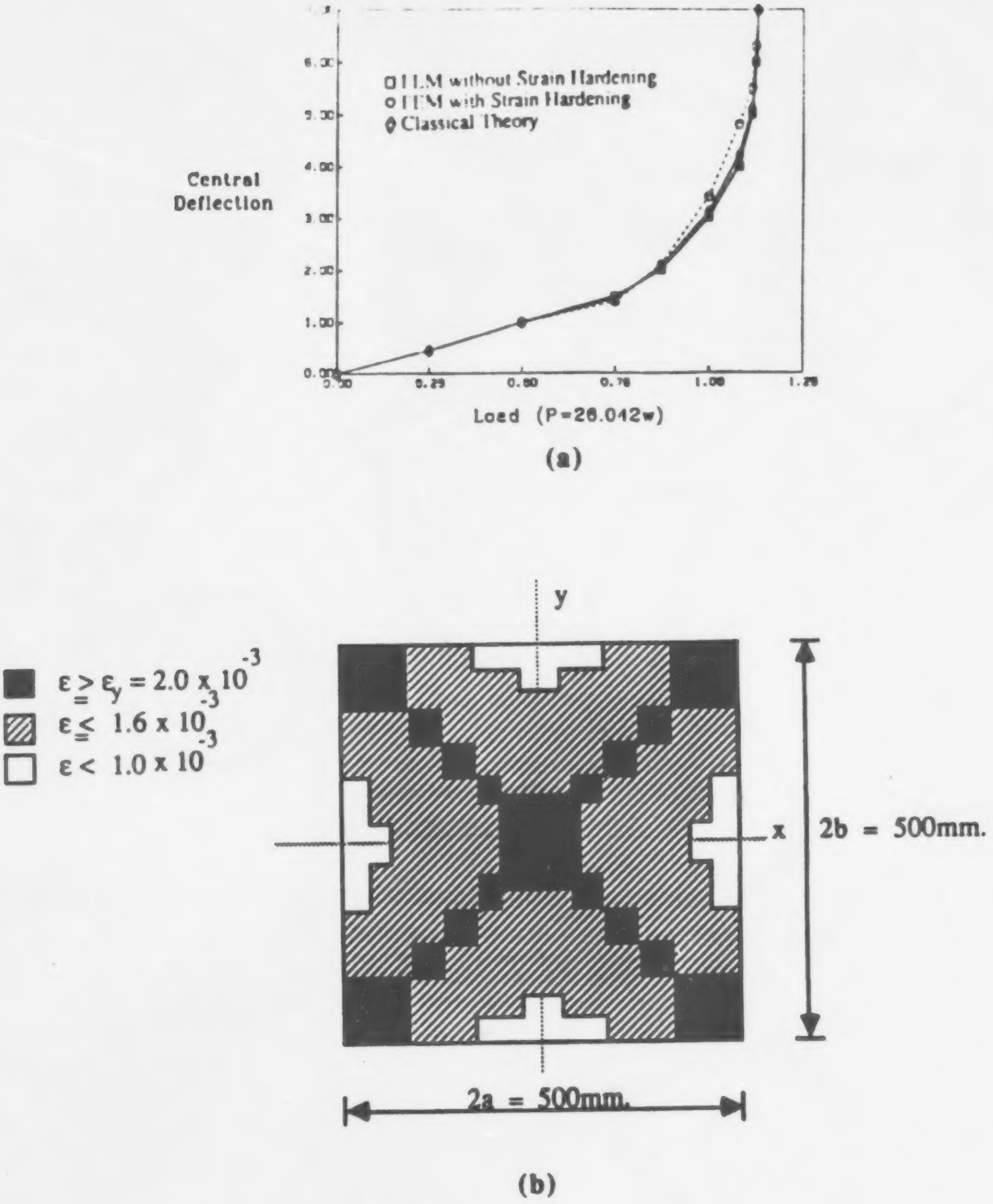

Fig. 25: Simply Supported Square Plate under Uniform Load
(a) Load-Central Point Deflection Curve
(b) Elastic and Plastic Zones at Collapse Load

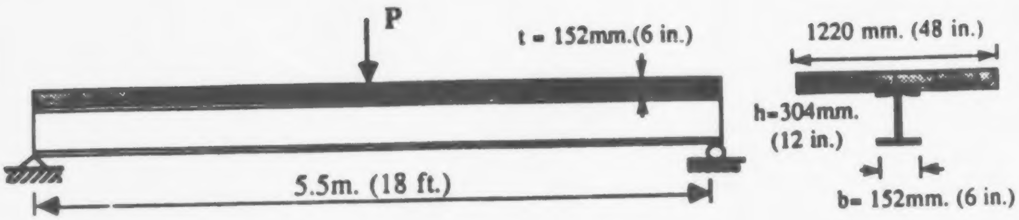
P
t = 152mm.(6 in.)
1220 mm. (48 in.)
h=304mm.
(12 in.)
b= 152mm. (6 in.)
5.5m. (18 ft.)

Elevation

cross section

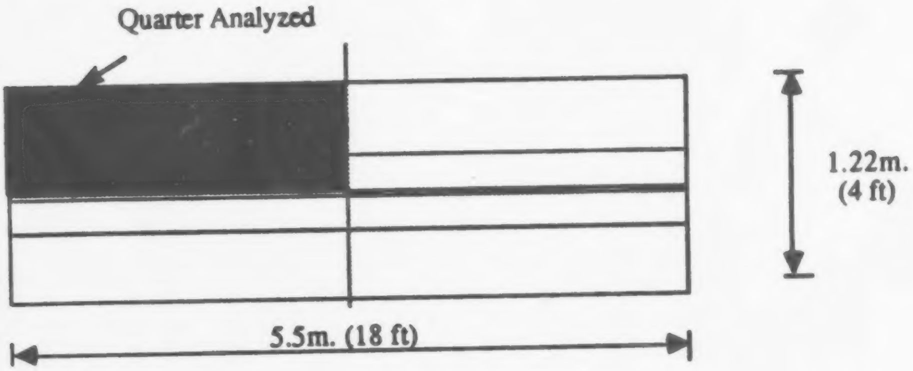
Quarter Analyzed
1.22m.
(4 ft)
5.5m. (18 ft)

Plan

Fig. 26: Yam and Chapman's Simply Supported Beam

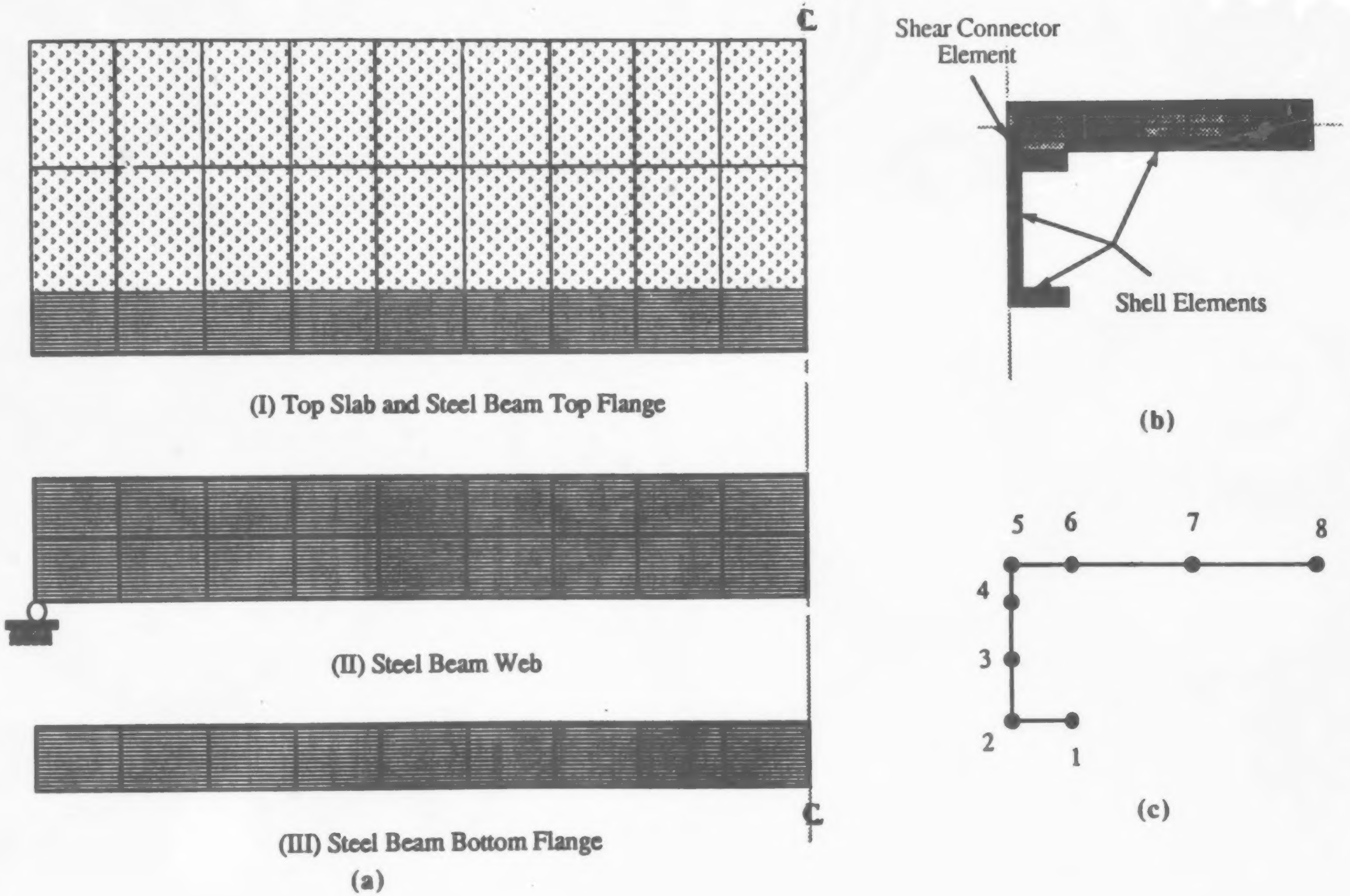
C
C
(I) Top Slab and Steel Beam Top Flange
(II) Steel Beam Web
(III) Steel Beam Bottom Flange
(a)
Shear Connector Element
Shell Elements
(b)
5
6
7
8
4
3
2
1
(c)

Fig. 27: Typical Finite Element Mesh Used
(a) Mesh Details for Different Parts
(b) Elements Used and Their Details
(c) Numbering Scheme

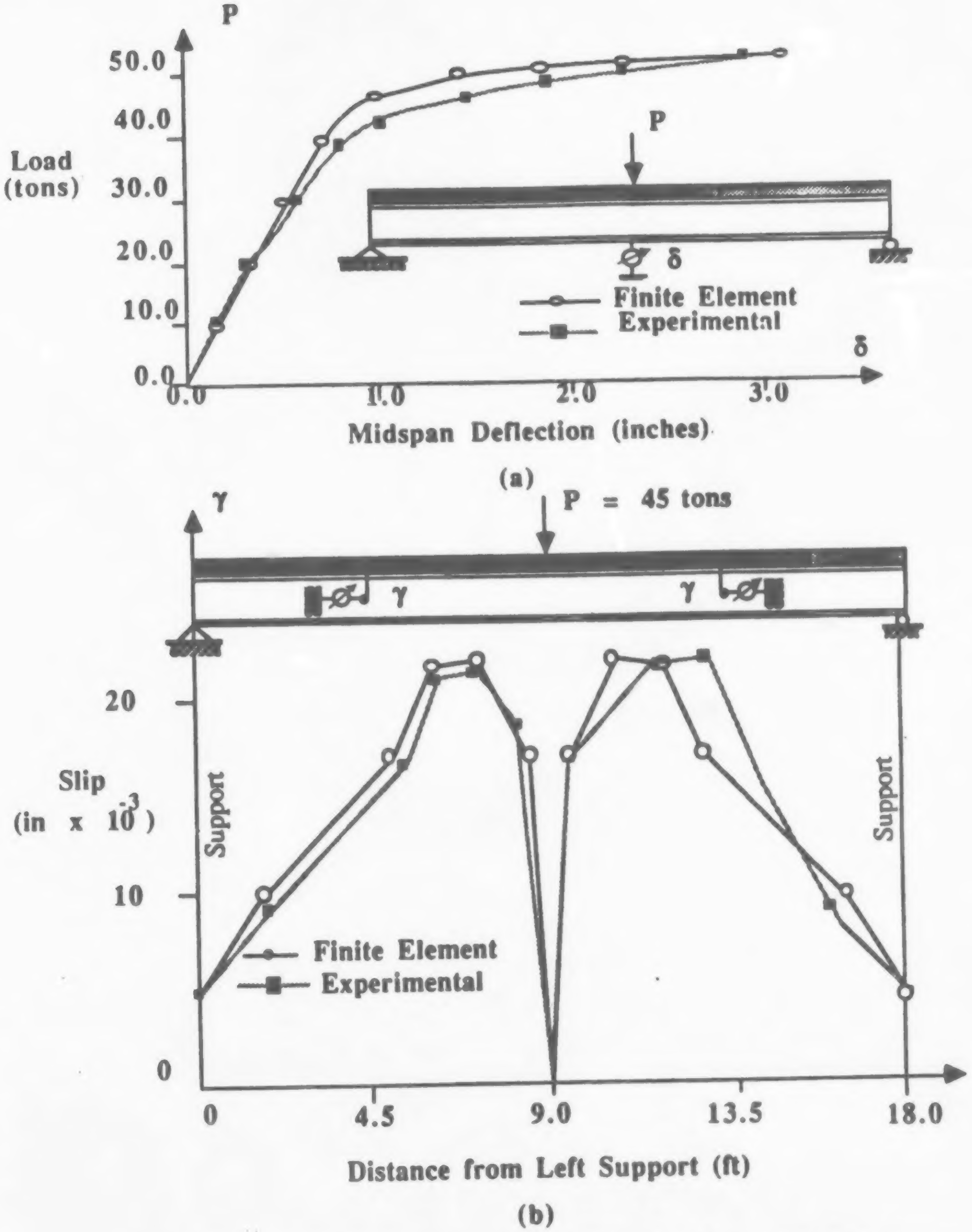

Fig. 28: Yam and Chapman's Simply Supported Beam
(a) Load Midspan Deflection Curve
(b) Slip Distribution along the Beam axis
at Load P=45 tons

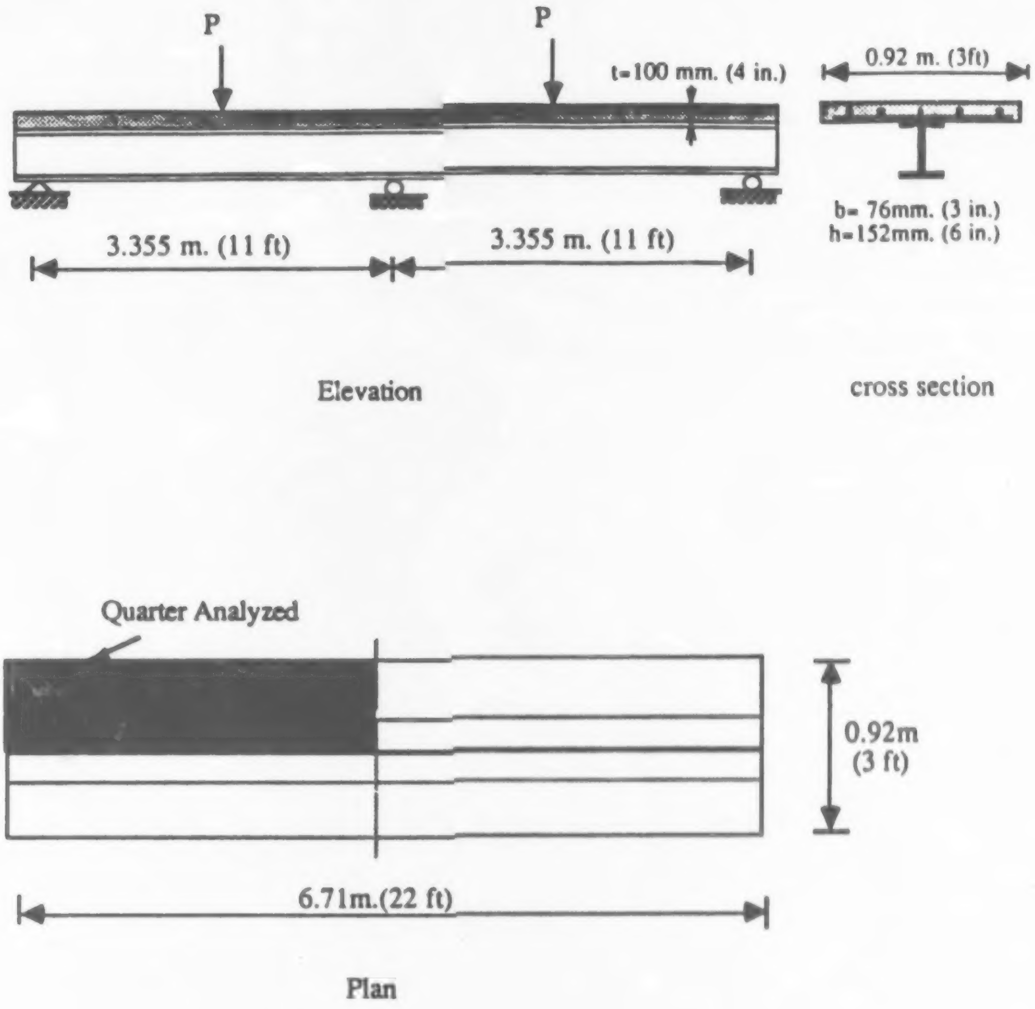
P
P
t=100 mm. (4 in.)
0.92 m. (3ft)
b= 76mm. (3 in.)
h=152mm. (6 in.)
3.355 m. (11 ft)
3.355 m. (11 ft)
Elevation
cross section
Quarter Analyzed
0.92m
(3 ft)
6.71m.(22 ft)
Plan

Fig. 29: Yam and Chapman's Continuous Beam

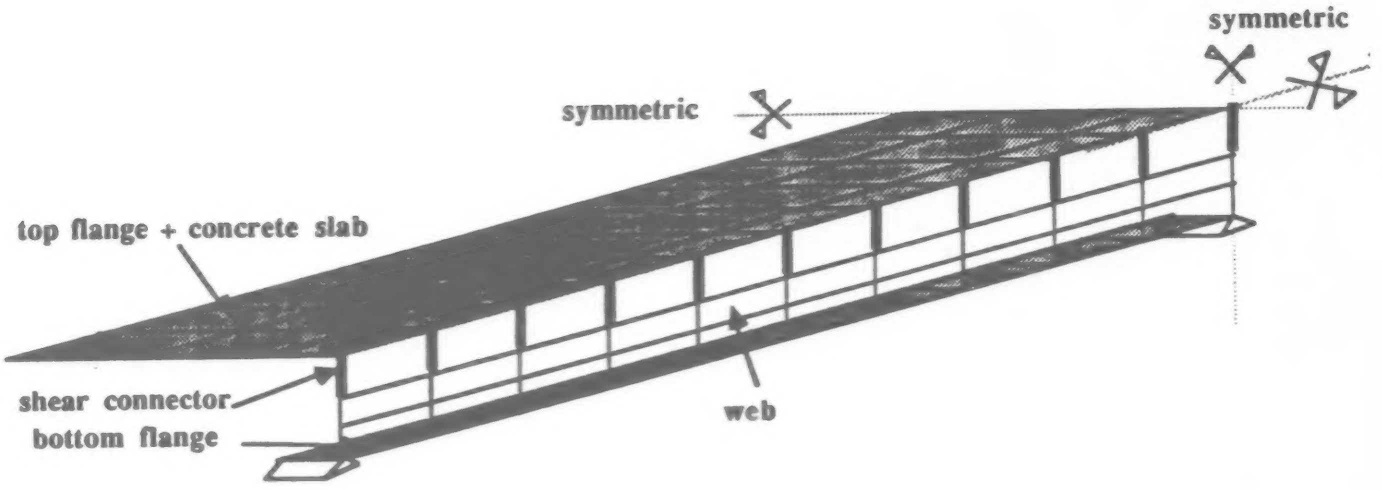
symmetric
symmetric
top flange + concrete slab
shear connector
bottom flange
web

Fig. 30: Finite Element Mesh Utilized

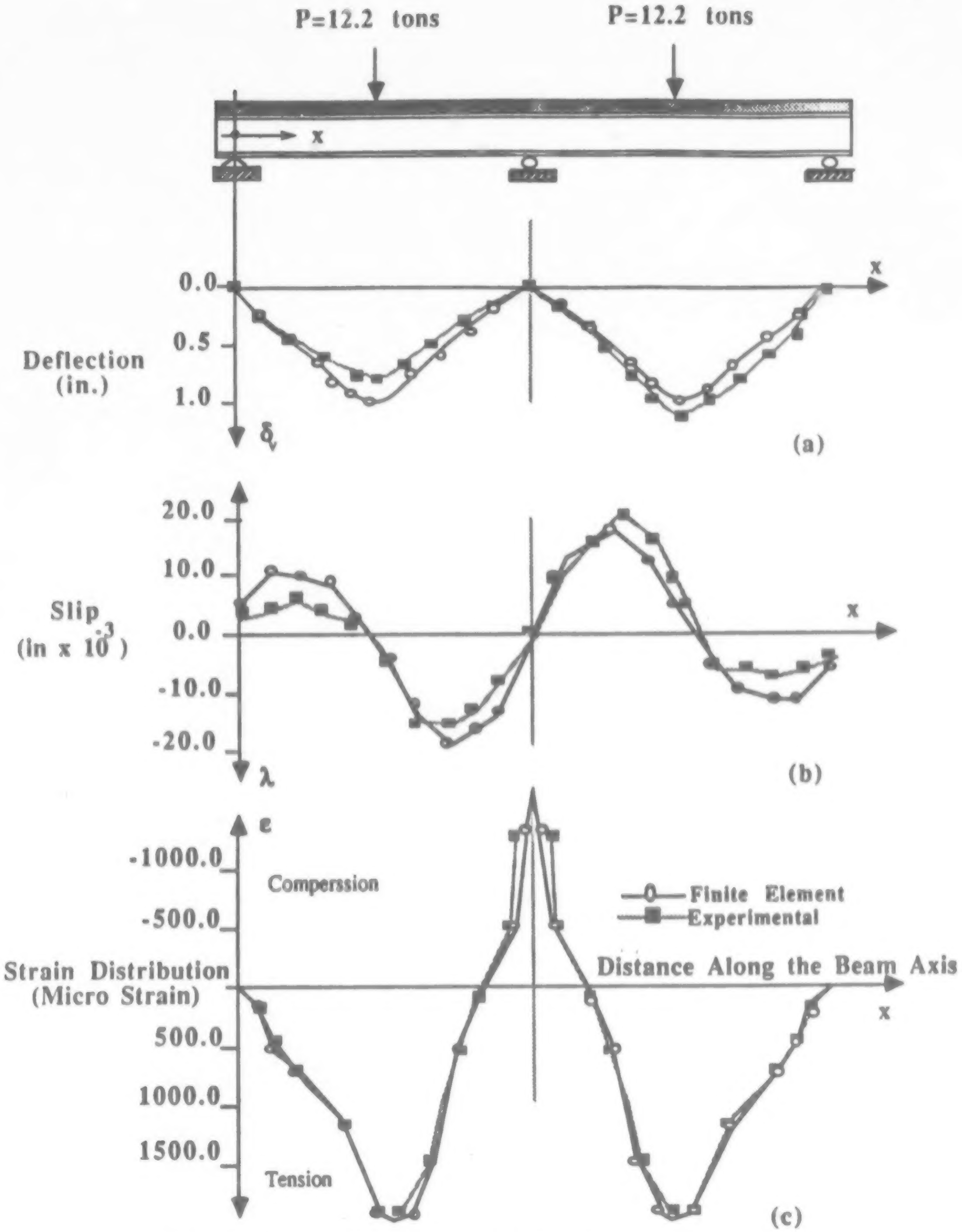

Fig. 31:: Yam and Chapman's Continous Beam
(a) Deflection Curve
(b) Slip Distribution along the Span
(c) Strain Profile along the span in the Bottom Flange of the Steel Beam at P = 12.2 tons

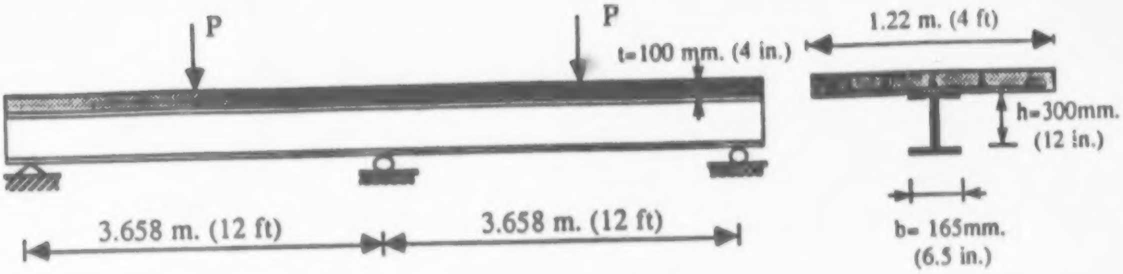
P
P
t=100 mm. (4 in.)
1.22 m. (4 ft)
h=300mm.
(12 in.)
3.658 m. (12 ft)
3.658 m. (12 ft)
b= 165mm.
(6.5 in.)

Elevation

cross section

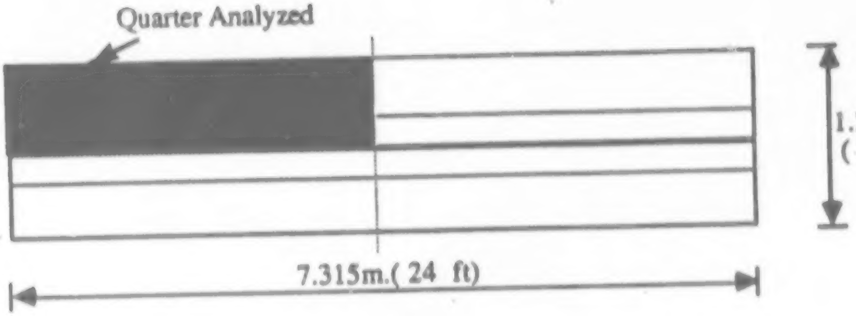
Quarter Analyzed
1.22m
(4ft)
7.315m.(24 ft)

Plan

Fig. 32: Univeristy of Alberta Continuous Beam CB2

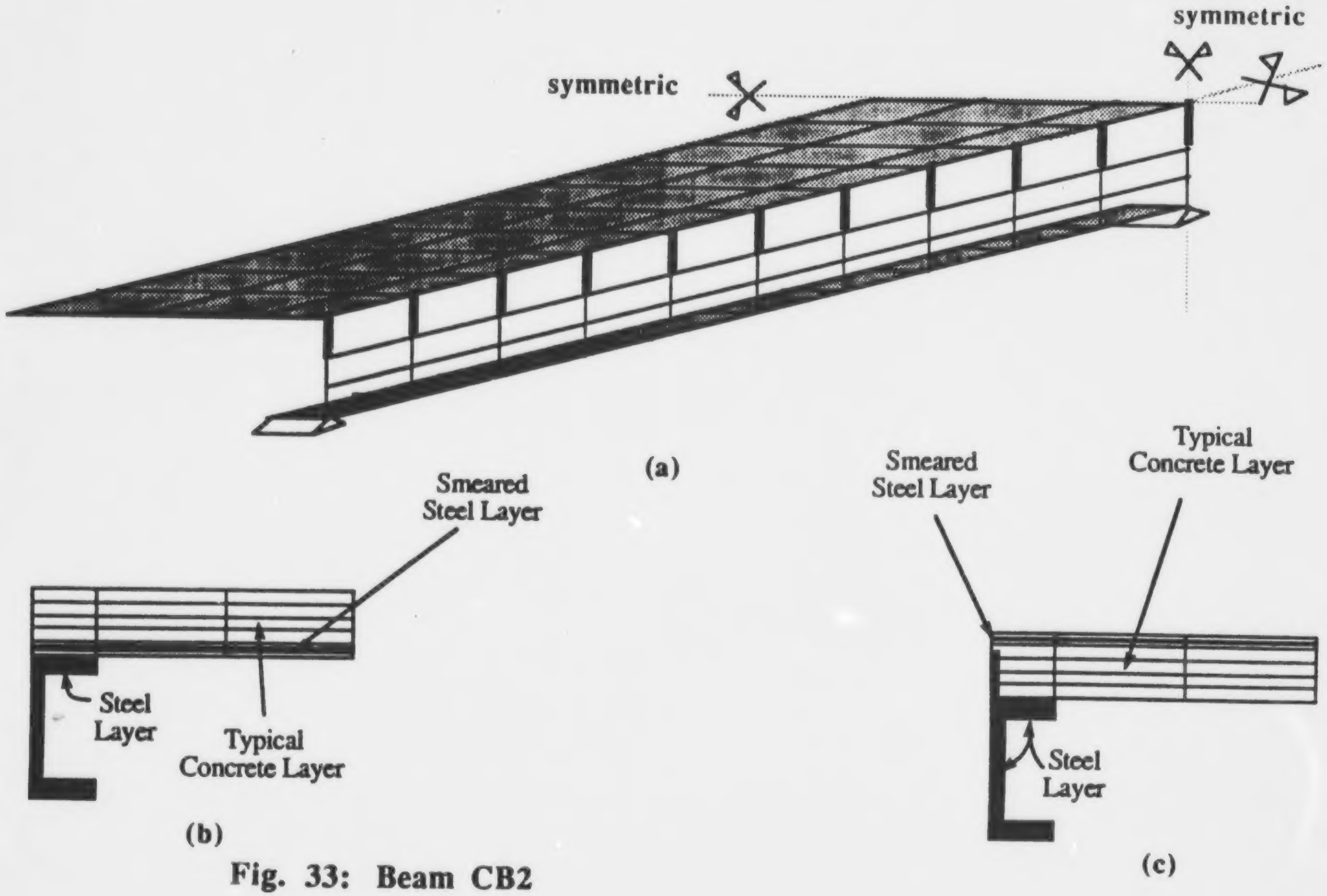
symmetric
symmetric
(a)
Smeared Steel Layer
Steel Layer
Typical Concrete Layer
(b)
Smeared Steel Layer
Typical Concrete Layer
Steel Layer
(c)

Fig. 33: Beam CB2

(a) Finite Element and Boundary Conditions
(b) Details of Shell Elements in the Positive Moment Regions
(c) Details of Shell Elements in the Negative Moments Regions

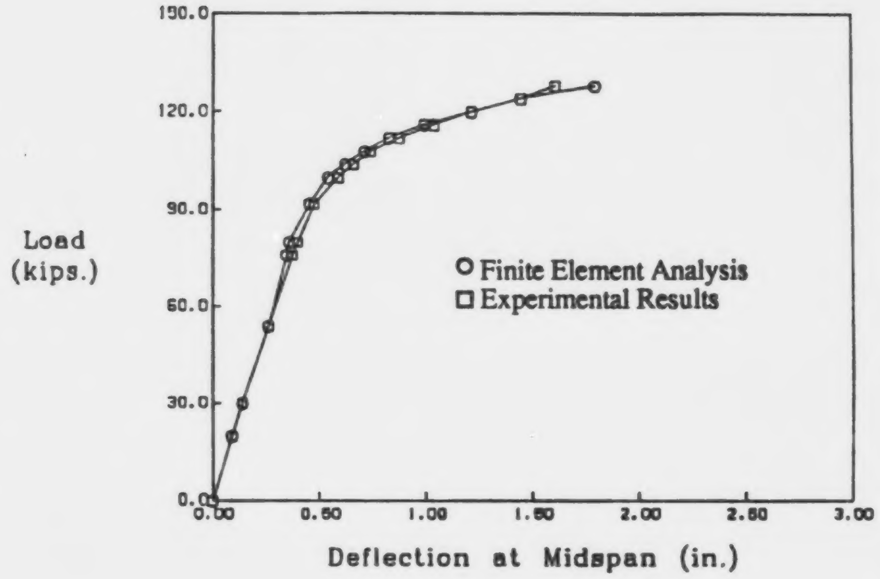

Fig. 34: Load Maximum Deflection of University of Alberta Continuous Beam

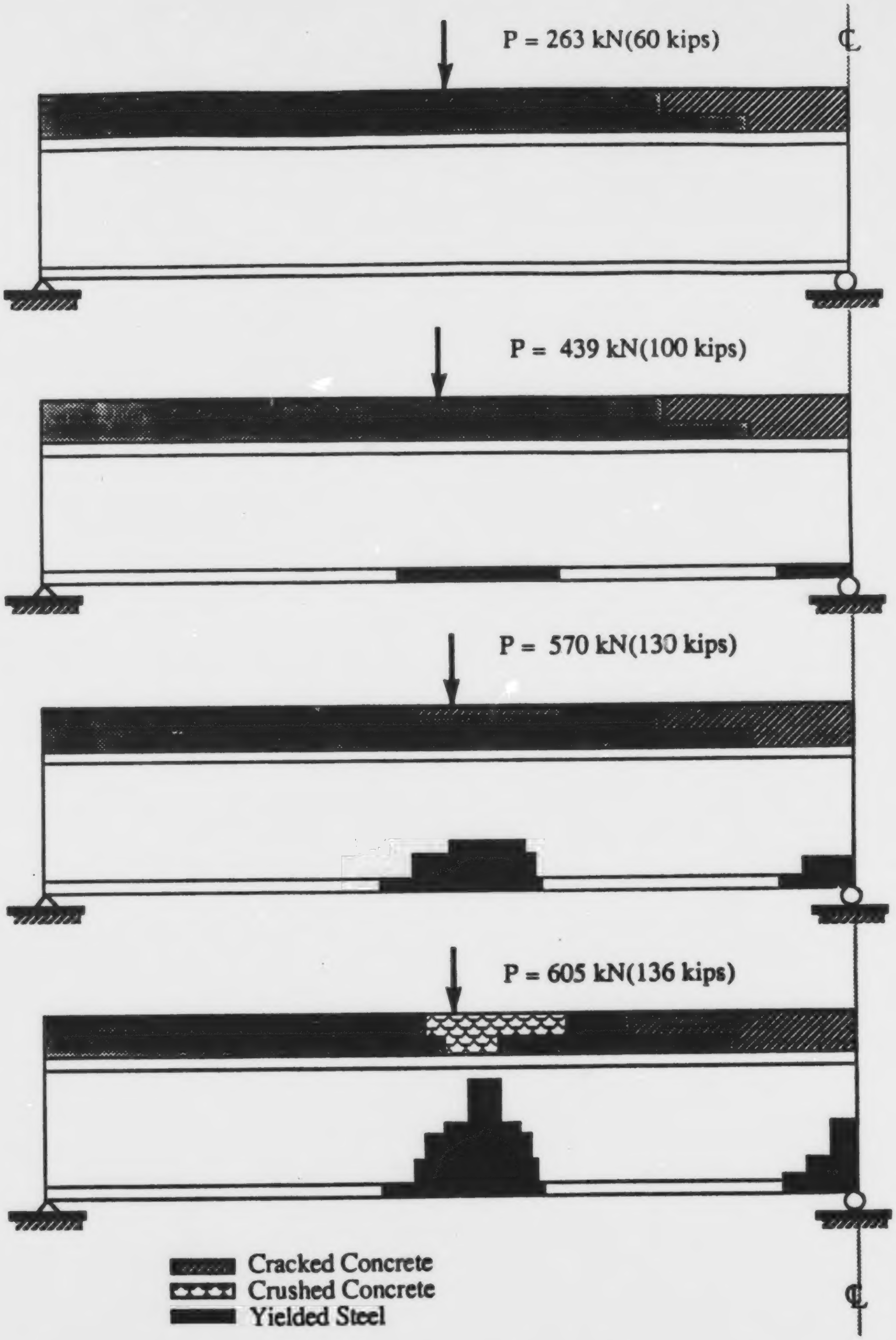
P = 263 kN(60 kips)
℄
P = 439 kN(100 kips)
P = 570 kN(130 kips)
P = 605 kN(136 kips)
Cracked Concrete
Crushed Concrete
Yielded Steel
℄

Fig. 35: Progression of Yielded and Cracked Regions Through the Depth for Univeristy of Alberta Continuous Beam CB2

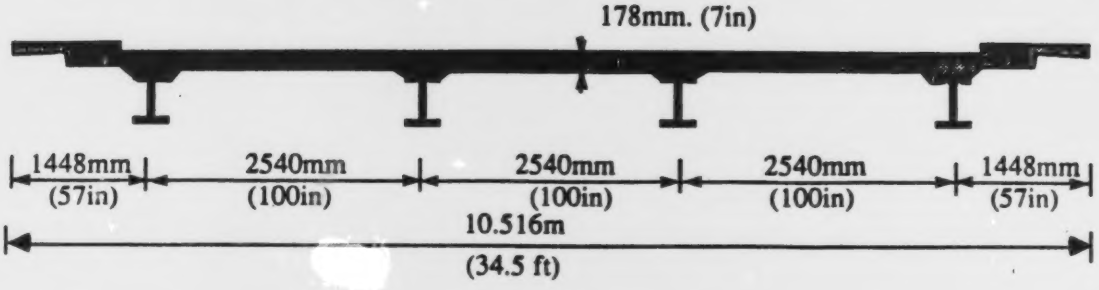
178mm. (7in)
1448mm
(57in)
2540mm
(100in)
2540mm
(100in)
2540mm
(100in)
1448mm
(57in)
10.516m
(34.5 ft)

Actual Cross Section

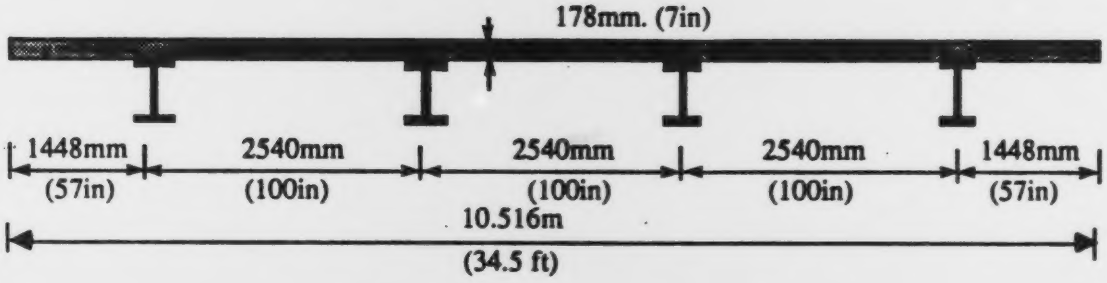
178mm. (7in)
1448mm
(57in)
2540mm
(100in)
2540mm
(100in)
2540mm
(100in)
1448mm
(57in)
10.516m
(34.5 ft)

Idealized Cross Section

Fig. 36: Actual and Idealized Cross Section of Tennessee Multigirder Bridge

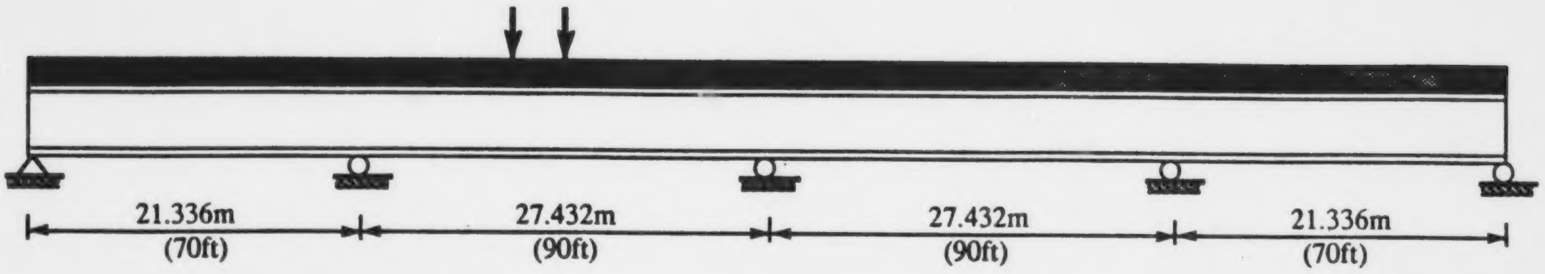
21.336m
(70ft)
27.432m
(90ft)
27.432m
(90ft)
21.336m
(70ft)

Elevation

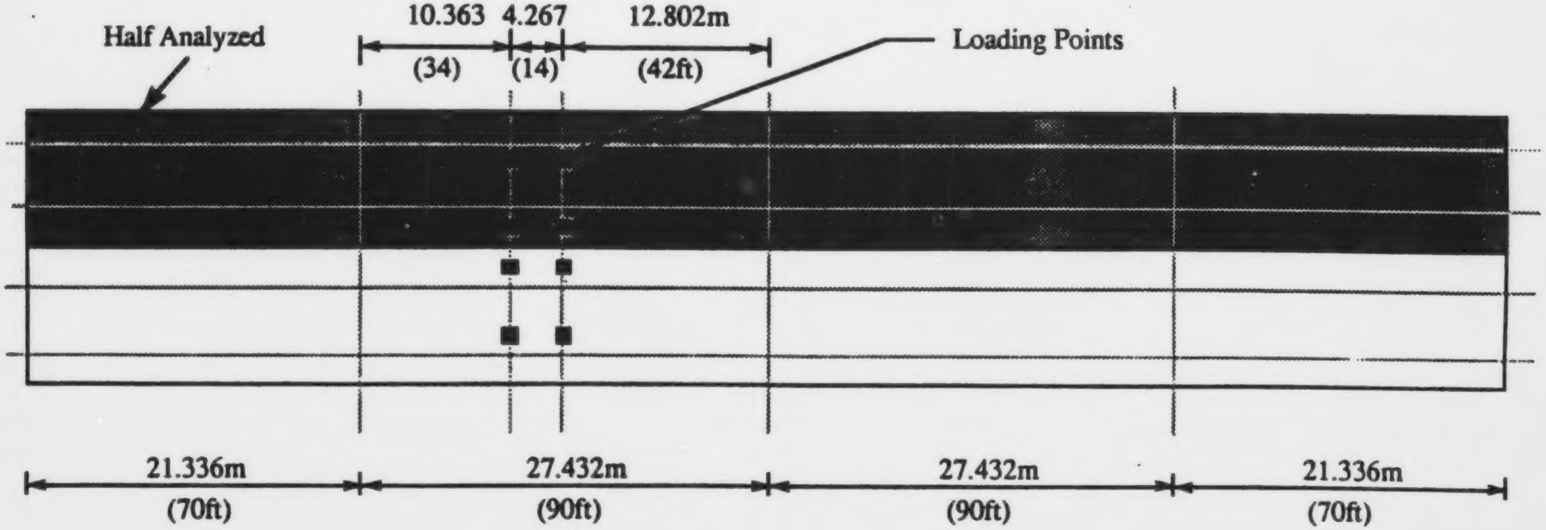
Half Analyzed
10.363
(34)
4.267
(14)
12.802m
(42ft)
Loading Points
21.336m
(70ft)
27.432m
(90ft)
27.432m
(90ft)
21.336m
(70ft)

Plan and Loading

Fig. 37: University of Tennessee Multigirder Bridge

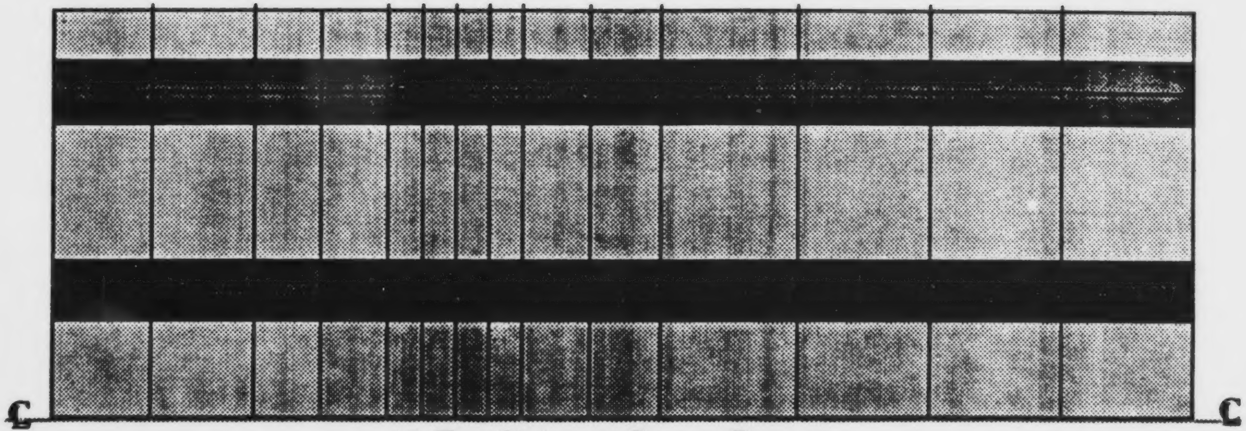

(a) Top Slab and Beams Flanges

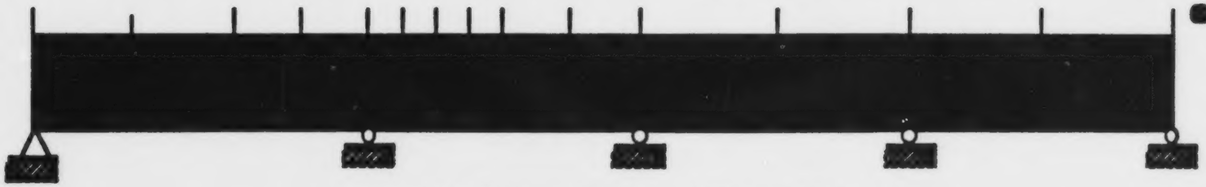

(b) Beams Web and Shear Studs

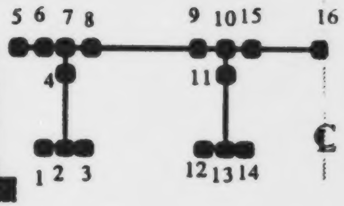
℄
5 6 7 8
9 10 15
16
4
11
1 2 3
12 13 14
℄

(d) Node Numbering

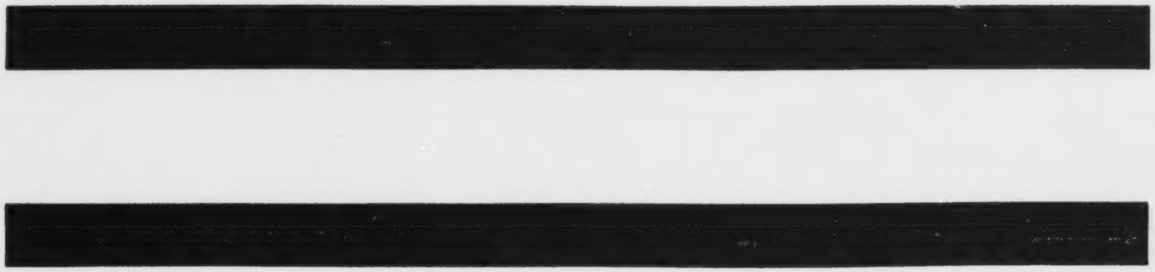

(c) Beams Bottom Flanges

Fig. 38: Finite Element Mesh Used for Tennessee Bridge

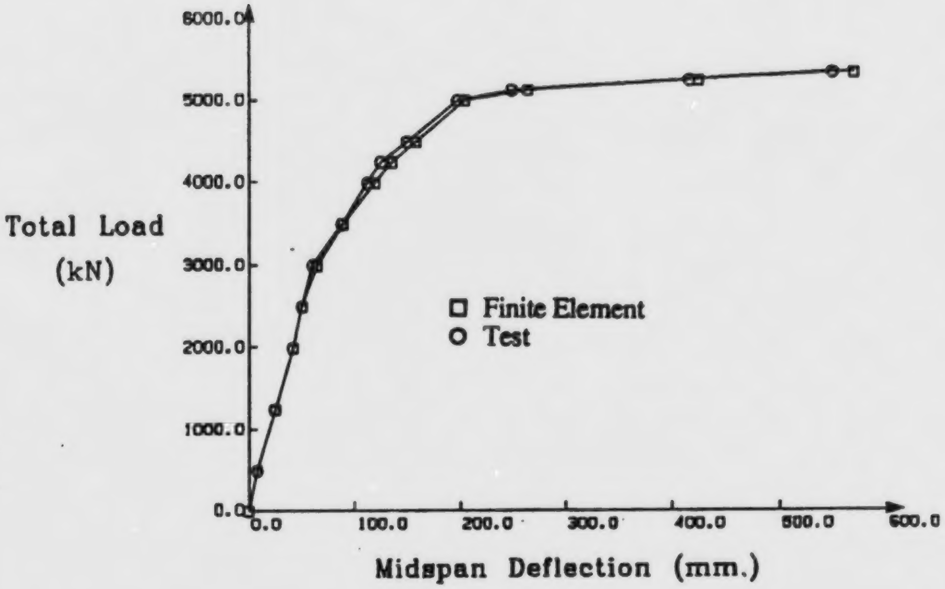

Fig. 39: Load Maximum Deflection Curve of University of Tennessee Multigirder Bridge

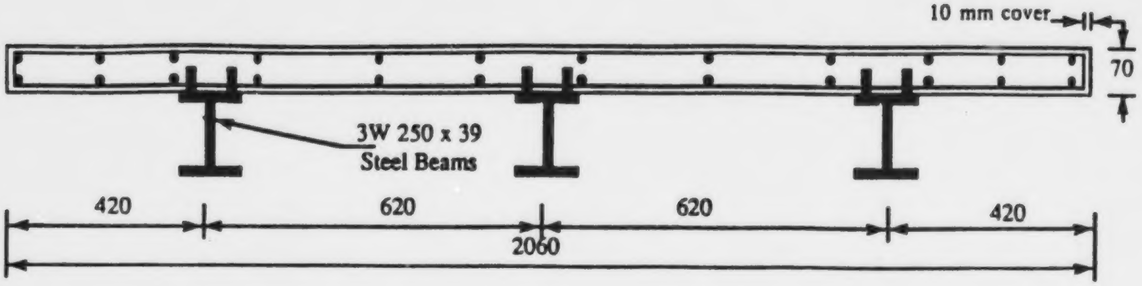
10 mm cover
70
3W 250 x 39
Steel Beams
420
620
620
420
2060

Cross Section

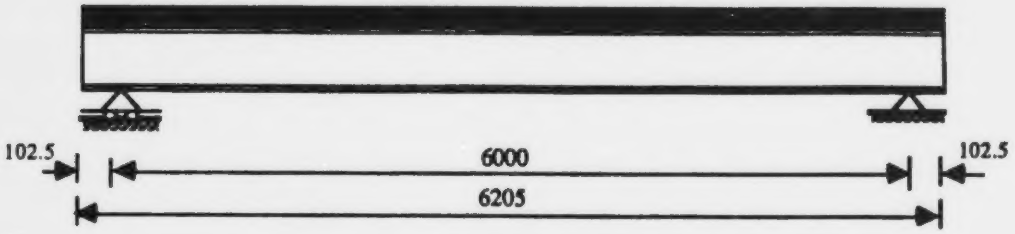
102.5
6000
102.5
6205

Elevation

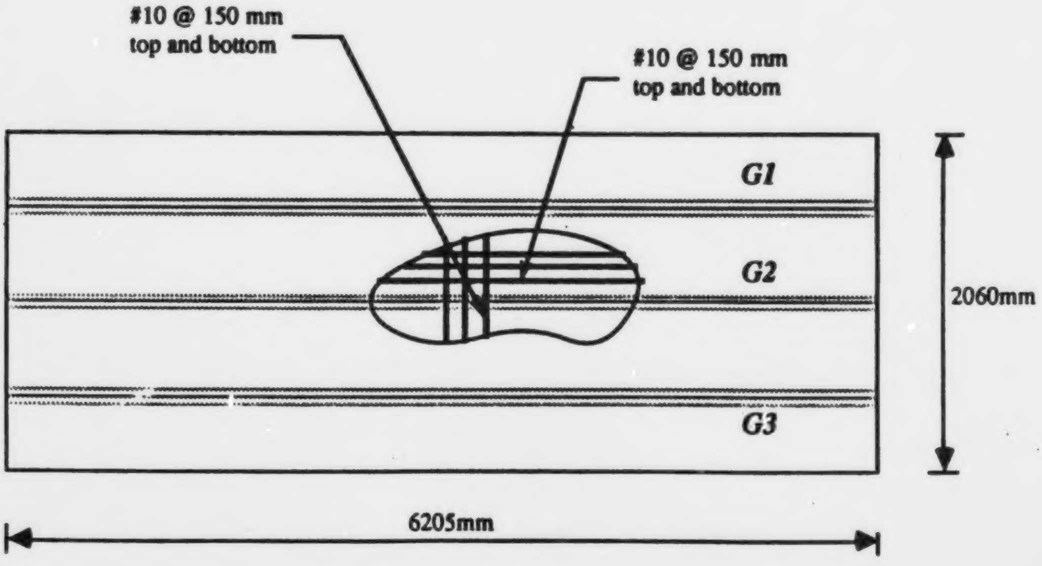
#10 @ 150 mm
top and bottom
#10 @ 150 mm
top and bottom
G1
G2
G3
2060mm
6205mm

Plan

Fig. 40: General Layout of Bridge Model

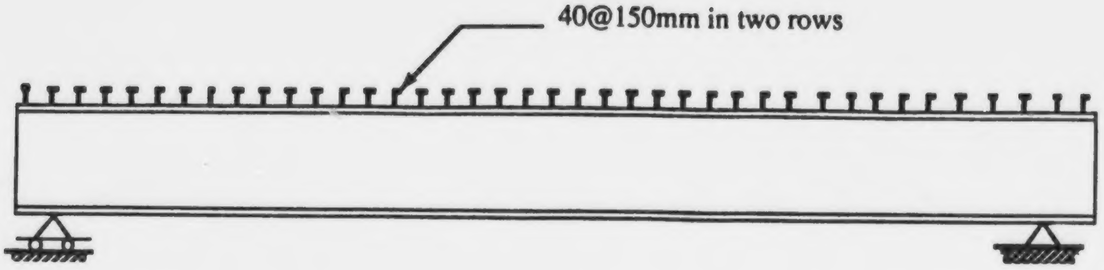
40@150mm in two rows

Shear Studs Distribution

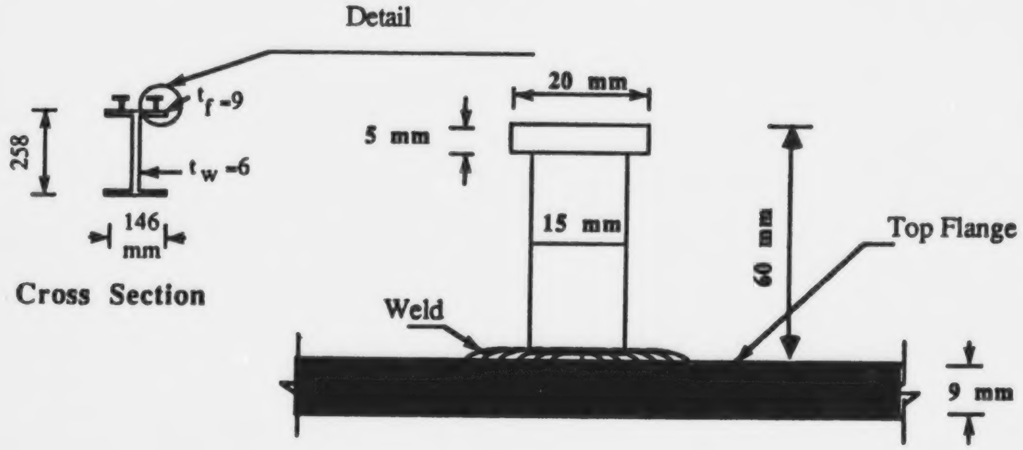
Detail
258
t_f =9
t_w =6
146 mm
20 mm
5 mm
15 mm
60 mm
Top Flange
Weld
9 mm

Cross Section

Shear Stud Dimensions

Fig. 41: Shear Studs Details

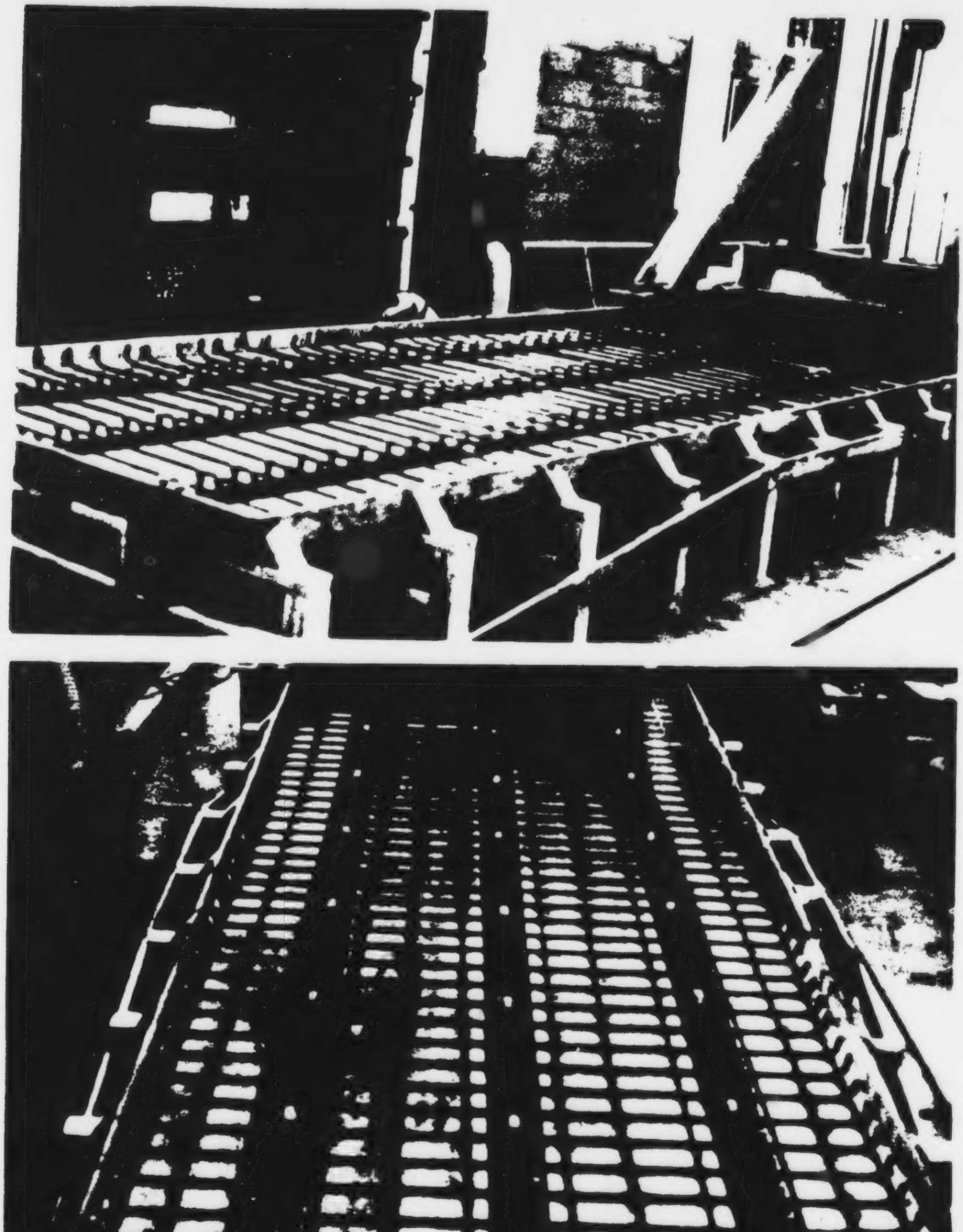

Fig. 42: Disposition of Bottom Reinforcement Layer

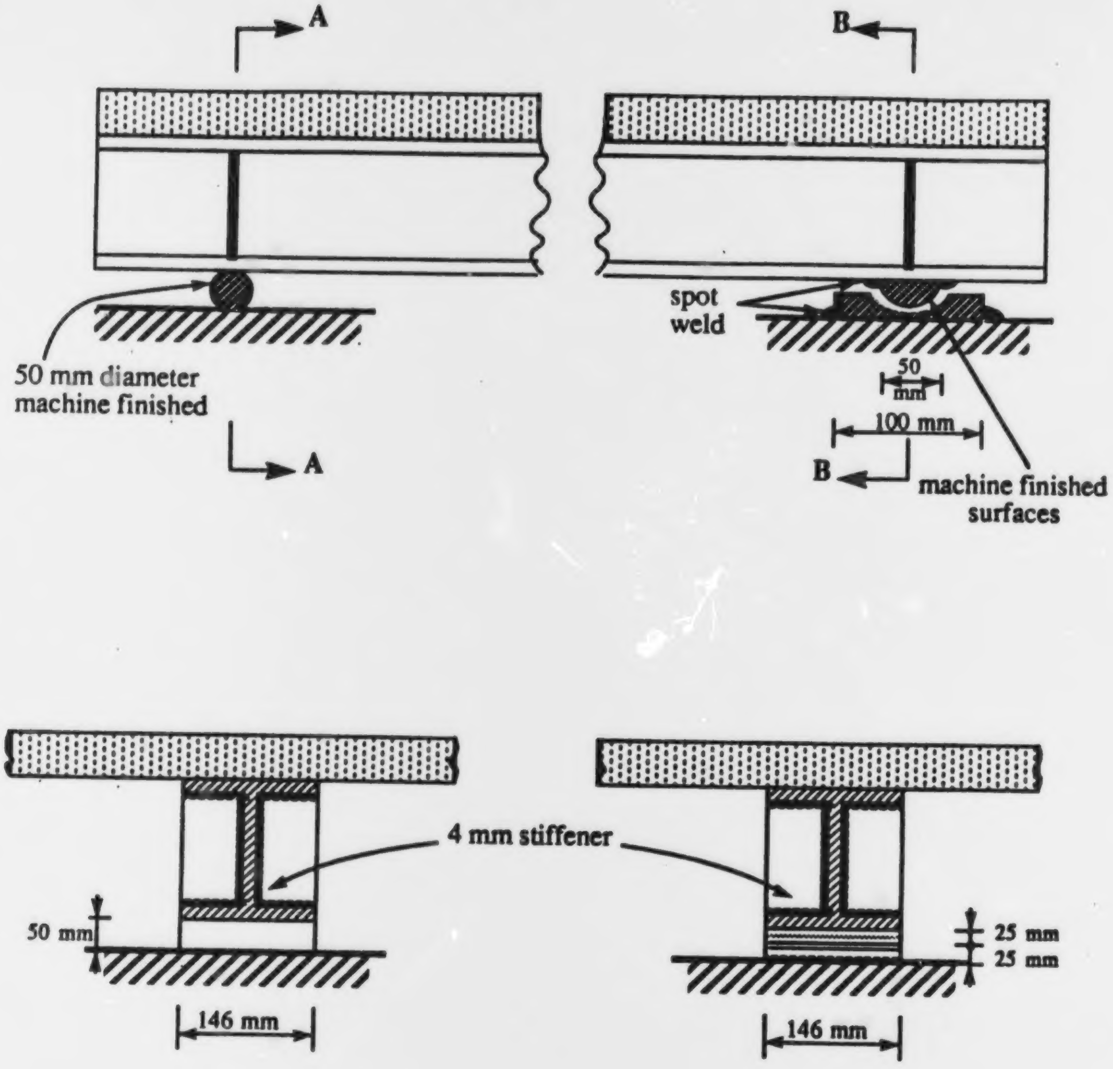
A
B
A
spot
weld
50 mm diameter
machine finished
50
mm
100 mm
B
machine finished
surfaces
A
4 mm stiffener
50 mm
25 mm
25 mm
146 mm
146 mm

Section A-A

Section B-B

Roller Support

Hinged Support

Fig. 43: Bridge Supports Detials

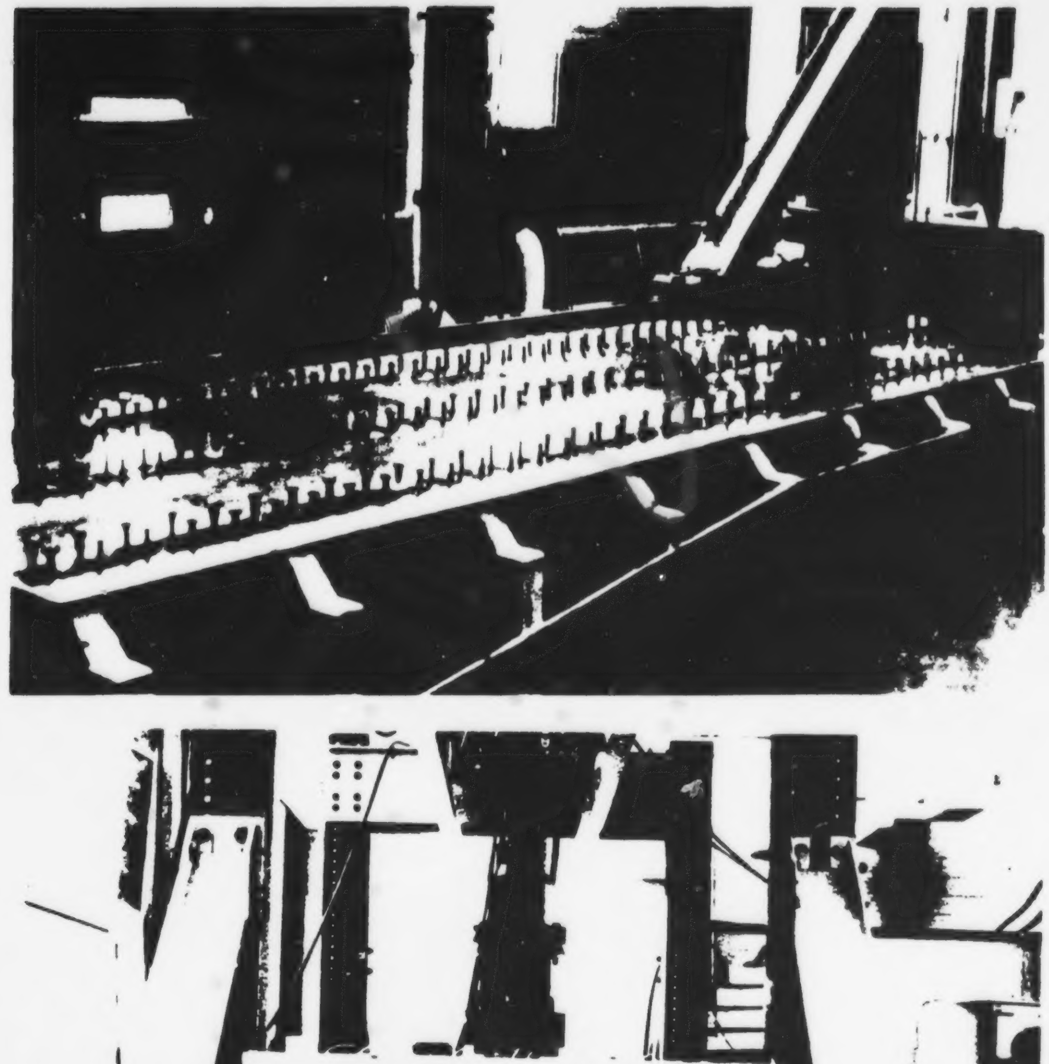

Fig. 44: Construction Stages of Bridge Model

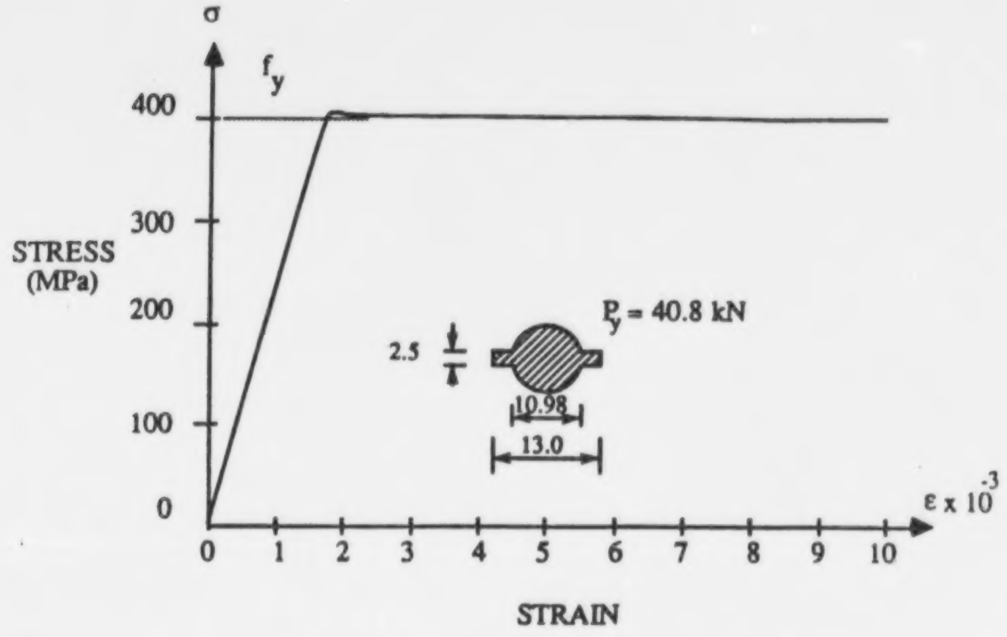

Fig. 45: Stress-Strain Relationship of Reinforcing Bars

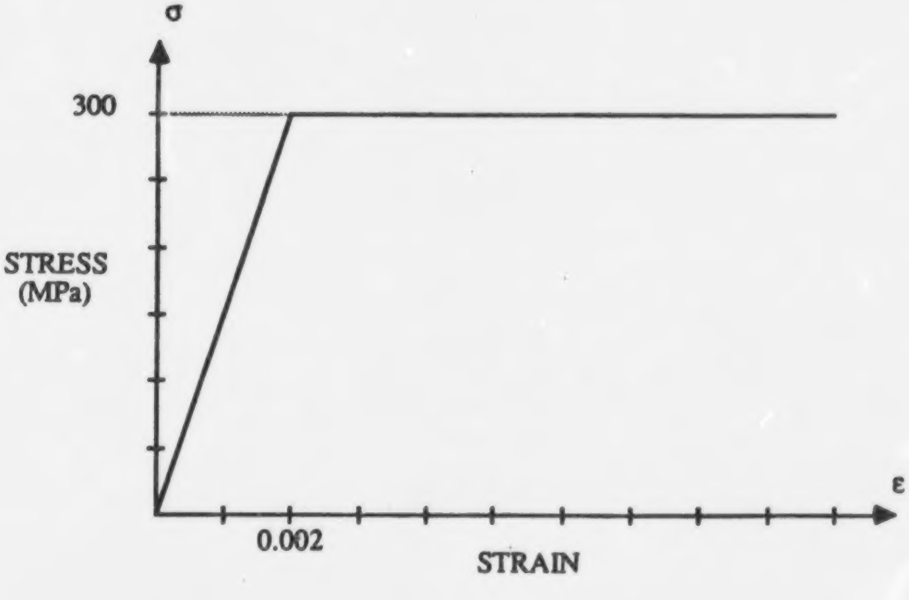

Fig. 46: Stress-Strain Relationship Used for Steel Beams

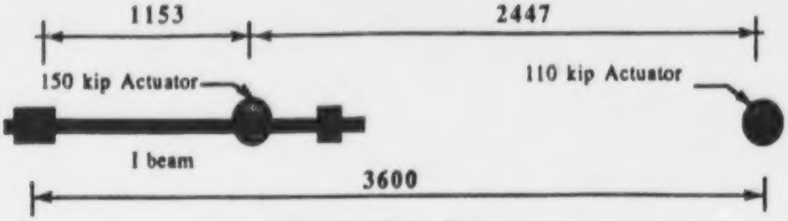
1153
2447
150 kip Actuator
110 kip Actuator
I beam
3600

Partial Top View

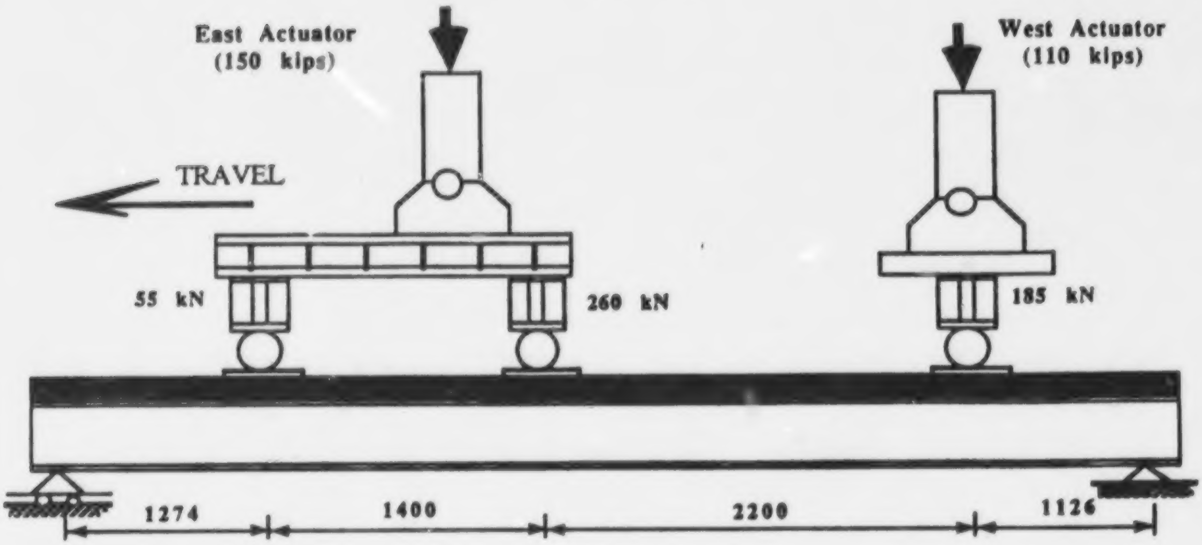
East Actuator
(150 kips)
West Actuator
(110 kips)
TRAVEL
55 kN
260 kN
185 kN
1274
1400
2200
1126

Elevation

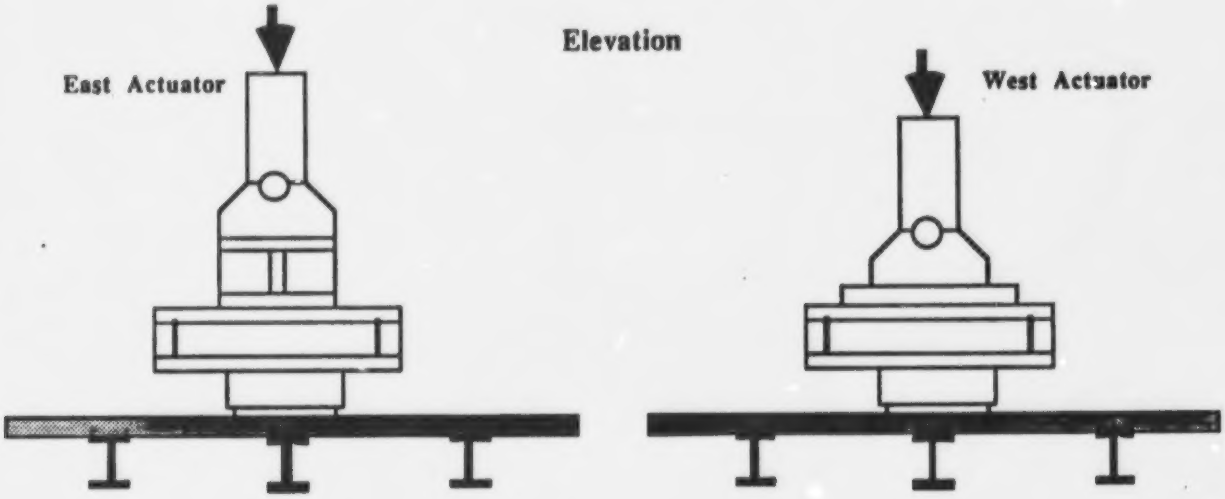
East Actuator
West Actuator

Side View

Fig. 47: Experimental Loading System

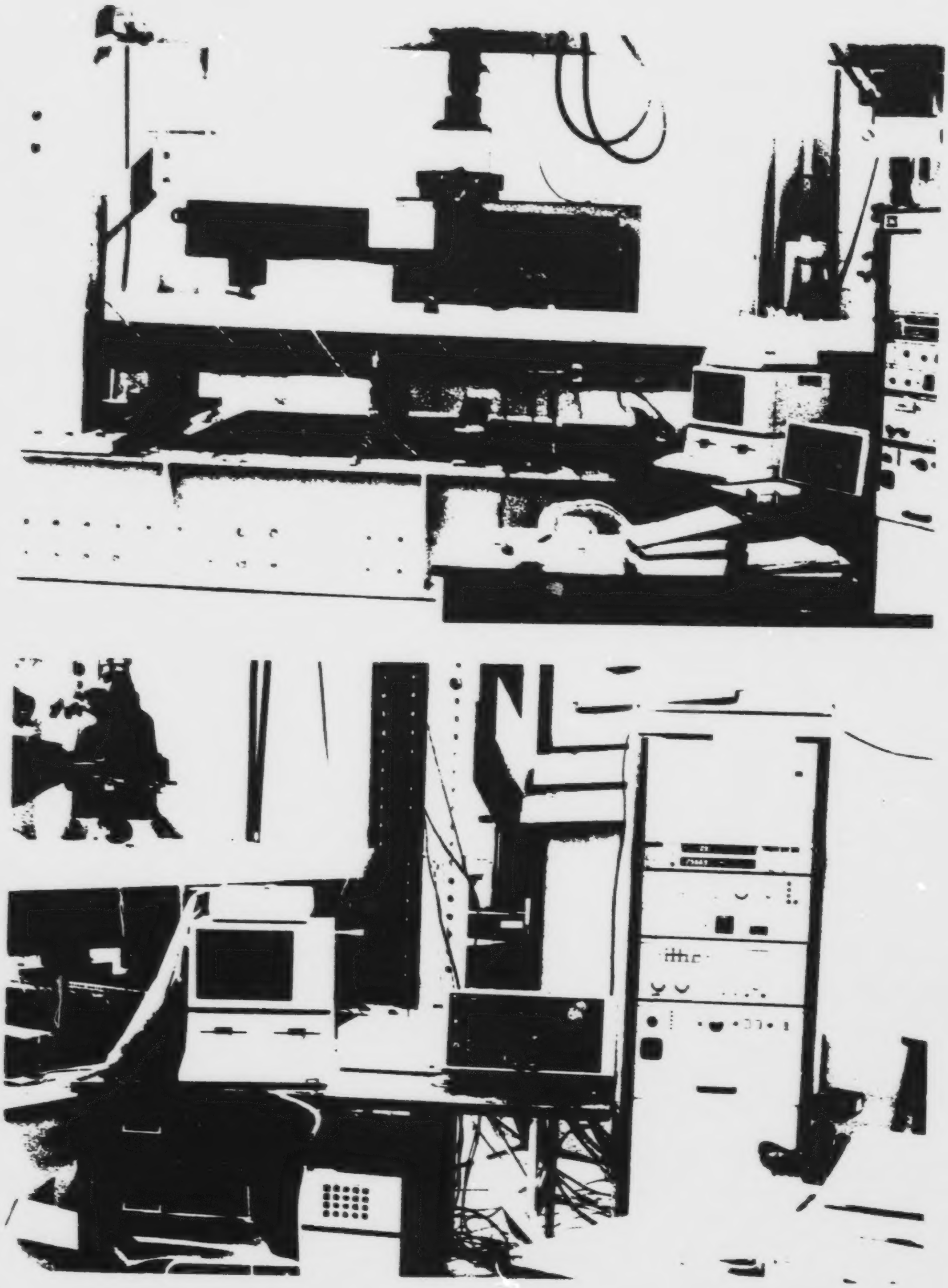

Fig. 48: Experimental Set-up

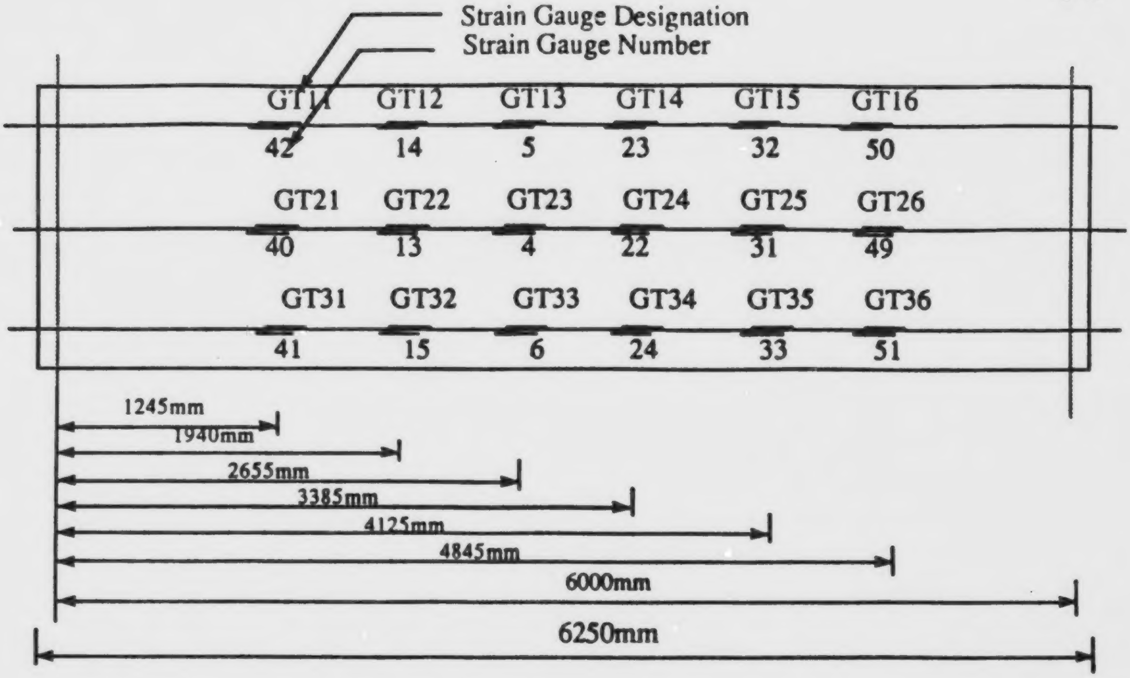
Strain Gauge Designation
Strain Gauge Number
GT11 GT12 GT13 GT14 GT15 GT16
42 14 5 23 32 50
GT21 GT22 GT23 GT24 GT25 GT26
40 13 4 22 31 49
GT31 GT32 GT33 GT34 GT35 GT36
41 15 6 24 33 51
1245mm
1940mm
2655mm
3385mm
4125mm
4845mm
6000mm
6250mm

(a) Beams Top Flanges

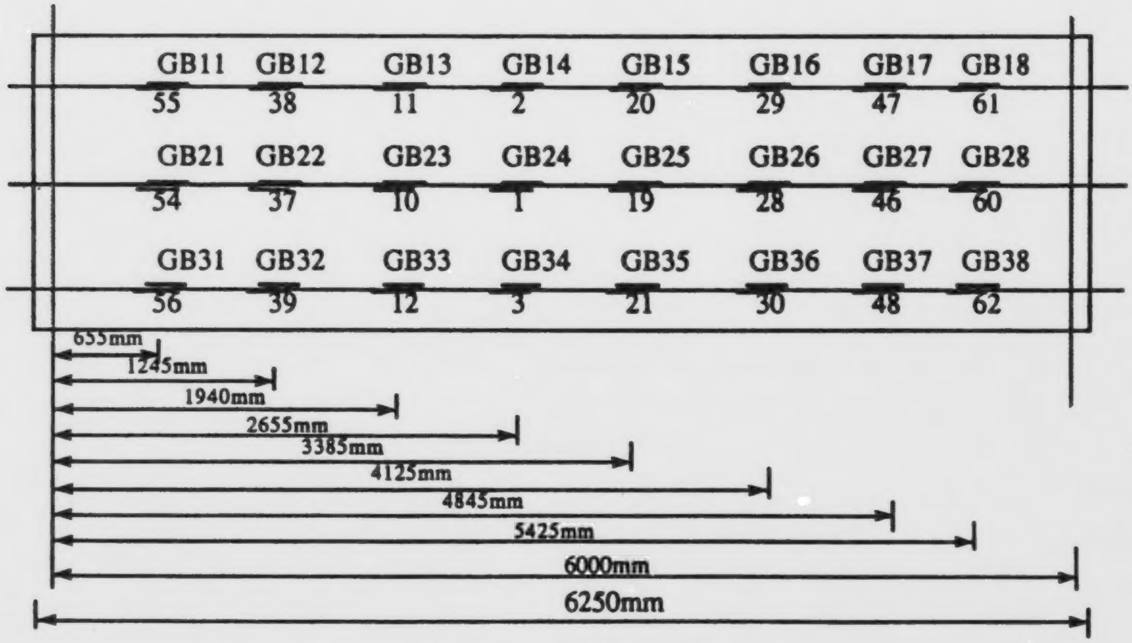
GB11 GB12 GB13 GB14 GB15 GB16 GB17 GB18
55 38 11 2 20 29 47 61
GB21 GB22 GB23 GB24 GB25 GB26 GB27 GB28
54 37 10 1 19 28 46 60
GB31 GB32 GB33 GB34 GB35 GB36 GB37 GB38
56 39 12 3 21 30 48 62
655mm
1245mm
1940mm
2655mm
3385mm
4125mm
4845mm
5425mm
6000mm
6250mm

(b) Beams Bottom Flanges

Fig. 49: : Longitudinal Strain Gauges Locations in the Steel Beams

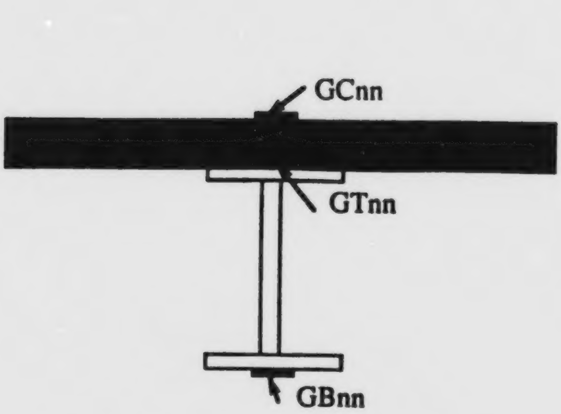
GCnn
GTnn
GBnn

(a) Typical Strain Gauge Locations
on the Cross-Section

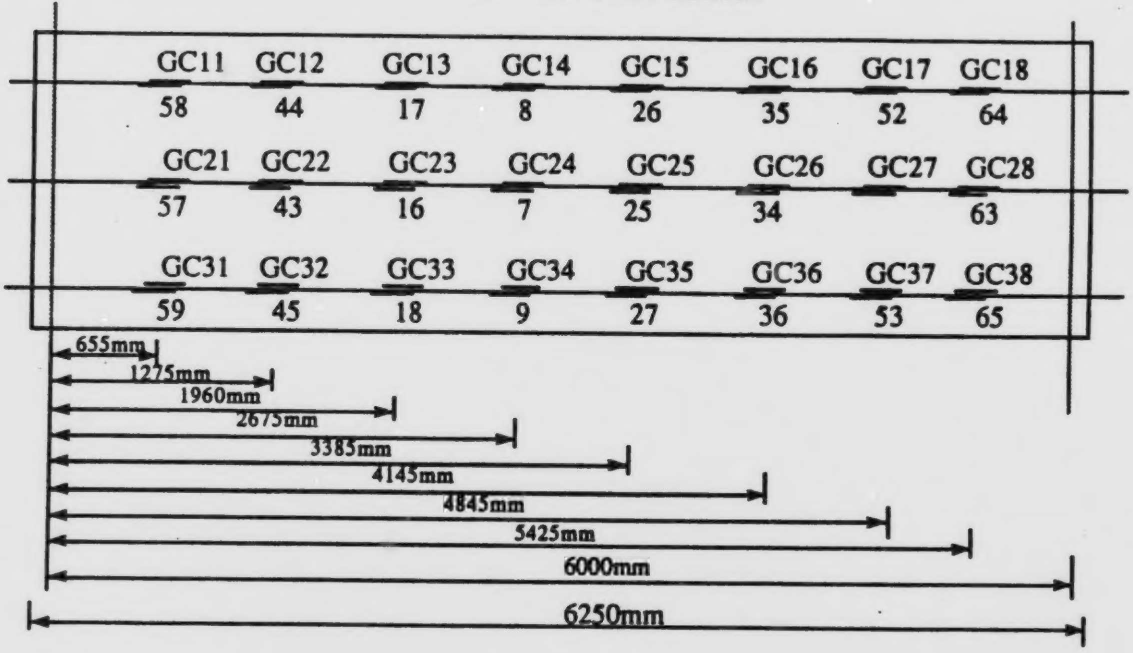
GC11 GC12 GC13 GC14 GC15 GC16 GC17 GC18
58 44 17 8 26 35 52 64
GC21 GC22 GC23 GC24 GC25 GC26 GC27 GC28
57 43 16 7 25 34 63
GC31 GC32 GC33 GC34 GC35 GC36 GC37 GC38
59 45 18 9 27 36 53 65
655mm
1275mm
1960mm
2675mm
3385mm
4145mm
4845mm
5425mm
6000mm
6250mm

(b) Top Concrete Surface

Fig. 50: Longitudinal Strain Gauges
Locations on the Concrete Surface

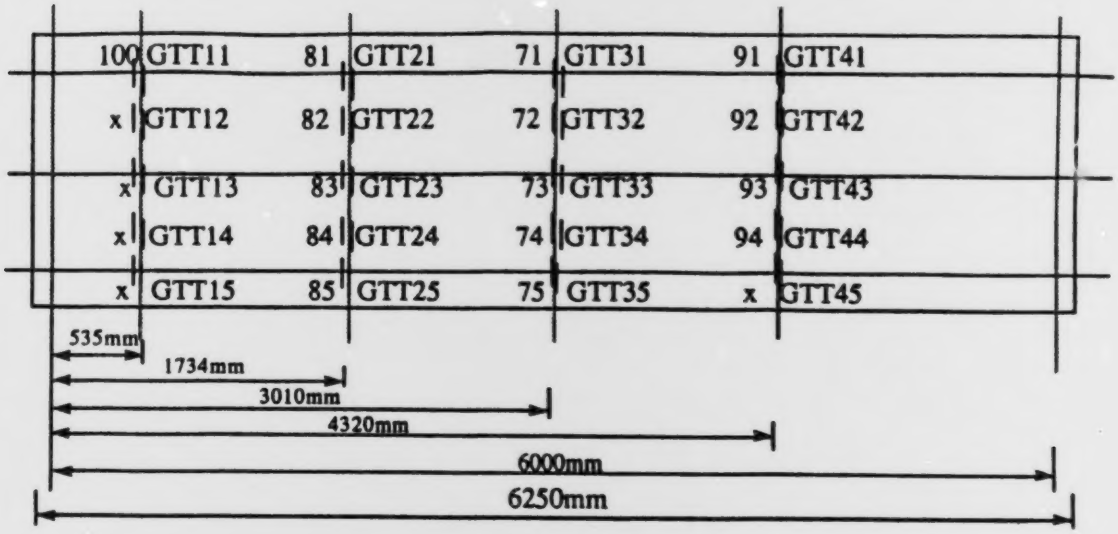
100 GTT11
81 GTT21
71 GTT31
91 GTT41
x GTT12
82 GTT22
72 GTT32
92 GTT42
x GTT13
83 GTT23
73 GTT33
93 GTT43
x GTT14
84 GTT24
74 GTT34
94 GTT44
x GTT15
85 GTT25
75 GTT35
x GTT45
535mm
1734mm
3010mm
4320mm
6000mm
6250mm

(a) Top Steel Layer

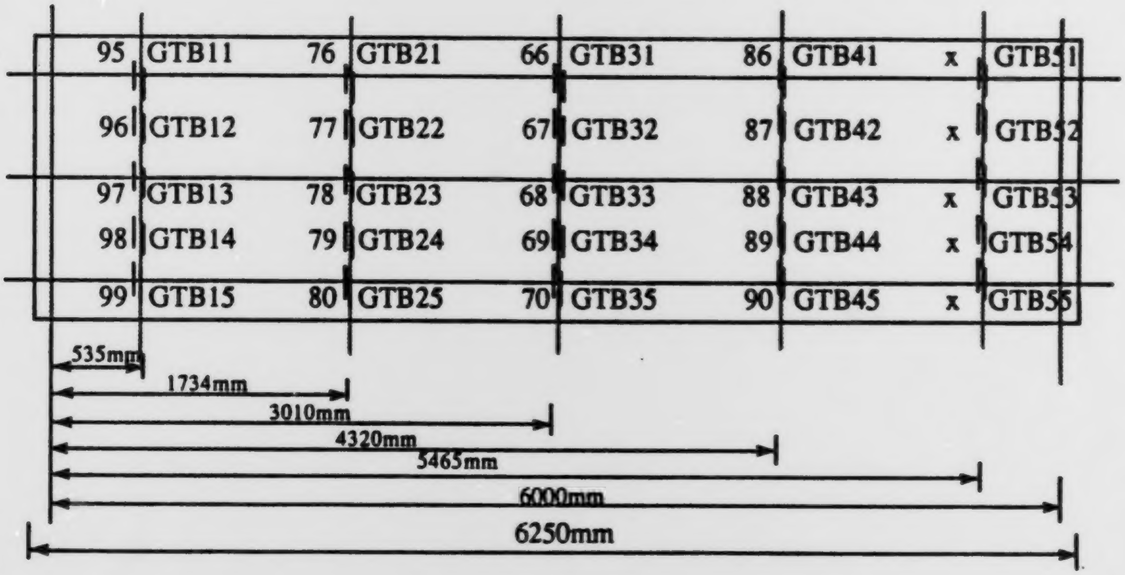
95 GTB11
76 GTB21
66 GTB31
86 GTB41
x GTB51
96 GTB12
77 GTB22
67 GTB32
87 GTB42
x GTB52
97 GTB13
78 GTB23
68 GTB33
88 GTB43
x GTB53
98 GTB14
79 GTB24
69 GTB34
89 GTB44
x GTB54
99 GTB15
80 GTB25
70 GTB35
90 GTB45
x GTB55
535mm
1734mm
3010mm
4320mm
5465mm
6000mm
6250mm

(b) Bottom Steel Layer

Fig. 51: Locations of Strain Gauges Attached to Transverse Slab Reinforcement

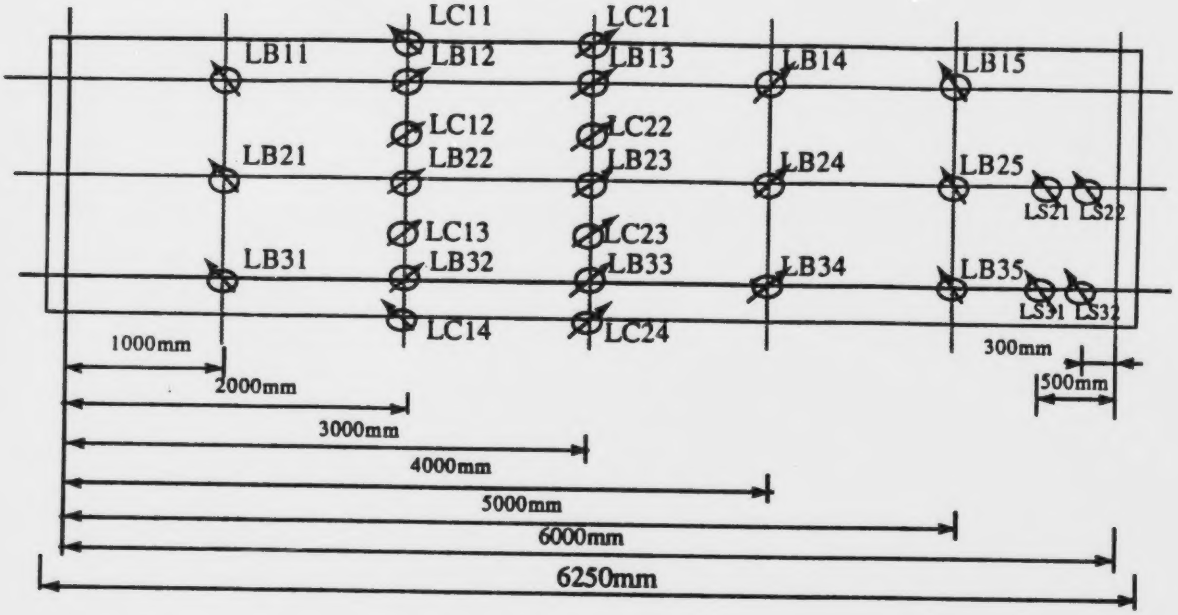
LC11
LC21
LB11
LB12
LB13
LB14
LB15
LC12
LC22
LB21
LB22
LB23
LB24
LB25
LS21
LS22
LC13
LC23
LB31
LB32
LB33
LB34
LB35
LS31
LS32
LC14
LC24
1000mm
2000mm
3000mm
4000mm
5000mm
6000mm
6250mm
300mm
500mm

LEGEND :-

LB LVDT for the beams deflection
LC LVDT for the concrete slab deflection
LS LVDT for the concrete-steel slip
⌀ 6" Stroke
⊘ 1.25" Stroke

Fig. 52: LVDT's Locations

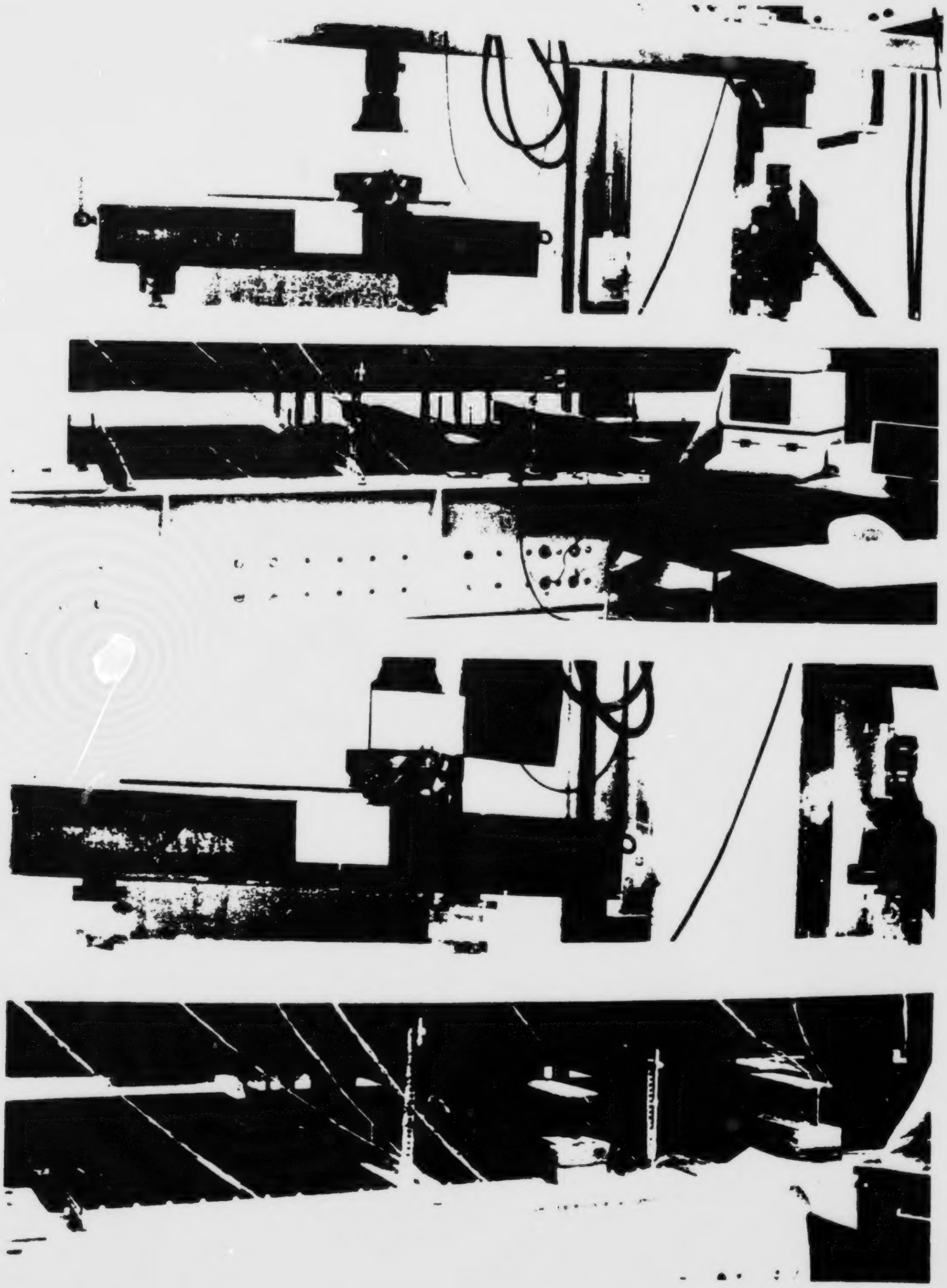

Fig. 53: Details of LVDT's Attachment

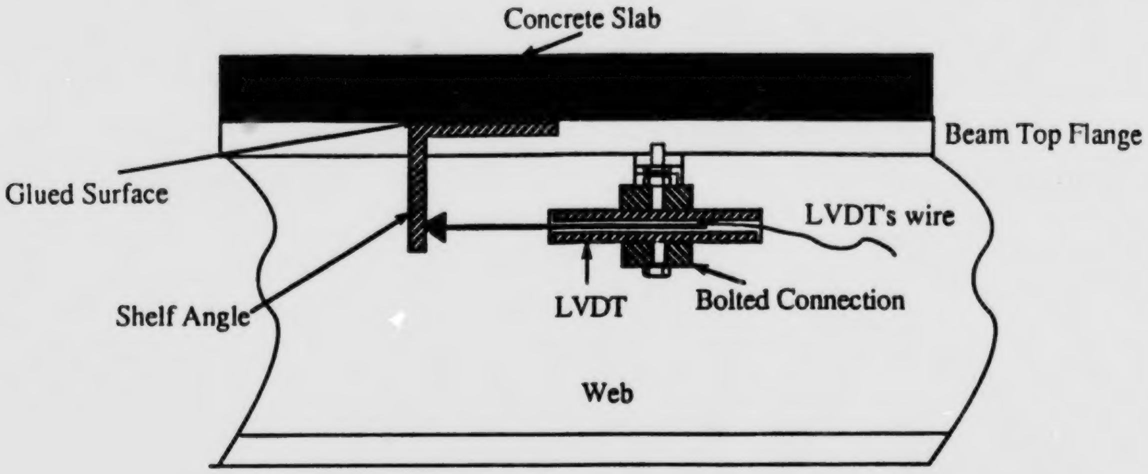
Concrete Slab
Beam Top Flange
Glued Surface
LVDT's wire
Shelf Angle
LVDT
Bolted Connection
Web

Elevation

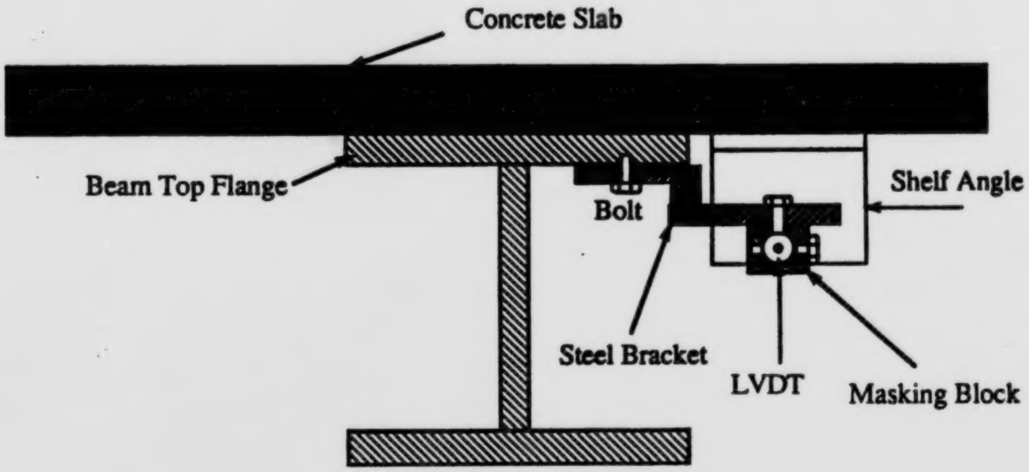
Concrete Slab
Beam Top Flange
Bolt
Shelf Angle
Steel Bracket
LVDT
Masking Block

Side View

Fig. 54: Schematic Detail of a Typical LVDT used for Slip Measurment

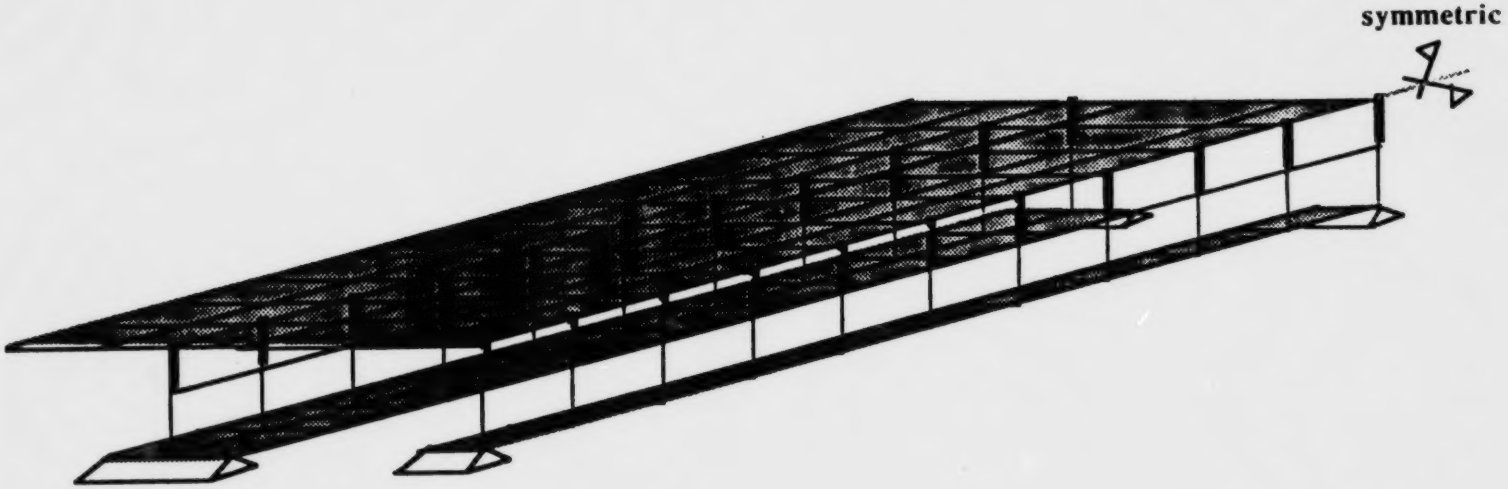

Fig. 55: Finite Element Idealization of Half Bridge

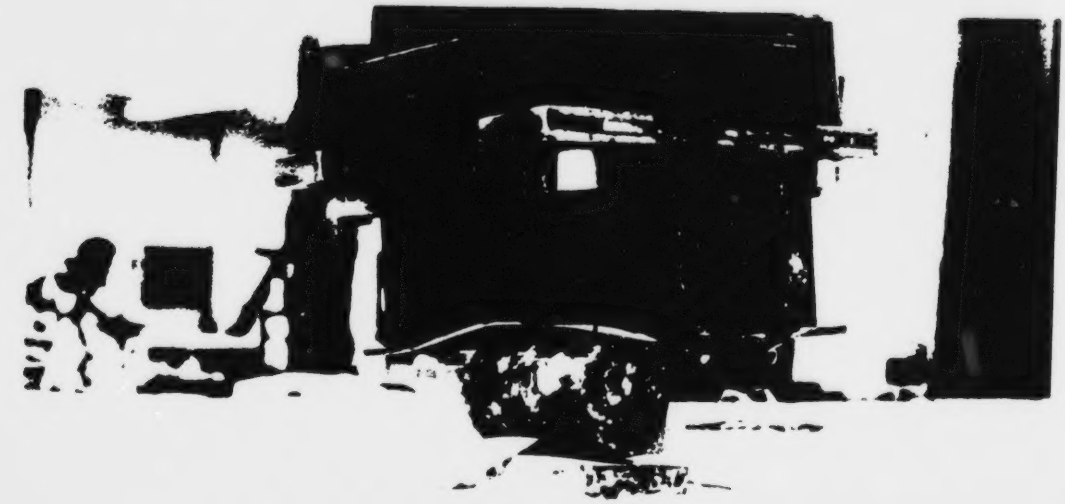

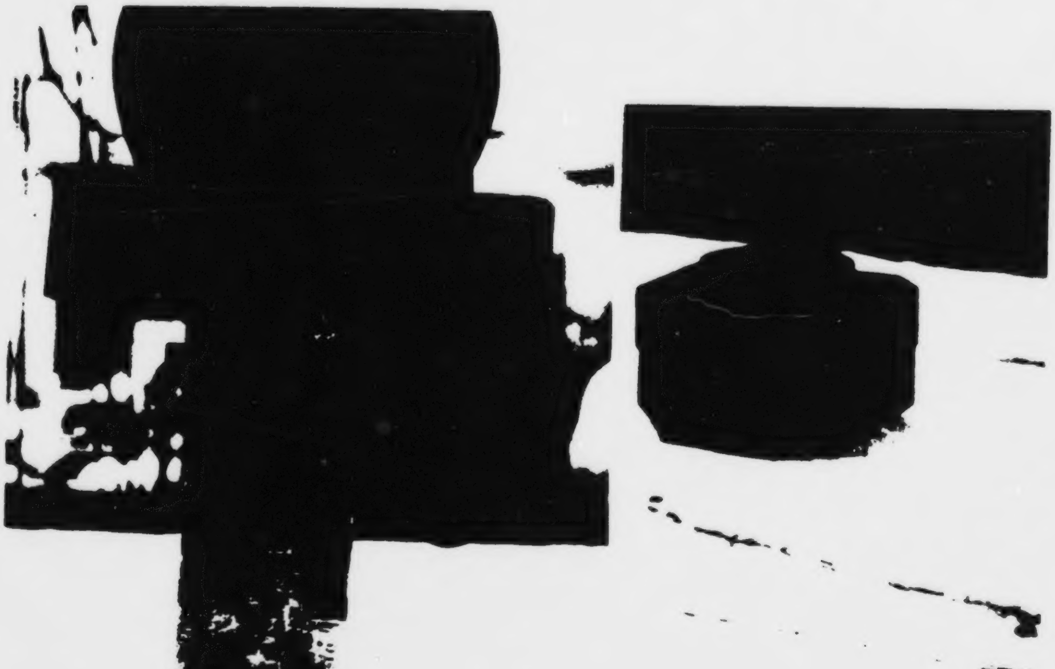

Fig. 56: Some Problems with Load Transfer Elements

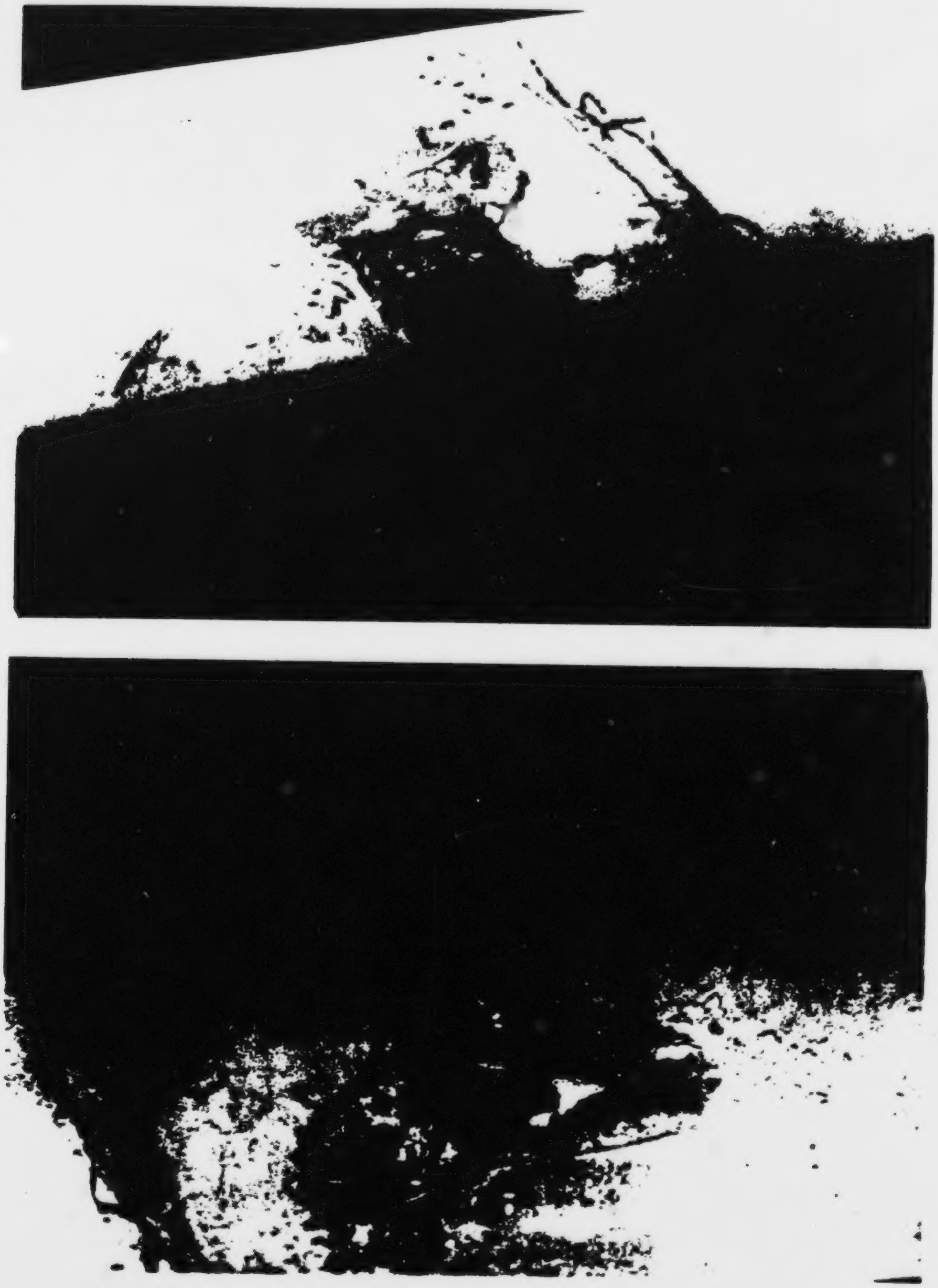

Fig. 57: Punching of Concrete under the Heaviest Concentrated Load

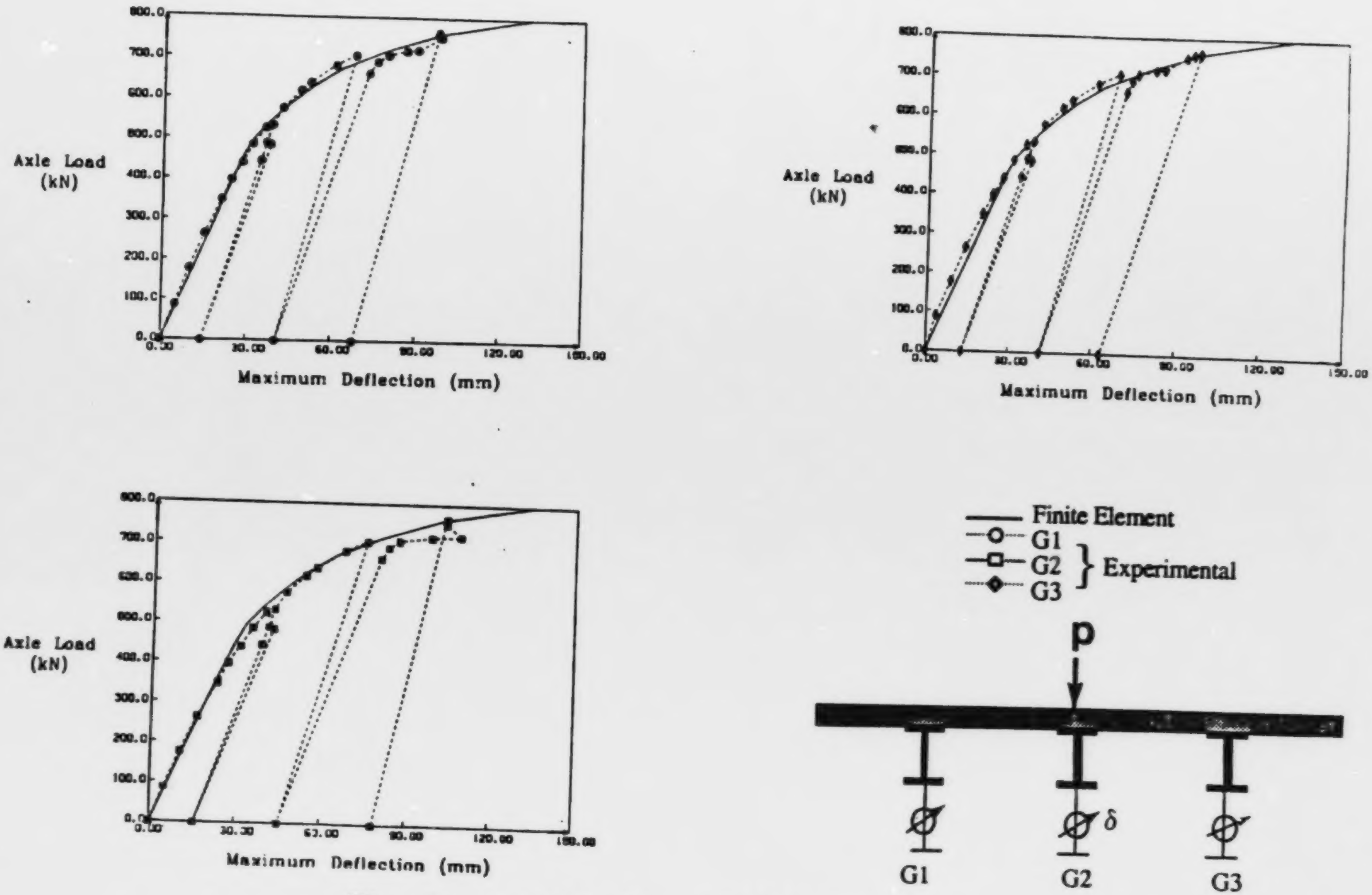

Fig. 58: Load-Maximum Deflection Curves of Bridge Girders

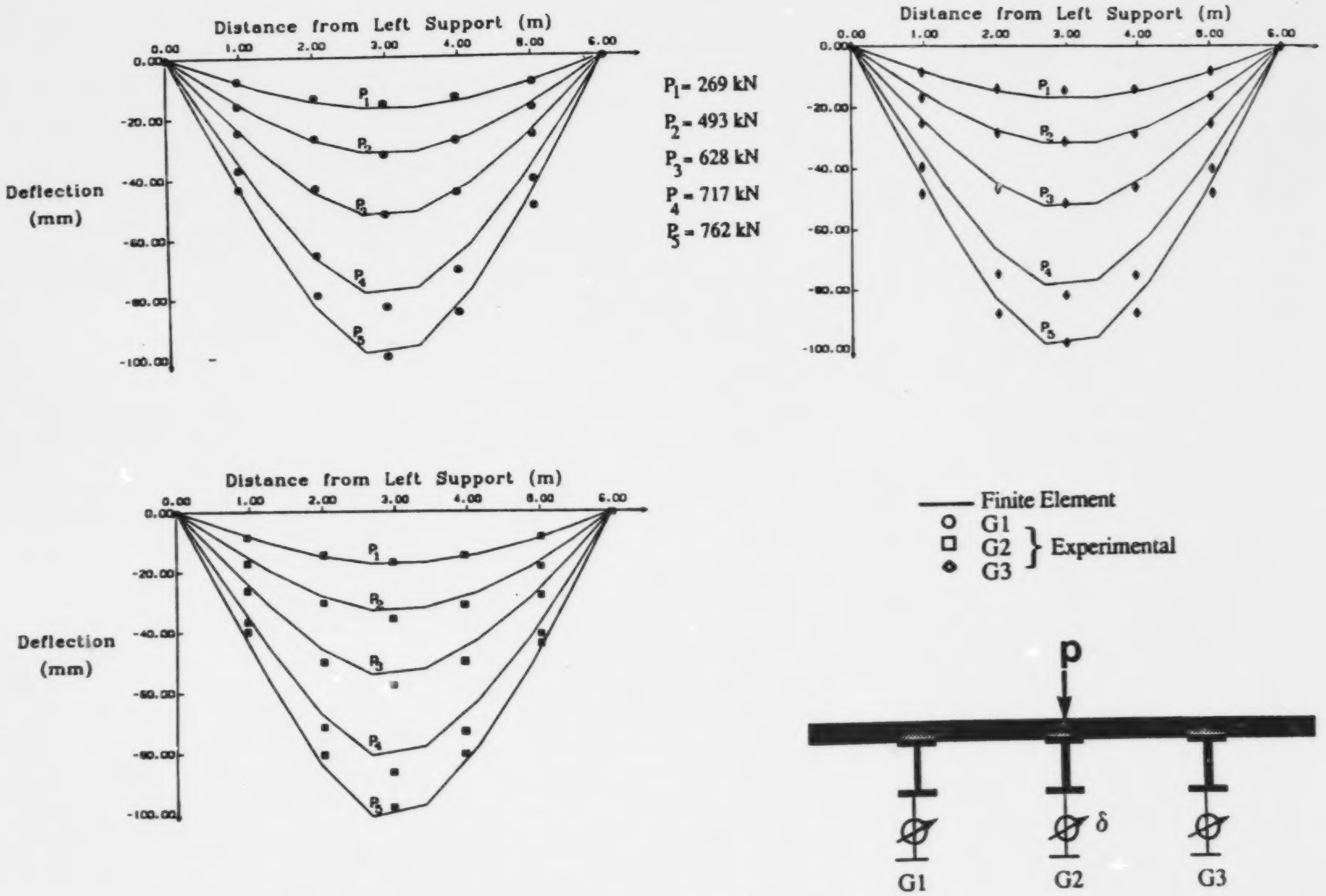

Fig. 59: Deflection Curves of Bridge Girders at Various Stages of Loading

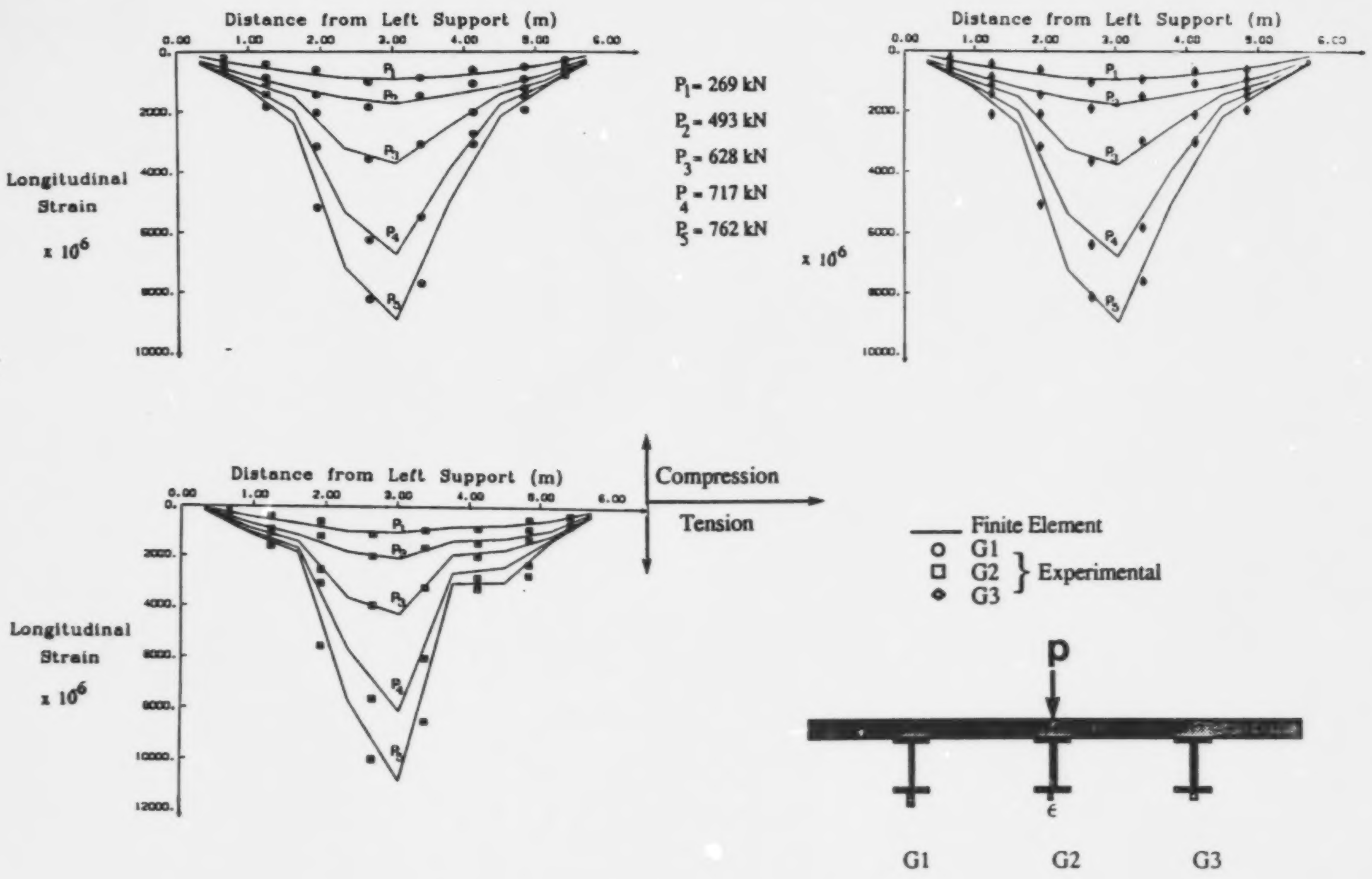

Fig. 60: Variation of Strain along the Bottom Flange of Bridge Girders

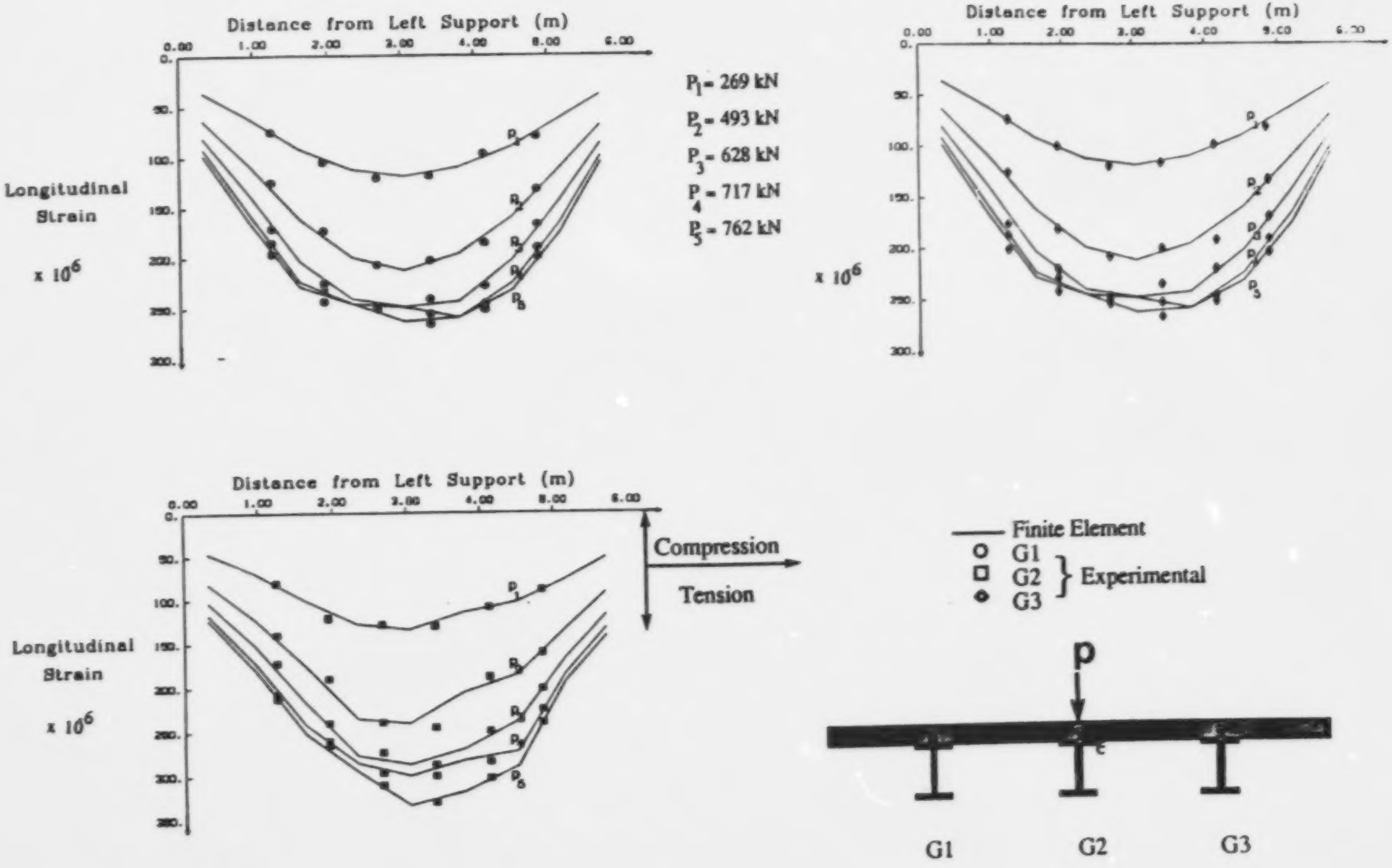

Fig. 61: Variation of Strain along the Top Flange of Bridge Girders

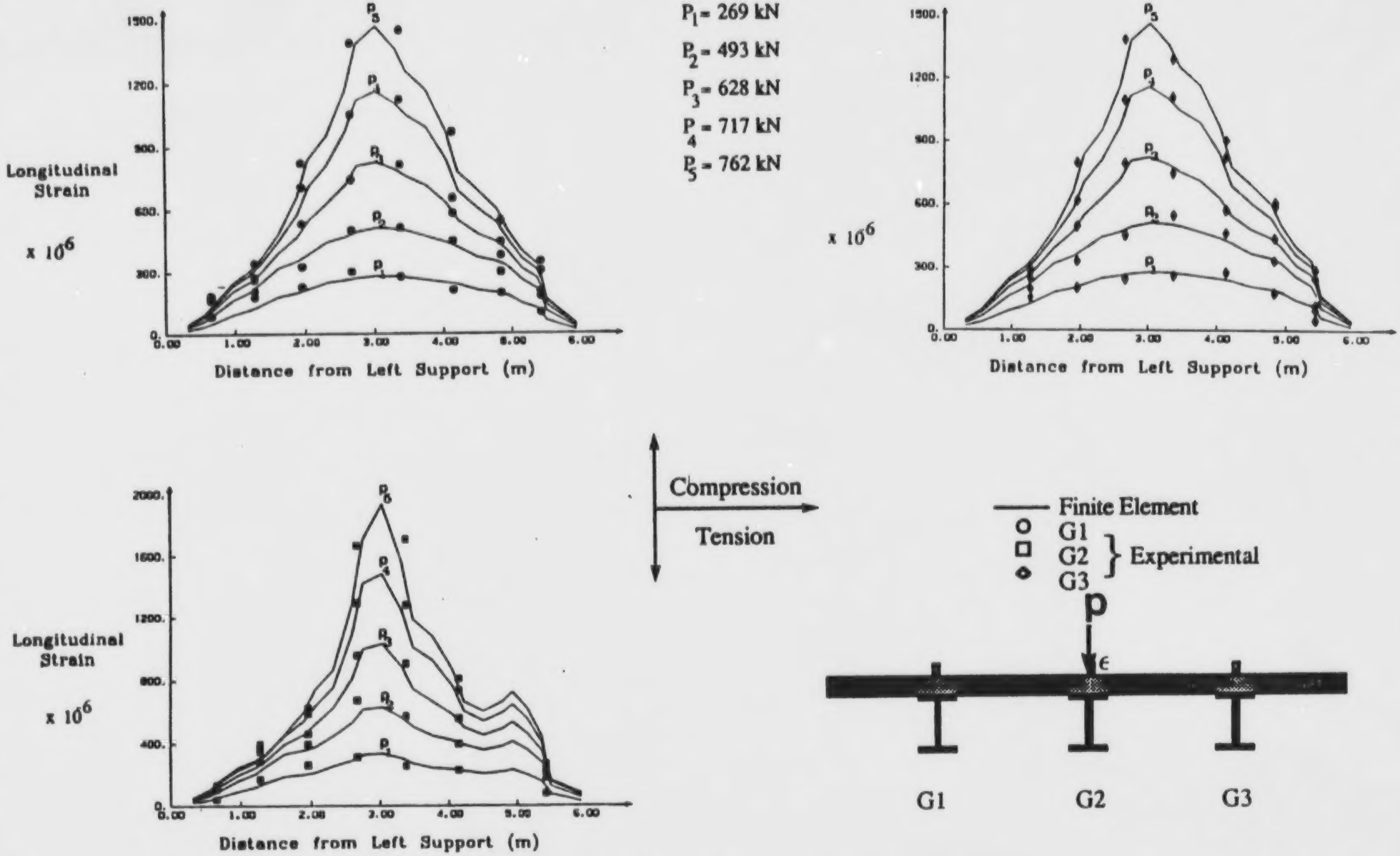

Fig. 62: Variation of Longitudinal Strain on the Top Surface of the Concrete Slab

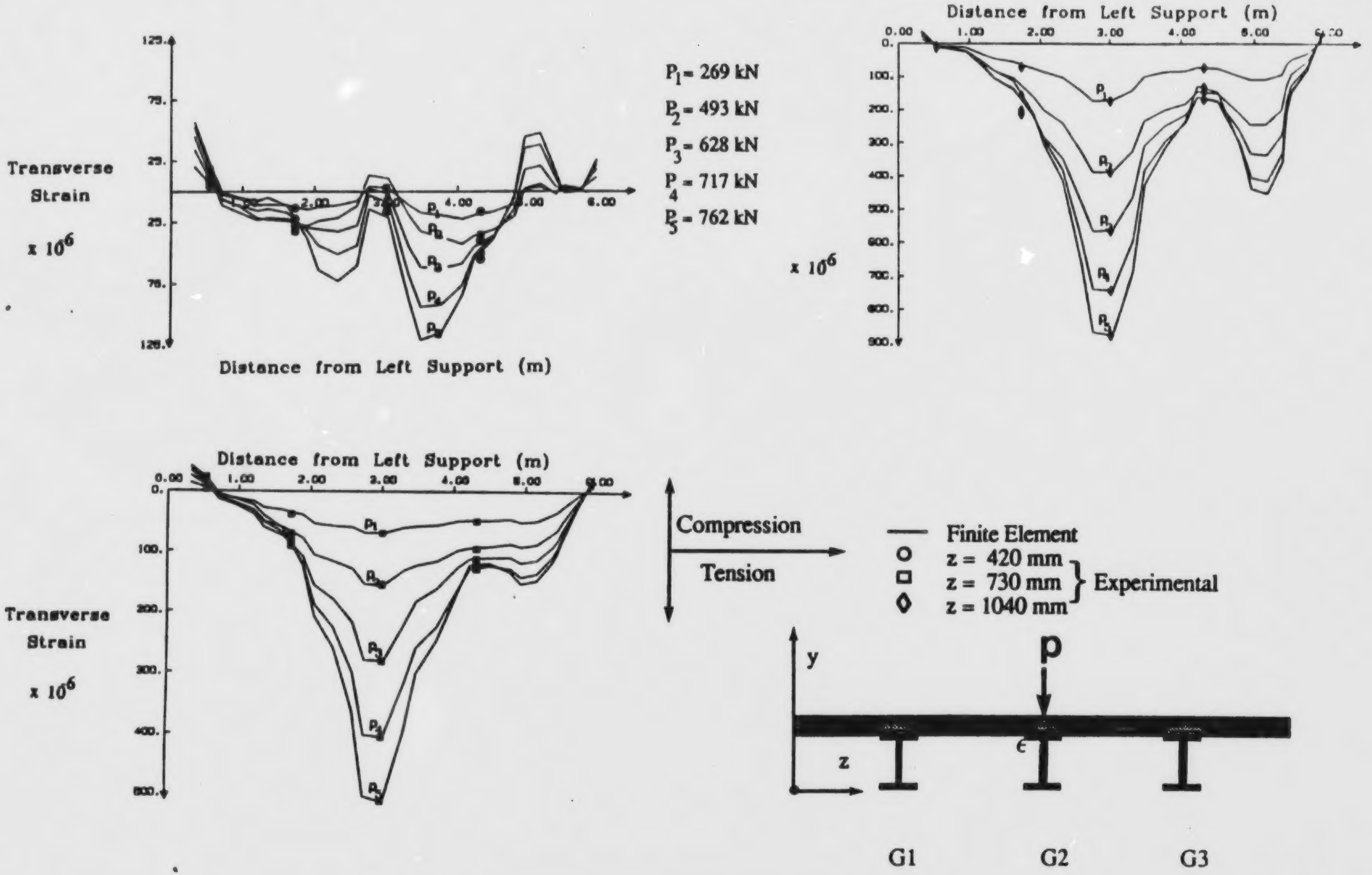

Fig. 63: Variation of Strain on the Bottom Transverse Steel Reinforcement Layer

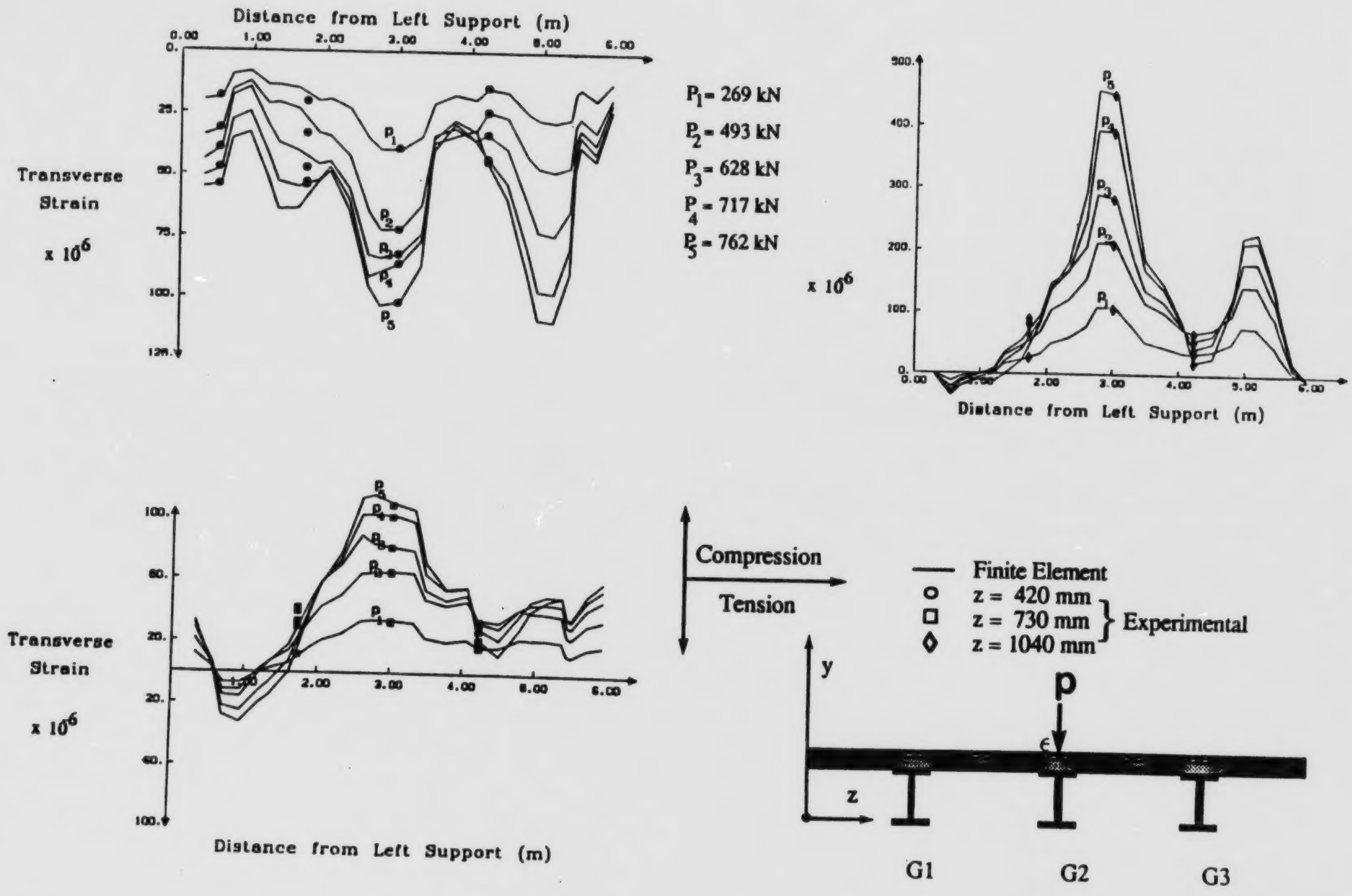

Fig. 64: Variation of Strain on the Top Transverse Steel Reinforcement Layer

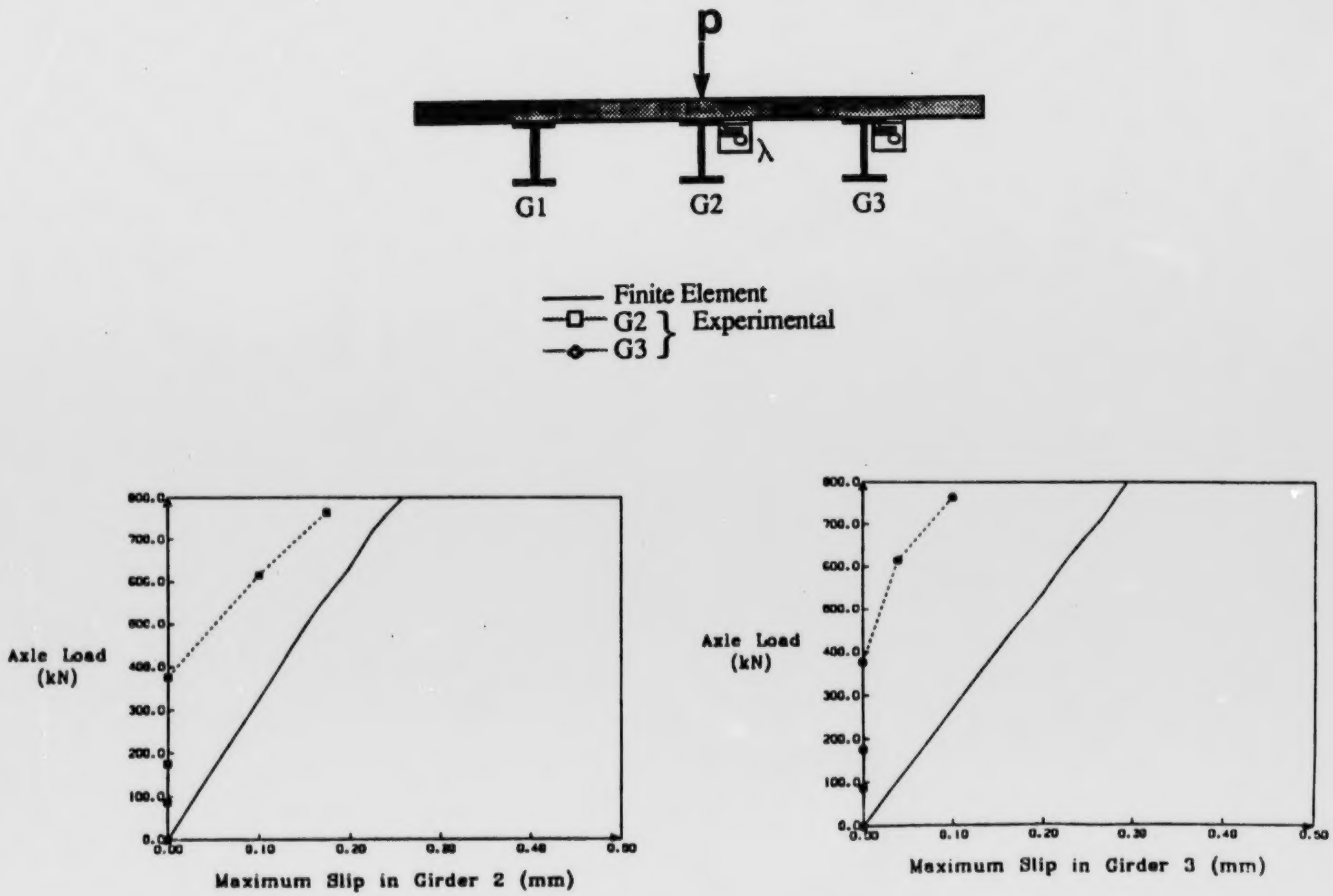

Fig. 65: Slip at Slab-Girder Interface at 500 mm from Right Support

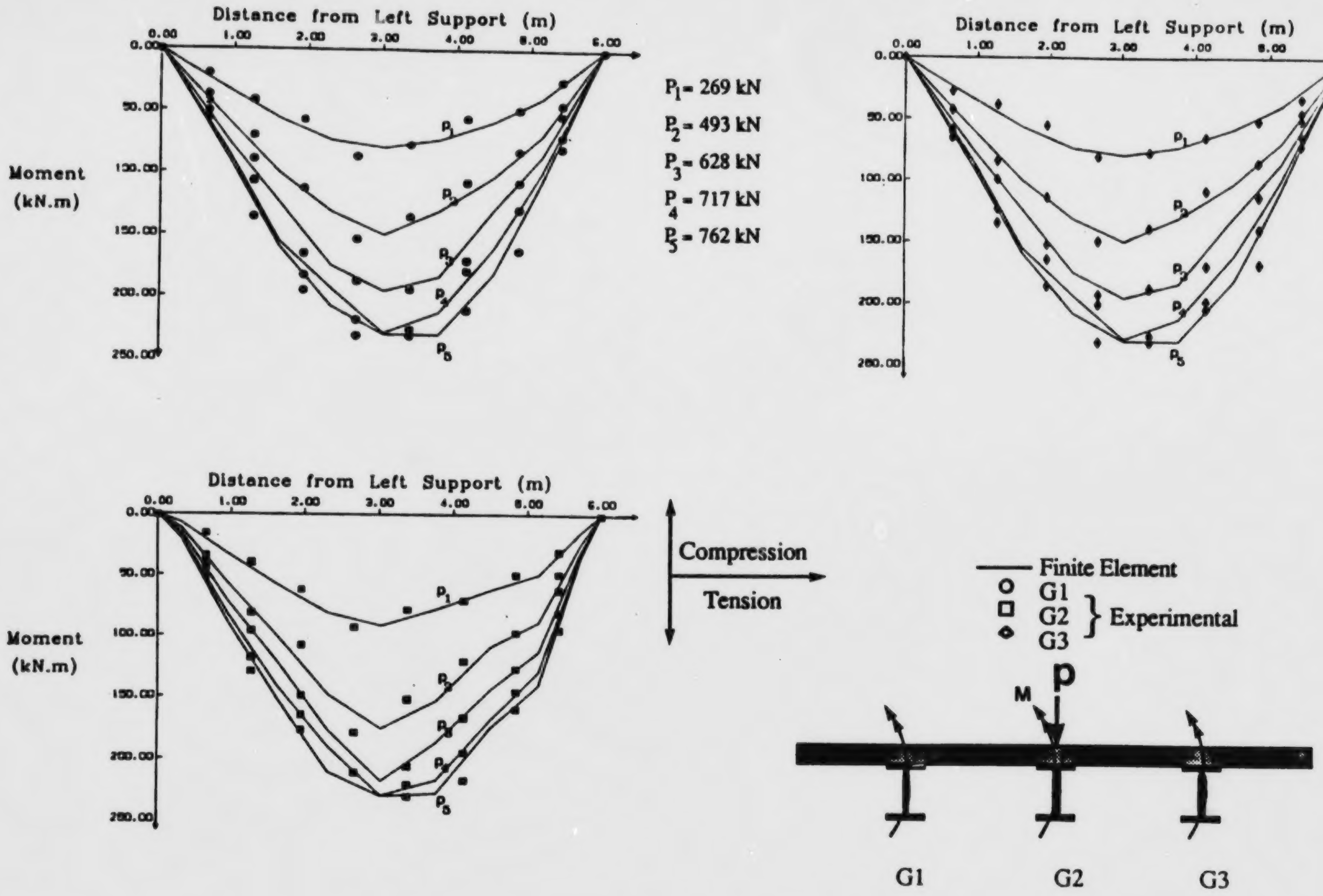

Fig. 66: Longitudinal Moment Variation in the Bridge Girders

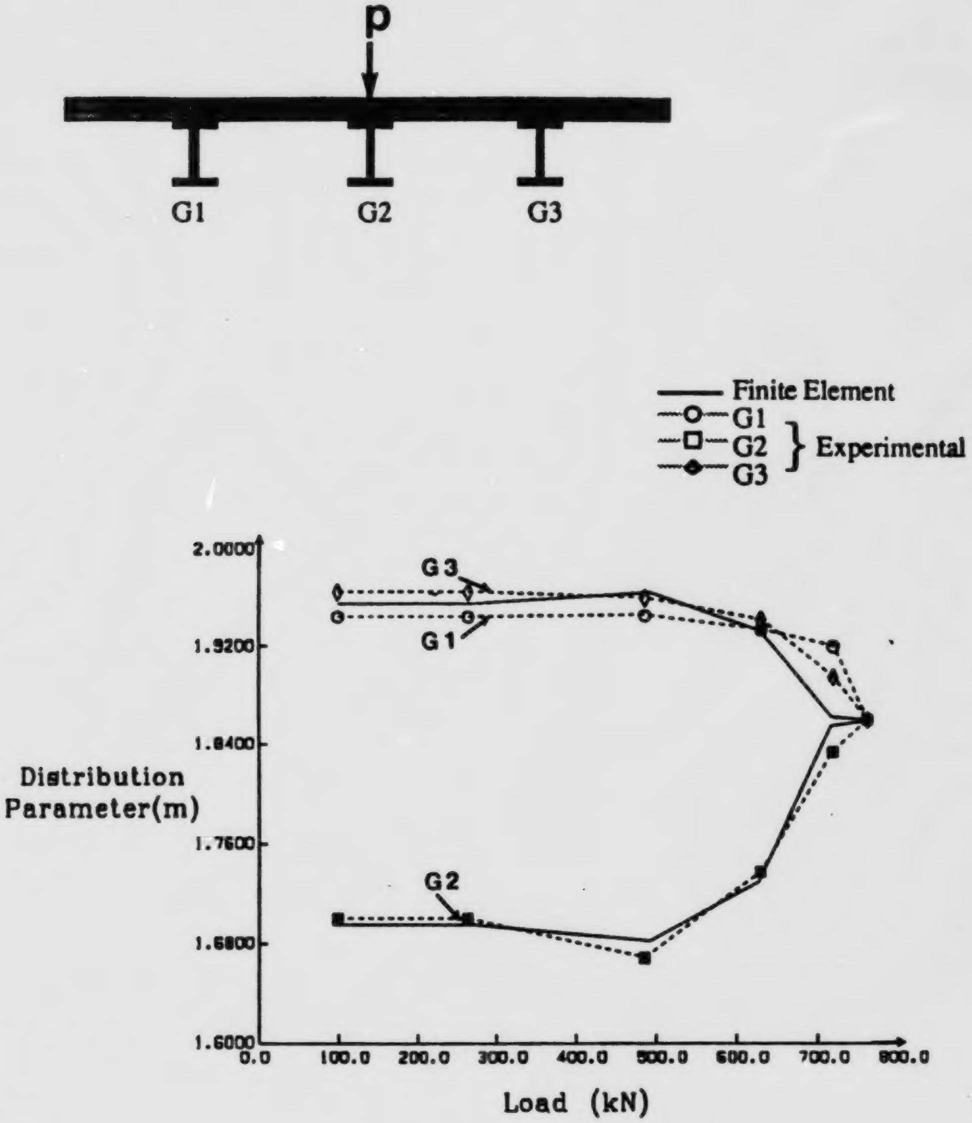

Fig. 67: Variation of the Girders Distribution Parameter with Increased Loading

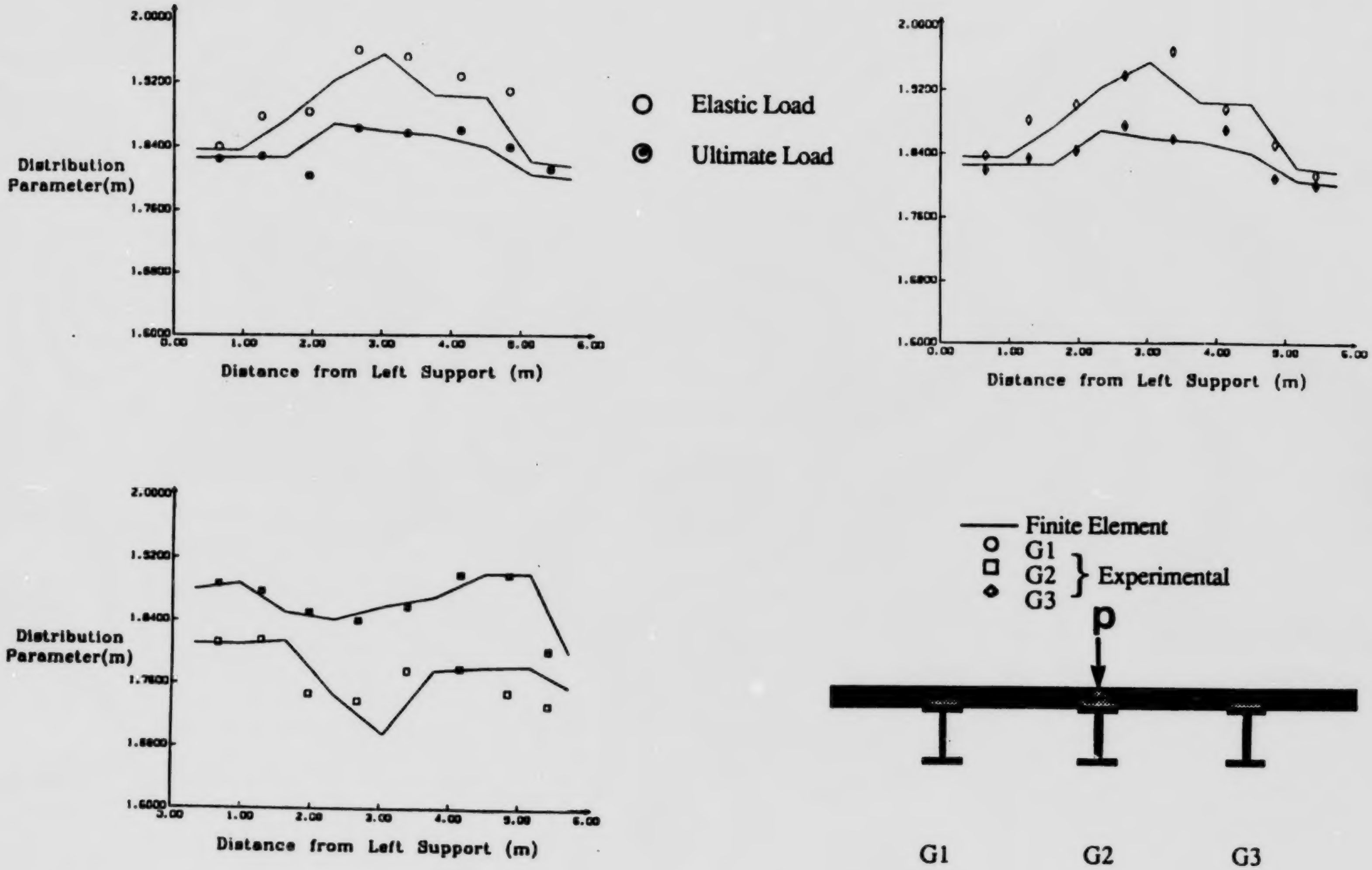

Fig. 68: Variation of Distribution Parameter along the Bridge Girders

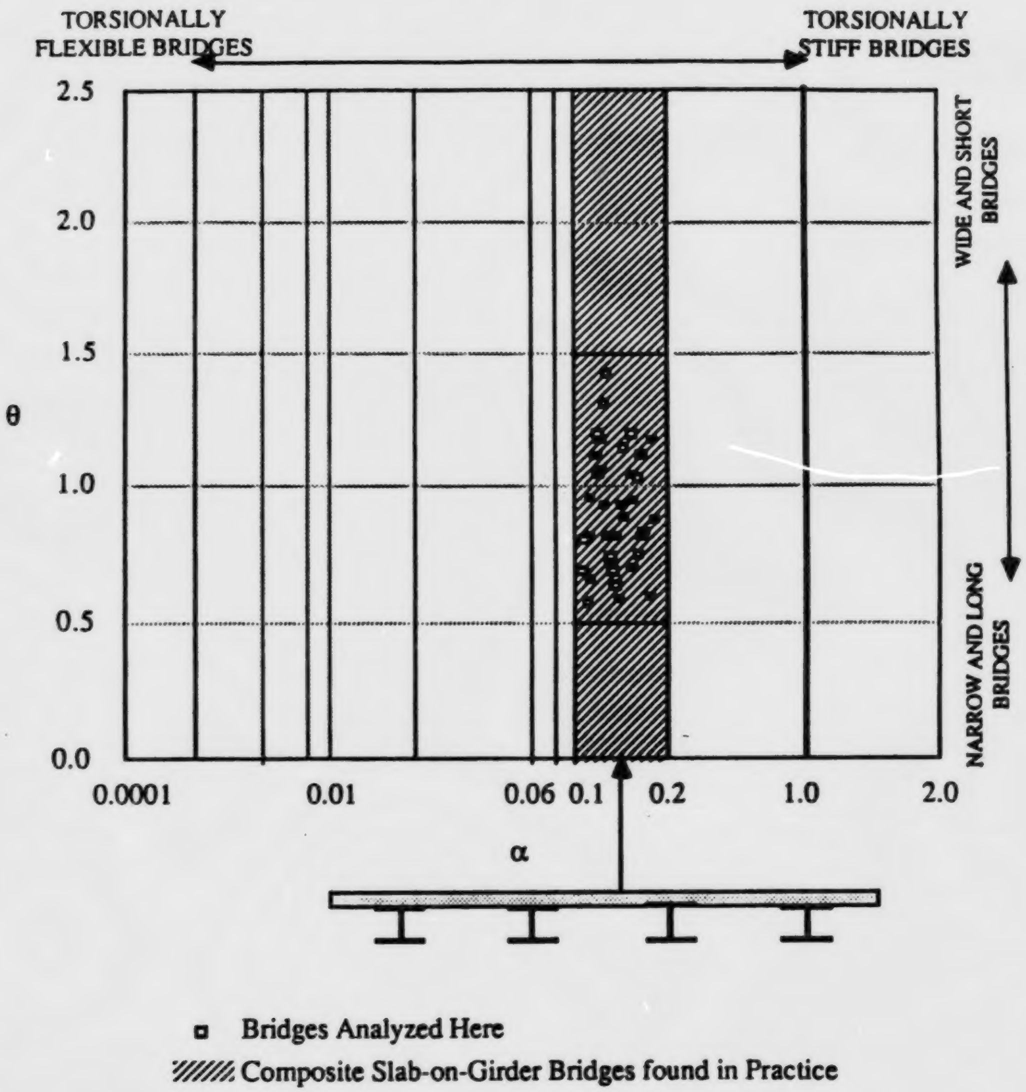

Fig. 69: The α–θ Plane Showing the Bridges Analyzed in this Study

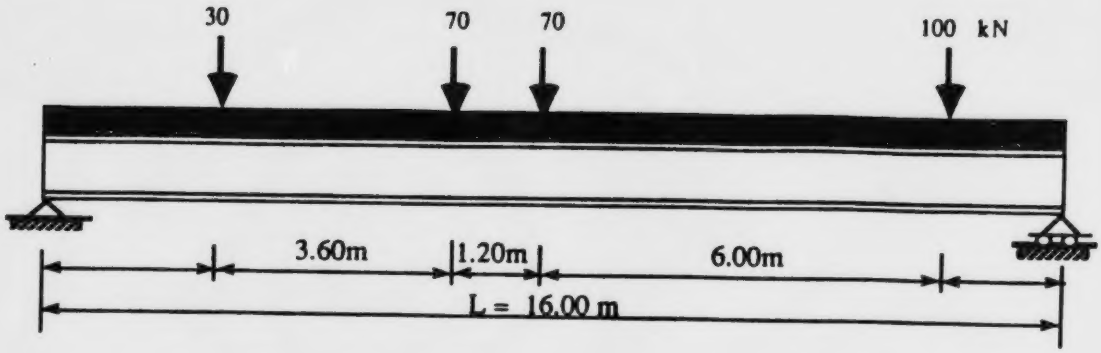
30
70
70
100 kN
3.60m
1.20m
6.00m
L = 16.00 m

(I) POSITION 1 (Produces Maximum Moment)

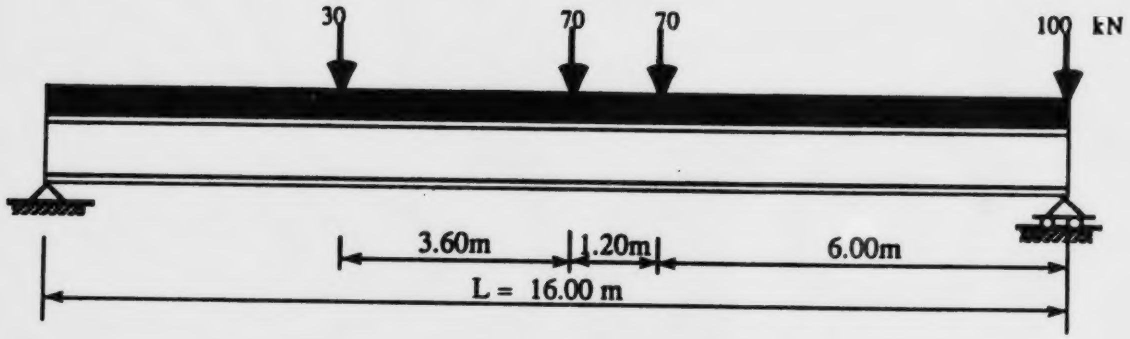
30
70
70
100 kN
3.60m
1.20m
6.00m
L = 16.00 m

(II) POSITION 2 (Produces Maximum Shear)

Fig. 70: Longitudinal Truck Positions Considered

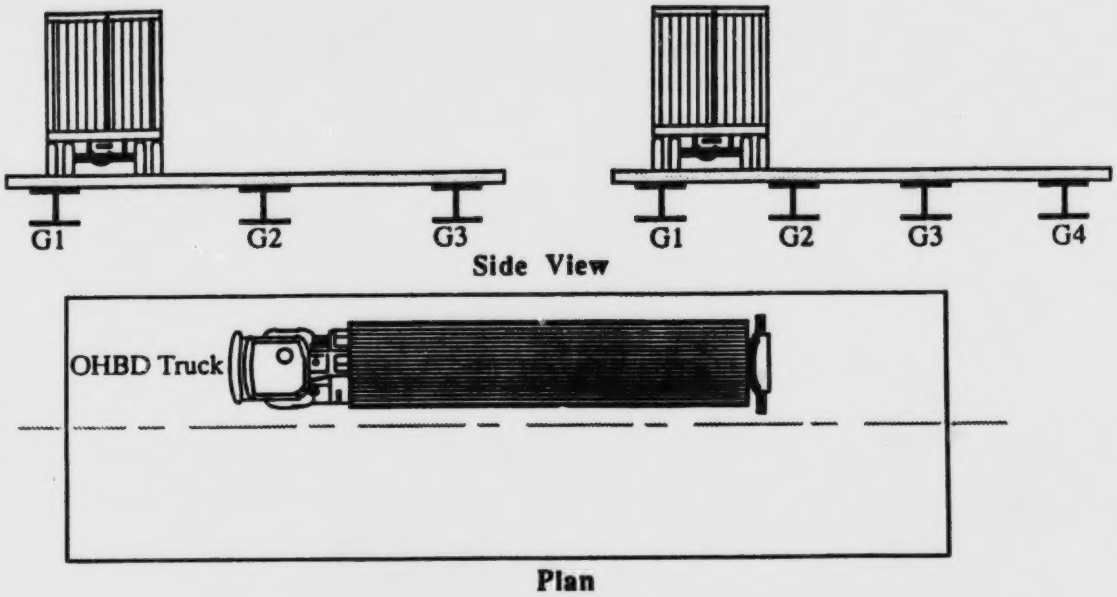
G1
G2
G3
G1
G2
G3
G4
Side View
OHBD Truck
Plan

(I) One Lane Loaded

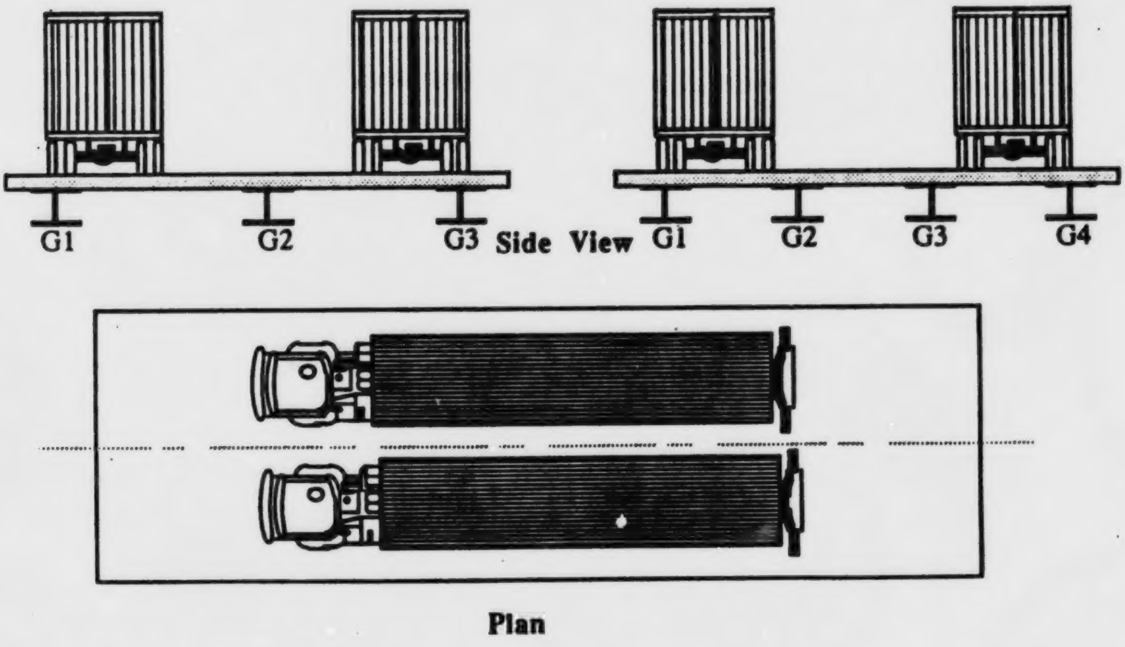
G1
G2
G3
Side View
G1
G2
G3
G4
Plan

(II) Two Lanes Loaded

Fig. 71: Transverse Truck Positions Considered

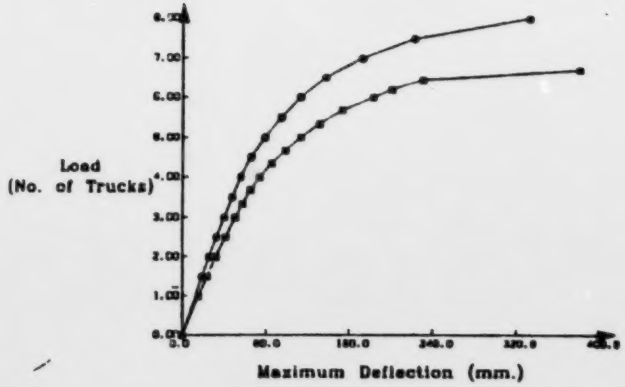

(i) Girder #1

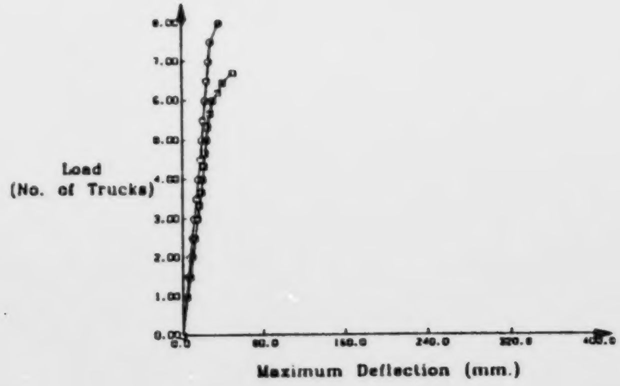

(iii) Girder #3

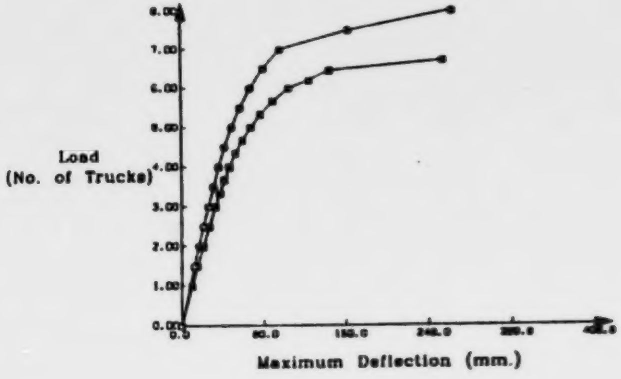

(ii) Girder #2

□ Position 1
○ Position 2

Fig. 72: Effect of Longitudinal Truck Position on Load-Maximum Deflection of Bridge LP1

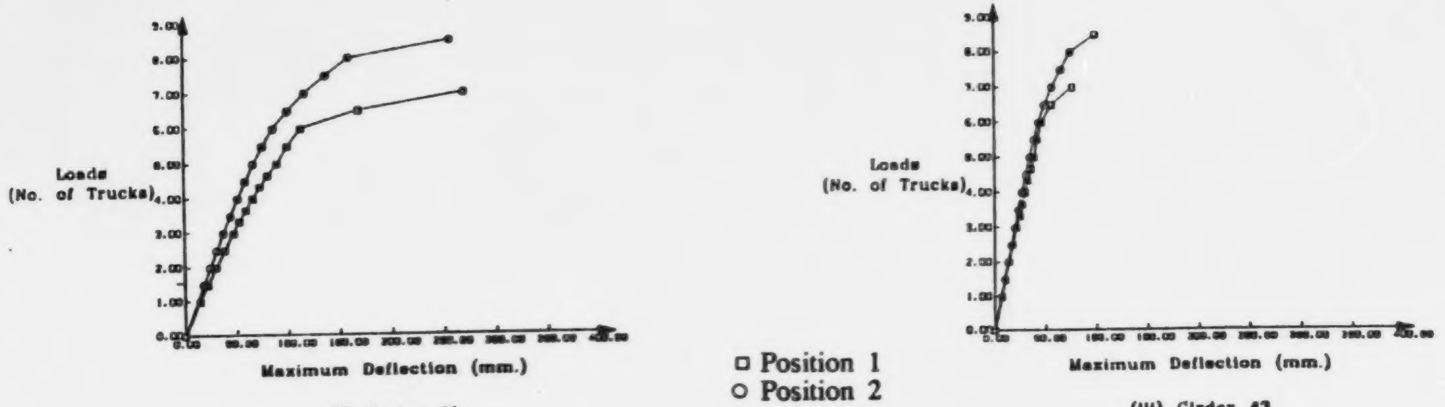

(i) Girder #1

(iii) Girder #3

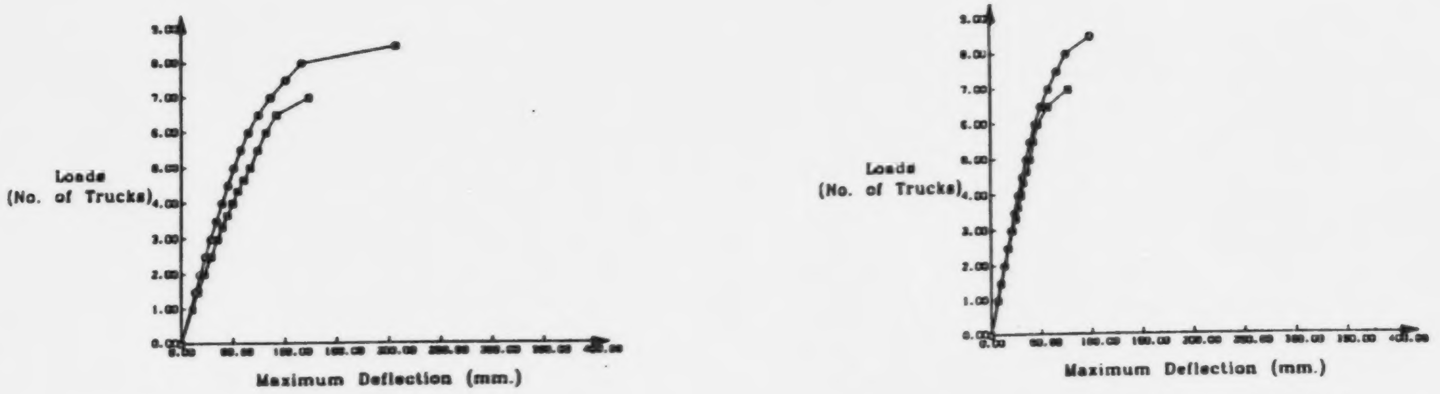

(ii) Girder #2

(iv) Girder #4

Fig. 73: Effect of Longitudinal Truck Position on Load-Maximum Deflection of Bridge LP2

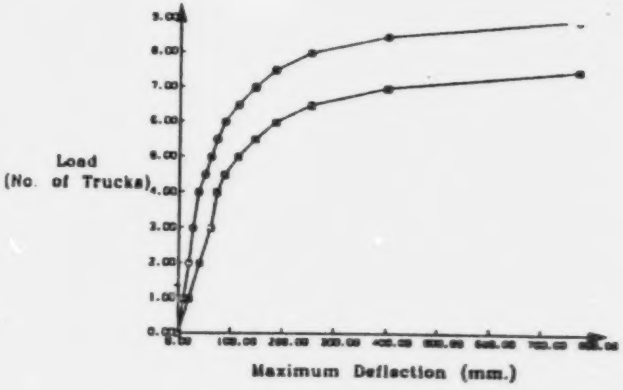

(i) Girder #1 &#3

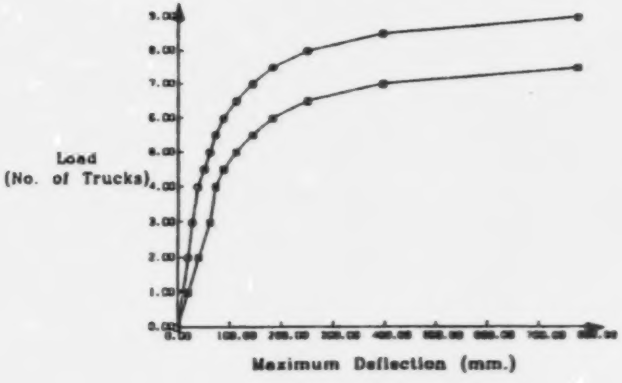

(ii) Girder #2

(I)Three Girder System (LP1)

◻ Position 1
○ Position 2

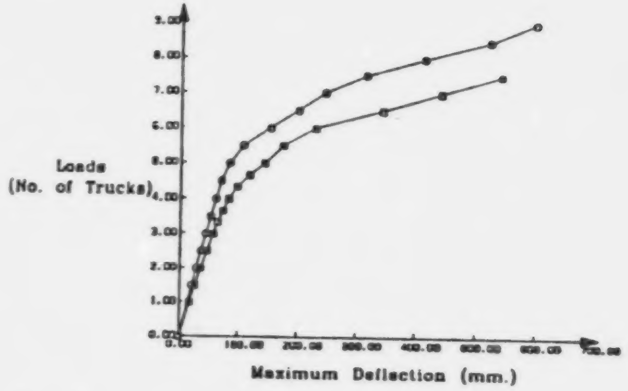

(i) Girder #1 & #4

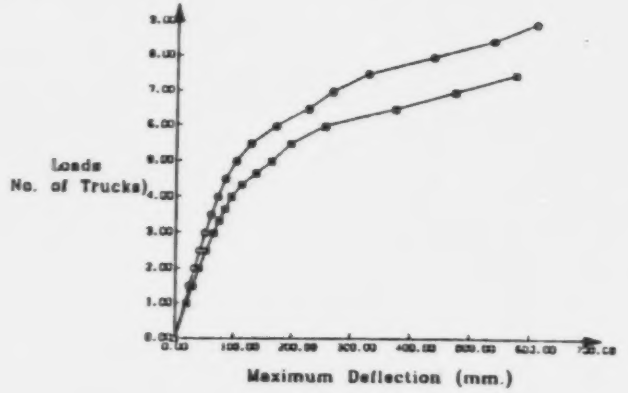

(ii) Girder #2 & #3

(II) F

Fig. 74: Effect of Longitudinal Truck Position on Load-Maximum Deflection of Bridges LP1 and LP2

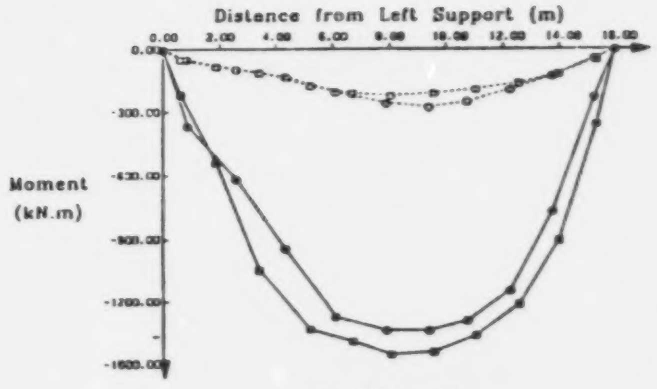

(i) Girder #1

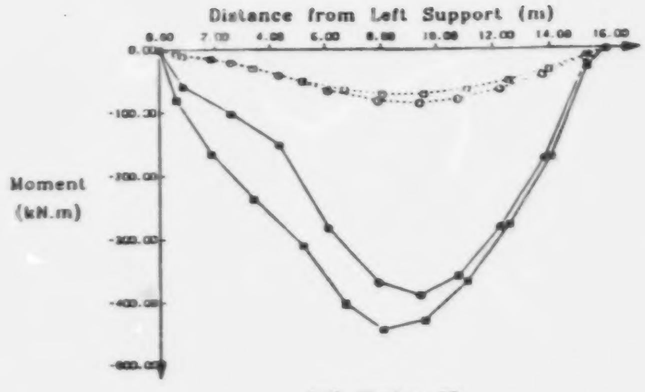

(iii) Girder #3

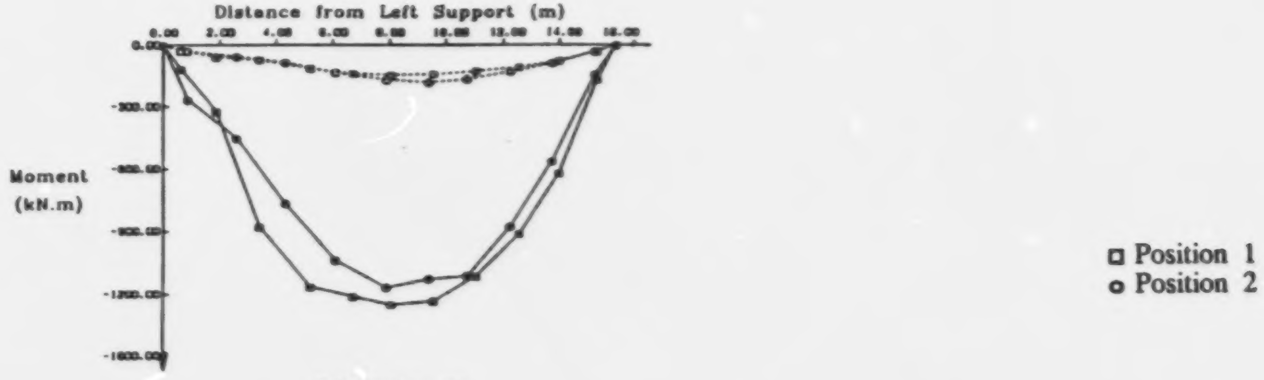

(ii) Girder #2

Fig. 75: Effect of Longitudinal Truck Position on Moment Distribution in Bridge LP1

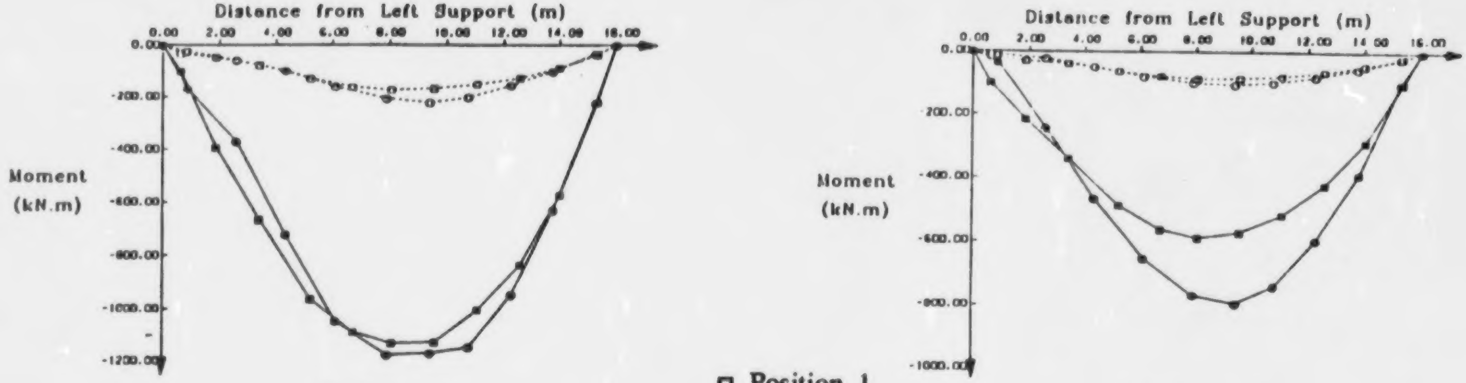

(i) Girder #1

□ Position 1
○ Position 2

(iii) Girder #3

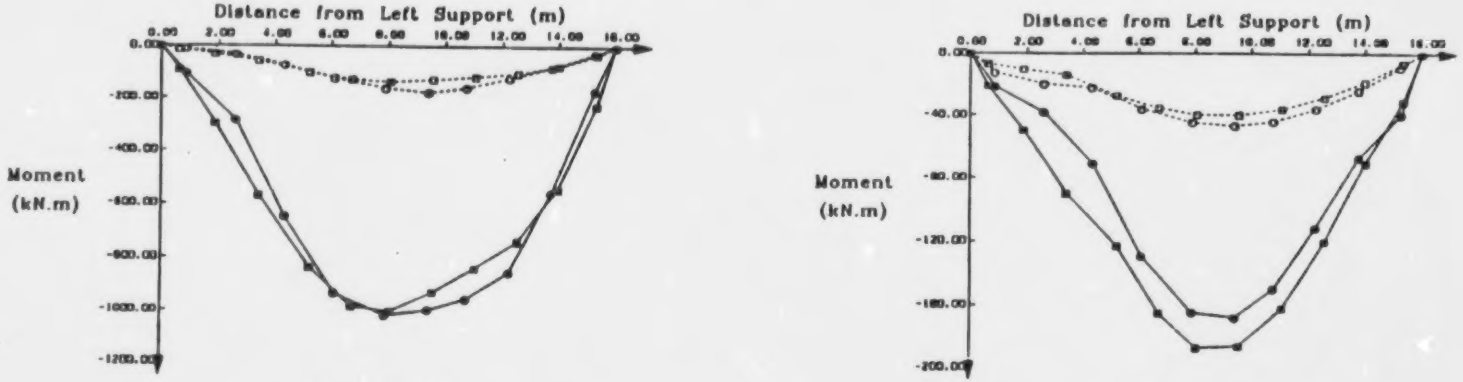

(ii) Girder #2

(iv) Girder #4

Fig. 76: Effect of Longitudinal Truck Position on Moment Distribution in Bridge LP2

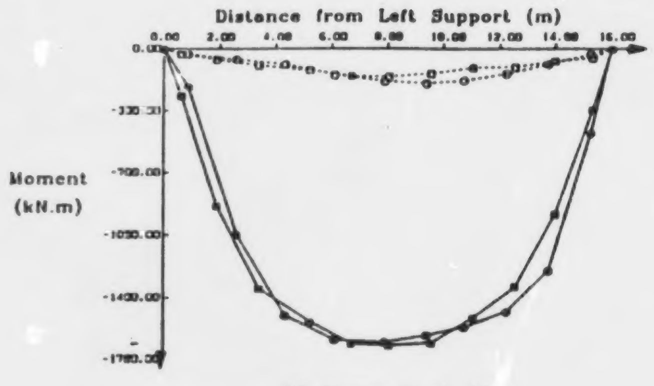

(i) Girder #1 & #3

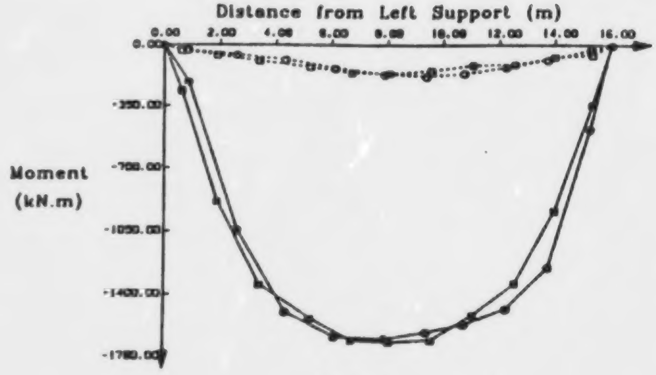

(ii) Girder #2

(I)Three Girder System (LP1)

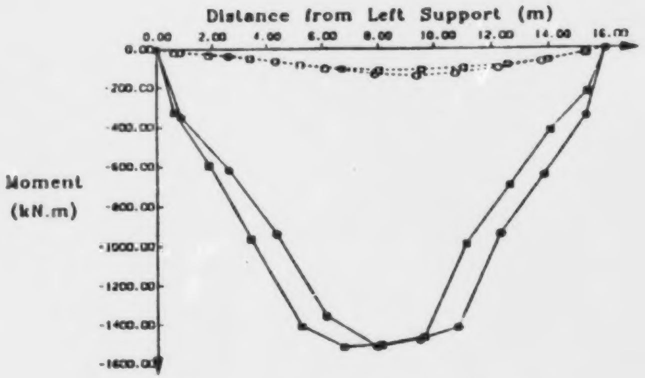

(i) Girder #1 & #4

□ Position 1
○ Position 2

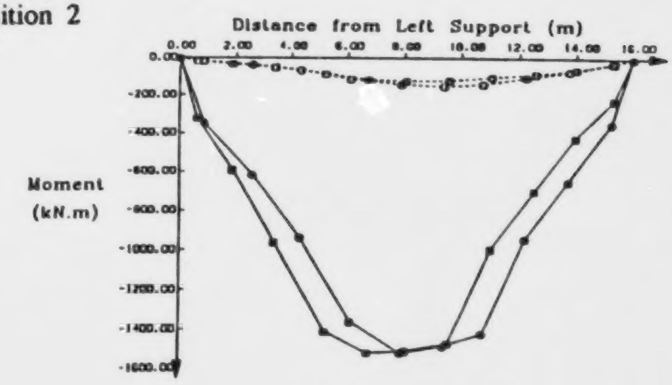

(ii) Girder #2 & #3

(II) Four Girder System (LP2)

Fig. 77: Effect of Longitudinal Truck Position on Moment Distribution in Bridges LP1 and LP2

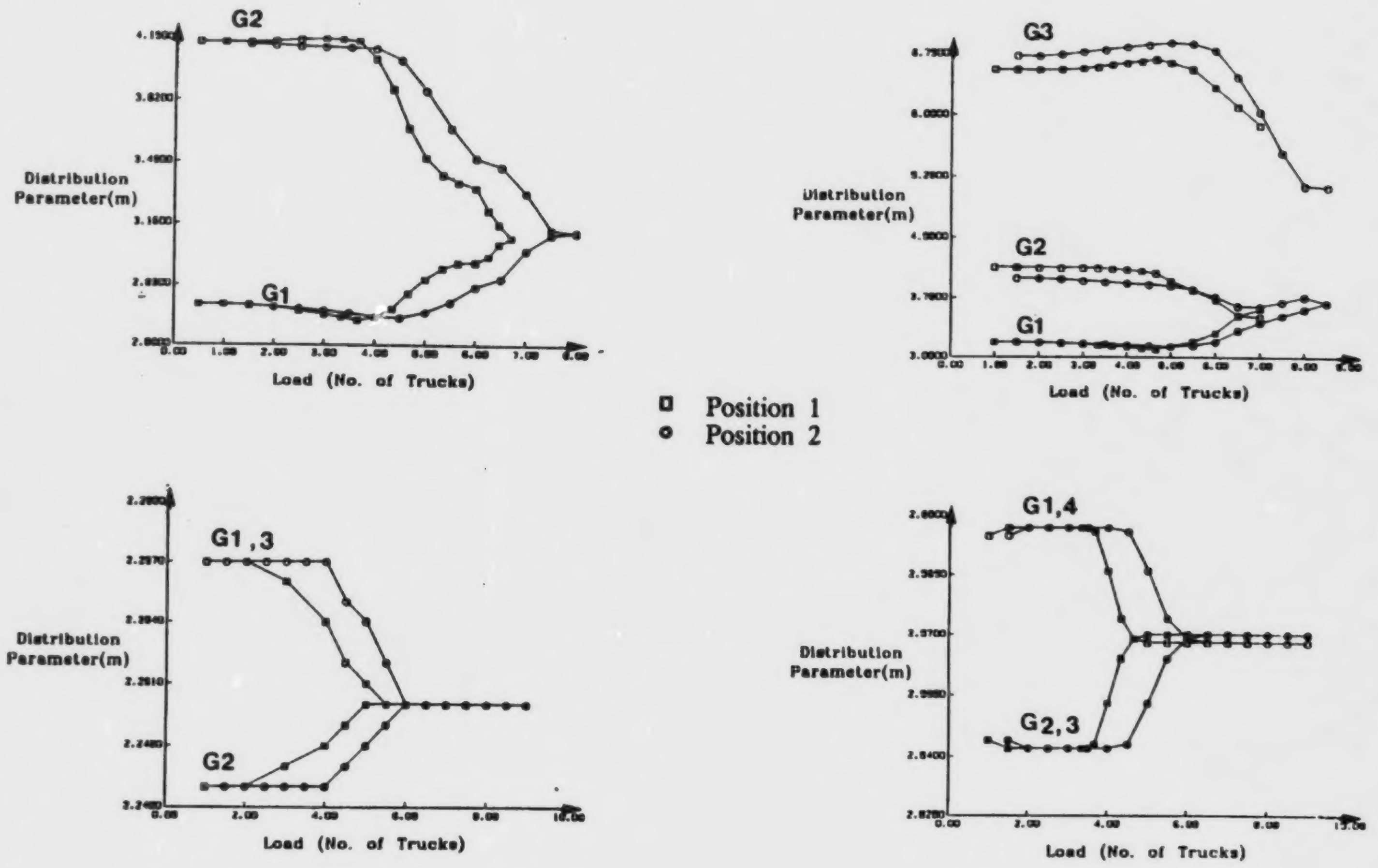

(I)Three Girder System (LP1)

(II) Four Girder System (LP2)

Fig. 78: Effect of Longitudinal Truck Position on Distribution Parameter D_d

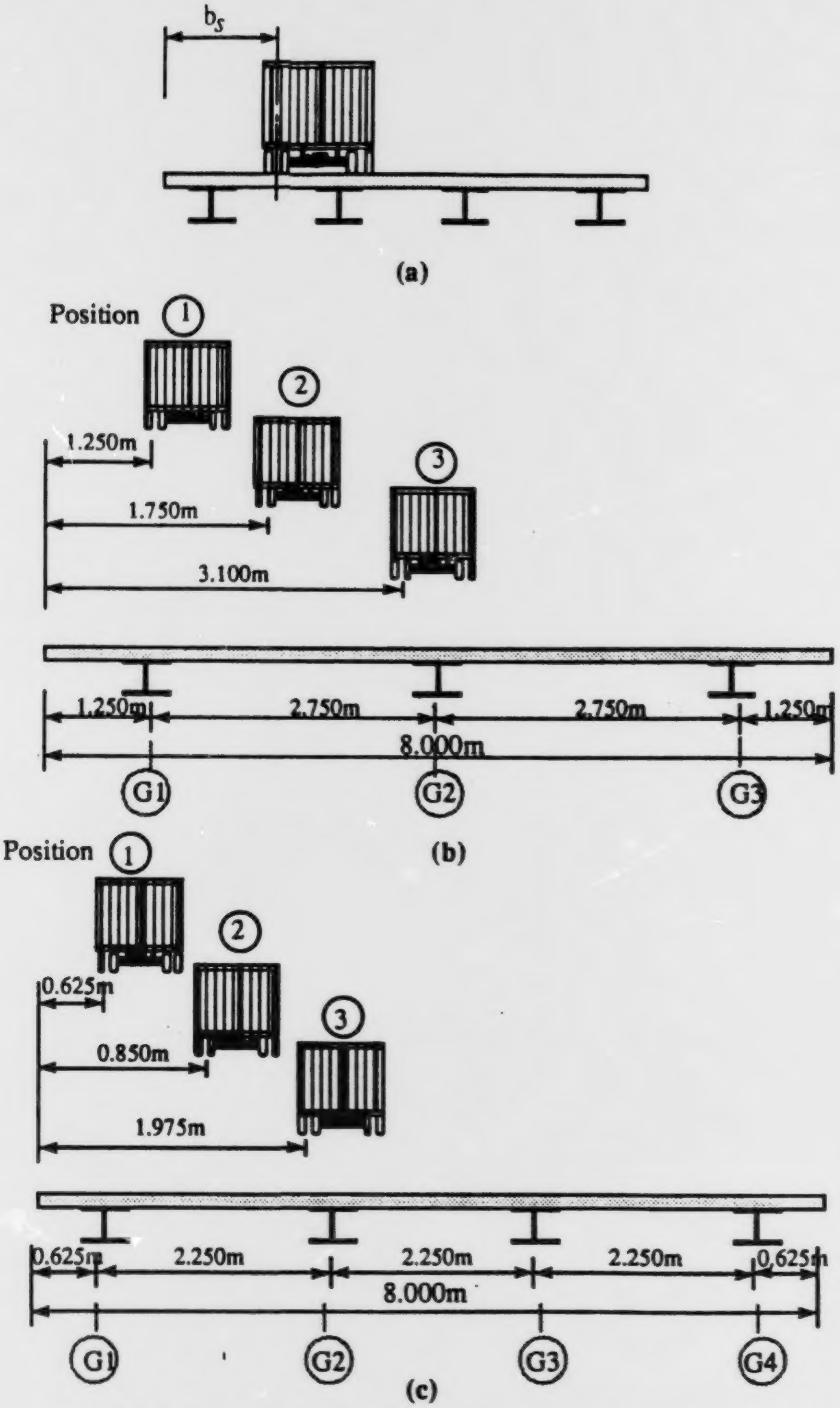

b_S
(a)
Position ①
②
③
1.250m
1.750m
3.100m
1.250m
2.750m
2.750m
1.250m
8.000m
G1
G2
G3
(b)
Position ①
②
③
0.625m
0.850m
1.975m
0.625m
2.250m
2.250m
2.250m
0.625m
8.000m
G1
G2
G3
G4
(c)

Fig. 79: Vehicle-Edge Distance
(a) Definition
(b) Distances Considered for Bridge LP1
(c) Distances Considered for Bridge LP2

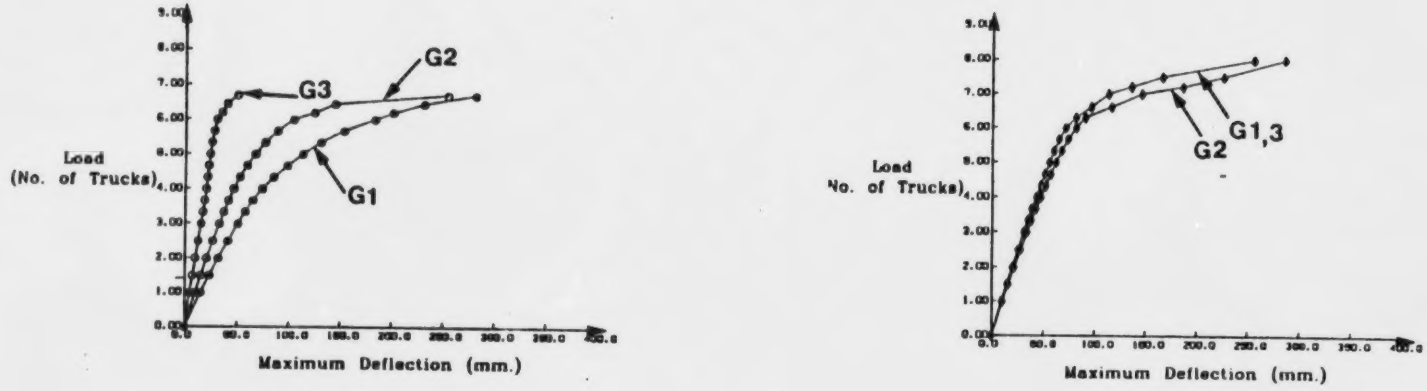

(a) Position #1

(c) Position #3

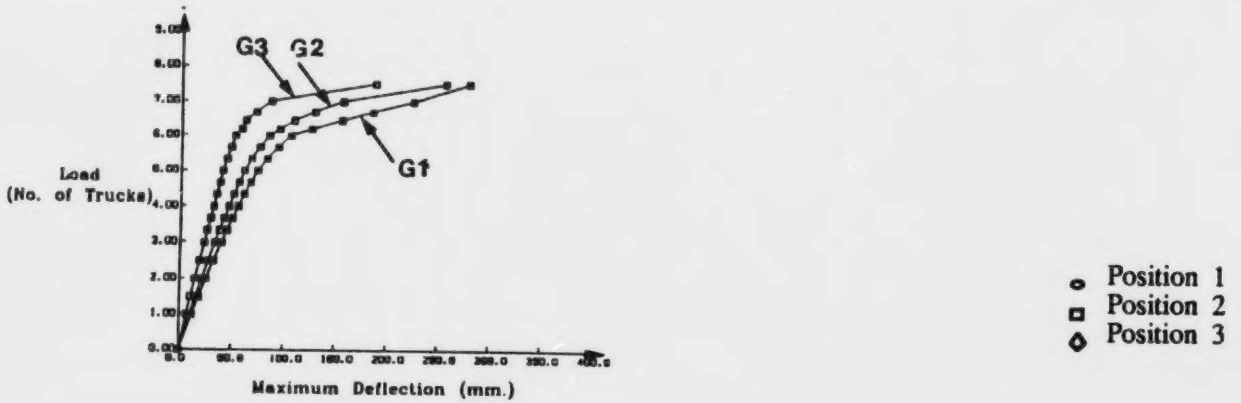

(b) Position #2

Fig. 80: Effect of Transverse Truck Position on Load-Maximum Deflection of Bridge LP1

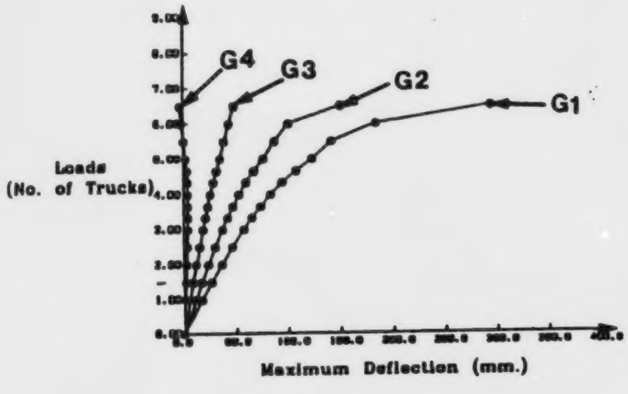

(a) Position #1

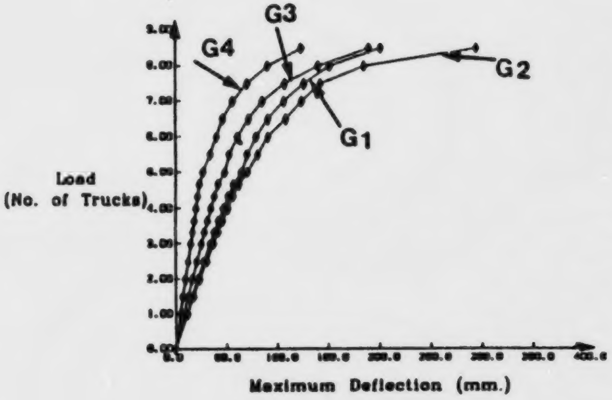

(c) Position #3

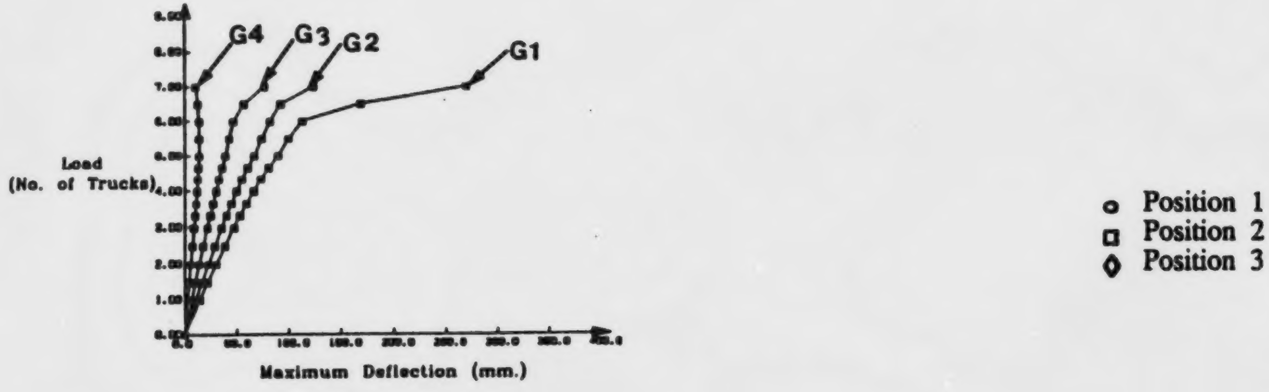

(b) Position #2

Fig. 81: Effect of Transverse Truck Position on Load-Maximum Deflection of Bridge LP2

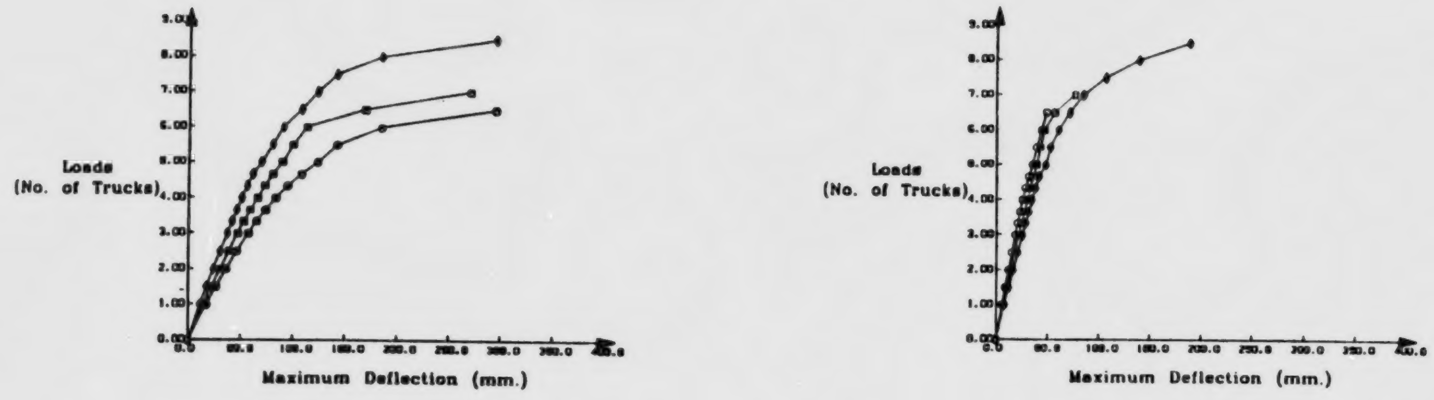

(i) Girder #1

(iii) Girder #3

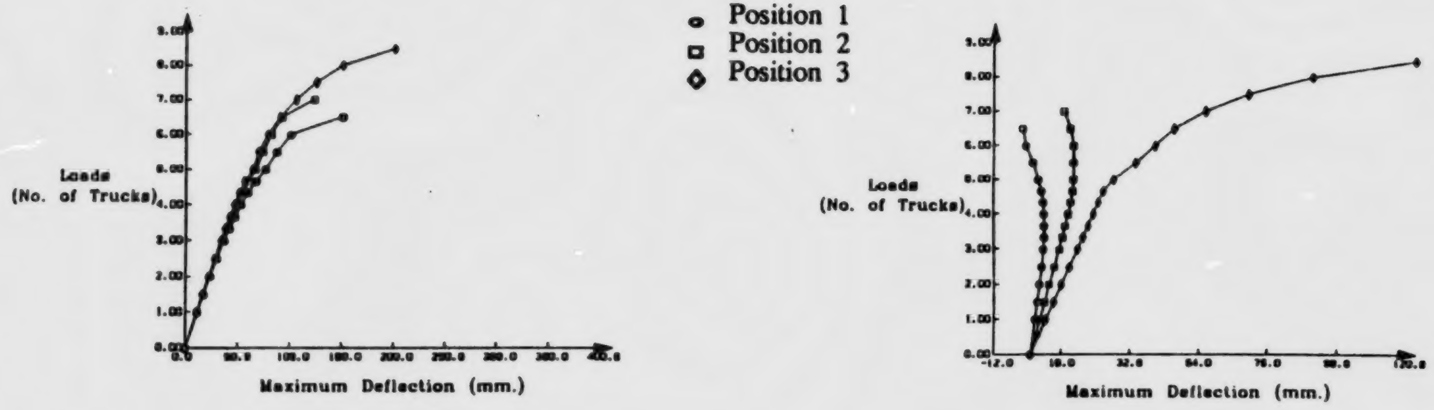

(ii) Girder #2

(iv) Girder #4

Fig. 82: Effect of Transverse Truck Position on Deflection Distribution among the Girders of Bridge LP2

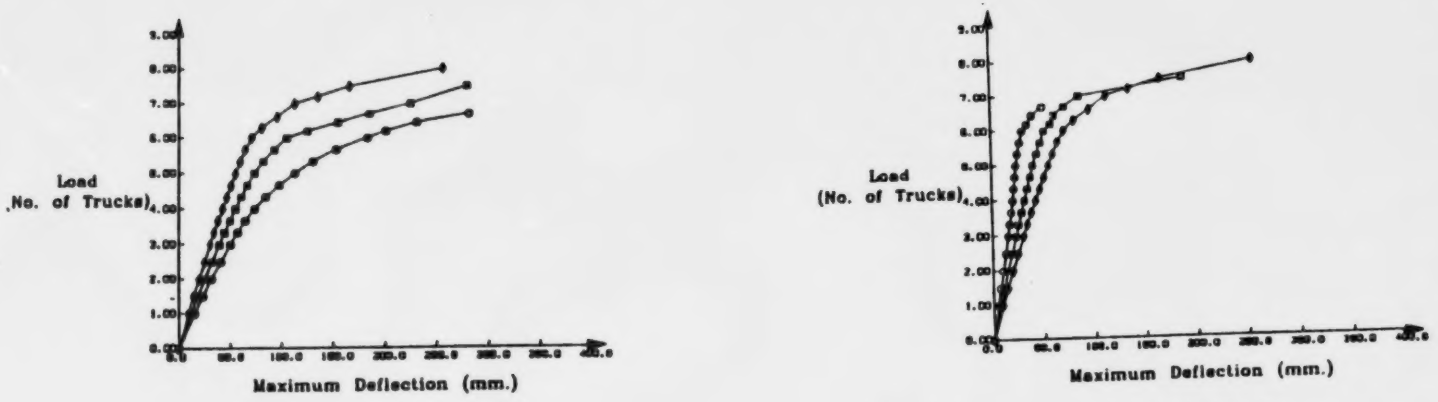

(i) Girder #1

(iii) Girder #3

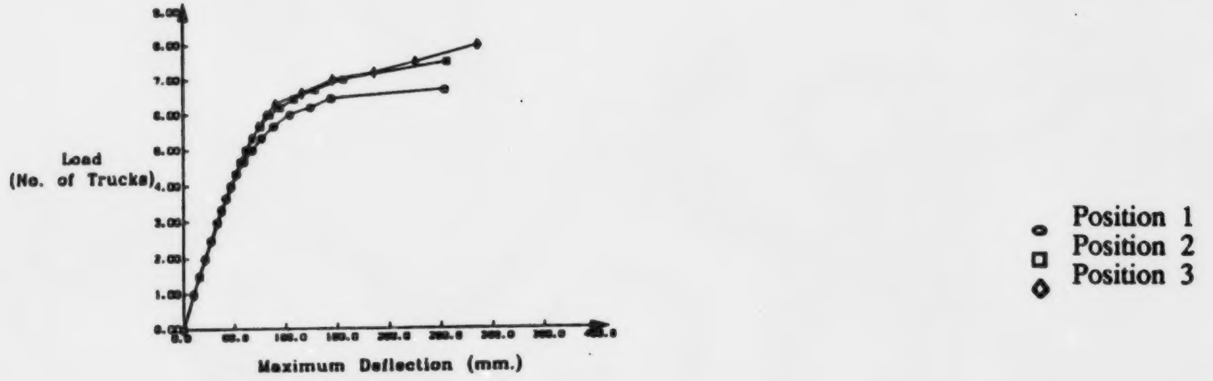

(ii) Girder #2

Fig. 83: Effect of Transverse Truck Position on Deflection Distribution among the Girders of Bridge LP1

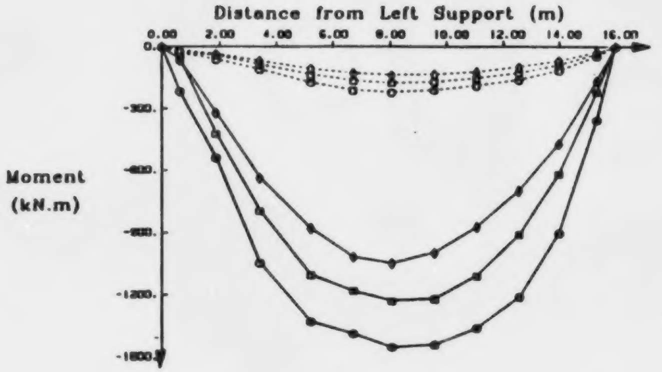

(i) Girder #1

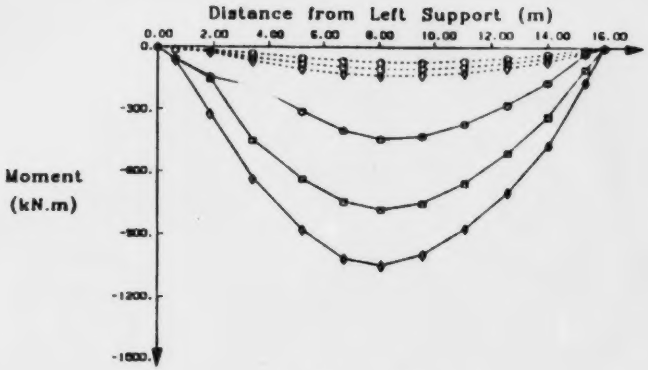

(iii) Girder #3

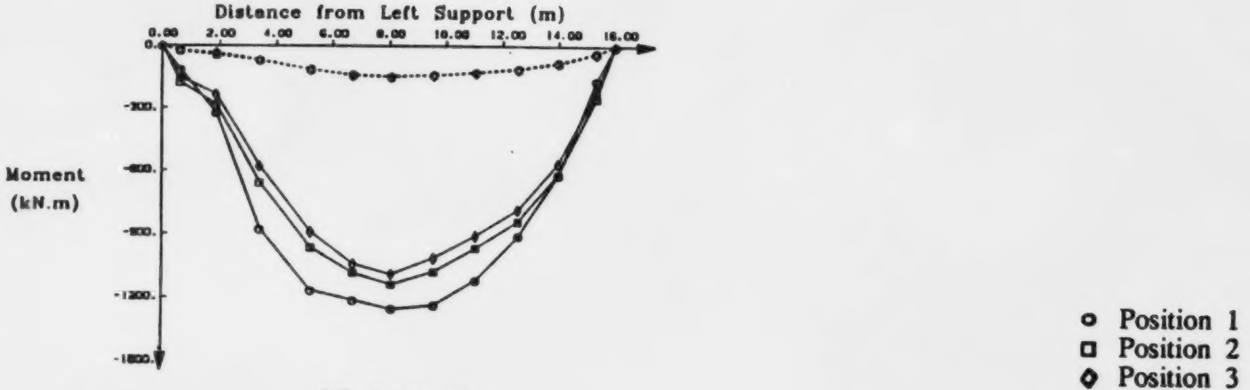

(ii) Girder #2

Fig. 84: Effect of Transverse Truck Position on Moment Distribution in Bridge LP1

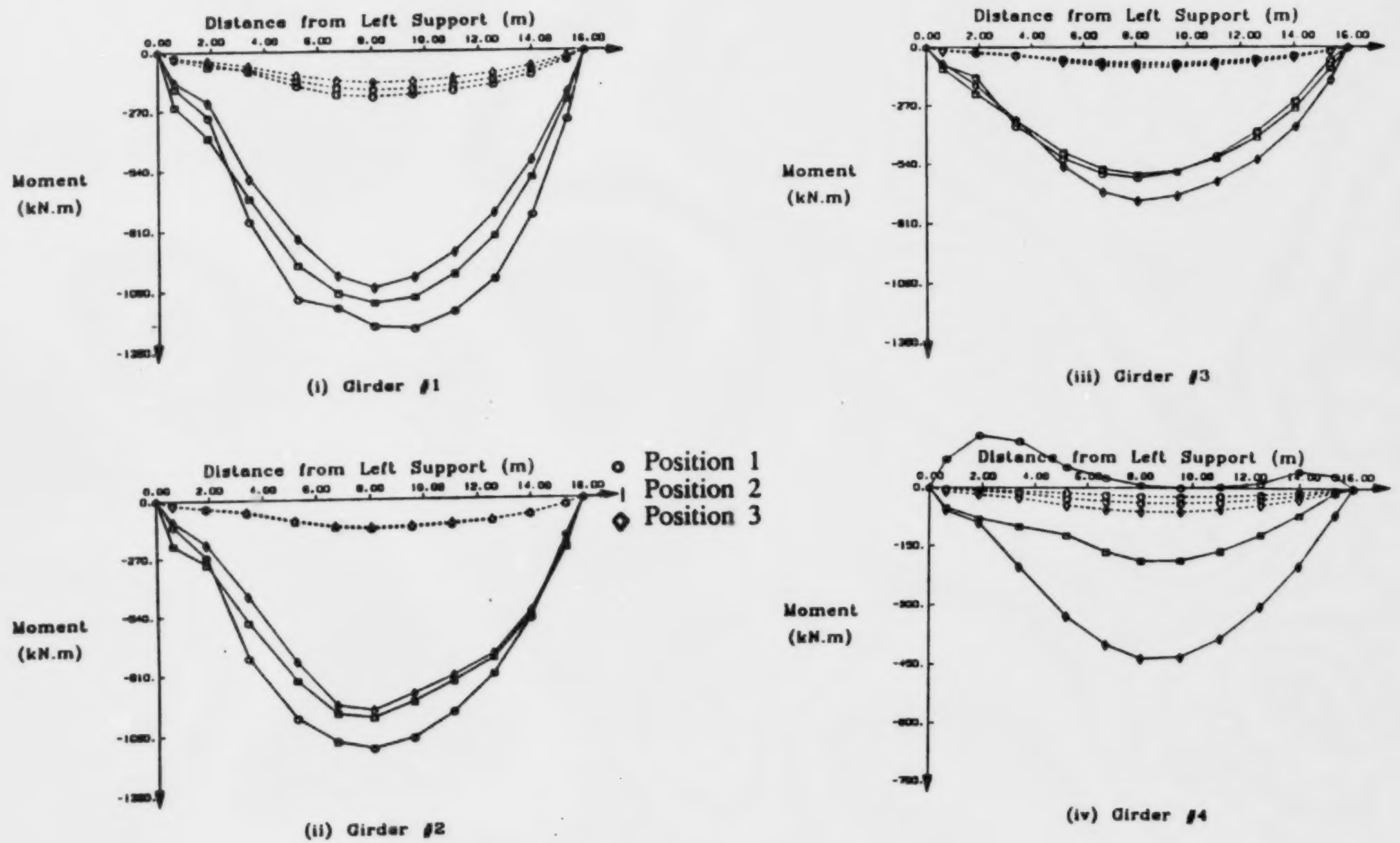

(i) Girder #1

(ii) Girder #2

(iii) Girder #3

(iv) Girder #4

Fig. 85: Effect of Transverse Truck Position on Moment Distribution in Bridge LP2

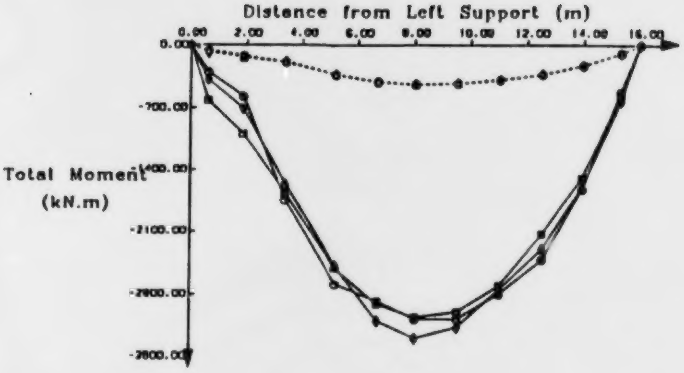

Fig. 86: Effect of Transverse Truck Position on Total Moment of Bridge LP1

○ Position 1
□ Position 2
◇ Position 3

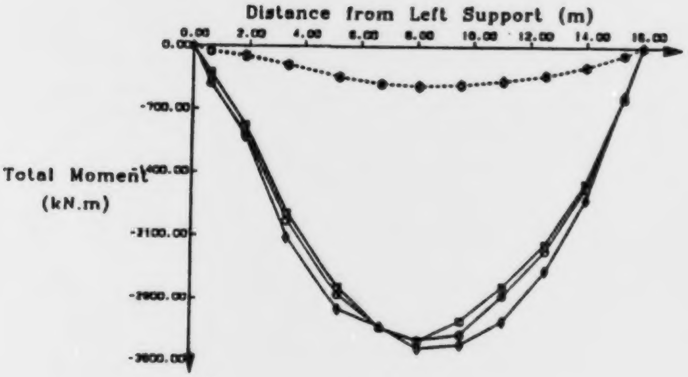

Fig. 87: Effect of Transverse Truck Position on Total Moment of Bridge LP2

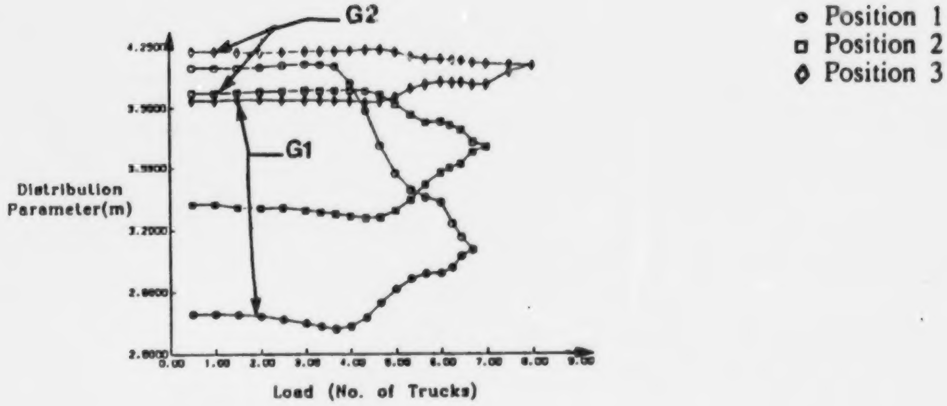

(a) Bridge LP1

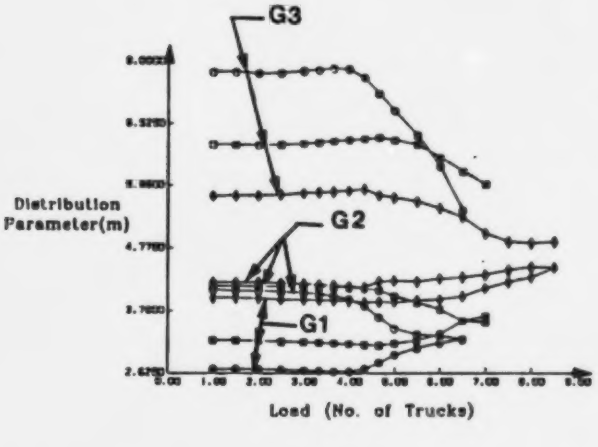

(b) Bridge LP2

Fig. 88: Effect of Transverse Truck Position on Distribution Parameter D_d

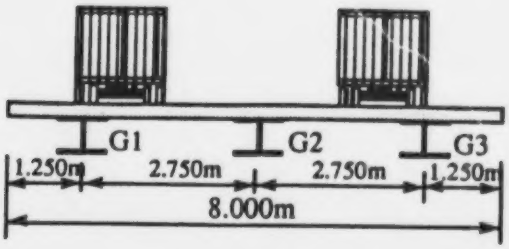
G1
G2
G3
1.250m
2.750m
2.750m
1.250m
8.000m

(a) Bridge BW1

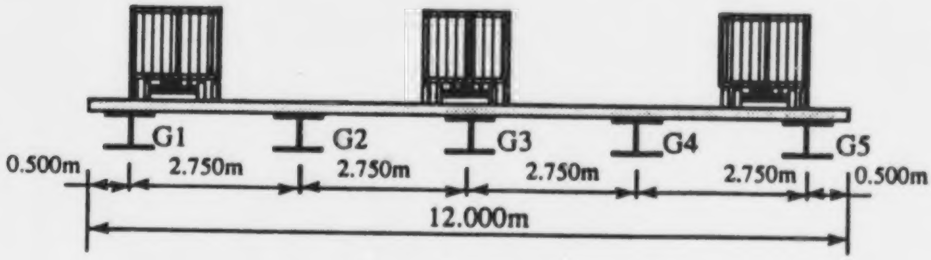
G1
G2
G3
G4
G5
0.500m
2.750m
2.750m
2.750m
2.750m
0.500m
12.000m

(b) Bridge BW2

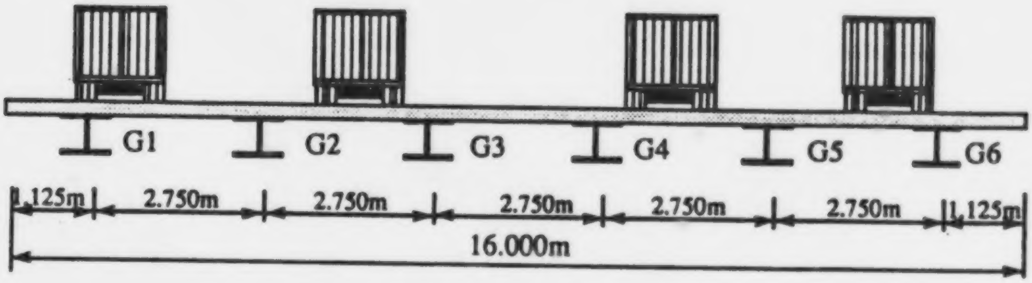
G1
G2
G3
G4
G5
G6
1.125m
2.750m
2.750m
2.750m
2.750m
2.750m
1.125m
16.000m

(c) Bridge BW3

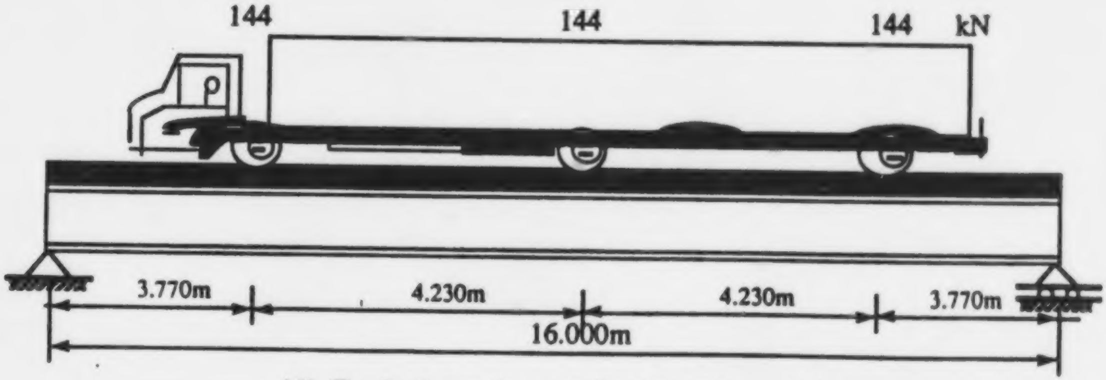
144
144
144
kN
3.770m
4.230m
4.230m
3.770m
16.000m

(d) Typical truck used in (a), (b), and (c)

Fig. 89: Bridge Geometry and Loading Used for Bridge Width Effect Study

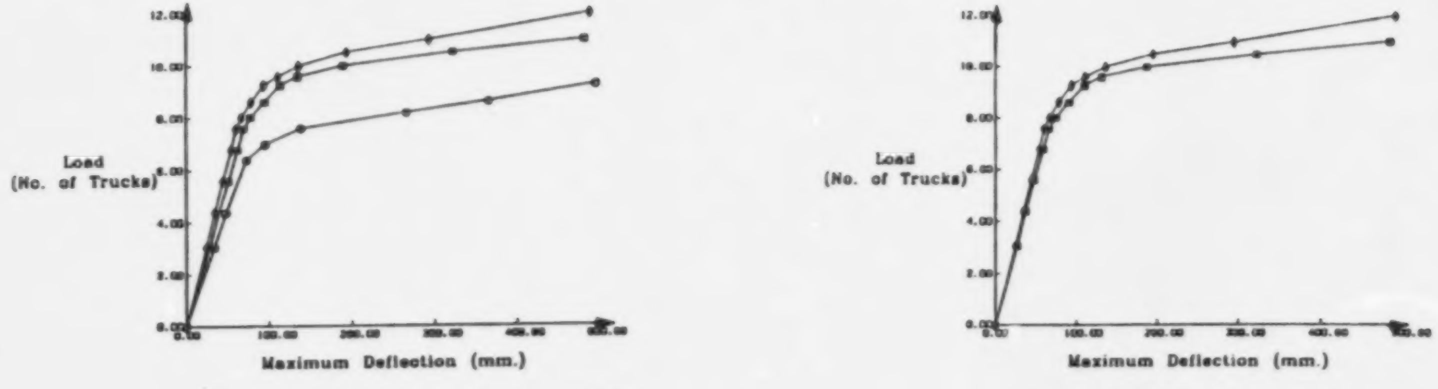

(i) External Girder G1+G3, G1+G5, & G1+G6

(iii) Internal Girder G2+G4, & G2+G5

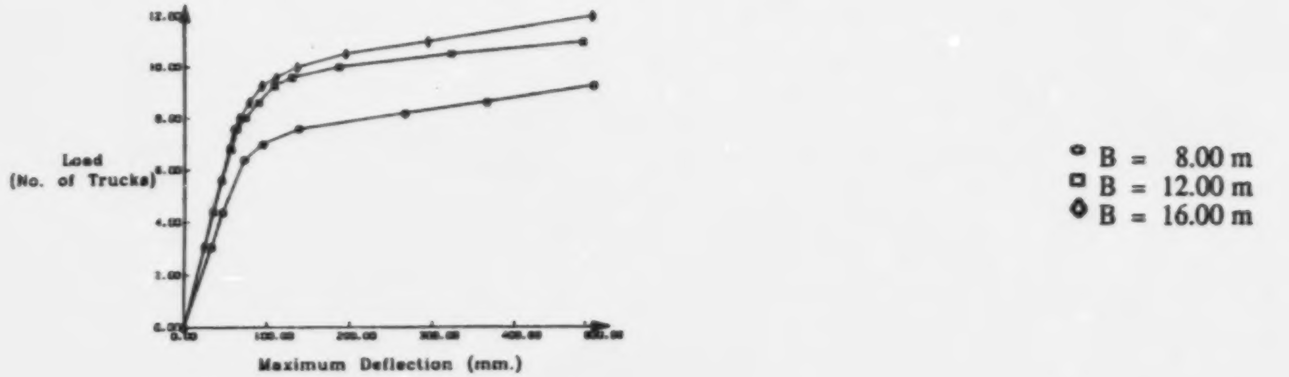

(ii) Centeral Girder G3, G3, & G3+G4

Fig. 90: Effect of Bridge Width on Load-Maximum Deflection of Bridges BW1, BW2, and BW3

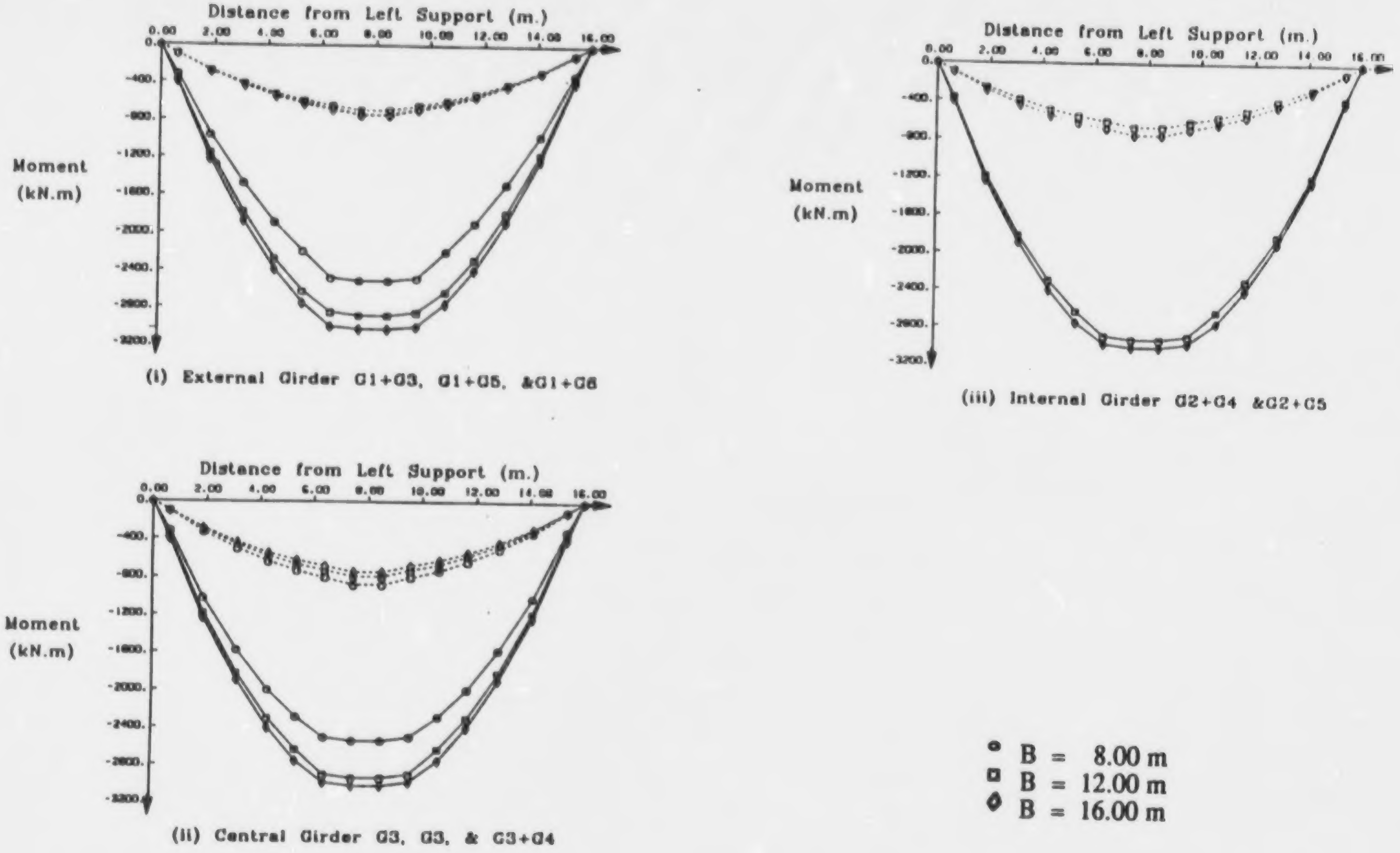

(i) External Girder G1+G3, G1+G5, &G1+G6

(iii) Internal Girder G2+G4 &G2+G5

(ii) Central Girder G3, G3, & G3+G4

Fig. 91: Effect of Bridge Width on Moment Distribution in Bridges BW1, BW2, and BW3

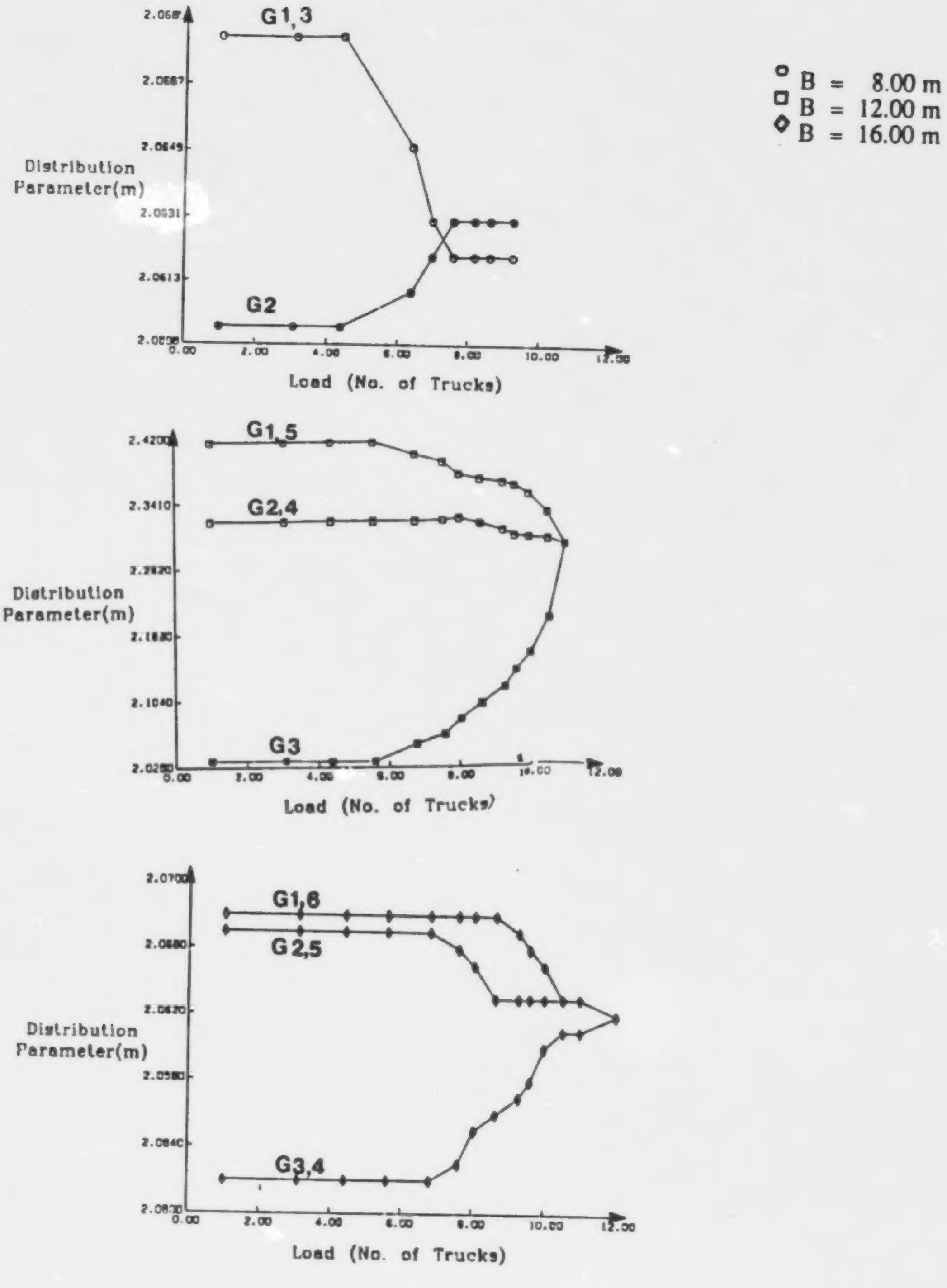

Fig. 92: Effect of Bridge Width on Distribution Parameter D_d

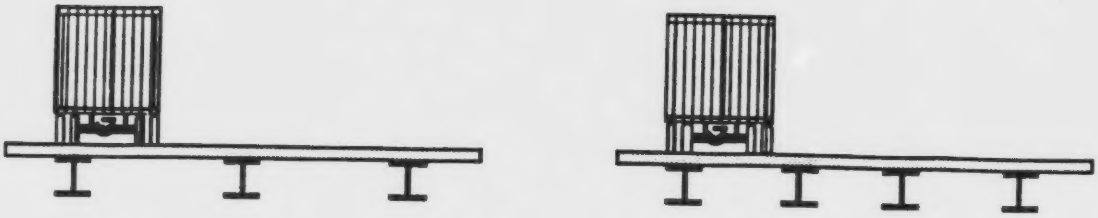

(i) Case 1

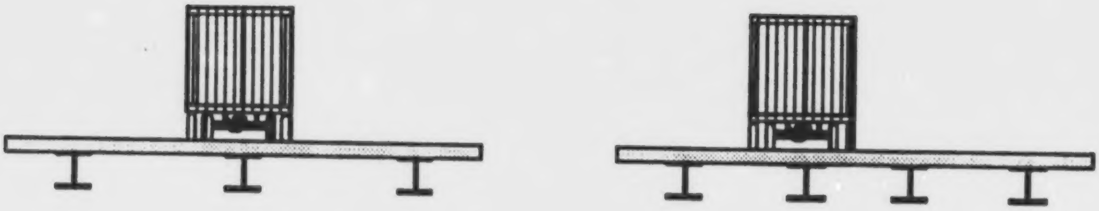

(ii) Case 2

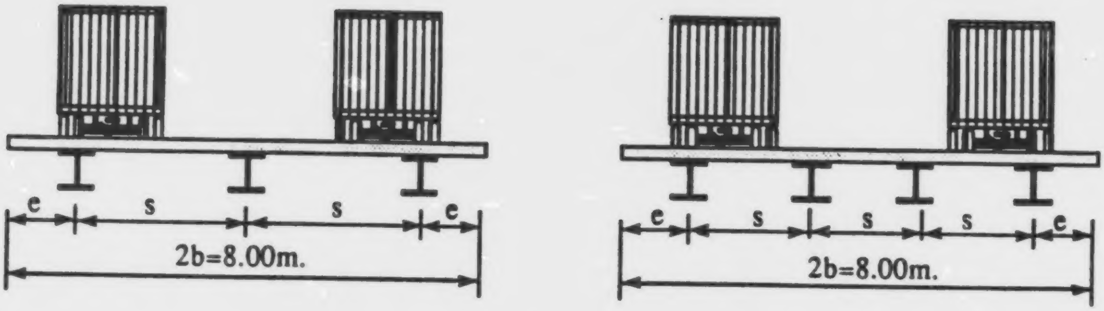
e
s
s
e
2b=8.00m.
e
s
s
s
e
2b=8.00m.

(iii) Case 3

(a) Three Girder System

(b) Four Girder System

Fig. 93: Transverse Loading Cases Used in Parameteric Study

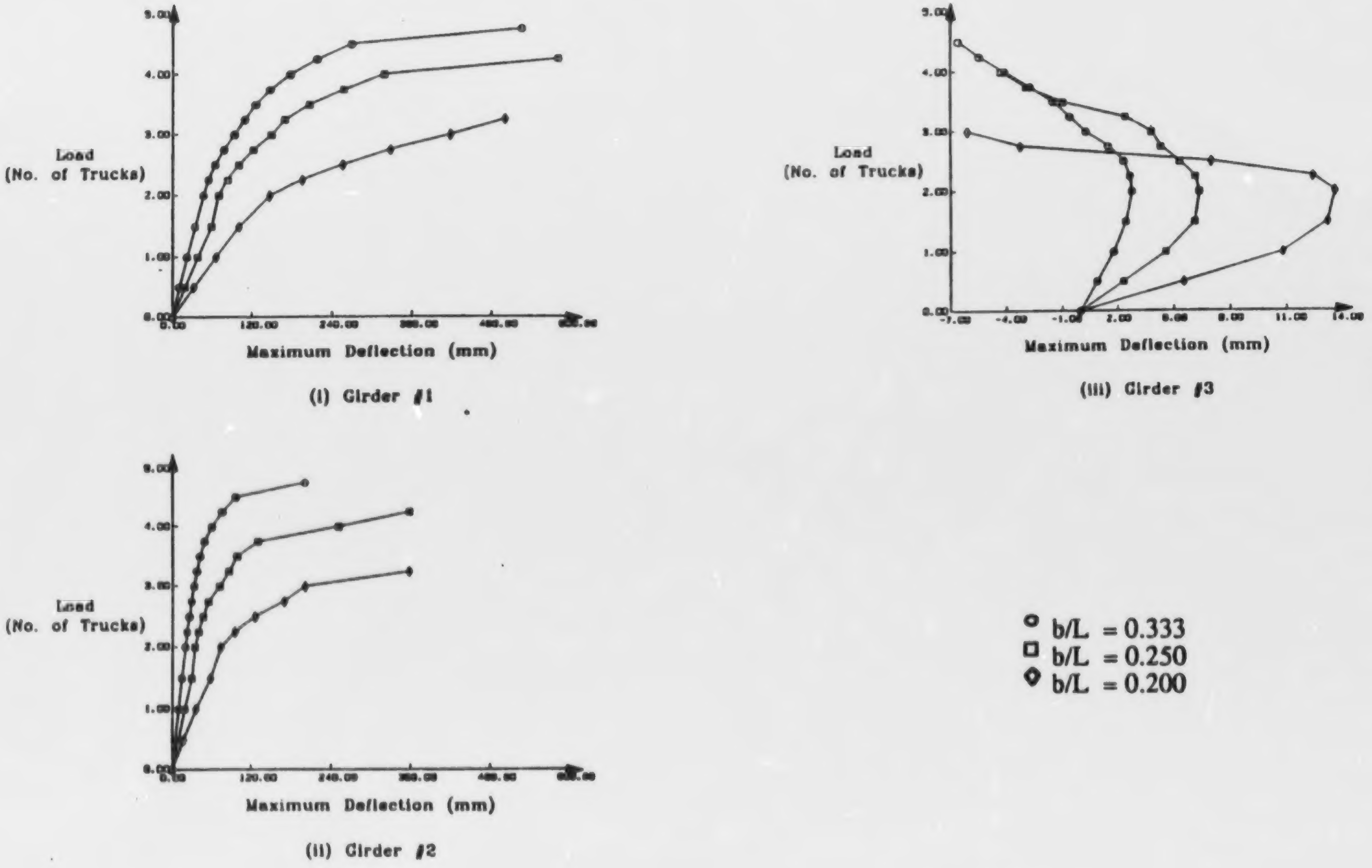

(i) Girder #1

(iii) Girder #3

(ii) Girder #2

Fig. 94: Effect of Span-Length to Width Ratio on
Load-Maximum Deflection of Bridges LW1, LW2, and LW3 (Case 1)

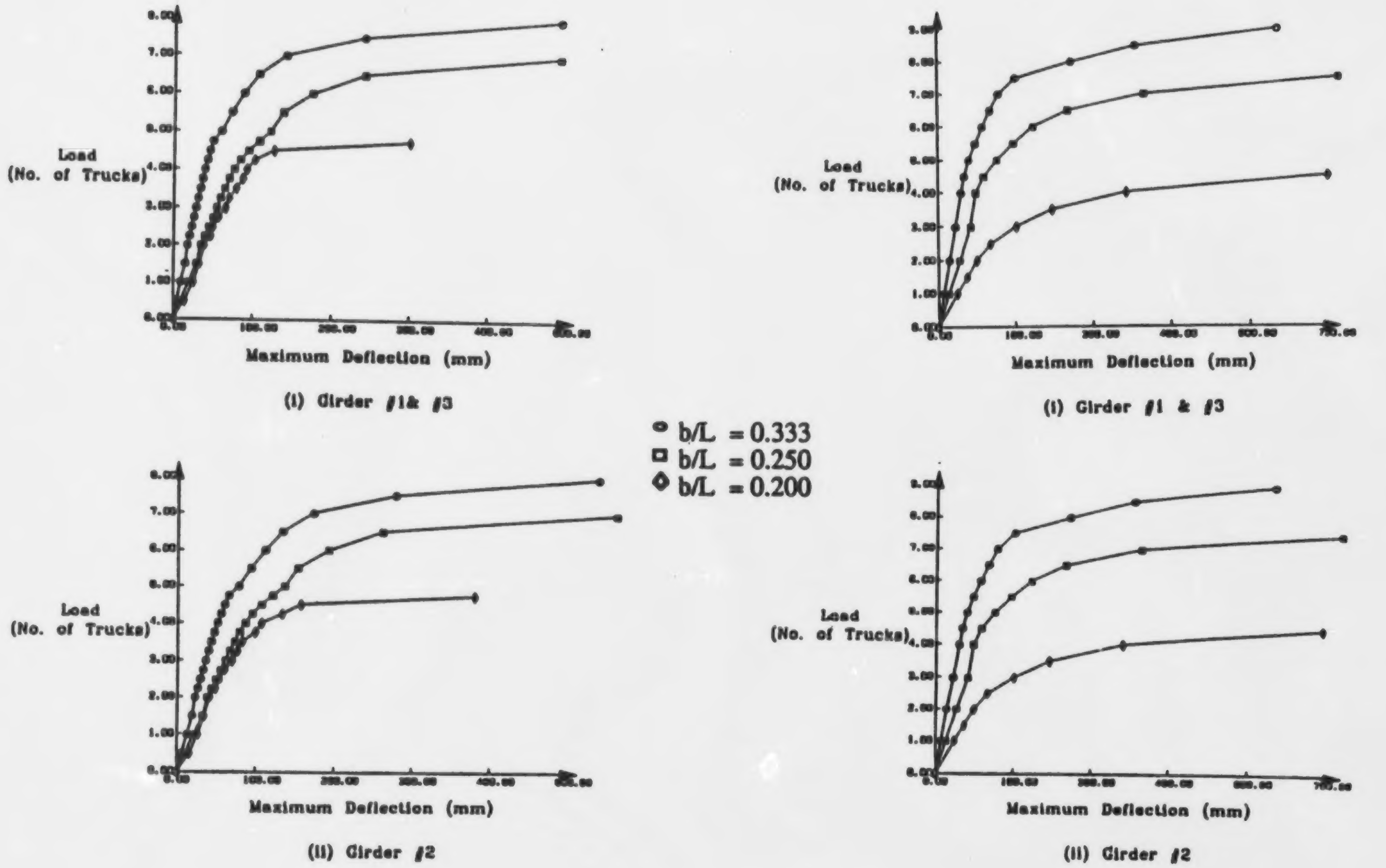

Fig. 95: Effect of Span-Length to Width Ratio on Load-Maximum Deflection of Bridges LW1, LW2, and LW3 (Case 2 and 3)

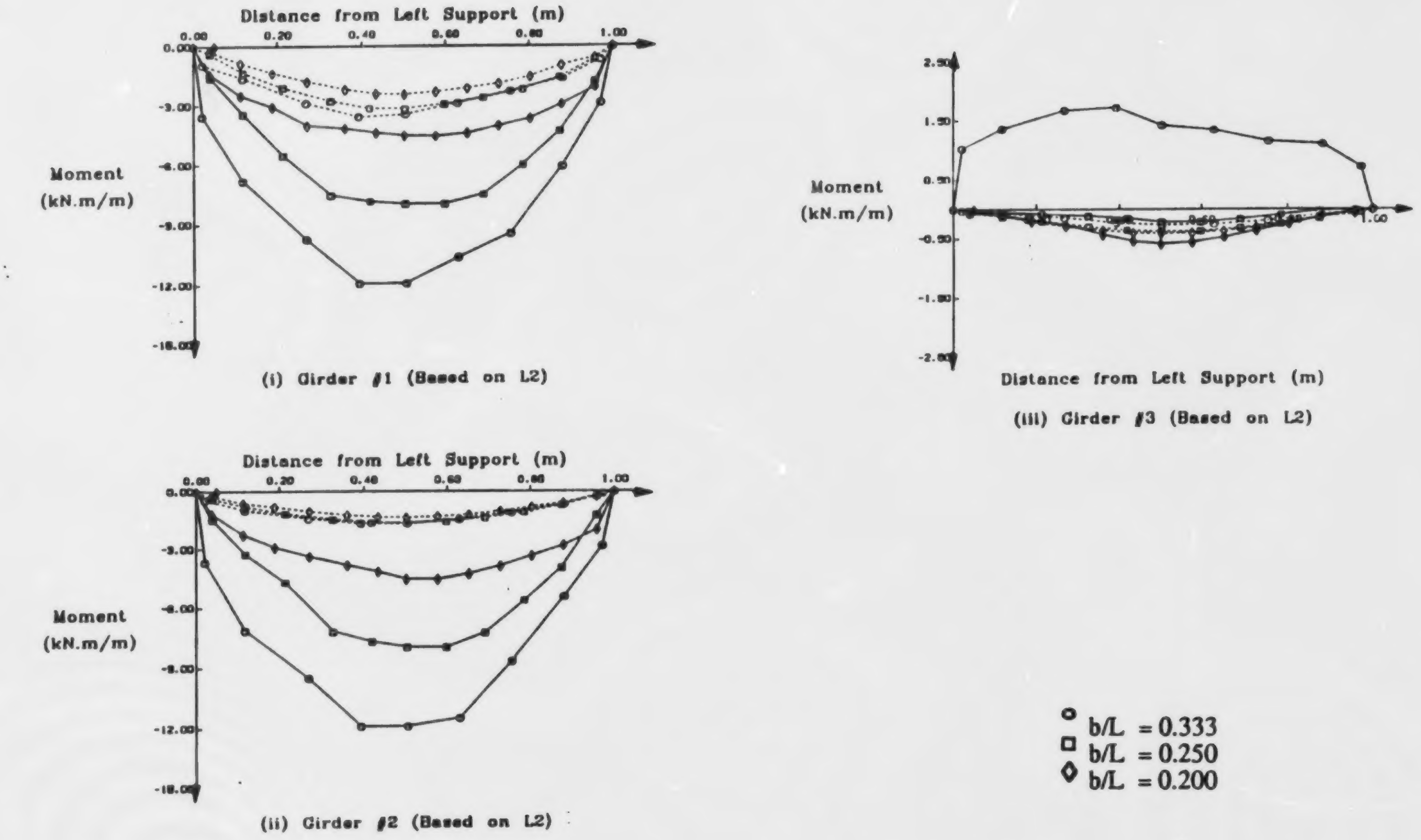

Fig.9 6: Effect of Span-Length to Width Ratio on Moment Distribution of Bridges LW1, LW2, and LW3 (Case 1)

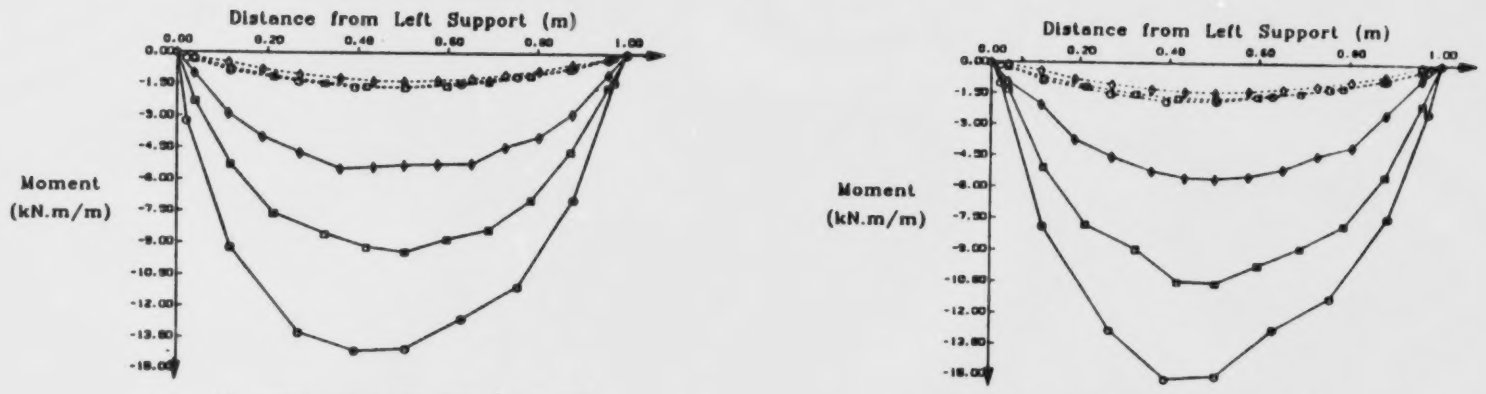

(i) Girder #1 & #3 (Based on L2)

(i) Girder #1 & #3 (Based on L2)

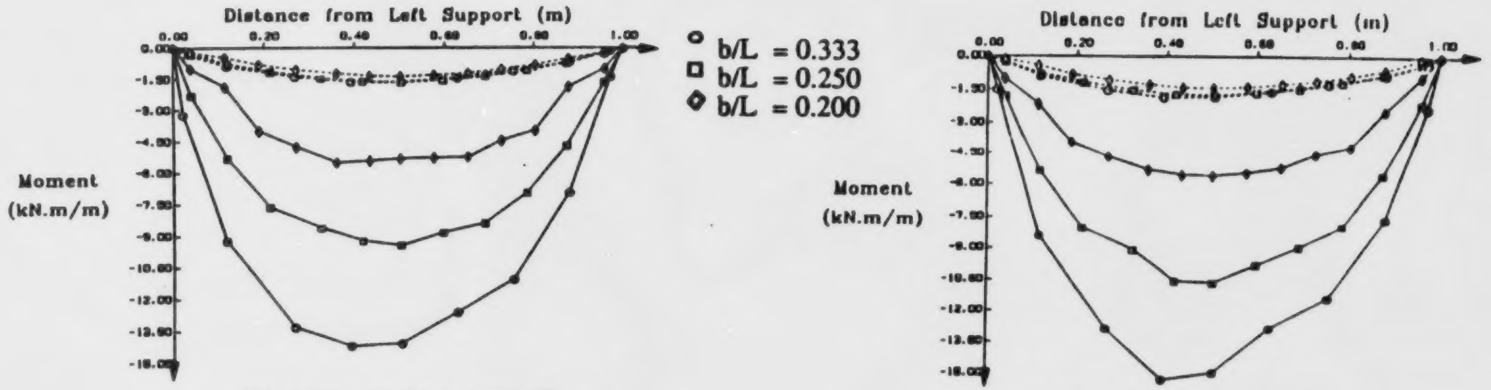

(ii) Girder #2 (Based on L2)

(ii) Girder #2 (Based on L2)

Fig. 97: Effect of Span-Length to Width Ratio on Moment Distribution of Bridges LW1, LW2, and LW3 (Case 2 and 3)

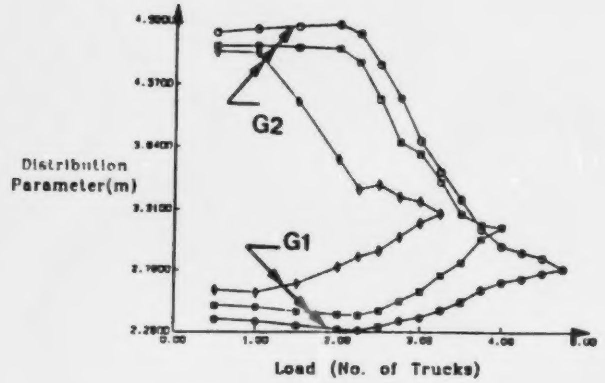

(i) External Girder Loaded

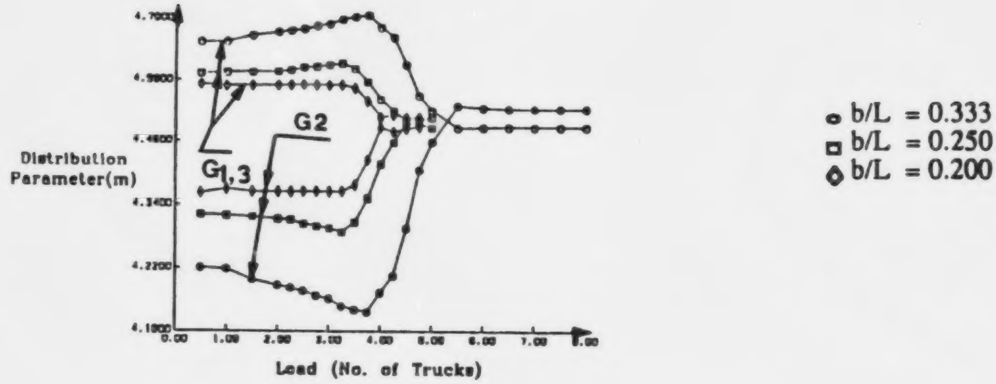

(ii) Internal Girder Loaded

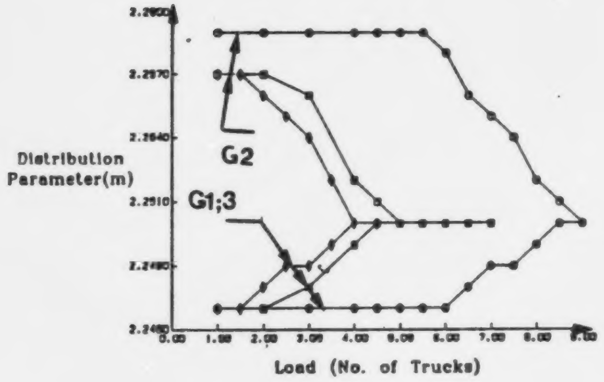

(iii) Both Lanes Loaded

Fig. 98: Effect of Span-Length to Width Ratio on Distribution Parameter D_d

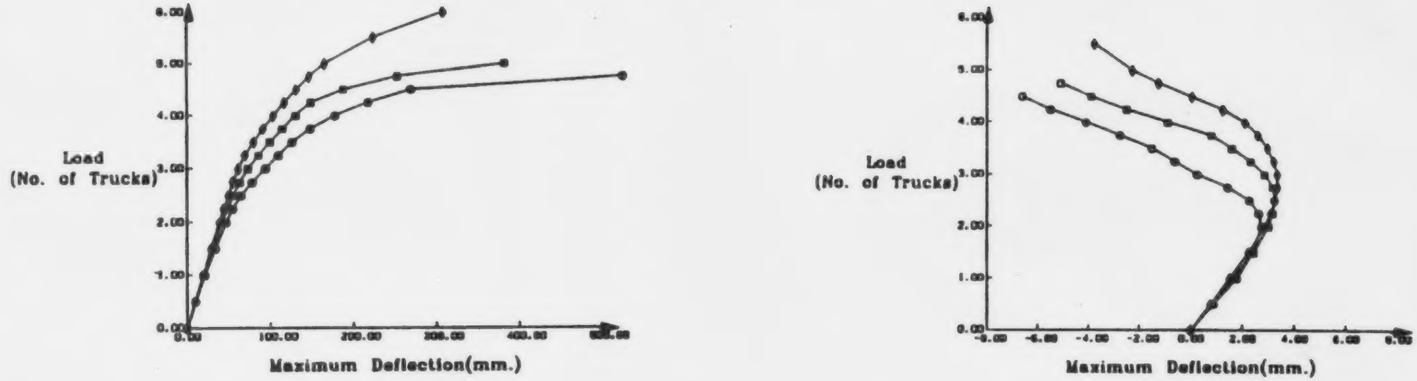

(i) Girder #1

(iii) Girder #3

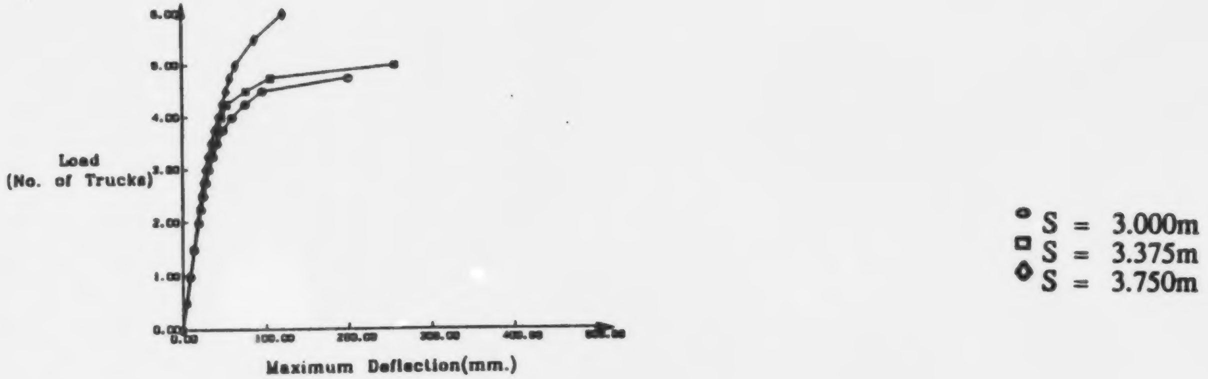

(ii) Girder #2

Fig. 99: Effect of Girder Spacing on Load-Maximum Deflection of Bridges GS1, GS2, and GS3 (Case 1)

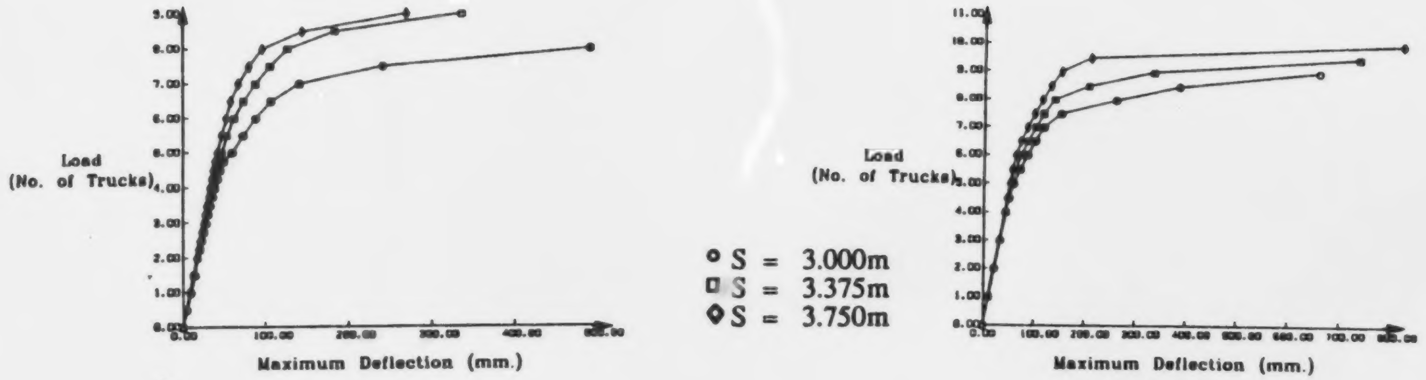

(i) Girder #1 & #3

(i) Girder #1 & #3

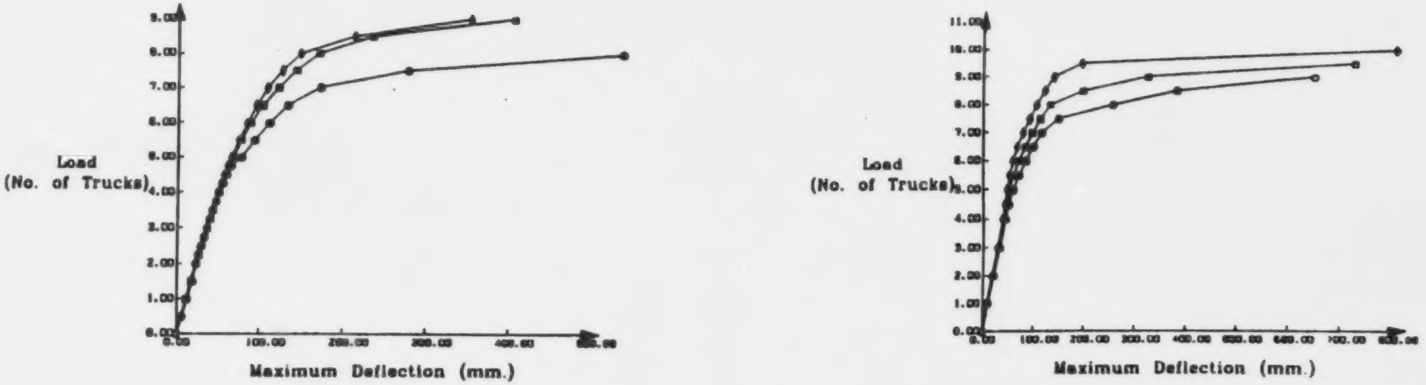

(ii) Girder #2

(ii) Girder #2

Fig. 100: Effect of Girder Spacing on Load-Maximum Deflection of Bridges GS1, GS2, and GS3 (Case 2 and3)

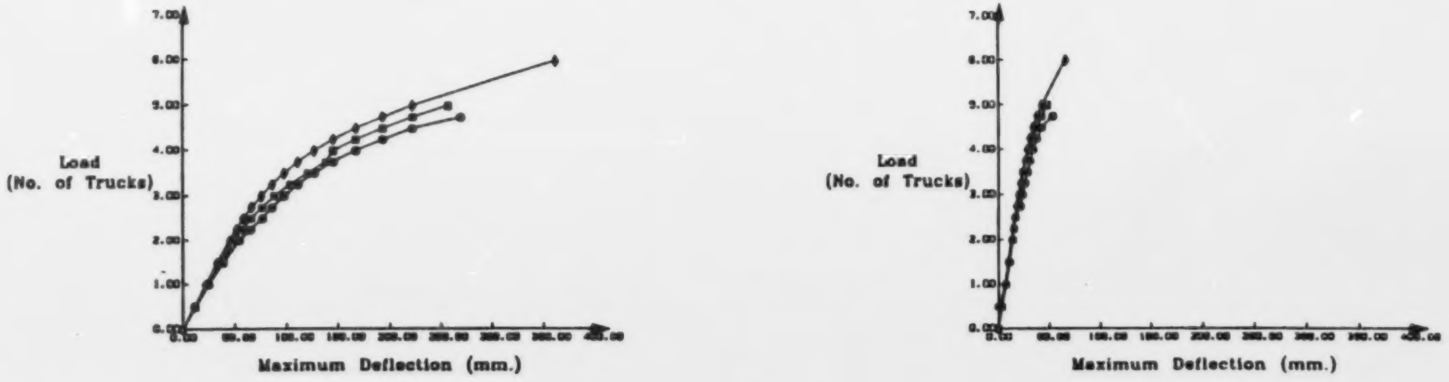

(i) Girder #1

(iii) Girder #3

○S = 2.000m
□S = 2.250m
◇S = 2.500m

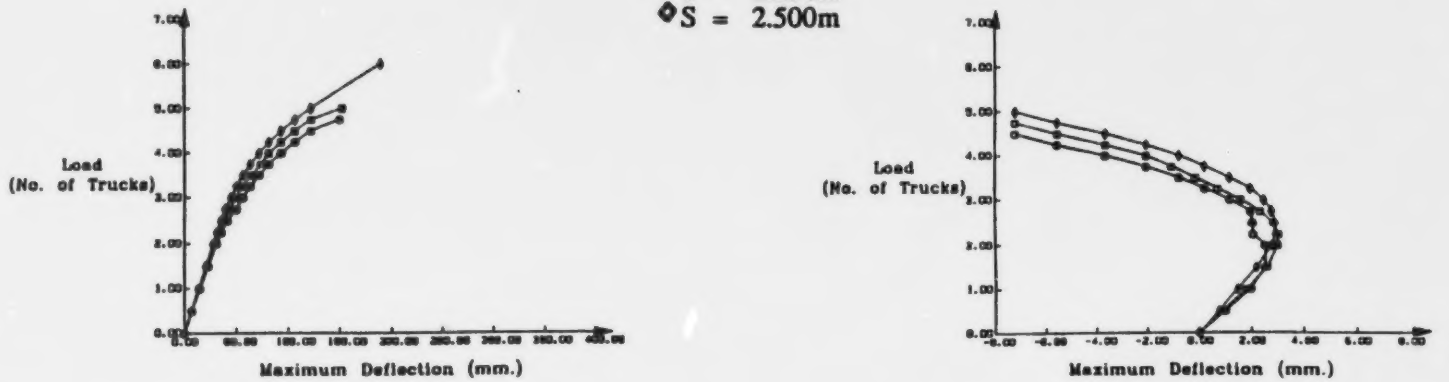

(ii) Girder #2

(iv) Girder #4

Fig. 101: Effect of Girder Spacing on Load-Maximum Deflection of Bridges GS4, GS5, and GS6 (Case 1)

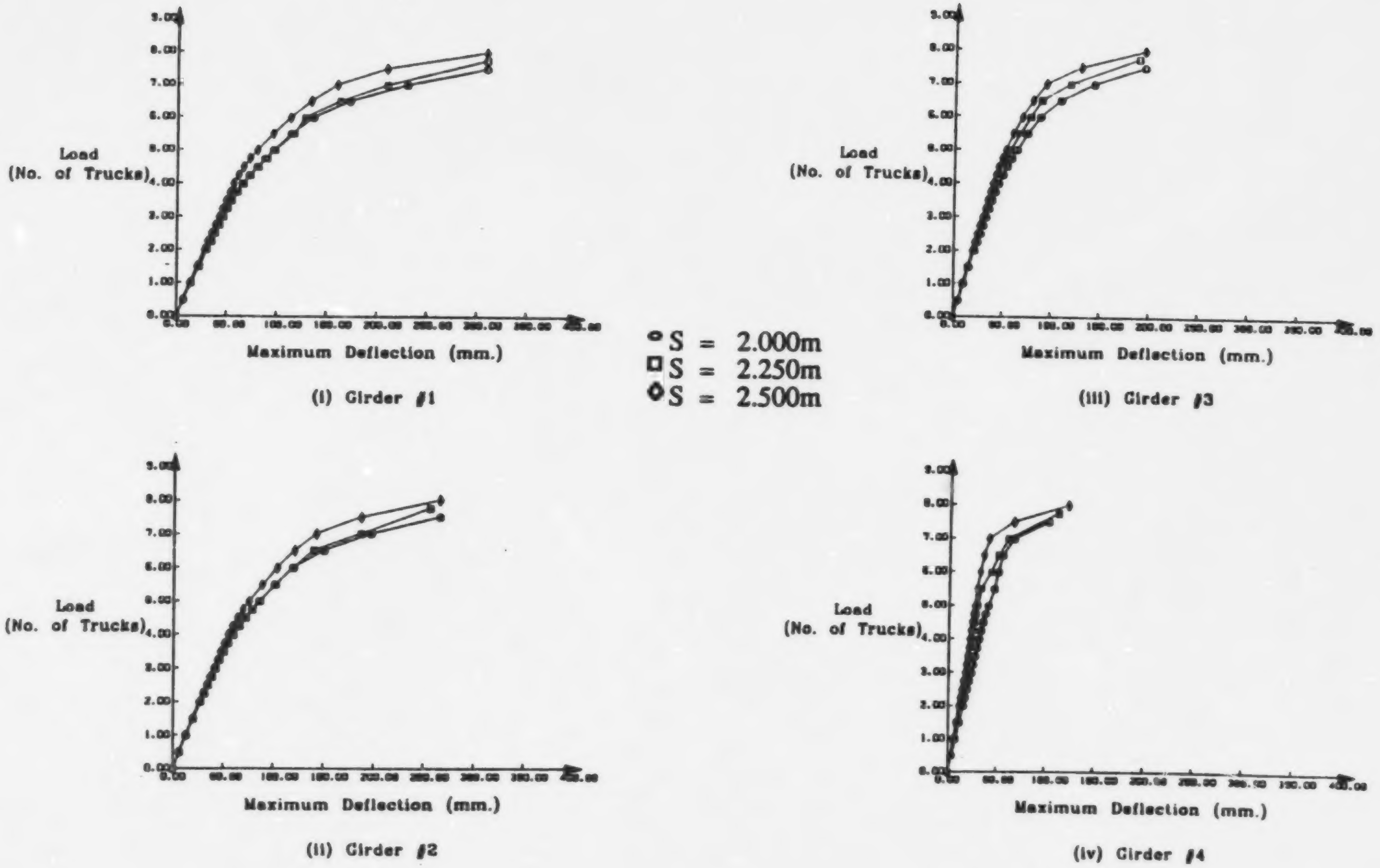

(i) Girder #1

(ii) Girder #2

(iii) Girder #3

(iv) Girder #4

Fig. 102: Effect of Girder Spacing on Load-Maximum Deflection of Bridges GS4, GS5, and GS6 (Case 2)

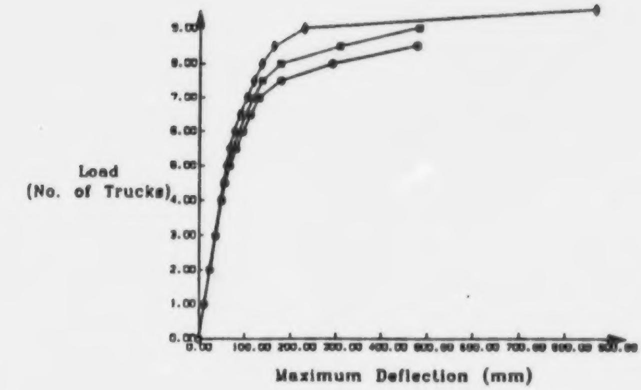

(i) Girder #1 & #4

○ S = 2.000m
□ S = 2.250m
◇ S = 2.500m

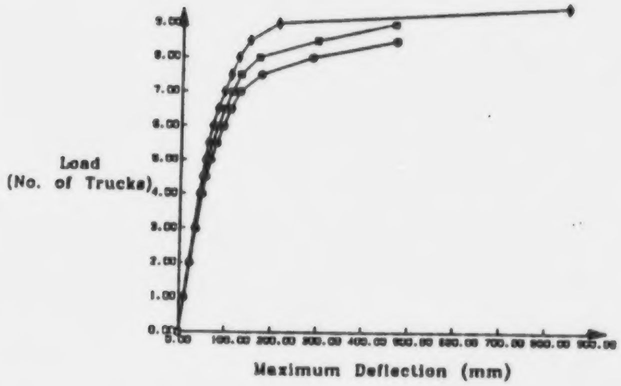

(ii) Girder #2 & #3

Fig. 103: Effect of Girder Spacing on Load-Maximum Deflection of Bridges GS4, GS5, and GS6 (Case 3)

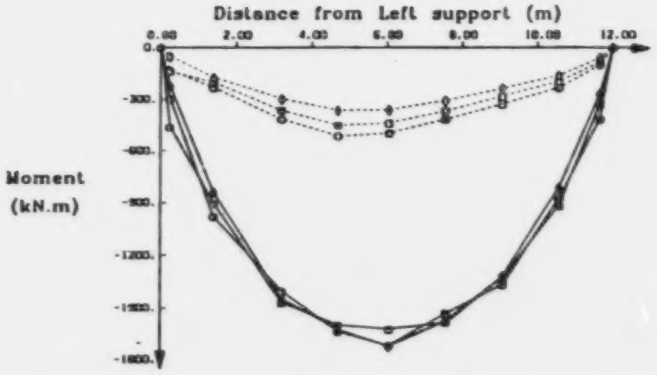

(i) Girder #1

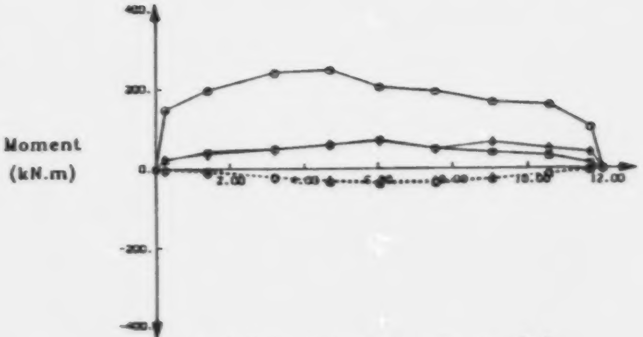

(iii) Girder #3

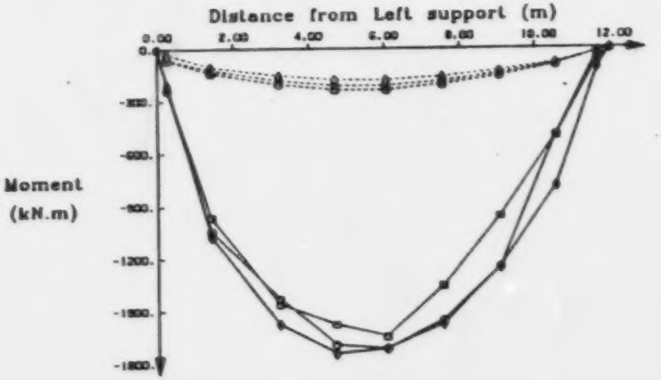

(ii) Girder #2

○ S = 3.000m
□ S = 3.375m
◇ S = 3.750m

Fig. 104: Effect of Girder Spacing on Moment Distribution of Bridges GS1, GS2, and GS3 (Case 1)

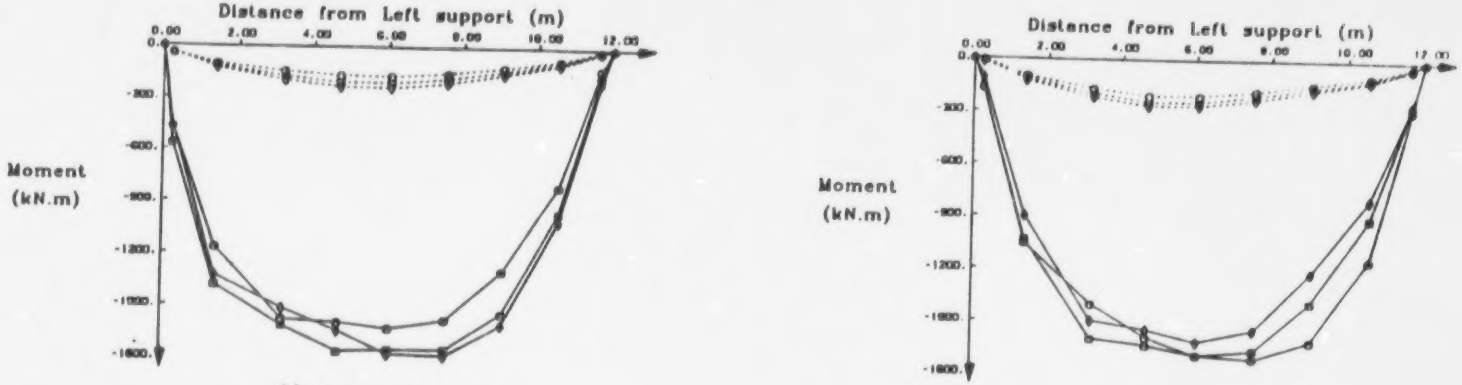

(i) Girder #1 & #3

(i) Girder #1 & #3

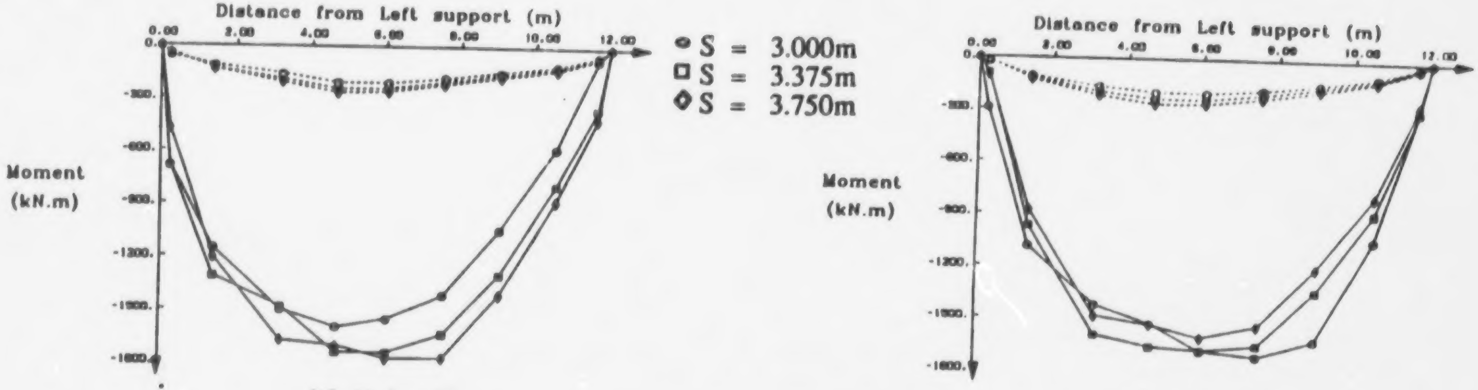

(ii) Girder #2

(ii) Girder #2

Fig. 105: Effect of Girder Spacing on Moment Distribution GS1, GS2, and GS3 (Case 2 and 3)

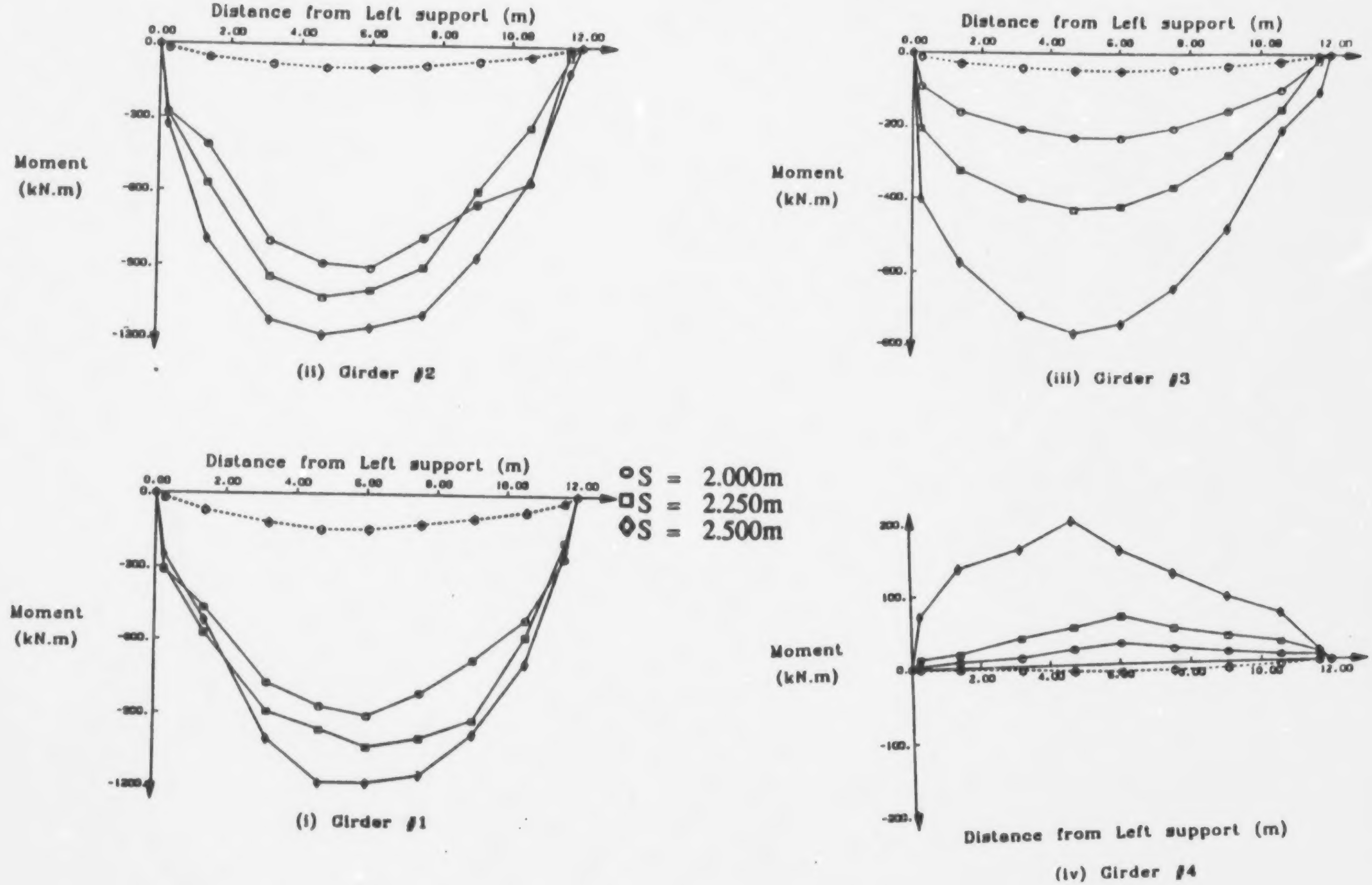

Fig. 106: Effect of Girder Spacing on Moment Distribution of Bridges GS4, GS5, and GS6 (Case 1)

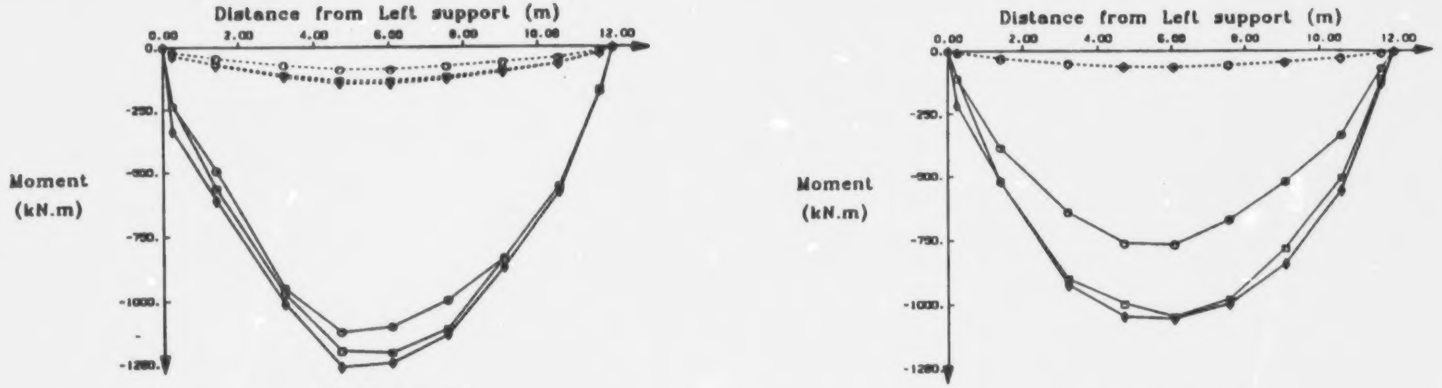

(i) Girder #1

(iii) Girder #3

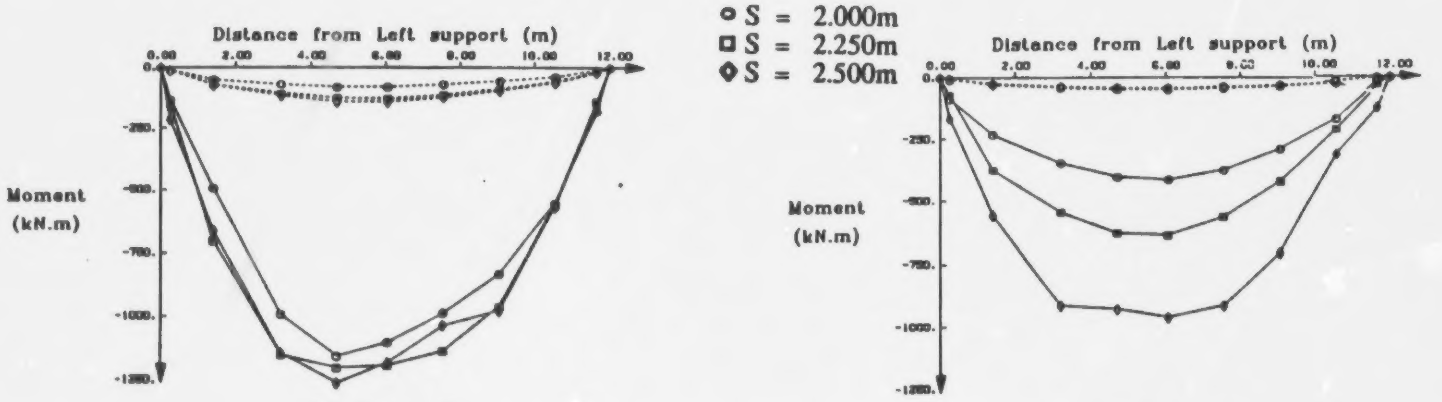

(ii) Girder #2

(iv) Girder #4

Fig. 107: Effect of Girder Spacing on Load-Maximum Deflection of Bridges GS4, GS5, and GS6 (Case 2)

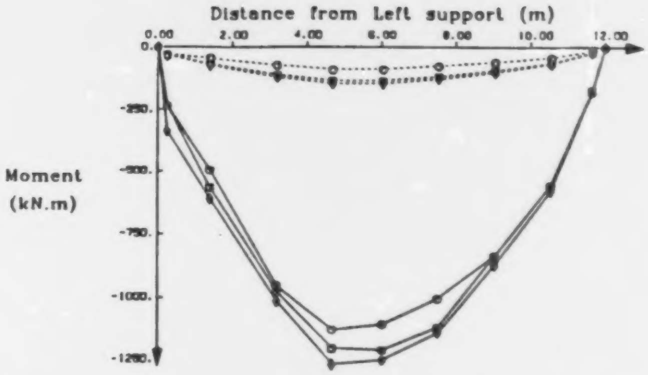

(i) Girder #1 & #4

○ S = 2.000m
□ S = 2.250m
◇ S = 2.500m

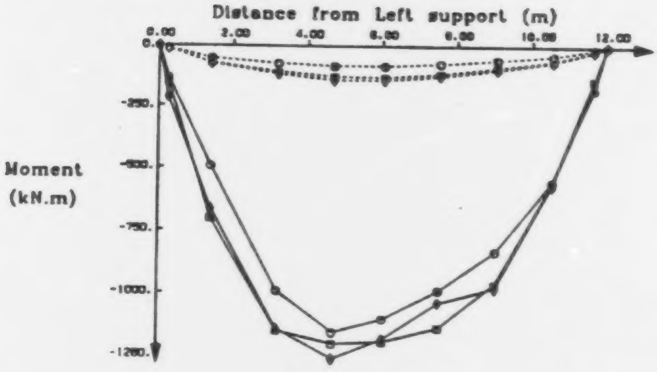

(ii) Girder #2 & #3

Fig. 108: Effect of Girder Spacing on Moment Distribution of Bridges GS4, GS5, and GS6 (Case 3)

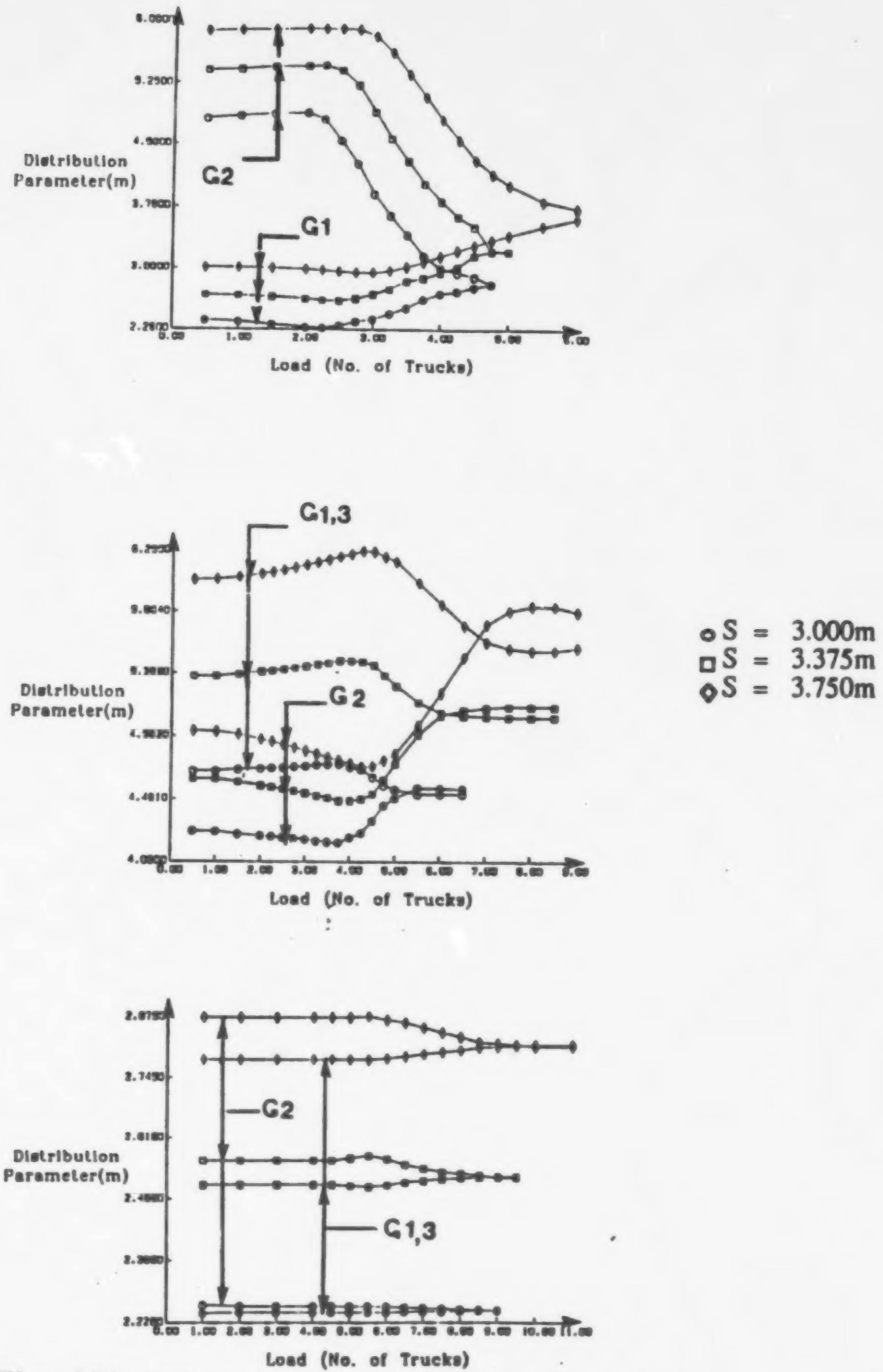

Fig. 109: Effect of Girder Spacing on Distribution Parameter D_d

(Bridges GS1, GS2, and GS3)

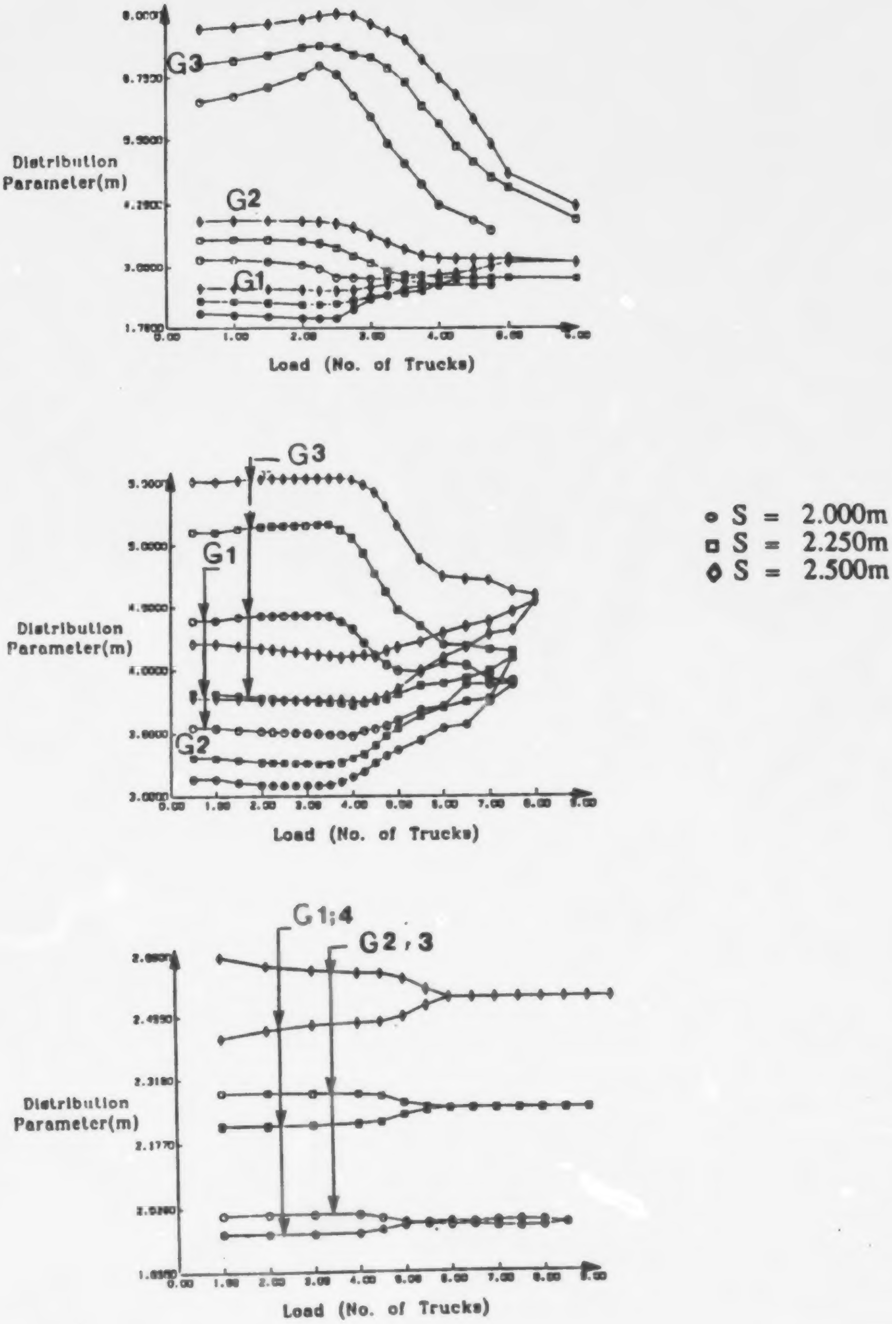

Fig. 110: Effect of Girder Spacing on Distribution Parameter D_d (Bridges GS4, GS5, and GS6)

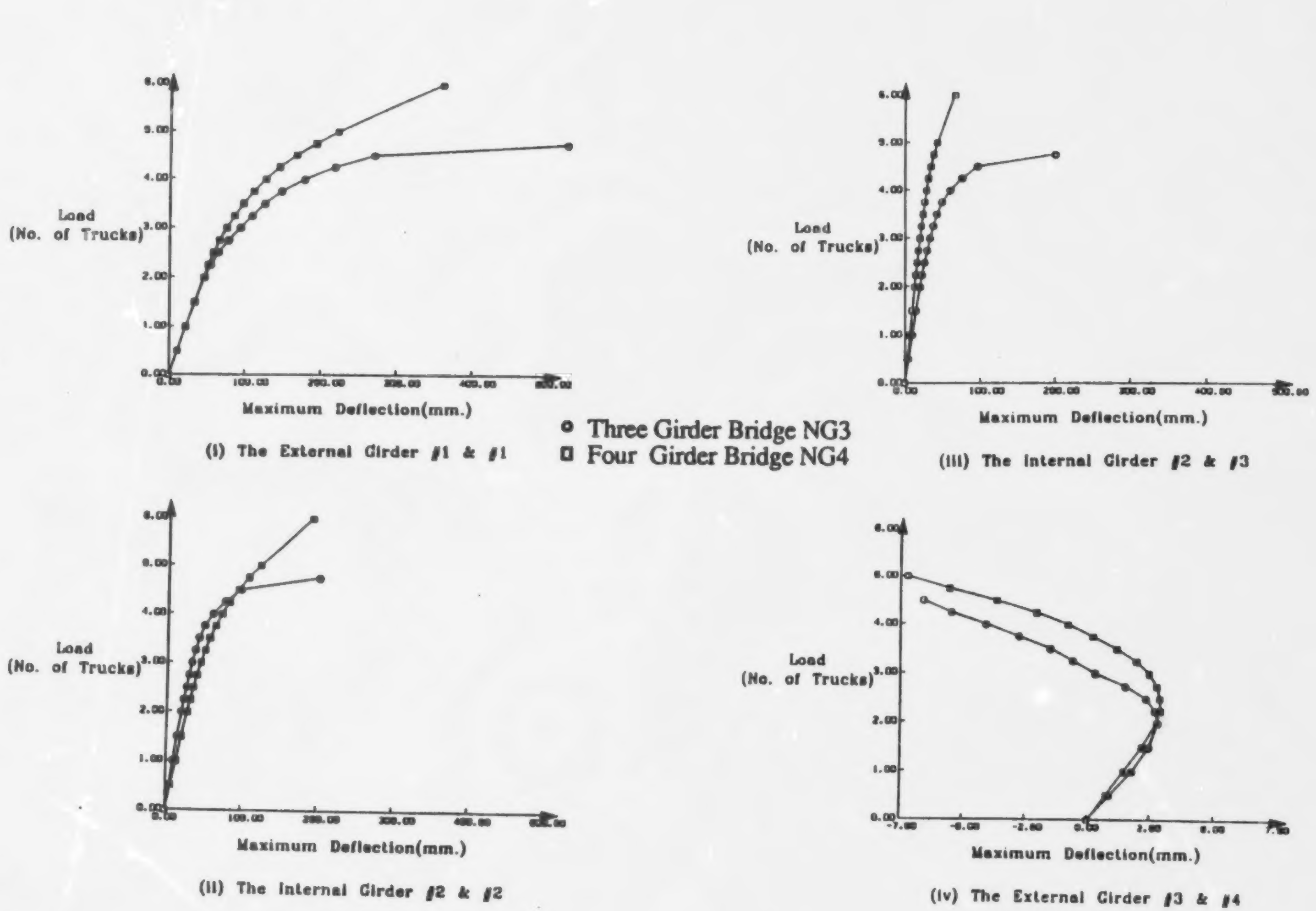

(i) The External Girder #1 & #1

(iii) The Internal Girder #2 & #3

(ii) The Internal Girder #2 & #2

(iv) The External Girder #3 & #4

Fig. 111: Effect of Number of Girders on Load-Maximum Deflection of Bridges NG3 and NG4 (Case 1)

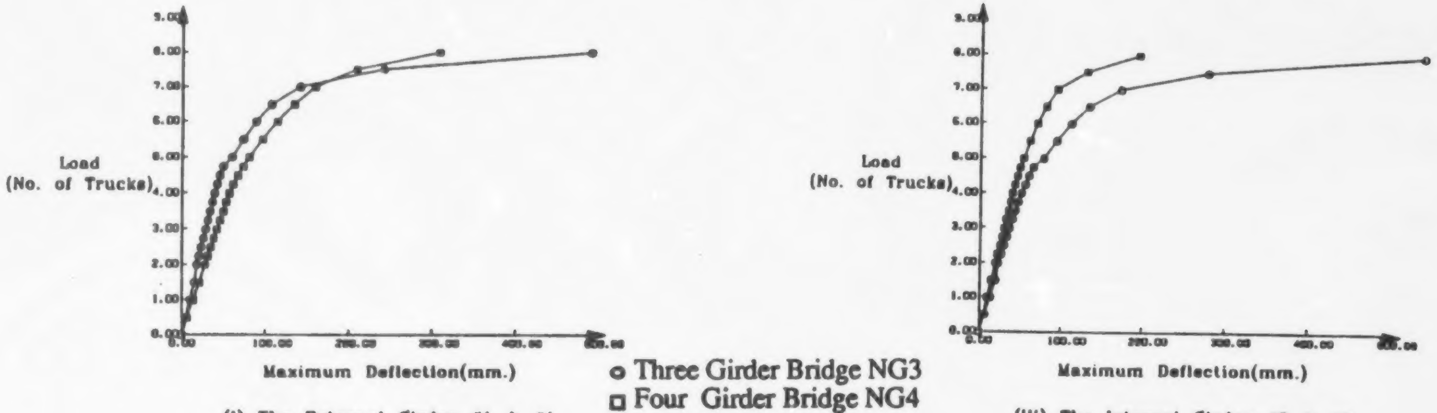

(i) The External Girder #1 & #1

(iii) The Internal Girder #2 & #3

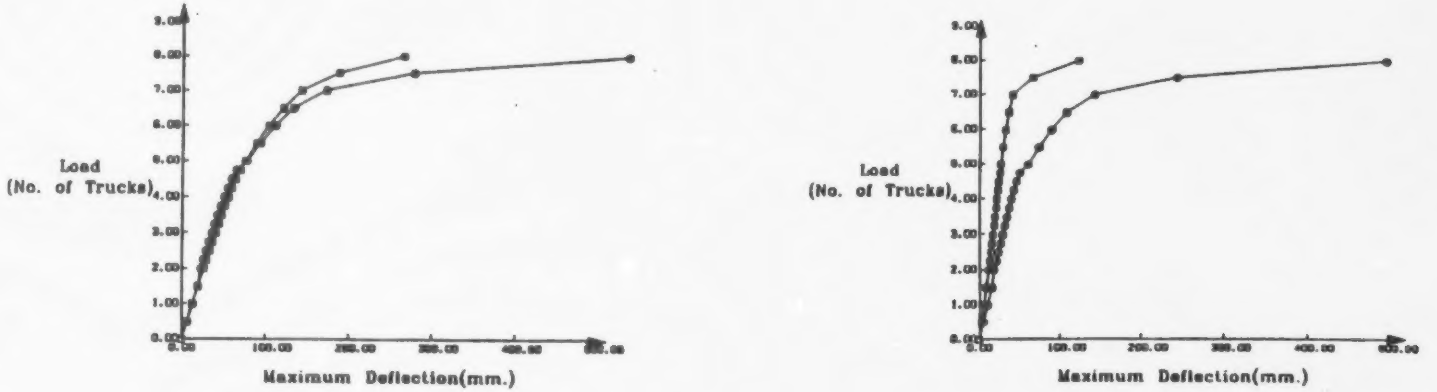

(ii) The Internal Girder #2 & #2

(iv) The External Girder #3 & #4

Fig. 112: Effect of Number of Girders on Load-Maximum Deflection of Bridges NG3 and NG4 (Case 2)

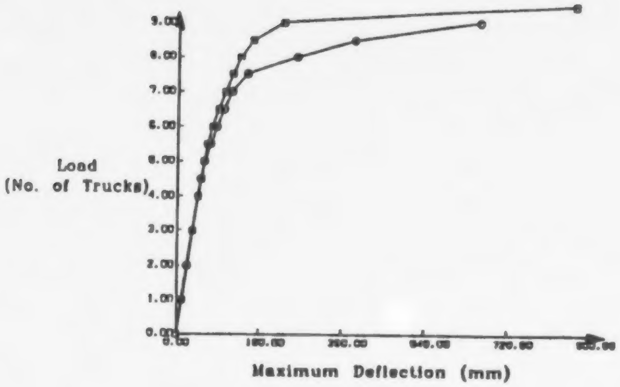

(i) The External Girder (#1&#1) or (#3&#4)

○Three Girder Bridge NG3
□Four Girder Bridge NG4

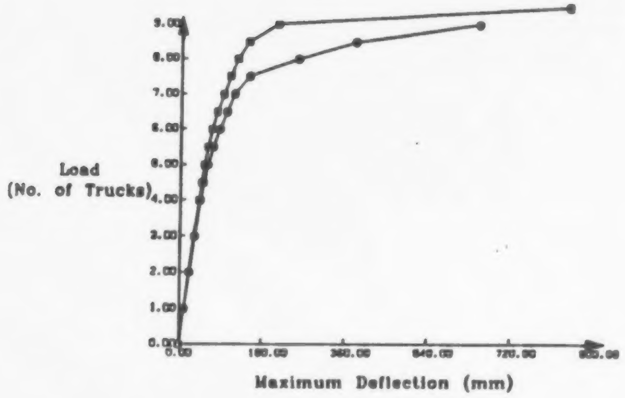

(ii) The Internal Girder (#2&#2) or (#2&#3)

Fig. 113: Effect of Number of Girders on Load-Maximum Deflection of Bridges NG3 and NG4 (Case 3)

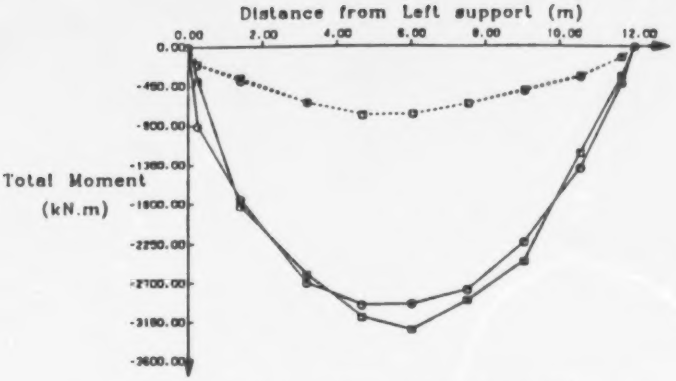

(I) One Lane Loaded (case #1)

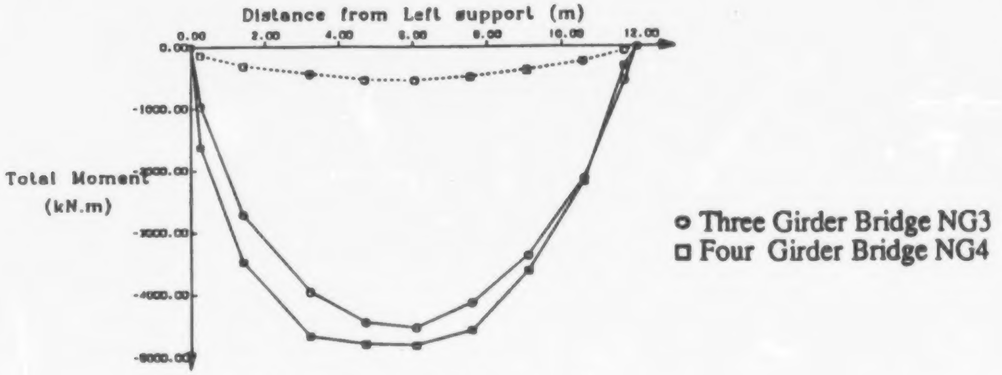

(II) One Lane Loaded (case #2)

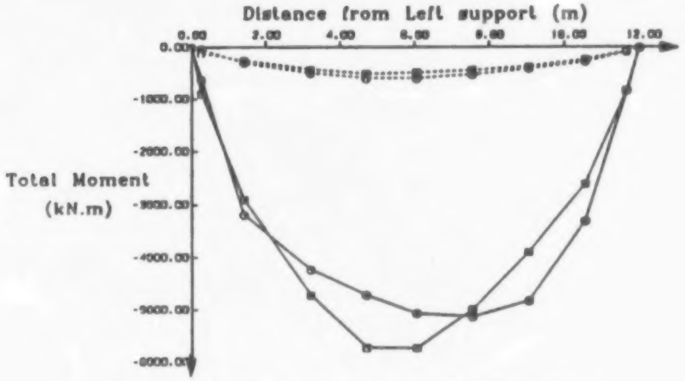

(III) Two Lanes Loaded (Case #3)

Fig. 114: Effect of Number of Girders on Total Moments in Bridges NG3 and NG4

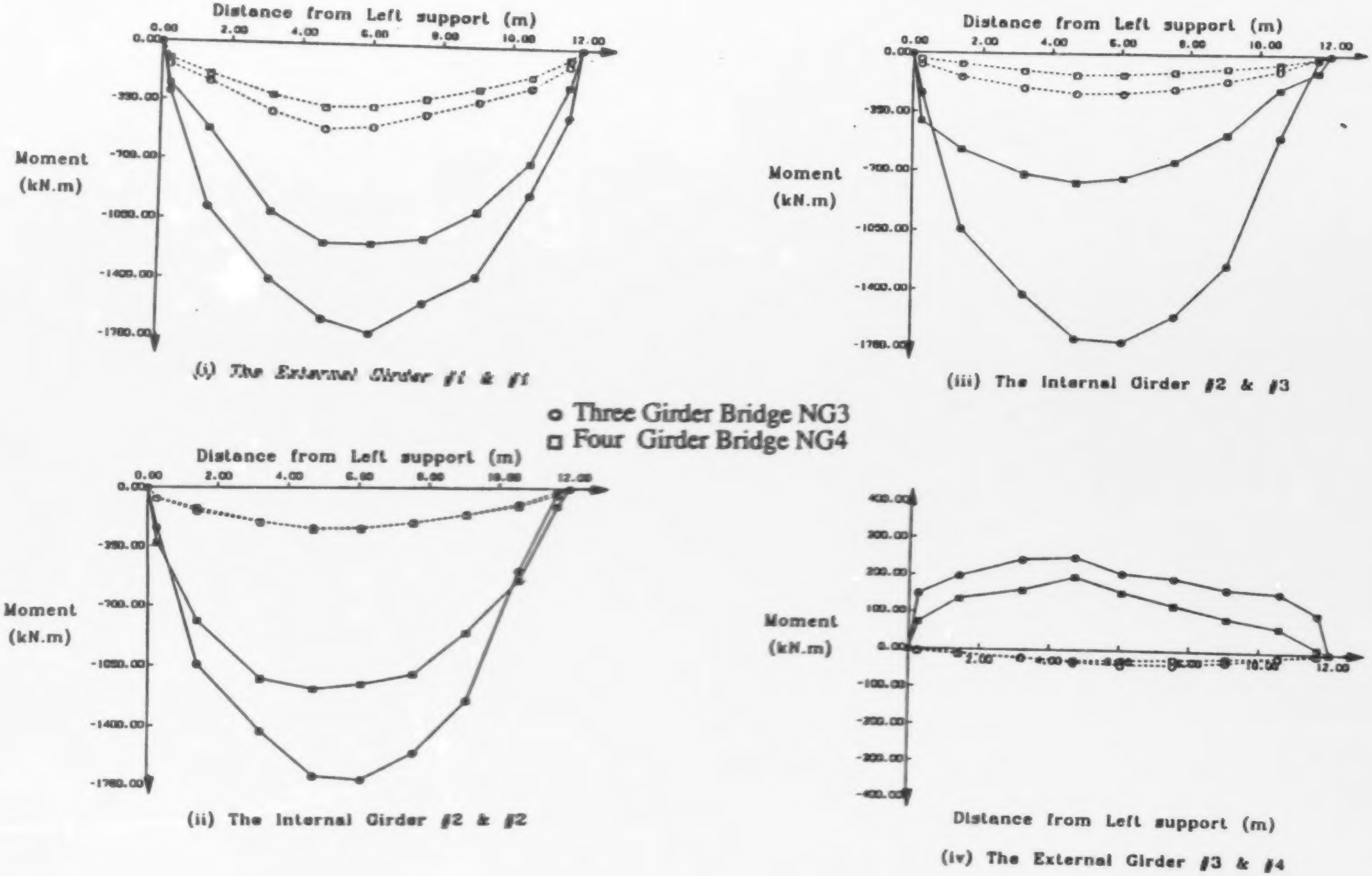

(i) The External Girder #1 & #1

(iii) The Internal Girder #2 & #3

(ii) The Internal Girder #2 & #2

(iv) The External Girder #3 & #4

Fig. 115: Effect of Number of Girders on Moment Distribution in Bridges NG3 and NG4 (Case 1)

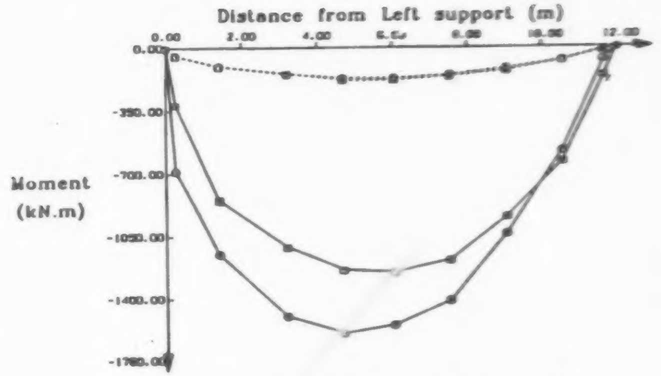

(i) The External Girder #1 & #1

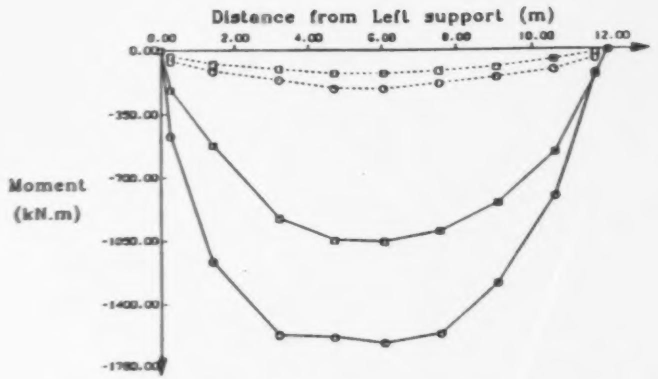

(iii) The Internal Girder #2 & #3

○ Three Girder Bridge NG3
□ Four Girder Bridge NG4

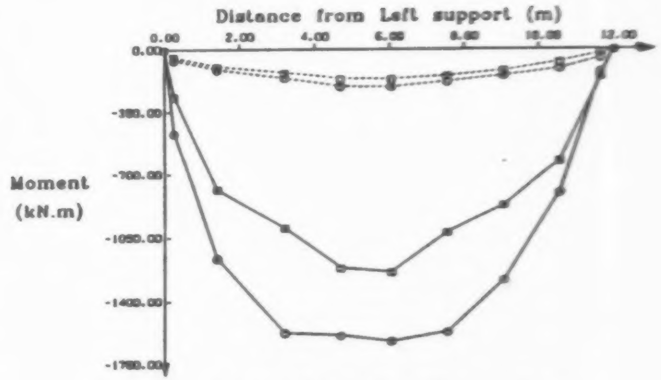

(ii) The Internal Girder #2 & #2

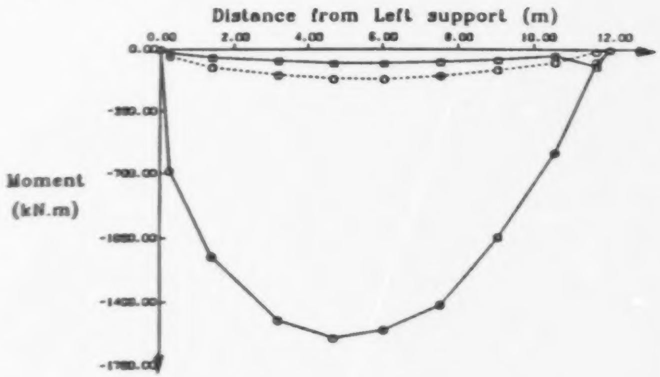

(iv) The External Girder #3 & #4

Fig. 116: Effect of Number of Girders on Moment Distribution in Bridges NG3 and NG4 (Case 2)

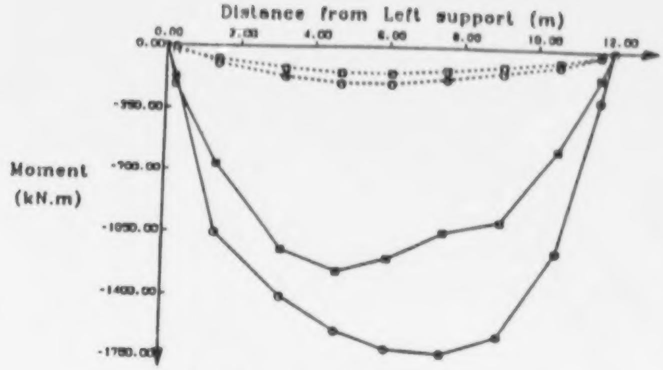

(i) The External Girder (#1&#1) or (#3&#4)

○ Three Girder Bridge NG3
□ Four Girder Bridge NG4

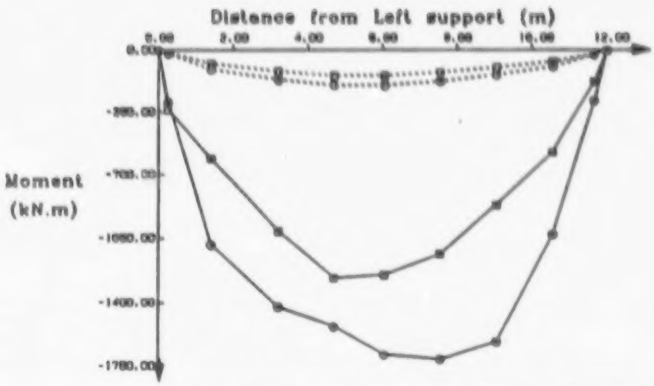

(ii) The Internal Girder (#2&#2) or (#2&#3)

Fig. 117: Effect of Number of Girders on Moment Distribution in Bridges NG3 and NG4 (Case 3)

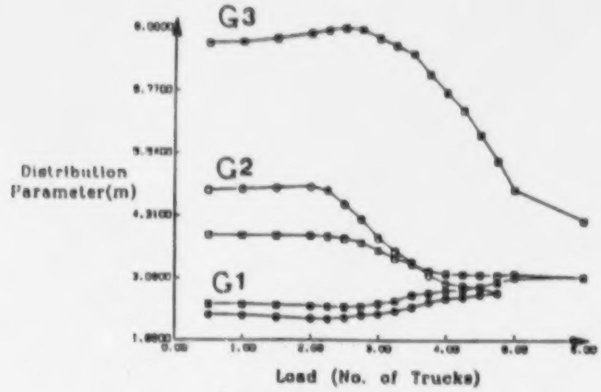

(I) Total Number of Girders (case #1)

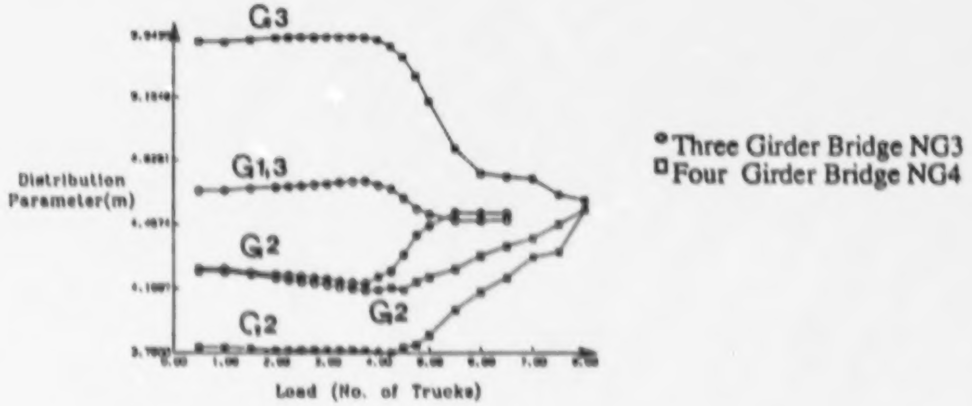

(II) Total Number of Girders (Case #2)

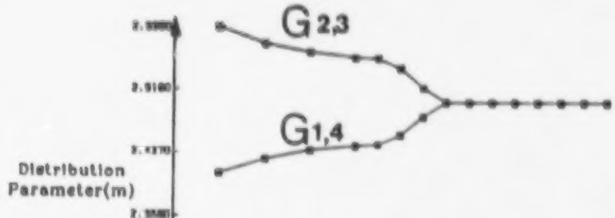

(III) Total Number of Girders (case #3)

Fig. 118: Effect of Number of Girders on Distribution Parameter D_d

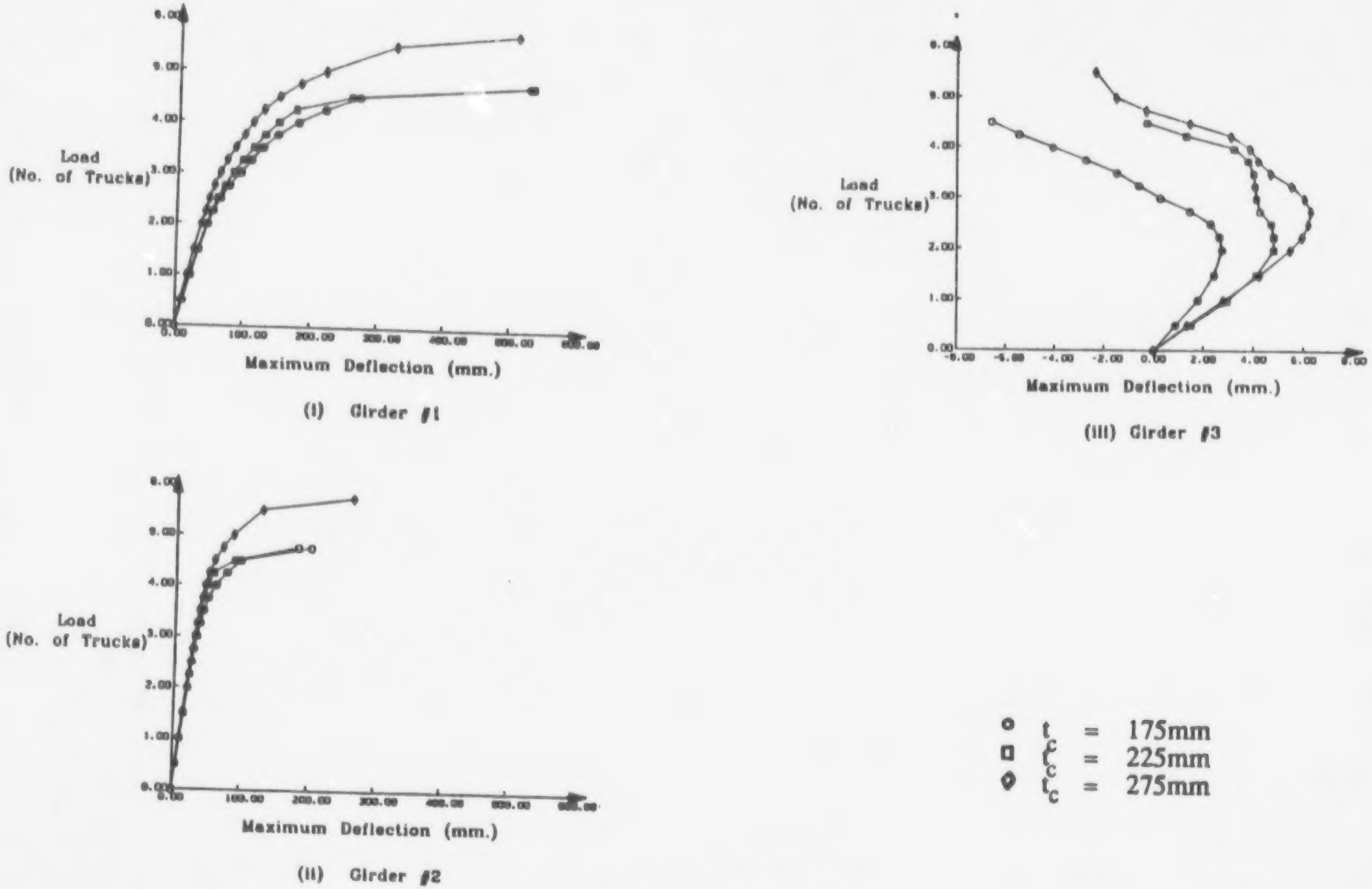

Fig. 119: Effect of Slab-Girder Stiffness Ratio on Load-Maximum Deflection of Bridges ST1, ST2, and ST3 (Case 1)

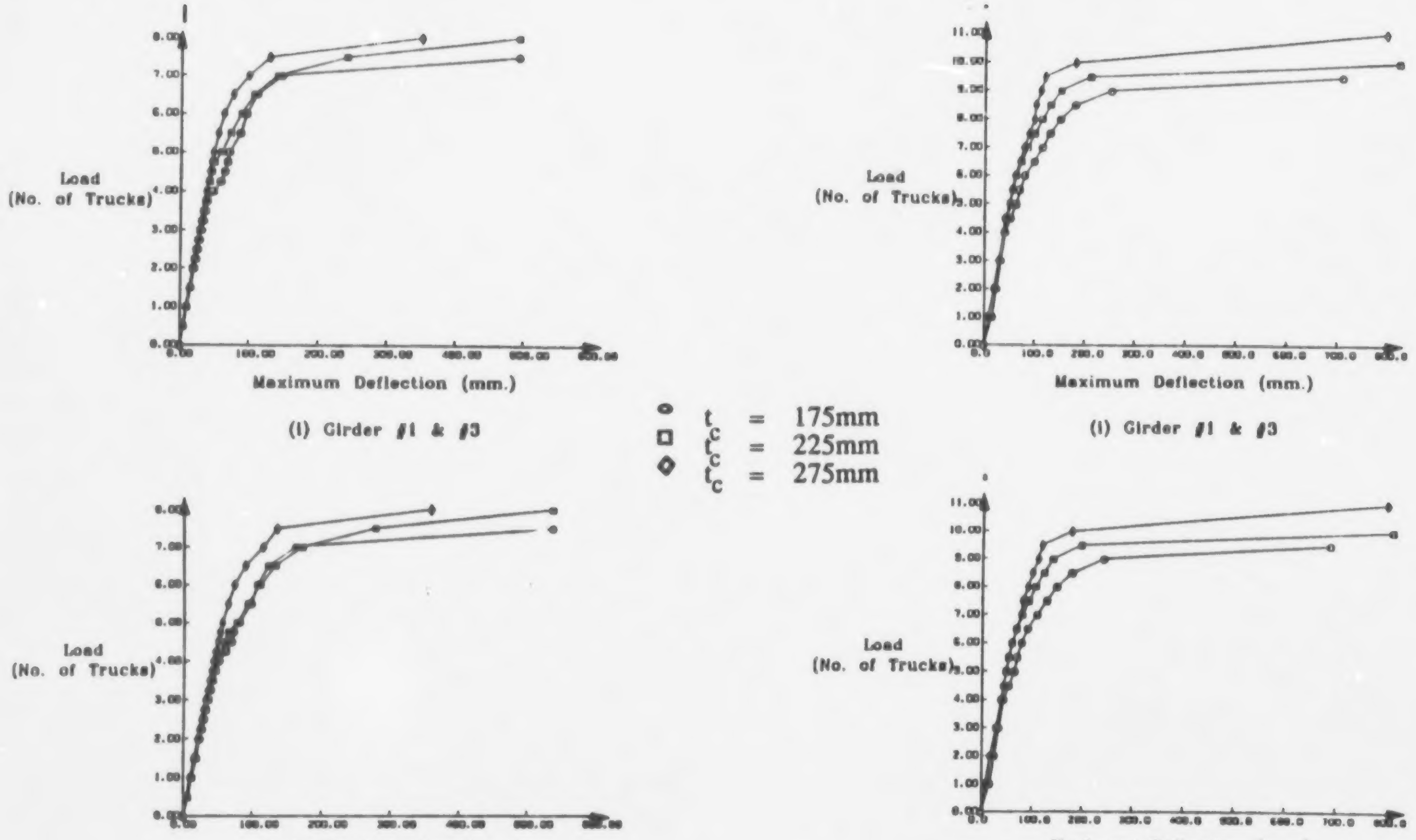

(i) Girder #1 & #3

(i) Girder #1 & #3

(ii) Girder #2

(ii) Girder #2

Fig. 120: Effect of Slab-Girder Stiffness Ratio on Load-Maximum Deflection of Bridges ST1, ST2, and ST3 (Case 2 and 3)

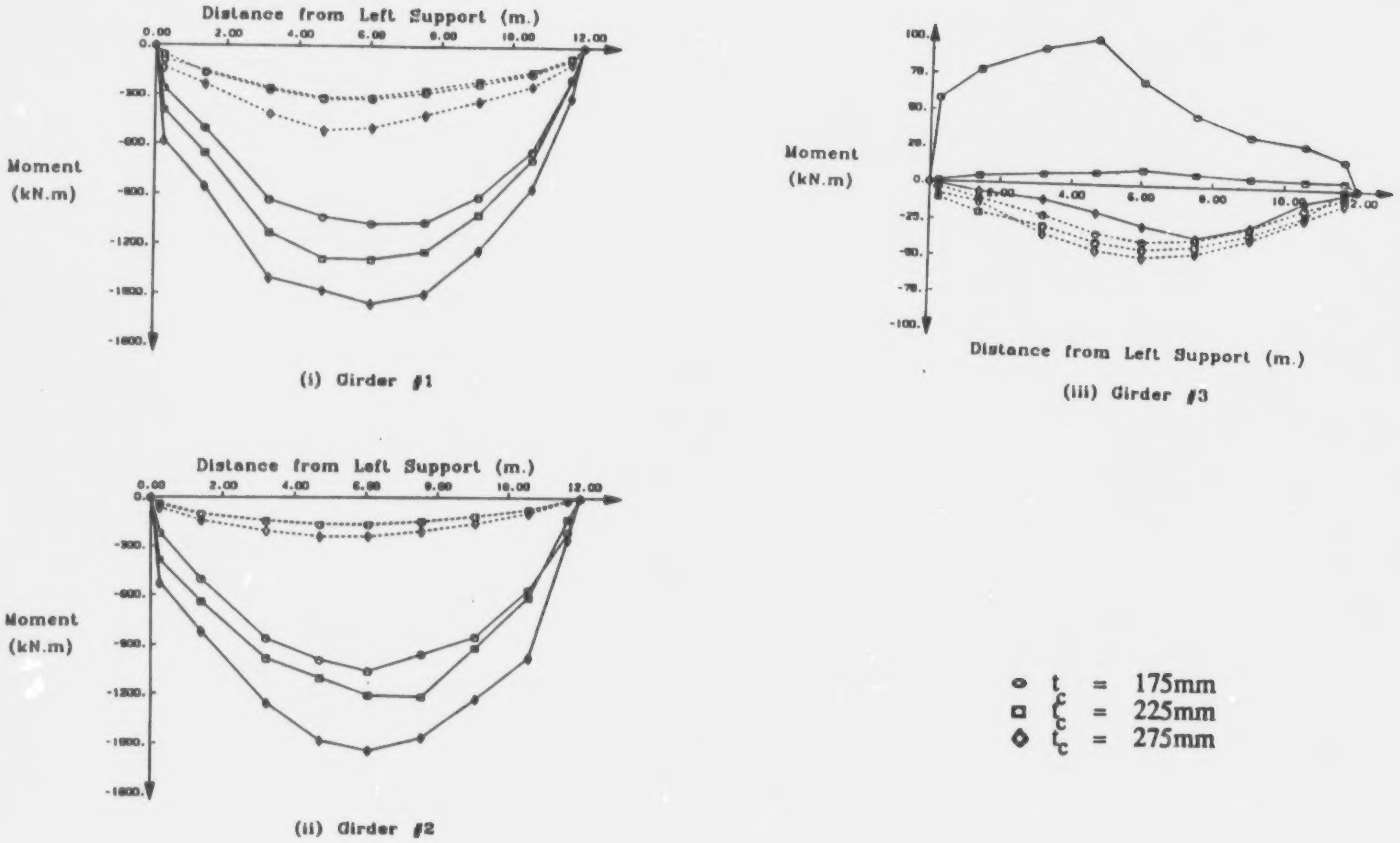

(i) Girder #1

(ii) Girder #2

(iii) Girder #3

Fig. 121: Effect of Slab-Girder Stiffness Ratio on Moment Distribution in Bridges ST1, ST2, and ST3 (Case 1)

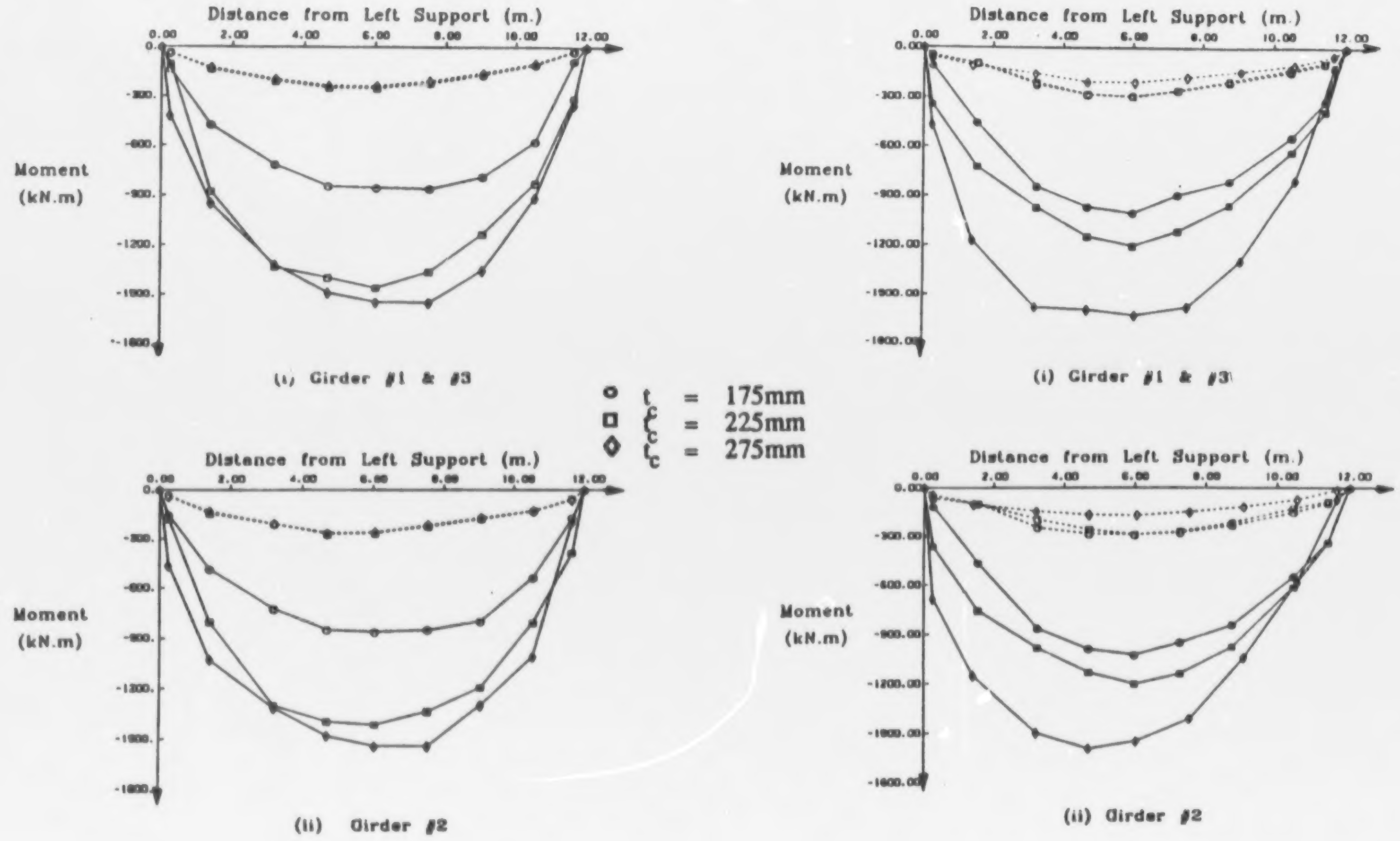

(i) Girder #1 & #3

(i) Girder #1 & #3

(ii) Girder #2

(ii) Girder #2

Fig. 122: Effect of Slab-Girder Stiffness Ratio on Moment Distribution in Bridges ST1, ST2, and ST3 (Case 2&3)

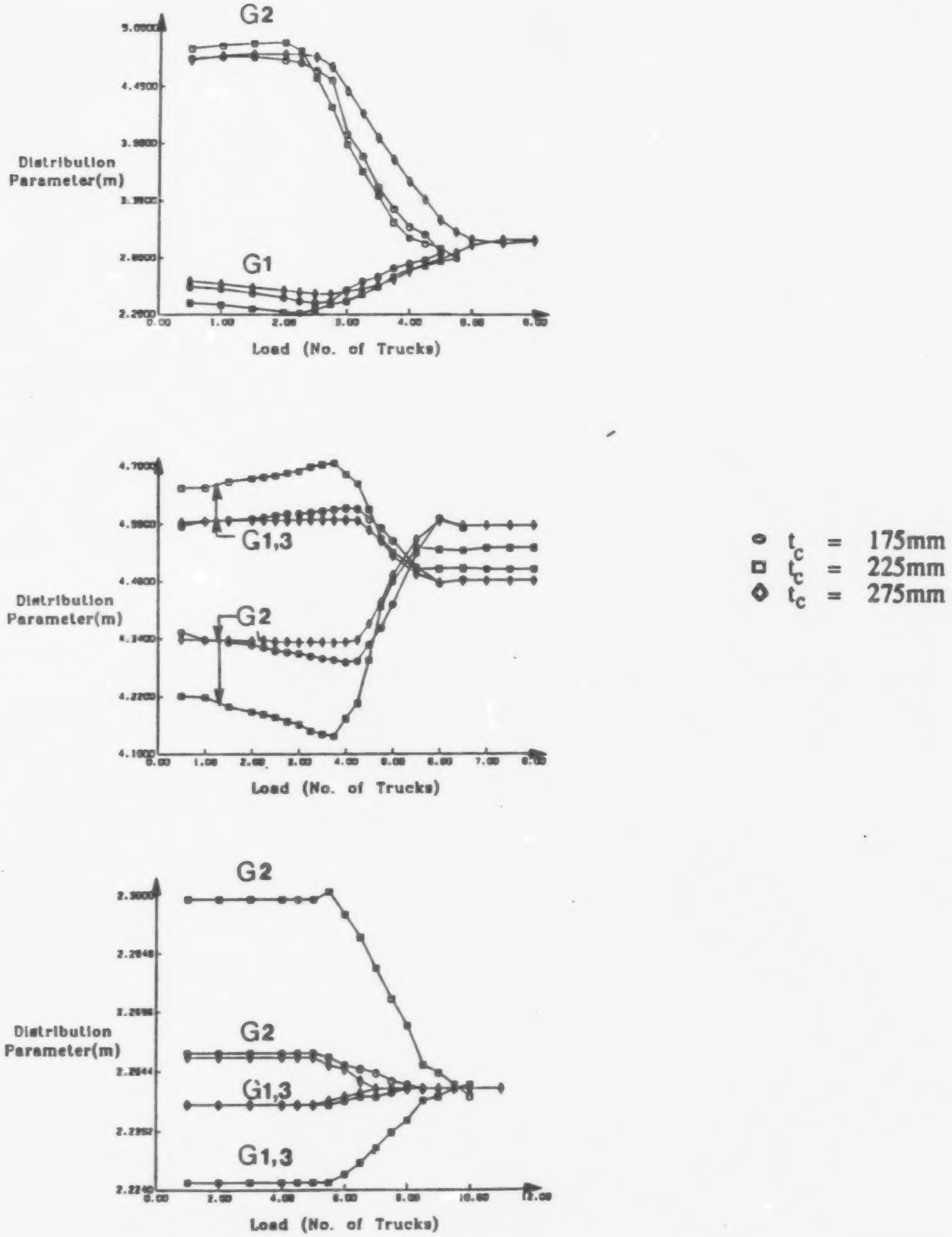

Fig. 123: Effect of Slab-Girder Stiffness on Distribution Parameter D_d

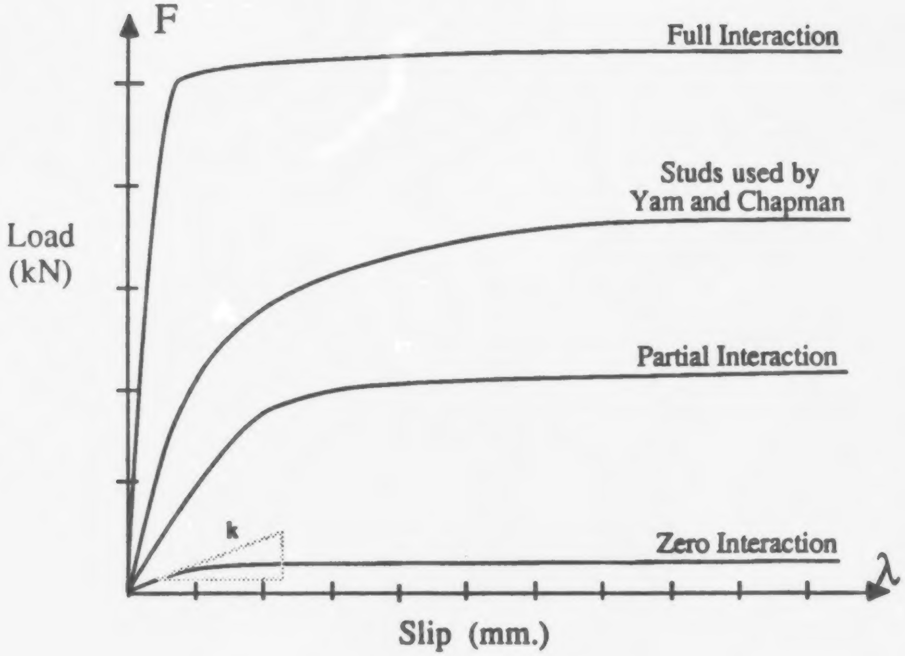

Fig. 124: Shear Connector Load-Slip Relationships Employed in the Analysis

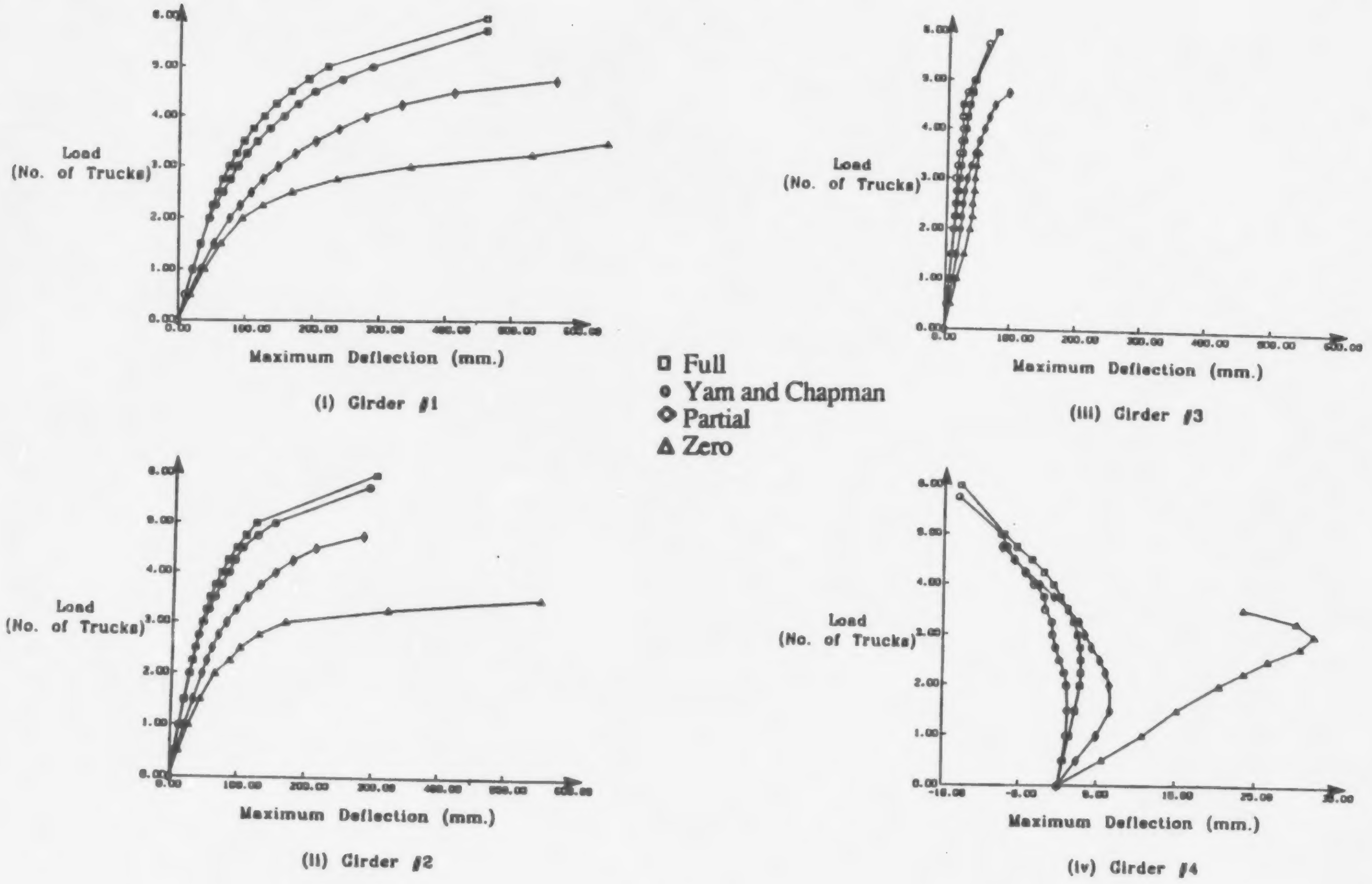

(i) Girder #1

(ii) Girder #2

(iii) Girder #3

(iv) Girder #4

Fig. 125: Effect of Degree of Interaction on Load-Maximum Deflection of Bridges DI1, DI2, DI3 and DI4 (Case 1)

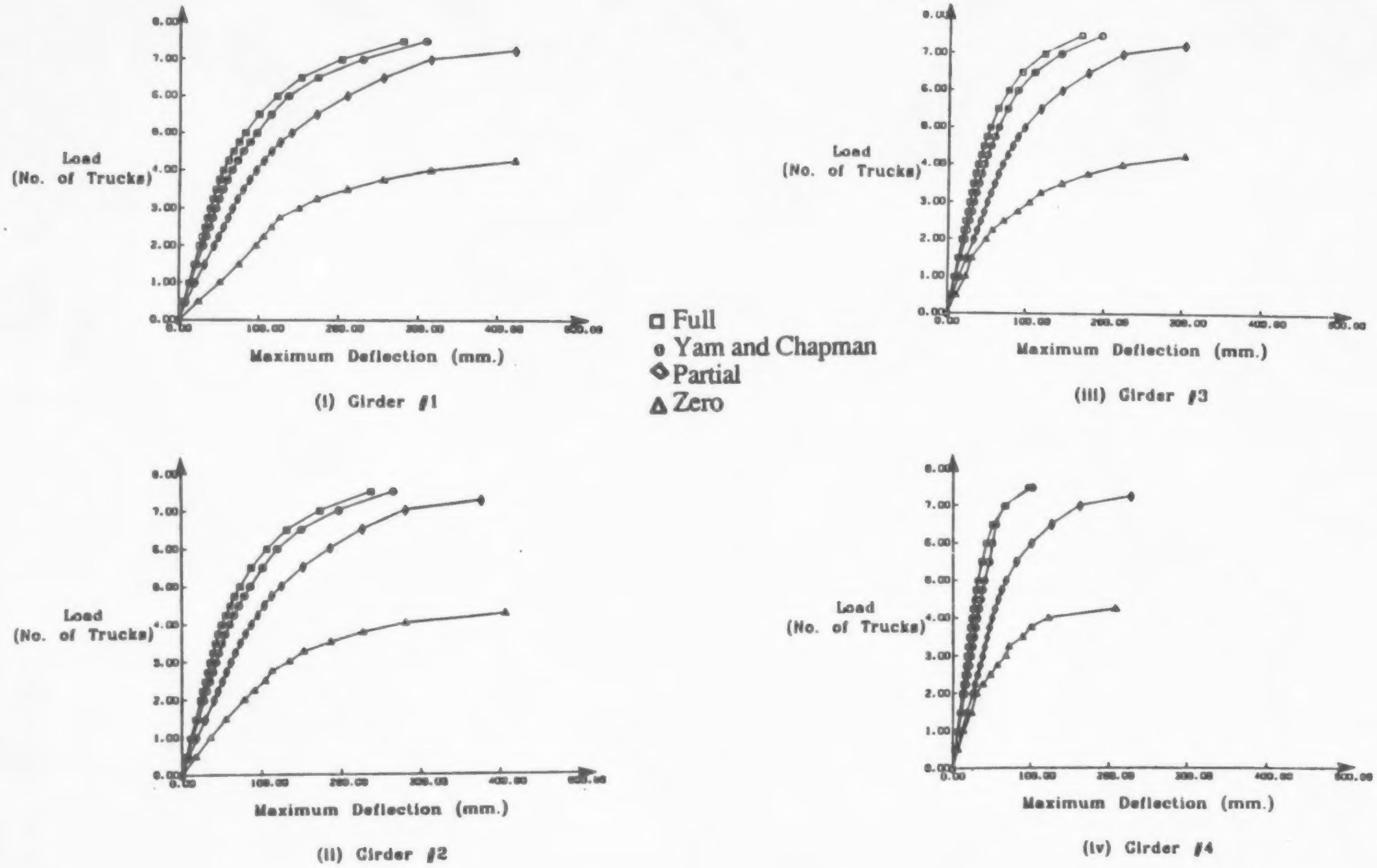

(i) Girder #1

(iii) Girder #3

(ii) Girder #2

(iv) Girder #4

Fig. 126: Effect of Degree of Interaction on Load-Maximum Deflection of Bridges DI1, DI2, DI3 and DI4 (Case 2)

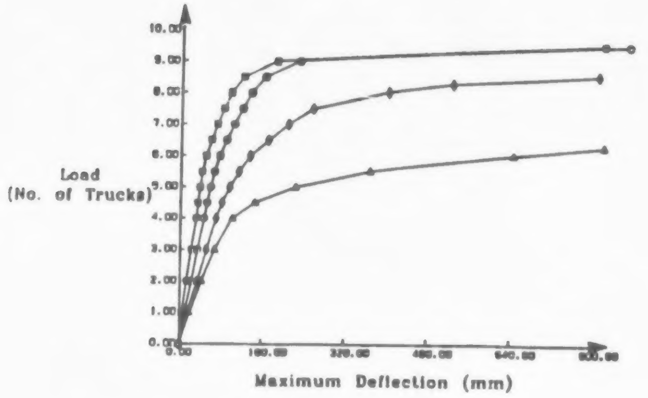

(i) Girder #1 & #4

□ Full
○ Yam and Chapman
◇ Partial
△ Zero

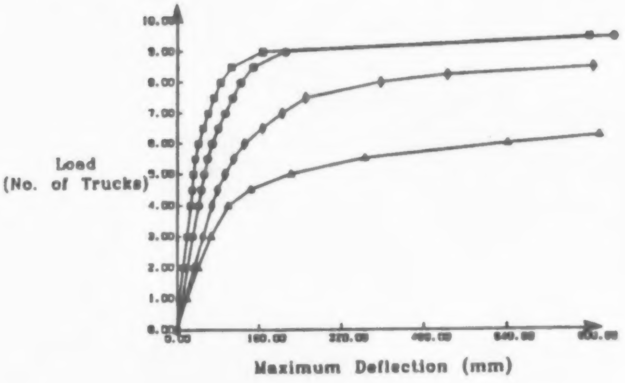

(i) Girder #2 & #3

Fig. 127: Effect of Degree of Interaction on Load-Maximum Deflection of Bridges DI1, DI2, DI3 and DI4 (Case 3)

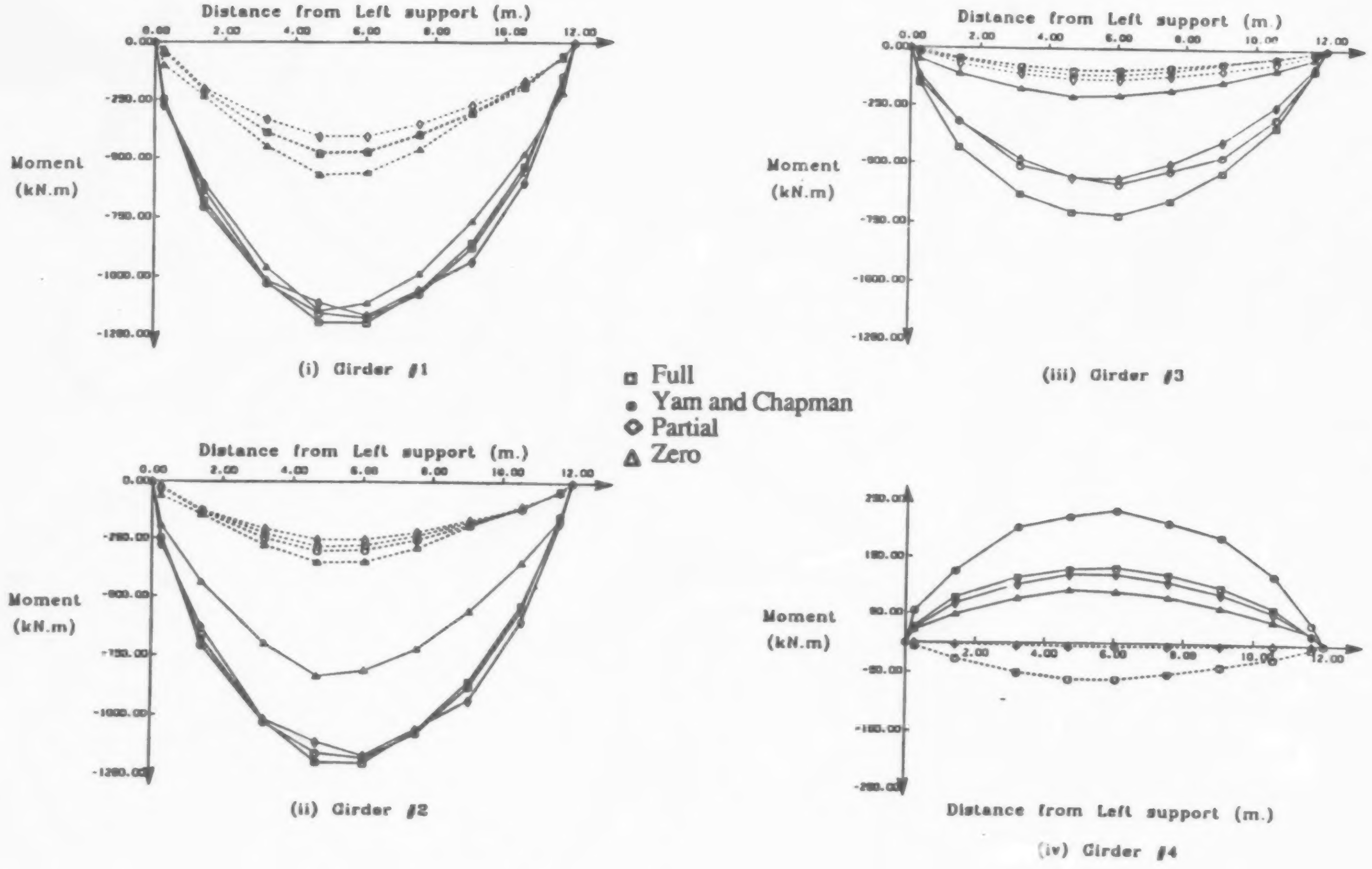

(i) Girder #1

(ii) Girder #2

(iii) Girder #3

(iv) Girder #4

Fig. 128: Effect of Degree of Interaction on Moment Distribution in Bridges DI1, DI2, DI3 and DI4 (Case 1)

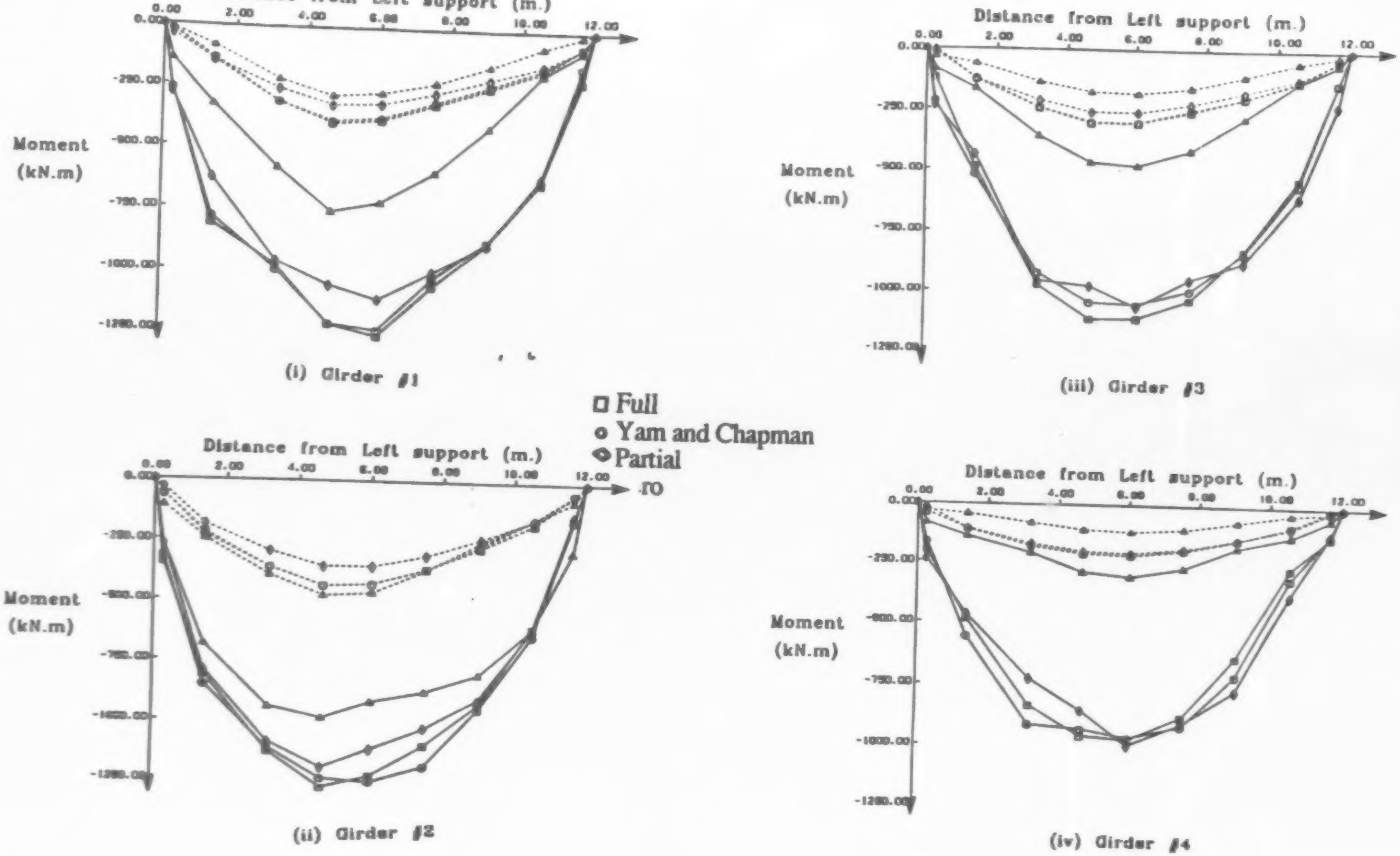

(i) Girder #1

(ii) Girder #2

(iii) Girder #3

(iv) Girder #4

Fig. 129: Effect of Degree of Interaction on Moment Distribution in Bridges DI1, DI2, DI3 and DI4 (Case 2)

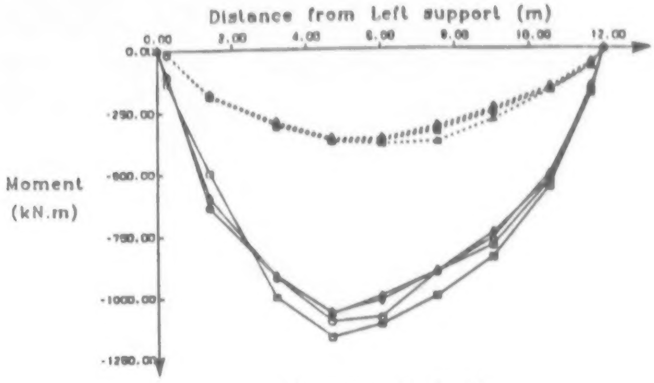

(i) Girder #1 & #4

□ Full
● Yam and Chapman
◇ Partial
△ Zero

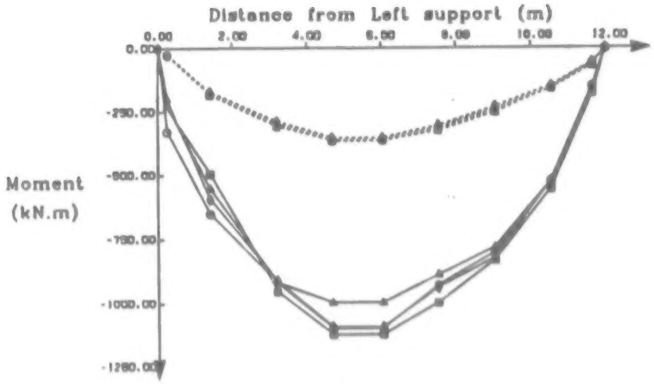

(i) Girder #2 & #3

Fig. 130: Effect of Degree of Interaction on Moment Distribution in Bridges DI1, DI2, DI3 and DI4 (Case 3)

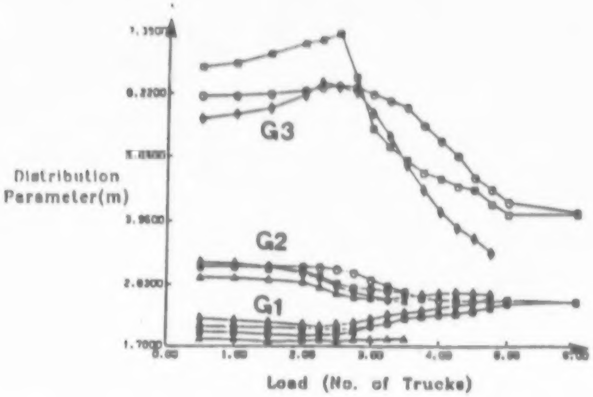

(case #1)

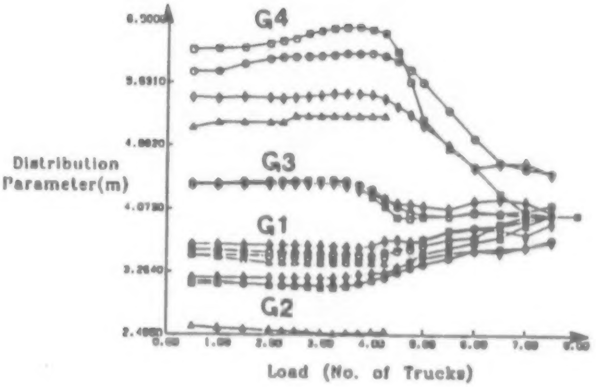

(case #2)

□ Full
○ Yam and Chapman
◇ Partial
△ Zero

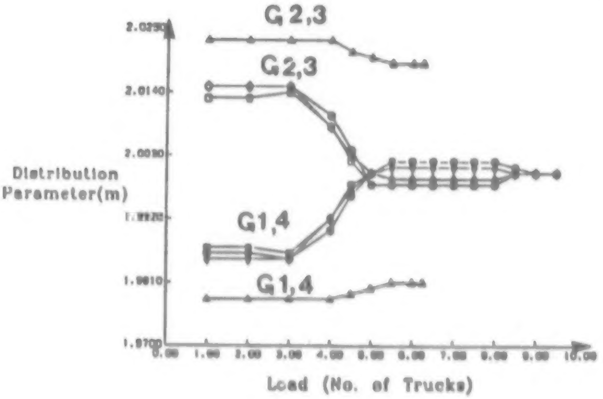

(case #3)

Fig. 131: Effect of Degree of interaction on Distribution Parameter D_d

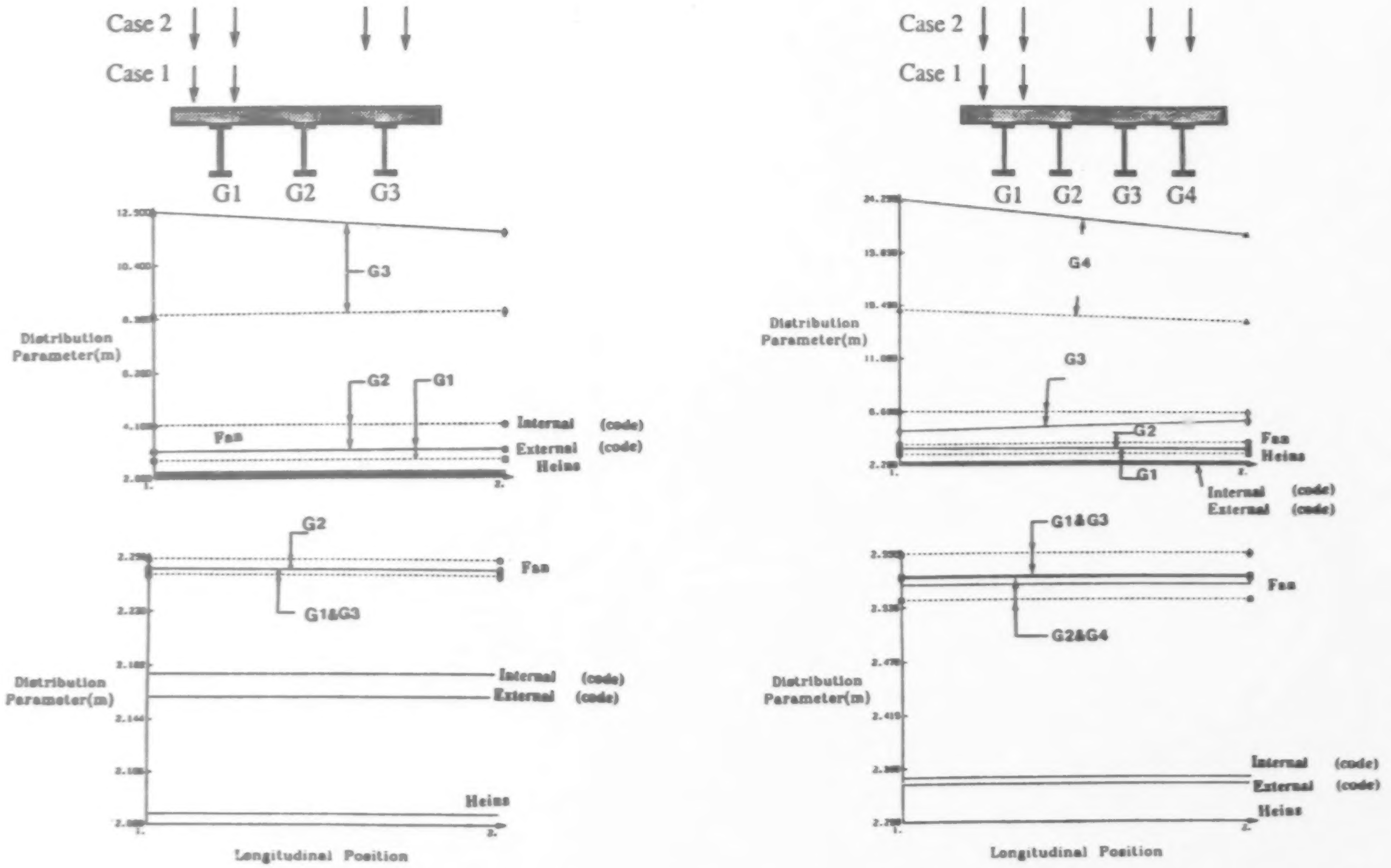

Fig. 132: Variation of Distribution Parameter, D_d, with Longitudinal Position of the Truck

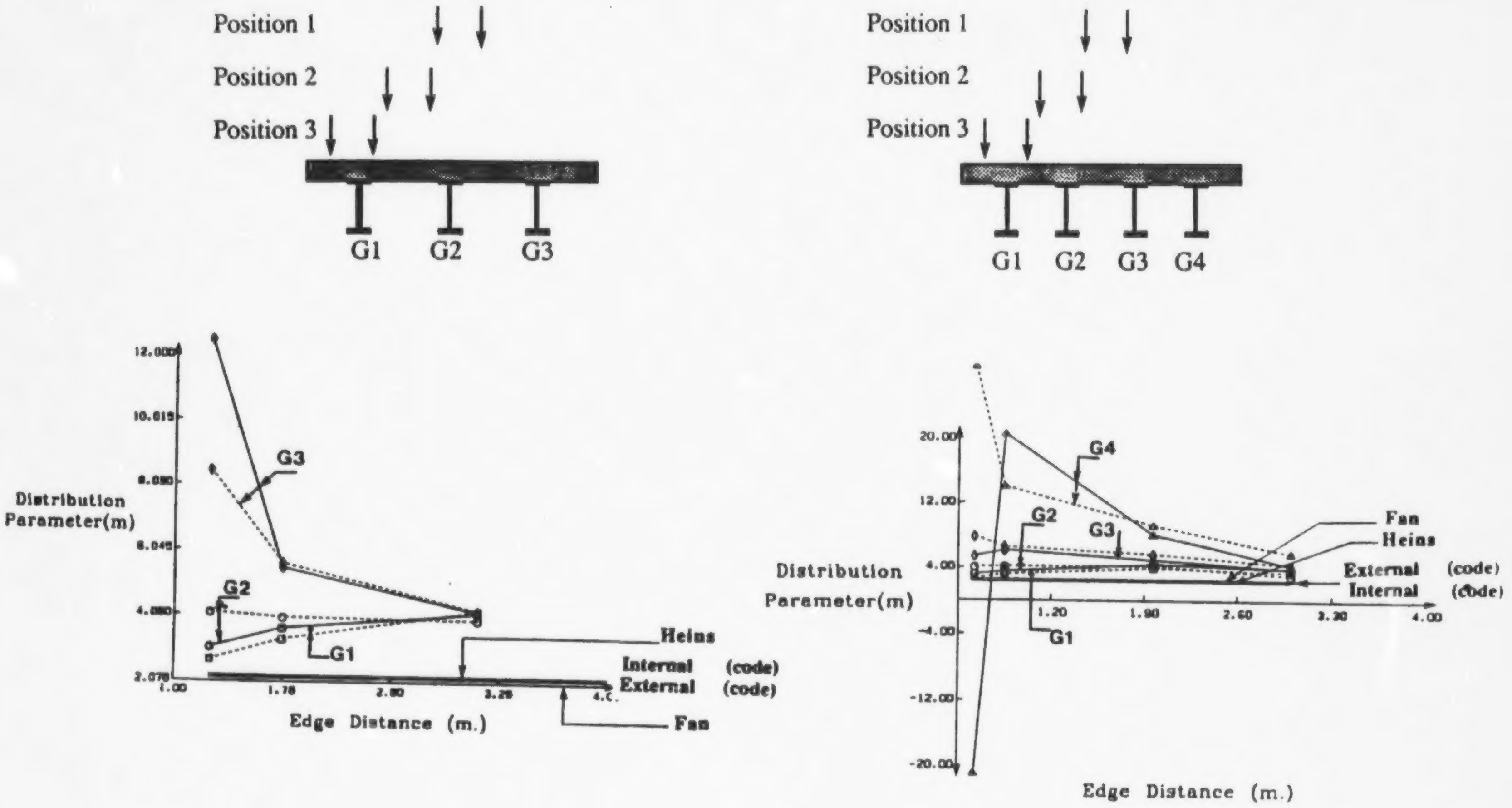

Fig. 133: Variation of Distribution Parameter, D_d, with Transverse Position of the Truck

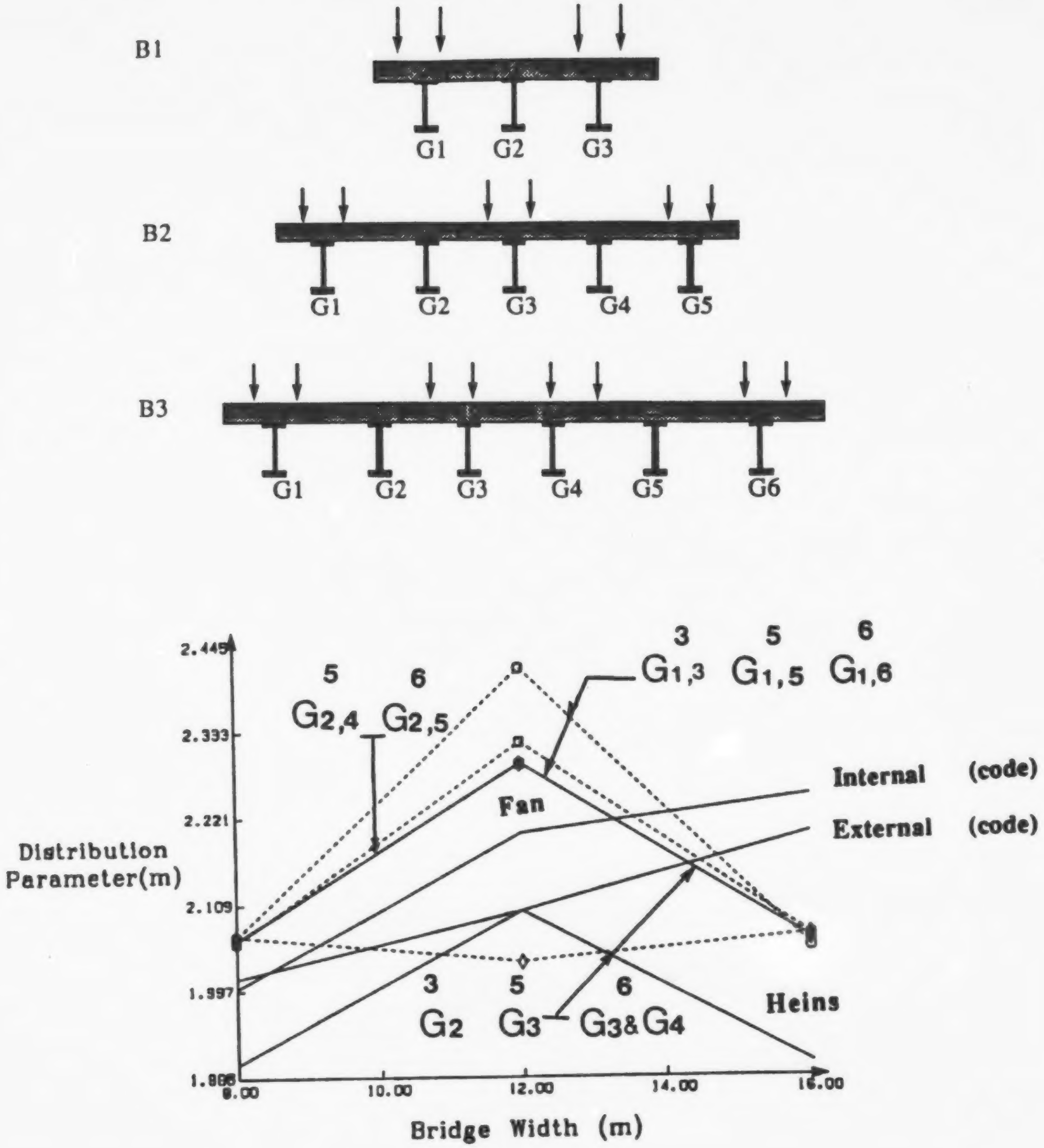

Fig. 134: Variation of Distribution Parameter, D_d, with Bridge Width

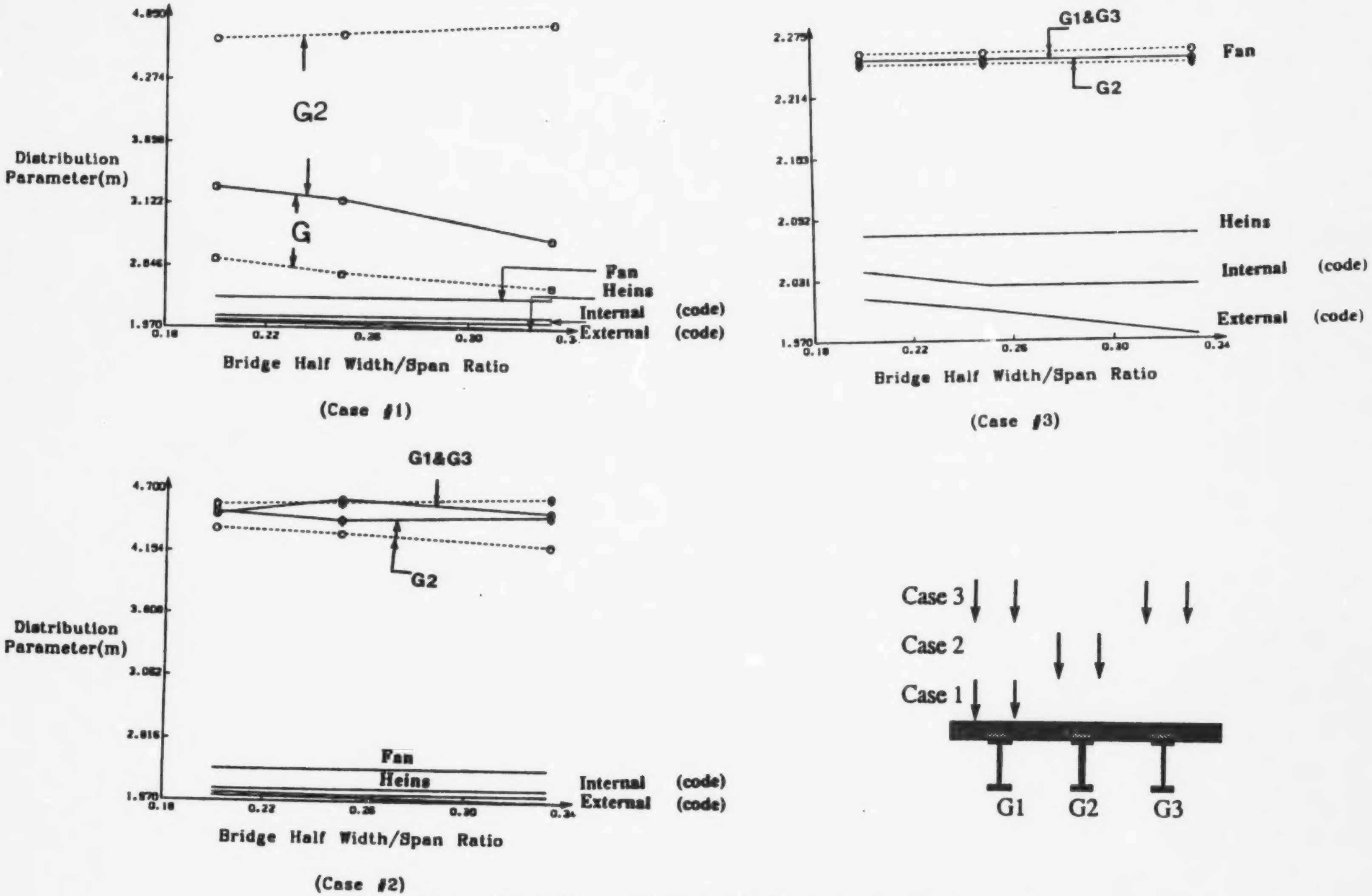

(Case #1)

(Case #3)

(Case #2)

Fig. 135: Variation of Distribution Parameter, D_d, with Bridge Width/Span Ratio

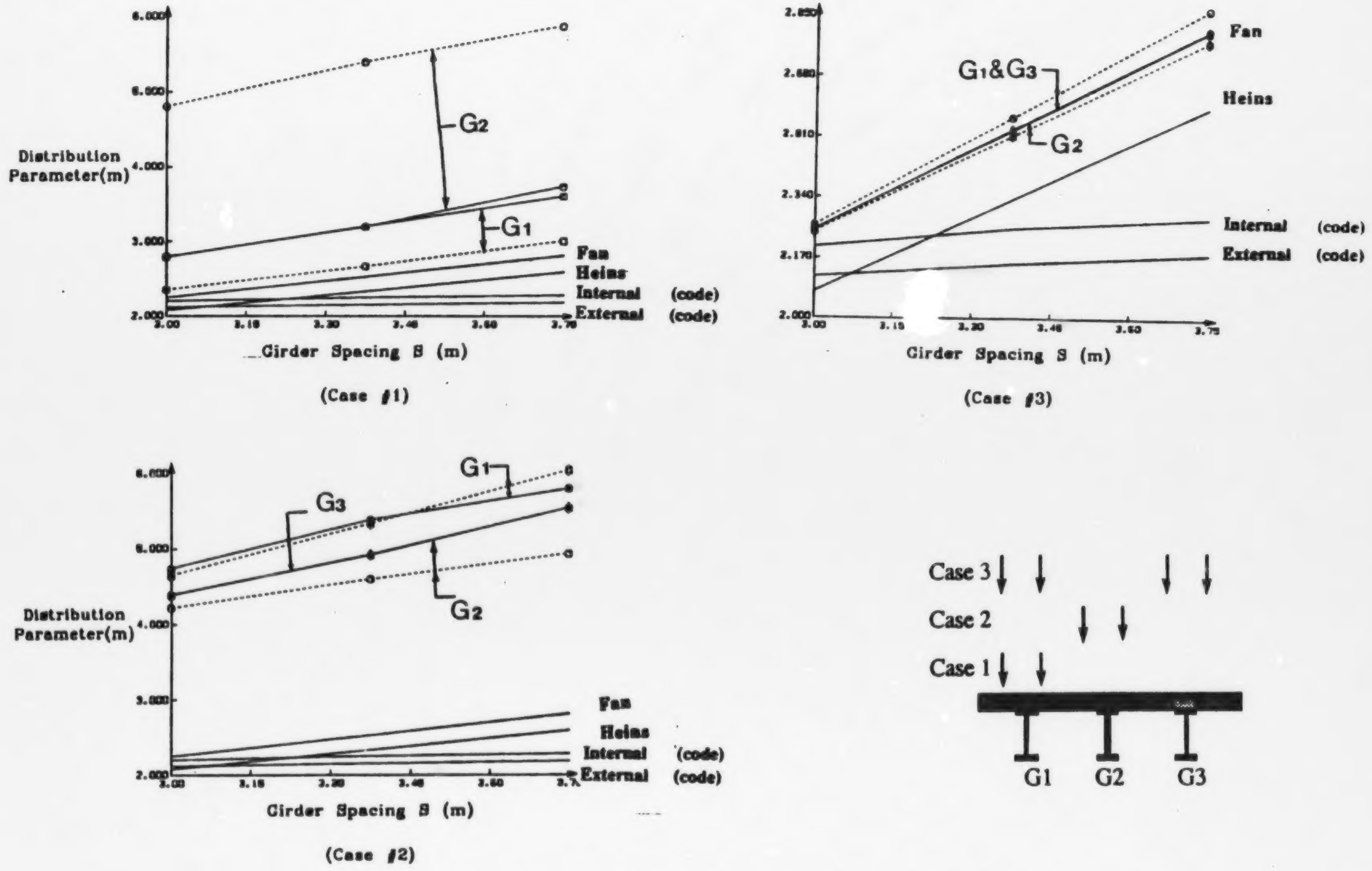

(Case #1)

(Case #3)

(Case #2)

Fig. 136: Variation of Distribution Parameter, D_d, with Girder Spacing (Three Girder System)

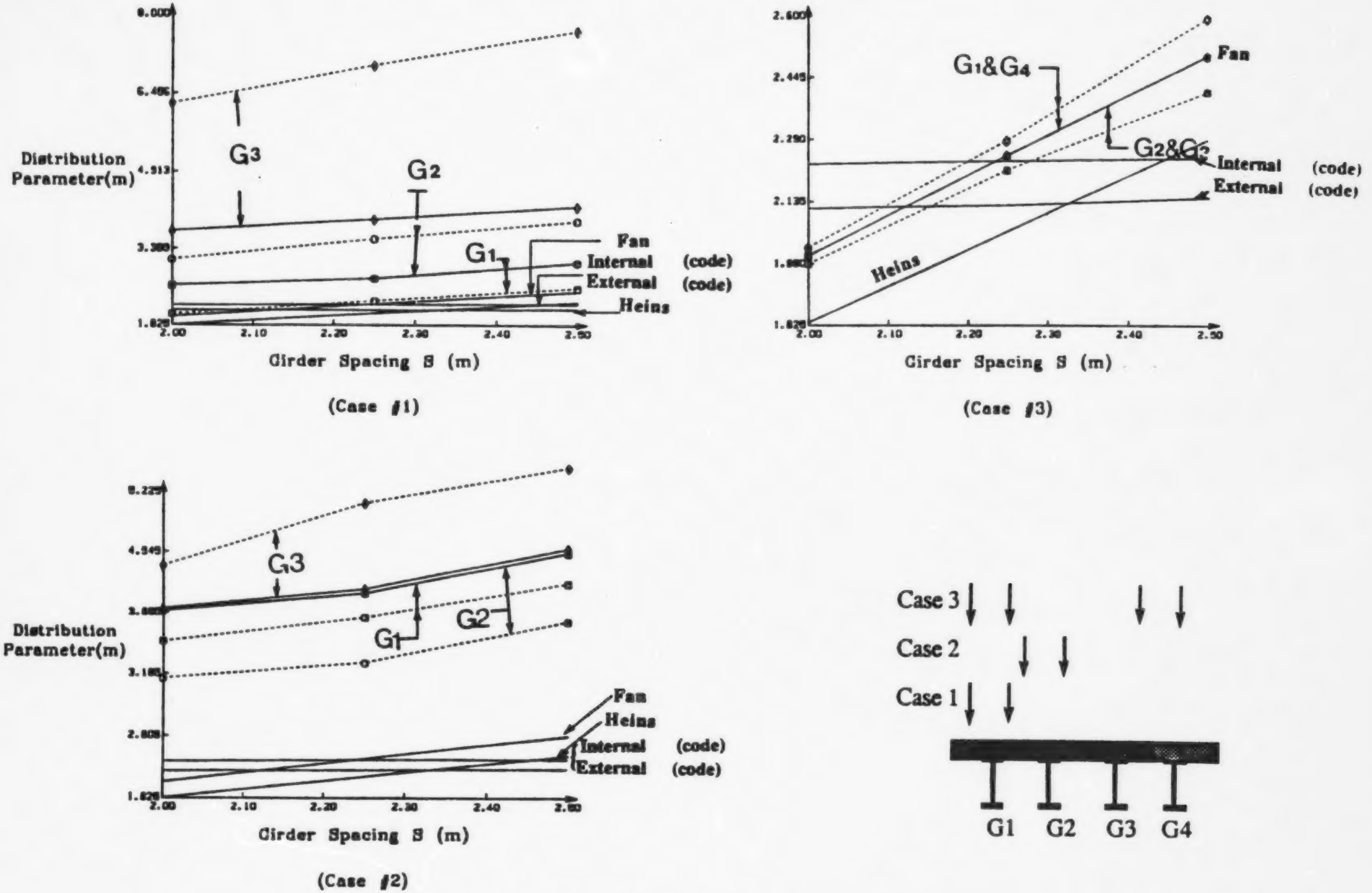

Fig. 137: Variation of Distribution Parameter, D_d, with Girder Spacing (Four Girder System)

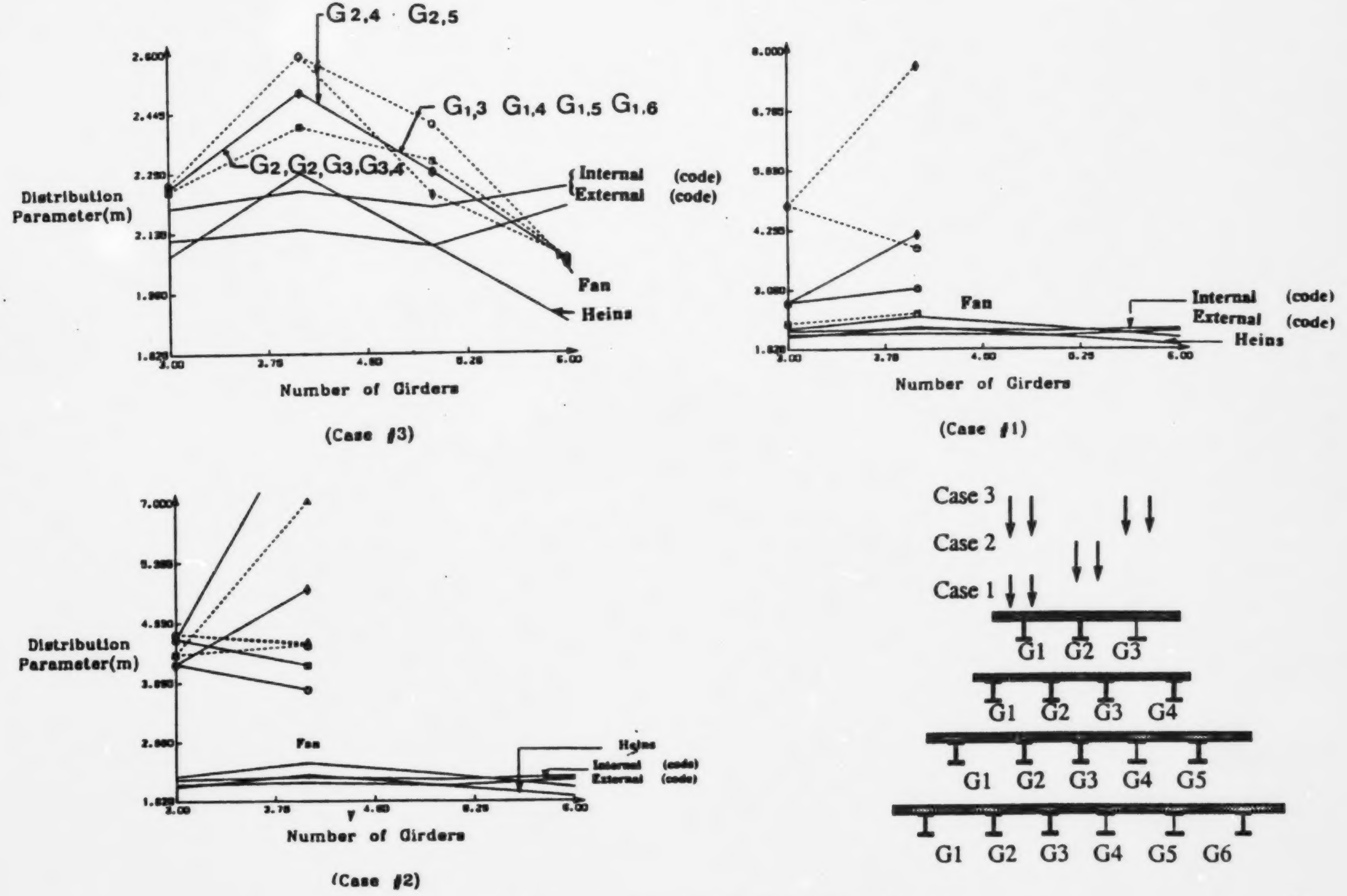

Fig. 138: Variation of Distribution Parameter, D_d, with Number of Girders

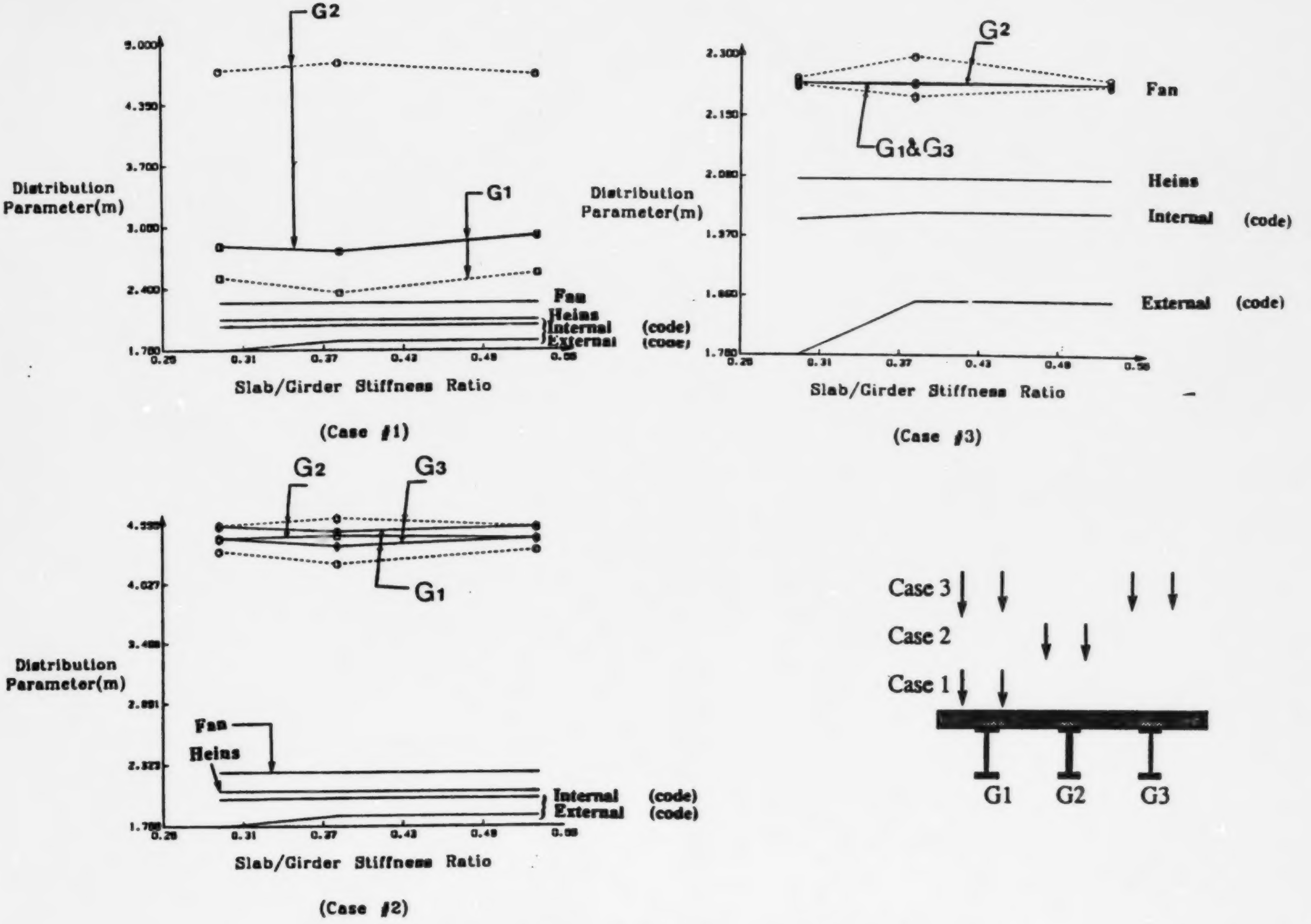

(Case #1)

(Case #3)

(Case #2)

Fig. 139: Variation of Distribution Parameter, D_d, with Slab/Girder Stiffness Ratio

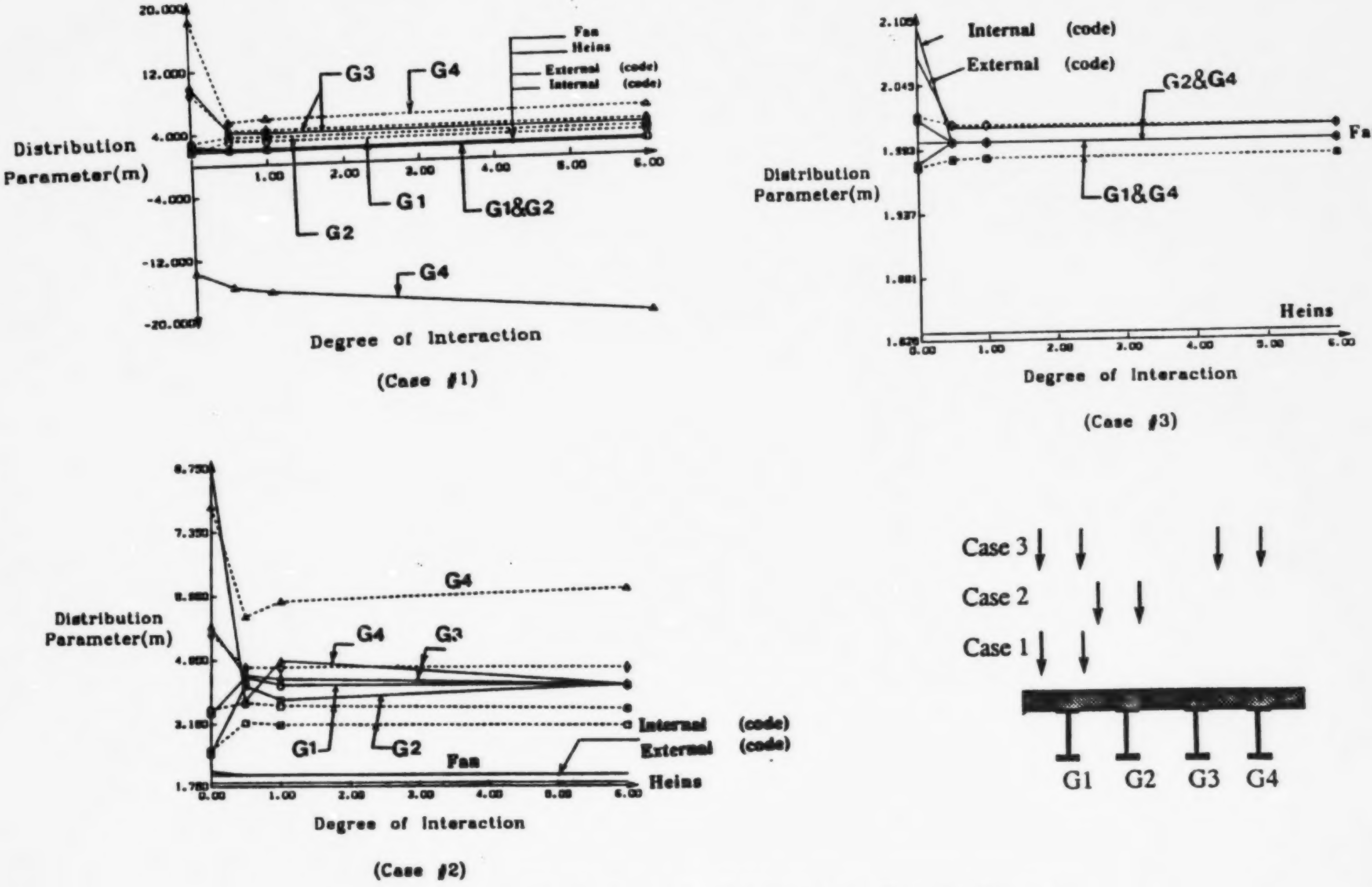

(Case #1)

(Case #3)

(Case #2)

Fig. 140: Variation of Distribution Parameter, D_d, with Degree of Interaction

Appendix A

Dimension and Structural Details of the Bridges Analyzed

Notation

l	bridge length (m)
$2b$	bridge width (m)
S	girder spacing (m)
NL	number of lanes
NG	number of girders
W	girder section number
t_c	concrete slab thickness (mm)
$(A_s)_t$	area of the top reinforcement layer (mm^2/m)
$(A_s)_b$	area of the bottom reinforcement layer (mm^2/m)

Bridges of section 6.4.1.1 and 6.4.1.2

Bridge	l	2b	S	NL	NG	W	t_c	$(A_s)_t$	$(A_s)_b$
LP1	16.00	8.00	2.750	2	3	W610 × 125	225	400.0	400.0
LP2	16.00	8.00	2.500	2	4	W610 × 125	225	400.0	400.0

Bridges of section 6.4.2

Bridge	l	2b	S	NL	NG	W	t_c	$(A_s)_t$	$(A_s)_b$
BW1	16.00	8.00	2.750	2	3	W610 × 125	225	400.0	400.0
BW2	16.00	12.00	2.750	3	5	W610 × 125	225	400.0	400.0
BW3	16.00	16.00	2.750	4	6	W610 × 125	225	400.0	400.0

Bridges of section 6.4.3

Bridge	l	2b	S	NL	NG	W	t_c	$(A_s)_t$	$(A_s)_b$
LB1	12.00	8.00	3.000	2	3	W610 × 125	225	400.0	400.0
LB2	16.00	8.00	3.000	2	3	W690 × 170	225	400.0	400.0
LB3	20.00	8.00	3.000	2	3	W760 × 161	225	400.0	400.0

Bridges of section 6.4.4

Bridge	l	2b	S	NL	NG	W	t_c	$(A_s)_t$	$(A_s)_b$
GS1	12.00	8.00	3.750	2	3	W610 × 155	225	400.0	400.0
GS2	12.00	8.00	3.375	2	3	W610 × 140	225	400.0	400.0
GS3	12.00	8.00	3.000	2	3	W610 × 125	225	400.0	400.0
GS4	12.00	8.00	2.500	2	4	W530 × 123	225	400.0	400.0
GS5	12.00	8.00	2.250	2	4	W530 × 109	225	400.0	400.0
GS6	12.00	8.00	2.000	2	4	W530 × 101	225	400.0	400.0

Bridges of section 6.4.5

Bridge	l	2b	S	NL	NG	W	t_c	$(A_s)_t$	$(A_s)_b$
NG3	16.00	8.00	2.750	2	3	W610 × 125	225	400.0	400.0
NG4	16.00	8.00	2.500	2	4	W610 × 125	225	400.0	400.0
NG5	16.00	8.00	2.750	3	5	W610 × 125	225	400.0	400.0
NG6	16.00	8.00	2.750	4	6	W610 × 125	225	400.0	400.0

Bridges of section 6.4.6

Bridge	l	2b	S	NL	NG	W	t_c	$(A_s)_t$	$(A_s)_b$
ST1	12.00	8.00	3.000	2	4	W610 × 125	175	400.0	400.0
ST2	12.00	8.00	3.000	2	4	W610 × 125	225	400.0	400.0
ST3	12.00	8.00	3.000	2	4	W610 × 125	275	400.0	400.0

Bridges of section 6.4.7

Bridge	l	2b	S	NL	NG	W	t_c	$(A_s)_t$	$(A_s)_b$
DI1	12.00	8.00	2.500	2	4	W530 × 123	225	400.0	400.0
DI2	12.00	8.00	2.500	2	4	W530 × 123	225	400.0	400.0
DI3	12.00	8.00	2.500	2	4	W530 × 123	225	400.0	400.0
DI4	12.00	8.00	2.500	2	4	W530 × 123	225	400.0	400.0

Appendix B

Flexural and Torsional Parameters for Some Bridges Analyzed

Notation

l	bridge length (m)
$2b$	bridge width (m)
S	girder spacing (m)
NL	number of lanes
NG	number of girders
α	characterizing torsional parameter
θ	characterizing flexural parameter
(D_x)	longitudinal flexural rigidity per unit width $\frac{mm^4}{mm}$ (concrete unit)
$(D_x)_s$	longitudinal flexural rigidity of the slab per unit width $\frac{mm^4}{mm}$ (concrete unit)
$(D_x)_G$	longitudinal flexural rigidity of the beam per unit width $\frac{mm^4}{mm}$ (concrete unit)
(D_y)	transverse flexural rigidity per unit width $\frac{mm^4}{mm}$ (concrete unit)
(D_{xy}), (D_{yx})	longitudinal torsional rigidity per unit width $\frac{mm^4}{mm}$ (concrete unit)
(D_1), (D_2)	transverse torsional rigidity per unit width $\frac{mm^4}{mm}$ (concrete unit)
$(D_d)_{ext}$	distribution parameter of external portions (m)
$(D_d)_{int}$	distribution parameter of internal portions (m)

Table B-1

Bridge	BW1	BW2	BW3
$2b$	8	12	16
D_x	31.335×10^{10}	31.335×10^{10}	31.335×10^{10}
D_y	2.719×10^{10}	2.719×10^{10}	2.719×10^{10}
$D_{xy} = D_{yx}$	2.311×10^{10}	2.311×10^{10}	2.311×10^{10}
$D_1 = D_2$	0.408×10^{10}	0.408×10^{10}	0.408×10^{10}
α	0.29457	0.29457	0.29457
θ	$1.8245 \frac{b}{l}$	$1.8245 \frac{b}{l}$	$1.8245 \frac{b}{l}$
θ	0.46062	0.6909	0.92124
$(D_x)_{ext}$	2.013	2.100	2.200
$(D_x)_{int}$	2.000	2.200	2.250

Table B-2

Bridge	LW1	LW2	LW3
$\frac{b}{l}$	1.5	2.0	2.50
D_x	25.116×10^{10}	38.685×10^{10}	42.079×10^{10}
D_y	2.719×10^{10}	2.719×10^{10}	2.719×10^{10}
$D_{xy} = D_{yx}$	2.311×10^{10}	2.311×10^{10}	2.311×10^{10}
$D_1 = D_2$	0.408×10^{10}	0.408×10^{10}	0.408×10^{10}
α	$\frac{c_1}{\sqrt{D_x}}$	$\frac{c_1}{\sqrt{D_x}}$	$\frac{c_1}{\sqrt{D_x}}$
α	0.32903	0.26511	0.25420
θ	$c_2 R {D_x}^{0.25}$	$c_2 R {D_x}^{0.25}$	$c_2 R {D_x}^{0.25}$
θ	0.5811	0.4855	0.3967
$(D_x)_{ext}$	2.013	2.013	2.013
$(D_x)_{int}$	1.975	2.000	2.013

Table B-3

Bridge	ST1	ST2	ST3
t_c	175	225	275
$(D_x)_s$	3912×10^6	5300×10^6	7575×10^6
$(D_x)_G$	13362×10^6	13893×10^6	14267×10^6
D_x	17274×10^6	19193×10^6	21842×10^6
$\frac{(D_x)_s}{(D_x)_G}$	0.293	0.382	0.531
α	0.1432	0.1882	0.1920
θ	0.8710	0.7596	0.7522
$(D_x)_{ext}$	2.00	2.013	2.013
$(D_x)_{int}$	1.75	1.85	1.85